Mechanical Behaviour of Ti6Al4V Lattice Structures Fabricated by Electron Beam Powder Bed Fusion

Yawen Huang

A thesis submitted to
Auckland University of Technology
in fulfilment of the requirements for the degree of
Doctor of Philosophy (PhD)

2025
School of Engineering, Computer and Mathematical Sciences

Abstract

The development of Additive manufacturing (AM) techniques, such as electron beam powder bed fusion (EBPBF) or electron beam melting (EBM), allows the production of light-weight metallic objects with complex structures, such as lattice structures and cellular porous structures with limited geometrical constrains. In recent years, PBF-fabricated lattice structures with tailored mechanical properties have successfully been designed and manufactured for various applications such as aero engineering and biomedical engineering, as demonstrated in numerous published works. The mechanical properties of the PBF lattices have been extensively investigated considering uniaxial loadings. However, in the real-life applications, the loading can occur in varied directions and the mechanical properties of the PBF lattices can be affected by the different loading directions (LDs). Therefore, the anisotropic mechanical behaviour of the lattice structures must be well understood. Even though published works have confirmed that the mechanical behaviour of PBF lattices structures is affected by the geometrical features, process-induced defects and post-process treatments, limited attention has been given to the effect of LD with respect to the unit cell direction of the lattice.

For biomedical implant applications, particularly in hip implants, compressive loading is dominant, thus, this PhD research focuses on investigate the mechanical behaviour of the EBPBF fabricated Ti6Al4V simple-cubic cell based lattice structures under quasi-static and cyclic compressive loadings considering the orientation-dependant effects with respect to the LD. The SC unit cell has been chosen as it can provide a condition for studying the orientation effects without the ambiguity introduced by more complex unit cell geometries. A series of experimental quasi-static and fatigue tests and simulation models were conducted on different EBPBF lattice samples. Three groups of simple-cubic-cell-based lattice structures were produced by EBPBF with unit cell orientations (UCOs) of [001]//LD, [011]//LD and [111]//LD and subject to quasi-static testing and cyclic compressive testing, followed by detailed examinations. In addition, finite element models (FEMs) were conducted to analyse the compressive behaviour of the lattices. The combined effects of LD and UCO on quasi-static and cyclic compressive properties of the lattices have been studied and discussed, providing insight into the anisotropic quasi-static and fatigue behaviour of the lattices. Then an exploratory study has been conducted, porous femoral stem has been designed based on the findings in SC lattices to meet the required fatigue life of 5×10^6 cycles specified the international standard while maintaining the fully porous surface for bone ingrowth. FE simulations and fracture surface analysis has been conducted to identify the effects of stress concentrations and manufacturing defects on the fatigue strength of the produced porous femoral stems. In addition, the effects of surface defects on the fatigue performance of the EBPBF stems have been investigated using Kitagawa-Takahashi approach.

It has been found that both the quasi-static and cyclic behaviours of the simple cubic lattices are strongly dependent on their UCOs with respect to the LDs. Among the three groups of lattices, [001]//LD

specimens exhibited the most favourable quasi-static compressive strength, with yield strength up to 200% higher and a 4-6 times higher fracture strain than those of the [011]//LD and [111]//LD lattices, due to their less sensitivity to surface defects. Local stress concentrations were found in non-[001]//LD specimens, resulting in yielding and fracturing of these lattices under low loading levels.

Considerably greater orientation-dependent effects have been identified in the compressive fatigue behaviour of the lattices, [001]//LD lattices demonstrated approximately 800% higher fatigue strength at 5×10^6 cycles than the non-[001]//LD structures. The low fatigue strength of the non-[001]//LD lattices resulted from crack initiation readily occurring in the high-tension locations, specifically in the top and bottom nodes within each unit cell. The subsequent sideway growth of these cracks leading to fracturing along (001) will be shown. This failure mechanism is absent in [001]//LD lattices resulting in their significantly higher fatigue strength. Examining the data in the literature has revealed that fatigue strength values of all non-SC lattice structures are low, likely due to the same failure mechanism identified for non-[001]//LD SC lattices in this study.

The fatigue testing results of the porous femoral stems have suggested that the cracks always initiated at the tension-concentrated zone at lateral side of the stem. With topologically optimised reinforcement, the EBPBF porous stems have successfully met the required fatigue life as specified in the international standard while maintaining sufficient surface porosity for osseointegration. More importantly, the linear-fracture-mechanics-based analysis of surface defects on the EBPBF stems demonstrated that the lack-of-fusion defects on the stress-concentrated locations was the dominant factor contributing to the reduction of the fatigue life of the EBPBF stem components rather than surface roughness.

TABLE OF CONTENTS

List of Tables

List of Figures

Nomenclature

Symbols

a	Crack size, µm
A_0	Nominal cross-section area, mm^2
b	Number of struts
B	Fatigue strength exponent
C	Gibson-Ashby’s model constant
D	Diameter, mm
D_i	Constant in J-C failure model
D_p	Peak-Peak displacement, mm
d_s	Strut thickness/diameter, mm
E	Young’s modulus, GPa
E_T	Tangent modulus, MPa
F	Force, N
f	Frequency, Hz
H	Height, mm
h	Hatching distance, μm
I	Beam current, mA
j	Number of nodes
K	Stress concentration factor
k	Stiffness, N/mm
K'	Fatigue strength coefficient
l	Length, mm
L	Displacement, mm
L_C	Unit cell size, mm
L_P	Pore size/diameter, mm
M	Maxwell number
m	Threshold percentage for change in peak-peak displacement
$\widetilde{m}$	Mass, kg
M_b	Bending moment, $N \cdot mm$
N	Fatigue cycle
n_i	Gibson-Ashby’s model exponent
P	Power, W
$\bar{P}$	Porosity
P_b, P_c	Percentage of beam elements under bending or compression
R	Loading ratio
R_a, R_v	Roughness, µm
S	Strain energy density per unit mass
T	Temperature, ℃
U	Acceleration voltage, kV
v	Scanning speed, mm/s
V	Volume, mm^3
Y	Constant
α	Strut angle, ℃
γ	Shear strain
ε	Strain
$\dot{\varepsilon}^*$	strain ratio of given strain rate to the reference strain
ζ	Geometric function
θ	Angle, °
ν	Poisson's ratio
ρ	Density, kg/mm^3
$\bar{\rho}$	Relative density
σ	Stress, MPa
σ^*	Stress triaxiality
τ	Layer thickness, µm

Subscripts

0	Initial state or reference condition
c	Cell
eff	effective
f	failure
h	hydrostatic
i	Initiation state or reference state
L	Lattice structure
m	mean
M_S	Martensite starting
max	Maximum
min	Minimum
pl	plateau
p	Pore
q	equivalent
rev	Reversible
RO	Run-out
S	Solid or bulk material
s	Strut
VM	Von-mise
y	0.2% yield property or y-axis

Abbreviations

AB	As-built
AM	Additive manufacturing
AN	Anneal
AoI	Area of interest
BCC	Body-centred-cubic
BCCZ	Body-centred-cubic with Z-strut
BD	Building direction
CAD	Computer-aided design
CCD	Central composite design
CE	Chemical etching
CLB	Continuous laser beam
DIA	Diamond
DIC	Digital image correlation
EBM	Electron beam melting
EBPBF	Electron beam Powder bed fusion
EXP	Experiment
FCC	Face-centred cubic
FCCm	Modified face-centred cubic
FCCZ	Face-centred cubic with Z-strut
FEA	Finite element analysis
FEM	Finite element model
FO	Focus offset
FP	Fully porous
FSF	Fatigue safety factor
HA	Hydroxyapatite
HCF	High cycle fatigue
HCP	Hexagonal-closed packed
HIP	Hot isostatic pressing
HT	Heat treatment
J-C	Johnson-cook
KRZ	Kubisch raumzentrierten
LCF	Low cycle fatigue
LD	Loading direction
LED	Linear energy density
LoF	Lack of fusion
LPBF	Laser powder bed fusion
MLE	Maximum-Likehood Estimation
MOGA	Multi-objective genetic algorithm
PBF	Powder bed fusion
PLB	Pulsed laser beam
RCO	Rhombicuboctahedron
RD	Rhombic dodecahedron
RoI	Region of interest
RVE	Representative volume element
SC	Simple cubic
SED	Strain energy density
SEM	Scanning electron microscope
SF	Speed function
SLM	Selective laser melting
SR-L	Solid reinforcement with lattice
SSI	Ratio of stress change after the implantation
TC	Truncated cub
TCO	Truncated cuboctahedron
TEM	Transmission electron microscopy
THA	Total hip arthroplasty
TO	Topologically optimised
TPMS	Triply periodic minimal surfaces
UCO	Unit cell orientations
UCS	Ultimate compressive strength, MPa
UTS	Ultimate tensile strength, MPa
VED	Volumetric energy density
XRD	X-ray diffractometer

Attestation of Authorship

I hereby declare that this submission is my own work and that, to the best of my knowledge and belief, it contains no material previously published or written by another person (except were explicitly defined in the acknowledgements), nor used artificial intelligence tools or generative artificial intelligence tools (unless it is clearly stated, and referenced, along with the purpose of use), nor material which to a substantial extent has been submitted for the award of any other degree or diploma of a university or other institution of higher learning.

Yawen Huang

12/12/2025

Acknowledgements

The completion of this PhD thesis marks the culmination of an intensive period, spanning almost five years, defined by a constant cycle of reading, writing, modelling, testing, and examination. This dedication has finally brought me to the completion of this PhD thesis. Although I once viewed my master's degree as 'a complete period' in my academic journey, finding myself still on this path eight years later has been a rewarding, unexpected direction. This has certainly not been a journey that I can walk alone, and for that reason, those who shared these moments with me deserve my deepest gratitude.

First and foremost, my greatest appreciation goes to my supervisor, Prof. Zhan Chen. His unwavering help, guidance, professional working style, and profound passion for academic research inspired me from the very beginning of my PhD candidature. My thanks also extend to my secondary supervisor, Prof. Sarat Singamneni, and our dedicated technical team, Mark, Jim, Ross, BJ, and Dr. Yuan Tao, for their invaluable assistance throughout my candidature.

I would also like to extend my deepest gratitude to all my family members, especially my parents, for their consistent support in every regard. I am thankful to my partner for his understanding, support, and love throughout my entire candidature. The journey of a PhD can feel long, but knowing I had you all by my side made it clear that I would never walk alone. My sincere thanks are also extended to everyone I have worked with over the past years, each one of them has played a part in helping me become a better person.

Lastly, I would like to gratefully acknowledge the School of Engineering, Computer and Mathematical Sciences at Auckland University of Technology for the generous provision of the Doctoral Fees and Stipend Scholarship throughout my PhD candidature.

List of Publications

Peer-reviewed Journal Paper:

1. **Huang, Y.**, & Chen, Z. W. (2025). Electron beam powder bed fusion additive manufacturing of Ti6Al4V alloy lattice structures: orientation-dependent fatigue strength and crack growth behaviour under compressive cyclic loading. *Journal of the Mechanical Behavior of Biomedical Materials*, 107201.

   (Forms the basis of Chapter 5)
2. **Huang, Y.**, Chen, Z. W., Wan, A. R. O., Schmidt, K., Sefont, P., & Singamneni, S. (2024). Electron beam powder bed fusion additive manufacturing of Ti6Al4V alloy lattice structures: orientation-dependent compressive strength and fracture behavior. *The International Journal of Advanced Manufacturing Technology*, 132(7), 3299-3311.

   (Forms the basis of Chapter 4)

Conference Proceedings:

1. **Huang, Y.**, Wan, A. R. O., Schmidt, K., Sefont, P., Singamneni, S., & Chen, Z. W. (2023). Effects of cell orientation on compressive behaviour of electron beam powder bed fusion Ti6Al4V lattice structures. *Materials Today: Proceedings*.

1. Introduction

Additive manufacturing (AM), particularly Powder Bed Fusion (PBF), has revolutionised many industries such as automotive, aerospace and biomedical sectors, by offering a high degree of design flexibility and material efficiency. The advances in PBF enable the production of metamaterials with complex structures and controllable geometrical features, making it an ideal solution for various applications. Specifically, these PBF porous metamaterials demonstrate a promising potential in biomedical field and Ti6Al4V is one of the most favourable materials in biomedical sector. This chapter provides an overview of the PBF-built lattice structures and Ti6Al4V alloy, with a specific focus on their applications in load-bearing implants. In addition, the objectives of this PhD research are outlined in this chapter.

1.1. Powder Bed Fusion (PBF) Ti6Al4V Lattices

PBF is an AM technique where a pre-defined computer-aided design (CAD) model directs a focused laser or electron beam to selectively scan and melt the powdered material layer by layer to build a 3D object. As illustrated in Fig. 1.1, depending on the heat source, PBF techniques are categorized as laser [1] (LPBF), also known as selective laser melting (SLM) and electron beam PBF(EBPBF) or electron beam melting (EBM). LPBF requires an argon or nitrogen environment, while EBPBF operates in vacuum. EBPBF generally achieves significantly higher scanning speed (15–20 m/s[2]) compared to LPBF (0.3–10 m/s[3]). However, EBPBF usually offers rougher surface due to a larger beam size (200–400 μm[4]) and thicker powder layers (50–200 μm), in contrast to the smaller beam size (50–200 μm[5]) and thinner layer (20–60 μm) achieved by LPBF[1]. In LPBF process, a thin layer of powder with controlled thickness is spread and then fused pass-by-pass and layer-by-layer by the focused laser beam (400W[5]). In EBPBF process, each layer of powder is pre-scanned to reduce the temperature gradient[6], then fused according to the pre-defined geometry by the high-power electron beam (3500W). Resulting from the temperature gradient and local cooling rate, reduced residual stress can be offered by EBPBF and no post-process heat treatment is required[7].

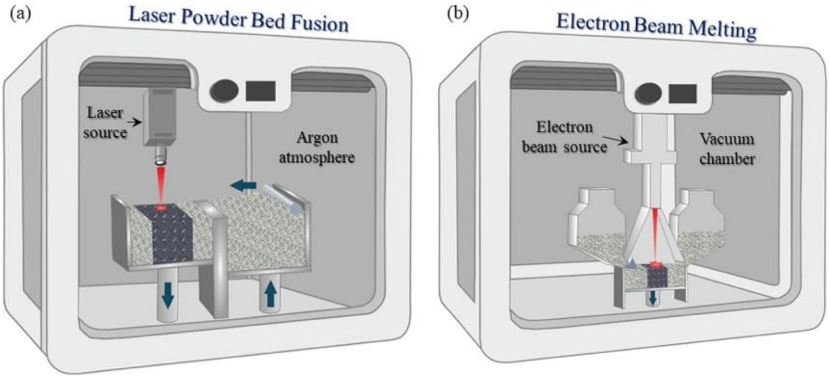

Fig. 1.1 Schematic representation of the PBF process: (a) LPBF and (b) EBPBF[8]

PBF processes can work with various materials, such as stainless steel[9–11], Ni-based super alloys[12–14], aluminium[15–17], tantalum[18–20], and titanium[21–23]. Titanium and its alloys, specifically, Ti6Al4V have been one of the most widely accepted materials in the biomedical field, due to its great combination of mechanical properties, corrosion resistance and biocompatibility[24–26]. Ti6Al4V is an α+β titanium alloy, which consists of hexagonal closed-packed (HCP) α crystalline structure and body-centred-cubic (BCC) β crystalline structure. The mechanical properties of Ti6Al4V can be optimised by balancing the α and β phases, where the α phase provides superior strength and the β phase offers ductility[27]. As shown in Fig. 1.2(a), the phase transformation in Ti6Al4V strongly depends on the thermal history and the cooling rate experienced during the fabrication process. When the alloy cools down from a complete β-phase (above the β-transus temperature, which is typically approximately995°C to 1050°C[28,29]), the transformation for β to α starts. An equilibrium α+β microstructure forms under slow cooling conditions, In contrast, rapid cooling from above β-transus temperature induces a diffusionless transformation, leading to a non-equilibrium martensite microstructure. Specifically, the cooling rates exceeding a critical threshold (410°C/s), combined with a low building temperature below the martensite start temperature T_{M_S}(575°C to 800°C) can result in the formation of α' martensite[30].

During the EBPBF process, the transformation of Ti6Al4V occurs in three distinct stages as shown in Fig. 1.2(b). In the first stage, the rapid initial cooling rate induces a diffusionless transformation, converting the β phase into α' martensite. During the second stage, at a steady chamber temperature (approximately 650–700°C), the microstructure changes to a mixture of α+β phases by diffusional transformation. In the last stage, the continued diffusion leads to coarsening of the microstructure, resulting in a stabilised α+β phase morphology[31]. The microstructure of EBPBF Ti6Al4V generally exhibits a columnar microstructure, containing columnar grains of prior β phase parallel to the building direction with fine Widmanstätten α platelets[32]. Conversely, in LPBF process, the absence of pre-heating causes the temperature to drop rapidly to the ambient conditions immediately after scanning. This rapid cooling induces a purely diffusionless transformation, resulting in the formation of brittle α' martensite phase rather than an equilibrium α+β morphology. This microstructure usually leads to high strength but low ductility. Therefore, post-process heat treatment is applied to LPBF-processed Ti6Al4V to transfer the α' martensite phase into a near-equilibrium lamellar α+β phase[33].

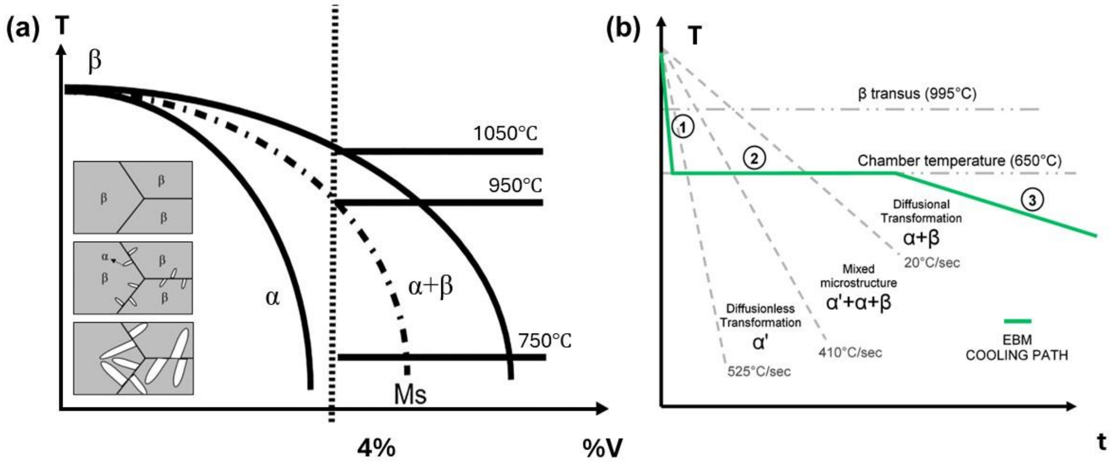

Fig. 1.2 (a)Phase diagram and solidification structures of the Ti–6Al–4V alloy[28,29] (b)Cooling path and critical cooling rates for Ti-6Al-4V microstructure formation in EBM[31]

Apart from the PBF fabricated bulk components, PBF porous cellular structures or lattice structures have attracted intensive attention for their ability to achieve controllable properties by tailoring geometrical features[34]. A lattice structure consists of a large number of unit cells and a unit cell is made by a certain number of struts joined in one or multiple nodes, an example is shown in Fig. 1.3. These lattice structures are difficult to be manufactured using the traditional techniques, while PBF offers the flexibility to produce these porous lattices with high geometrical complexity. A considerable amount of published works has been published on the fabrication and characterisation of these PBF Ti6Al4V lattice structures. For specific applications, such as biomedical hip implants, the compressive loading is dominant, thus numerous studies[1,24,34] have investigated the effects of geometrical features of the lattices such as strut size, unit cell topology and relative density, the process induced defects and post-process heat treatment on the compressive mechanical properties of these lattice structures. However, the majority of these studies have focused on the axial quasi-static properties of lattice structures, while data on their compressive fatigue behaviour remain limited. Moreover, the compressive loads experienced by the implant in service are multi-directional, while the anisotropic mechanical behaviour of the lattice structures has not been clearly addressed.

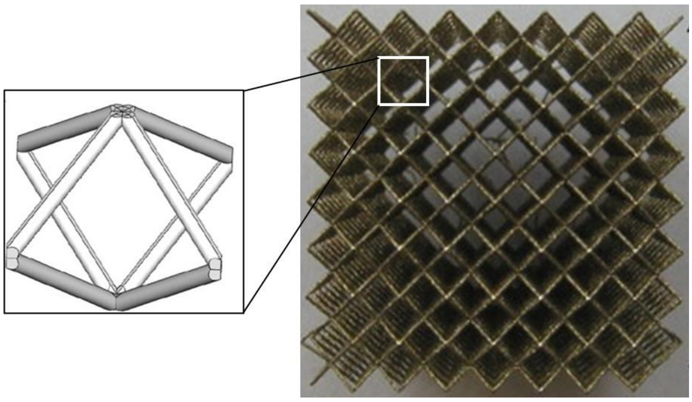

Fig. 1.3 Example of a lattice structure with body cubic centred BCC unit cells[35]

Furthermore, although EB-PBF offers the advantage of fabricating components with significantly lower residual stress than L-PBF due to its slower global cooling rate, the local cooling rate during the solidification of thin lattice struts remains heavily influenced by the specific lattice geometry[36]. Depending on the length and thickness of the struts, the local cooling rate varies significantly. These thermal variations then would dictate the resulting microstructure. Specifically, locally high cooling rates can promote the formation of fine and brittle fine α’ martensite, which can subsequently affect the mechanical behaviour of the fabricated components.

1.2. Biomedical Applications of PBF Ti6Al4V Lattices

The capability of PBF to fabricate parts with almost ultimate geometrical freedom makes PBF an attractive manufacturing technique, which allows the production of metallic products with complex structures. PBF-fabricated lattices have attracted extensive attention for the potential of femoral stems used in total hip arthroplasty (THA) to overcome the complications such as stress-shielding and implant loosening[24]. As illustrated in Fig. 1.4, the mismatch between Young’s modulus (110–230 GPa) of the current dense-metal based femoral stems on the market and that of human bone (0.3–30 GPa)[8,21] will result in most of the load being borne by the stiffer implant. The lack of stress simulation on the proximal femur can lead to bone resorption due to the lack of stress simulation on the proximal femur, which can lead to further implant loosening. In addition to stress shielding, the long-term fixation of the femoral stem is dependent on osseointegration. It has been reported that applying metallic porous structures in femoral implants to create a similarity to cancellous bone can effectively reduce stress shielding and ensure the bone in-growth rate [37–39]. As shown in Fig. 1.5, compared to the fixation provided by bone ingrowth on the roughened nonporous surface, porous structures can offer a larger surface area and enhanced mechanical interlocking for bone ingrowth[40,41].

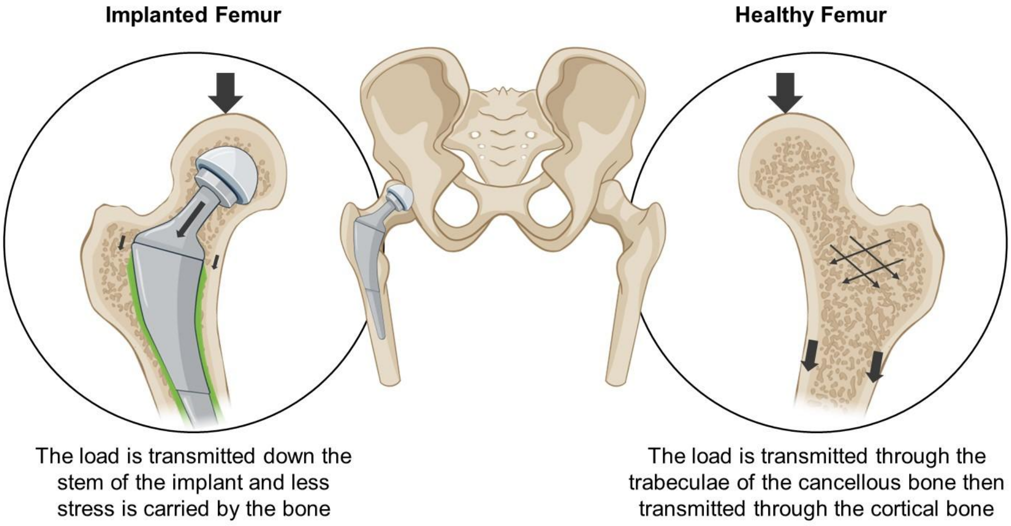

Fig. 1.4 Schematic of bodyweight transmitted through solid implant and health femur

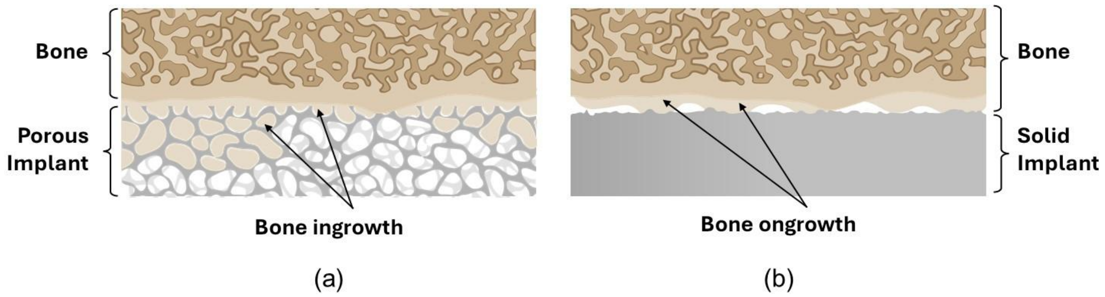

Fig. 1.5 Schematic representation showing the difference between: (a) bone ingrowth into porous implant and (b) bone ingrowth onto roughened dense implant surface

Once the femoral stem is implanted into the body, it needs to not only bear the bodyweight but also withstand the repeated loadings during daily activities. To ensure the long-term performance of the implant, fatigue is considered as a major focus in pre-clinical testing and analysis. As specified in ISO 7206-4[42], the femoral stem implant should withstand at least 5×10^6 cycles under a maximum loading of 2300N. Although porous implants can reduce stress shielding and promote bone ingrowth, their fatigue strength is generally lower than that of the solid ones[21,24,43]. To date, limited studies on the fatigue strength of PBF porous femoral stem implants are available. Therefore, the fatigue performance of porous femoral stem implants should be carefully evaluated with the consideration of various design parameters to ensure both biocompatibility and mechanical integrity.

1.3. Aim of the Research and the Structure of the Thesis

Despite the promising potential of PBF lattice structures, the insufficient understanding of the anisotropic mechanical behaviour of these lattices and the uncertainties on fatigue strength is the two key factors that prevents the widespread clinical application of the highly porous structures for the orthopaedic applications. Therefore, this thesis aims to investigate the orientation-dependent mechanical behaviour of the EBPBF built Ti6Al4V lattice structures, thus to exhibit the combined effects of LD, UCOs and strut irregularity associated with EBPBF Ti6Al4V lattices on the compressive quasi-static and fatigue properties. In addition, to exhibit an exploratory design of porous femoral stem with sufficient fatigue life of 5×10^6 cycles as specified in the ISO 7206-4[42]. To achieve these objectives, the quasi-static and fatigue behaviour of the simple-cubic lattice structures with varied UCOs is investigated by experimental tests, numerical simulations and morphological analysis of fracture surfaces. Then the lattice-featured femoral stem implant is designed and topologically optimised to withstand the specified number of fatigue cycles.

Chapter 1 provides a general introduction of PBF Ti6Al4V lattices and an overview of their applications in the biomedical field. The recent studies on the mechanical behaviour of the PBF built lattices are reviewed in Chapter 2, primarily focusing on their quasi-static and fatigue performance. In addition, a contextual insight the recent advancements in PBF porous femoral stems is addressed in Chapter 2. The design of this study and the research methodologies are discussed in Chapter 3. In Chapter 4 and Chapter

5, the orientation-dependent quasi-static and fatigue behaviours of the lattice structures are discussed in detail, respectively. Then, the fatigue performance of the femoral stem is investigated in Chapter 6. Finally, a conclusion of this research summarising the findings of the effects of UCO on the mechanical properties of lattice structures for load-bearing implants, along with recommendations for future works aiming at further improving the porous portion while maintaining fatigue strength, are provided in Chapter 7.

2. Literature Review

This chapter extensively reviews the scope and findings of the published works on PBF lattices. It reviews various lattice designs for orthopaedic applications and the process-induced geometric variations associated with PBF. Following by a review on the quasi-static and fatigue responses of PBF lattices, discussing the experimentally and numerically investigated properties and the key factors affecting their mechanical behaviour. More importantly, the orientation dependant effects on both the quasi-static and cyclic mechanical behaviour of the lattices are reviewed highlighting that although UCO can significantly affect the stress distribution, deformation mode and failure mechanisms under both static and fatigue loadings, the available data on the orientation effects remain limited. Then a comparative review of solid and porous femoral stems is provided, discussing the complications of solid stems, while also addressing that the insufficient fatigue properties of the porous ones. Then the knowledge gap in literature is identified based on the reviewed published works, which forms as the basis for the research questions to be addressed.

2.1. PBF-Fabricated Lattice Structures

2.1.1. Geometric Design Parameters and Classification of PBF-Lattices

Lattice structures or architected cellular materials have well-defined periodic geometry, the mechanical properties of the lattices can be tailored by controlling the geometrical parameters. Relative density $\bar{\rho}$ is considered as the most important parameter of lattice structures, which is defined as the ratio of the density of the porous material ρ_L to the density of the bulk base material ρ_S by:

$$\bar{\rho} = \frac{\rho_L}{\rho_S} \tag{2.1}$$

and the porosity P is:

$$\bar{P} = 1 - \bar{\rho} \tag{2.2}$$

Gibson et al.[44,45] provided a theoretical framework to estimate the mechanical properties of lattice structures as a function of relative density. The correlated effective Young's modulus E_L and the compressive strength σ_L of the lattice with its relative density $\bar{\rho}$ by:

$$\frac{E_L}{E_S} = C_1 \left(\frac{\rho_L}{\rho_0}\right)^{n_1} = C_1 \bar{\rho}^{n_1} \tag{2.3}$$

and

$$\frac{\sigma_L}{\sigma_S} = C_2\left(\frac{\rho_L}{\rho_S}\right)^{n_2} = C_2\bar{\rho}^{n_2} \tag{2.4}$$

where subscripts L and S are used to distinguish between the properties of the lattice material and the solid material, respectively. The coefficients $\mathrm{C_i}$ and exponents $\mathrm{n_i}$ $(\mathrm{i} = 1{,}2)$ are related to the type of unit cell, depending on whether the lattice is bending- or stretching dominated, as soon will be explained. Gibson et al. predicted that, for ideal stretching-dominated lattices, $\mathrm{n_1} = \mathrm{n_2} = 1.0$, while for ideal bending-dominated structures, $\mathrm{n_1} = 2$ and $\mathrm{n_2} = 1.5$. Experimental data of Young's modulus and compressive strength of Ti6Al4V and CP-Ti lattices as a function of relative density, collected from published literature[23,46–53], is displayed in Fig. 2.1. The data gathered from the reviewed studies shows a rising trend in both elastic modulus and compressive strength as porosity decrease, aligning with the predictions from the Gibson-Ashby's model. However, discrepancies between the experimental data results and the predictions of ideal structures have been observed, which have been attributed to multiple factors[54,55], including process induced geometrical imperfections and local stress concentrations at cell nodes, as will be discussed in the following sections. Due to the limitations of Gibson-Ashby's accuracy and applicability for modern, engineered, and complex lattice structures, more advanced computational methods like FEA or experimental calibration are usually needed to complement or replace it.

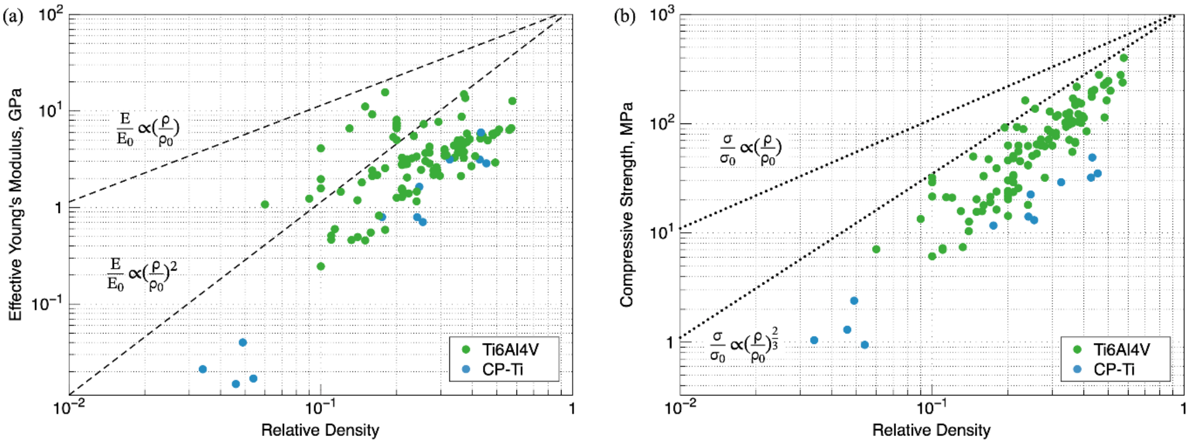

Fig. 2.1 Data collected from literature[23,46–53]: Relative density vs (a) Effective Young's modulus and (b) Compressive strength of PBF-processed Titanium lattice structures

Based on structural design and geometrical characteristics, lattices can also be categorised as strut-based lattices and triply periodic minimal surfaces (TPMS) cellular structures. The most commonly used strut-based lattices are shown in Fig. 2.2 (a) – (h), including face-centred cubic (FCC), body-centred cubic (BCC)[56], FCCZ, BCCZ[57], diamond[58], rhombic dodecahedron, G7[59] and simple cubic(SC)[52]. In addition, as shown in Fig. 2.2 (i), auxetic lattice exhibits negative Poisson's ratio with re-entrant unit cell can also designed and fabricated[50]. Typical TPMS lattices, including TPMS diamond[60], Gyroid[60], Schwarz P[61] and IWP[62], are presented in Fig. 2.2 (j) – (m). In strut-based lattices, nodes positioned at the vertices, edges or interior of the unit cell are connected by the struts. TPMS lattices, either sheet-based or ligament-based, are periodic structures controlled by mathematical algorithms, where the minimal surface defines surfaces with zero mean curvature at every point.

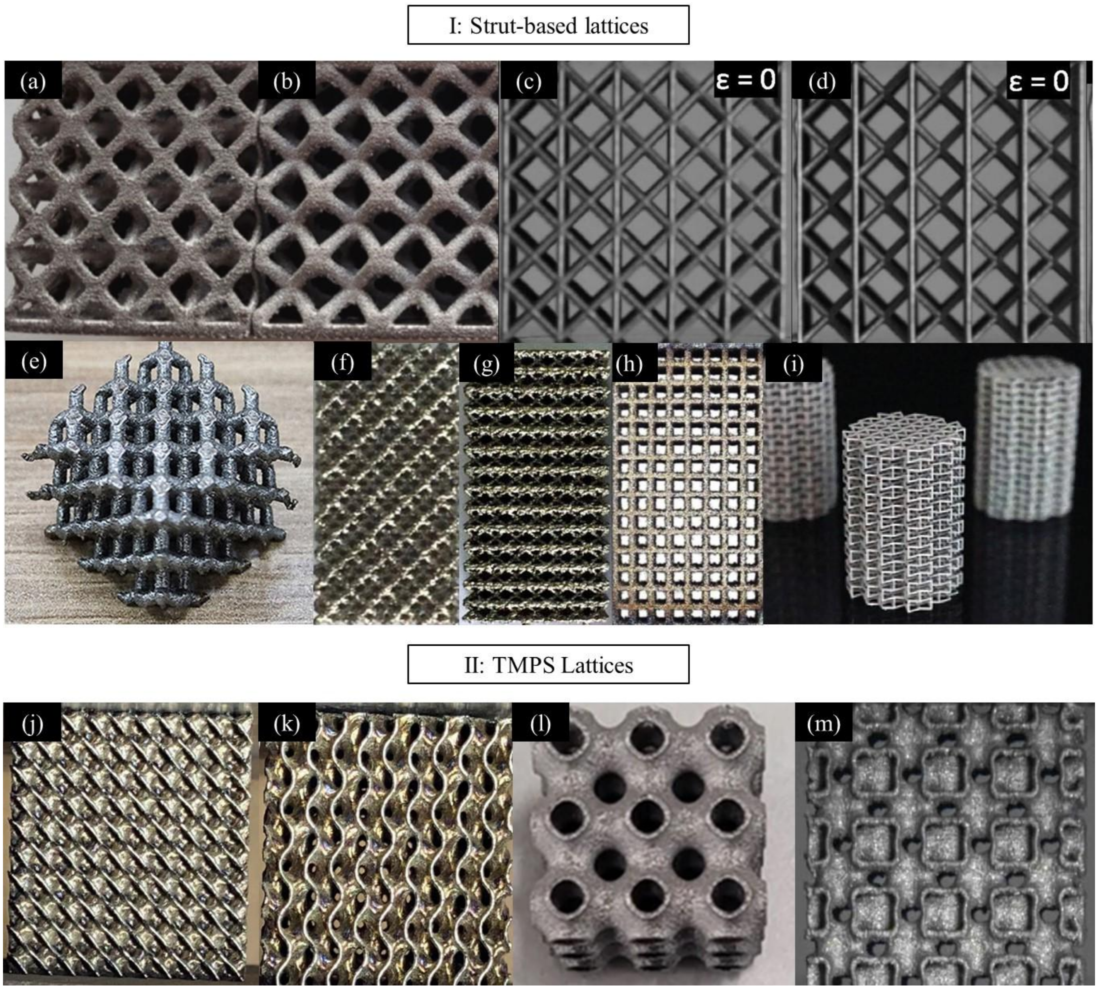

Fig. 2.2 Various types of lattices processed by powder bed fusion, I: strut-based lattices: (a) FCC[56], (b)BCC[56], (c) FCCZ[57], (d) BCCZ[57], (e) Diamond[58], (f) Rhombic Dodecahedron[59], (g) G7[59] , (h) Simple Cubic[52] and (i) Auxetic[50]; II: TPMS lattices: (a) TPMS diamond[60], (b) Gyroid[60], (l) Schwarz P[61] and (m) IWP[62]

Maxwell's criterion has been developed by Maxwell[63] to classify the strut-based lattice structures by nodal connectivity. As illustrated in Fig. 2.3, the Maxwell number M for 3D lattices is defined by:

$$M = b - 3j + 6 \tag{2.5}$$

where b is the number of struts, and j is the number of nodes. If M<0, the lattice is considered bending-dominated, the struts tend to bend with external loads and moments transferred to the nodes. If M≥0, the lattice is considered to be stretching-dominated, no bending stress occurs at the nodes as the struts can balance the external loads[56]. As shown in Fig. 2.4, the compressive stress-strain curves of lattices consist a linear elastic regime until yielding of struts due to bending or stretching, a plateau regime when cells start to collapse and a densification phase corresponding to the collapse of the cells reach contact to each other. Stretching-dominated structures generally exhibit higher initial stiffness and yield strength[64] and post-yield softening due to sudden failure resulted by buckling or brittle crush of a layer of cells[1]. In contrast, bending-dominated lattices display a relatively flat plateau over wide strain range, giving them exceptional energy-absorption properties[44]. The failure mechanism of bending- and stretching lattice structures has been investigated in multiple studies[47,48,65], revealing a layer-by-layer failure in stretching-dominated lattices and a shear band failure in bending-dominated structures. However, Maxwell-criterion may lead to oversimplified classification and incorrect categorisation. For example, some structures technically are technically defined as bending-dominated by Maxwell criterion, such as BCCZ and FCCZ, which are reinforced with Z-struts, exhibit stretching-dominated behaviour[10,66].

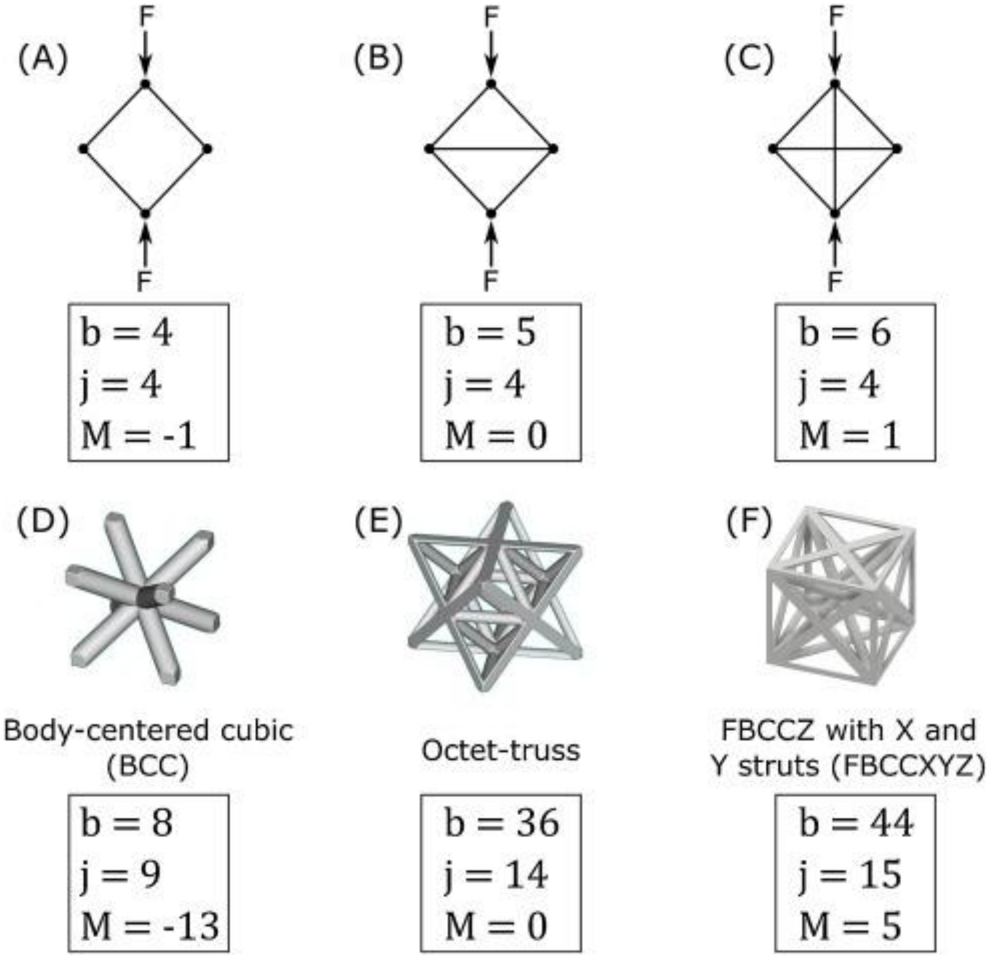

Fig. 2.3 Examples illustrate for the Maxwell number classification[1]

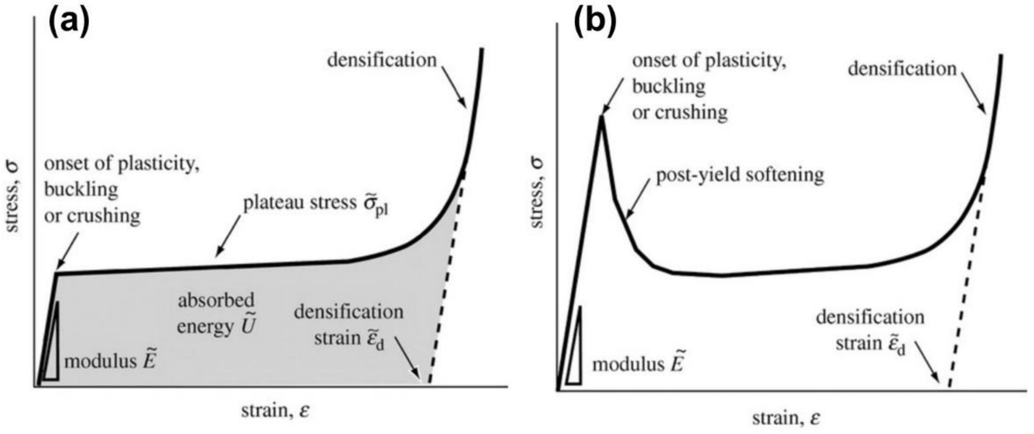

Fig. 2.4 Stress-strain curves of (a) bending-dominated lattice structures (b) stretching-dominated structures[1]

To further review the reliability of Maxwell-criterion-based Gibson-Ashby model in predicting the mechanical properties of PBF-fabricated lattice structures, a power regression analysis was conducted using data collected from literature. As summarised in Table. 2.1, there is a clear discrepancy between the experimental and theoretical scaling exponents. This deviation is attributed to the idealised assumptions of the theoretical model, which presumes perfectly uniform struts. However, PBF-fabricated thin struts inherently contain geometrical imperfections, such as manufacturing defects, surface roughness and irregular profiles, which can alter their mechanical response. Specifically, Maxwell's criterion predicts a stretching-dominated behaviour of SC lattices, corresponding to an ideal exponent of n_2=1. While the experimental exponents reported in several studies[47–49] align reasonably well with this prediction, the data reported from the other two studies[67,68] demonstrated severe deviations from the ideal value. Notably, these deviations are highly orientation-dependent, highlighting the limitations of the Gibson-Ashby model in predicting the mechanical behaviour of PBF-processed lattices.

Table. 2.1 Regression analysis of reported experimental quasi-static data of PBF fabricated lattices

			Effective Modulus			**Strength**			
Cell Type	**Maxwell Criterion**	**PBF**	C_1	n_1	R^2 (%)	C_2	n_2	R^2(%)	**Ref**
BCC	Bending	L-	0.15	1.67	66.74	0.14	1.14	66.56	[54]
BCCZ	Bending	L-	0.01	0.22	12.42	0.06	0.48	38.84	[54]
FCC	Bending	L-	0.37	1.94	99.97	1.18	1.75	99.79	[54]
FCCZ	Bending	L-	0.35	1.50	91.93	1.32	1.59	99.43	[54]
Diamond	Bending	L-	0.04	0.86	21.99	0.08	0.55	0.08	[54]
SC$_{[001]}$	Stretching	L-	0.15	0.93	37.02	0.64	1.23	64.09	[54]
SC$_{[001]}$	Stretching	L-	0.10	0.88	99.75	0.29	1.01	92.86	[47]
SC$_{[001]}$	Stretching	L-	0.09	0.74	92.01	0.35	1.21	100.00	[48]
SC$_{[001]}$	Stretching	EB-	0.04	0.63	96.48	0.41	1.32	99.50	[49]

SC$_{[001]}$	Stretching	EB-	0.14	2.42	99.19	1.48	1.88	98.92	[52]
SC$_{[001]}$	Stretching	L-	0.19	1.52	85.92	1.89	2.64	97.30	[67]
SC$_{[011]}$	Stretching	L-	0.19	1.92	99.97	0.56	2.06	97.85	[67]
SC$_{[001]}$	Stretching	EB-	0.11	0.99	98.85	0.73	1.72	99.95	[68]
SC$_{[011]}$	Stretching	EB-	0.27	2.40	98.65	0.99	2.30	99.90	[68]

For hip implant applications, the desired biomedical and mechanical properties can be achieved by tailoring the design parameters of lattices. Long human bones, such as femur and tibia, are primarily made up of cortical bone, characterising by a typical porosity of 5–10%, forms the dense outer shell of bones and accounts for approximately 80% of the total skeletal mass[69]. Under compression, cortical possess a yield strength of 131–224 MPa and a Young's modulus of 17–20 GPa along the longitudinal axis[70]. Trabecular bone or cancellous bone, features lattice-like structures that helps maintain bone strength, which is primarily found at the ends of long bones and within the body of short bones[71]. Trabecular bones exhibit skeletal-location-varied porosity (40%–95%) and anisotropic mechanical properties (Young's modulus ranging from 1–5 GPa and a compressive strength of 0.1–30 MPa along the loading axis)[72]. In addition, the pore size of lattices within the range of 0.1 to 1.5mm[71] is recommended to optimise bone in-growth. A minimum pore size of 0.1–0.2 mm is suggested for initial cell ingrowth[73,74], while a larger pore size greater than 1mm is recommended for promote the cell proliferation and reduce cell occlusion[74].

2.1.2. Microstructure and Process-Induced Defects

Multiple studies have compared the microstructures of LPBF and EBPBF Ti6Al4V components. Zhao et al.[75] have analysed the X-ray diffractometer (XRD) patterns and transmission electron microscopy (TEM) of both LPBF and EBPBF alloys, where most of the peaks in both samples were indexed as α/α' phase. However, β-phase peaks were only presented in EBPBF samples. It has been observed that the EBPBF samples consist of α-lamellas and a small amount of β phases, while the LPBF samples contained thinner and longer α' martensitic laths. Compared to EBPBF samples, the microstructure of LPBF samples were less sensitive to the part size.

The difference in microstructure of EBPBF bulk sample and open cellular foam specimens has been studied by Murr et al.[76]. As shown in Fig. 2.5(a)–(b), the microstructure of the dense sample consists of a coarse mixture of α+β phases, while a finer microstructure with α' martensite is presented in the foam specimens. Similar fine microstructures of EBPBF open cellular lattice were also reported in other studies[77,78]. The typical microstructure of the EBPBF fabricated lattices structures[78] is presented in Fig. 2.5(c)–(f), showing the columnar β grains parallel to the BD (z-axis) on the vertical strut in Fig. 2.5(d). The microstructure of the unmelted powder on the horizontal strut appears to be basket-wave-like structure shown in Fig. 2.5(c). Fig. 2.5(d) shows the diffusionless α'-martensite observed in the area close to the building platform. The distribution of phases reflects to the varying thermal conditions due to the heat flux from the electron beam towards the build platform.

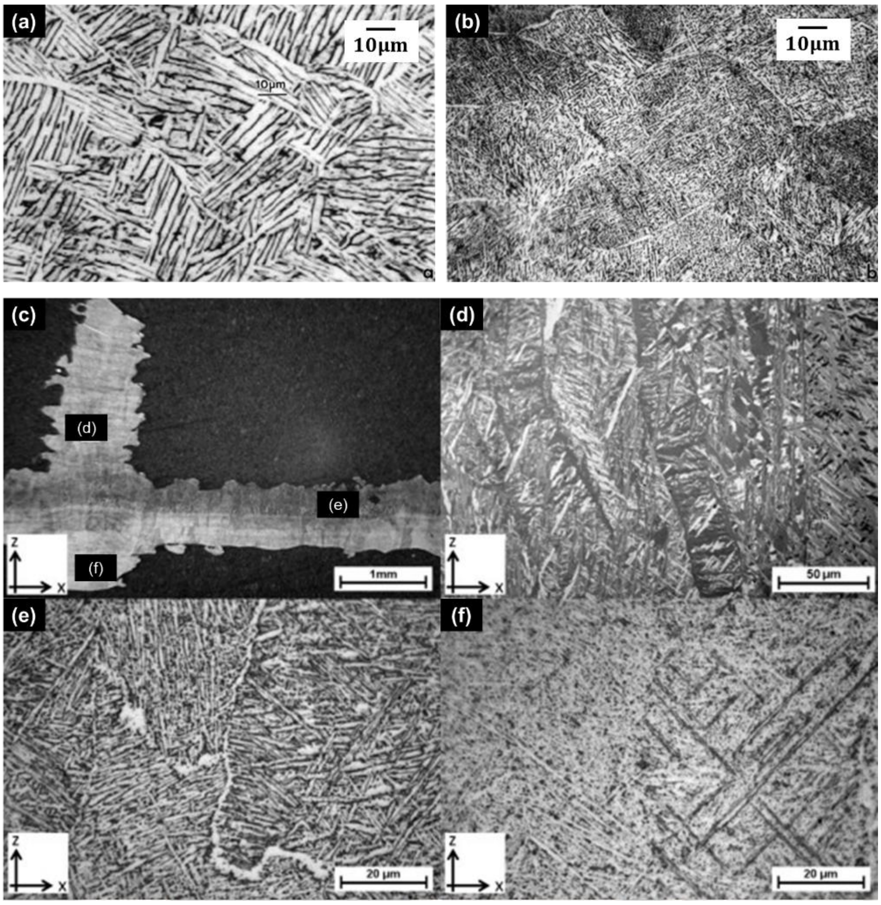

Fig. 2.5 Optical micrographs EBPBF built (a) dense sample, (b) foam[2], (c–f) simple cubic lattice[78]

In general, geometrical variations exists between PBF fabricated lattices and their as-designed counterparts. The as-built lattices typically contain geometric imperfections such as internal porosity and external surface defects as shown in Fig. 2.6. As reviewed by Zhang et al.[79], internal pores are induced during the fusion of metal powders, which can be controlled by optimising the processing parameters. Due to the layer-by-layer nature and the heat transfer mechanism of PBF, dimensional inaccuracies, such as irregular cross-sections, deviations in strut diameters from the designed values, strut waviness and material accumulation, are usually can be observed in PBF-processed lattices[80–82]. Strut-orientation-dependant dimensional deviations have also been observed by Melancon et al.[83], reporting an increasing strut waviness with decreasing strut angle. External surface defects are usually formed due to instable melting pools, which can be observed by comparing the down-skin and up-skin surfaces and can be quantified by using the surface roughness parameter R_a. Multiple studies[80,84,85] observed that R_a value of down-skin surface was found to be much higher than that of up-skin surfaces, due to local over-melting at down-skin surfaces. Compared to LPBF, higher energy density and scanning speed in EBPBF usually result in rougher surface[86–88]. The staircase effect is also a well-known phenomenon in PBF processes. The angled surfaces are fabricated with layer-thickness-sized ridges, resulting in discrepancies between the designed and fabricated geometries and reduced surface quality[89,90].

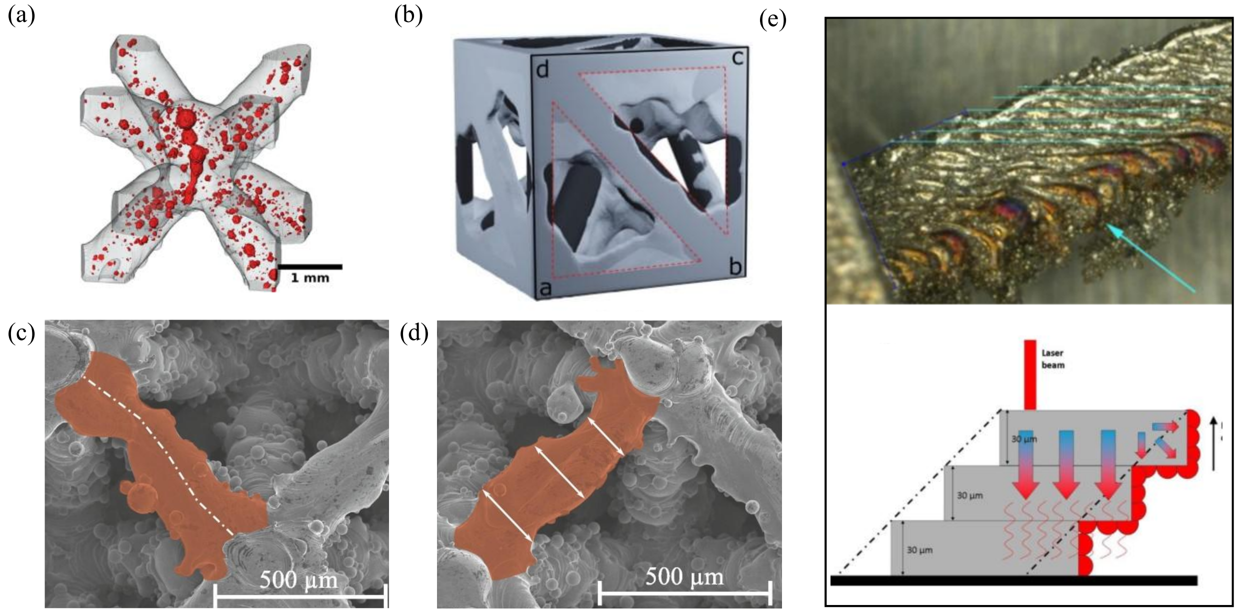

Fig. 2.6 Examples of geometric imperfections in PBF-processed lattices: (a) internal porosity[91], (b) material accumulation at nodes[80], (c) variation in strut thickness and (d) strut waviness[83] and (e)stair-case effect[89,90]

2.2. Quasi-static Properties of PBF Lattices and Orientation Effects

2.2.1. Experimentally investigated compressive properties

In general, the compressive quasi-static properties of lattice structures are evaluated based on ISO 13314-2011[92]. The prescribed geometry is illustrated in Fig. 2.7, where the width or diameter of the specimen must be at least ten times of its unit cell size. Additionally, it is suggested that solid plates can be built together with the porous part to ensure the planarity of the contact surfaces between the porous specimen and the mechanical testing machine[93]. The compressive stress σ and strain ε are defined by:

$$\sigma = \frac{F}{A_0} \tag{2.6}$$

and

$$\varepsilon = \frac{\Delta l}{l_0} \tag{2.7}$$

where F is the compressive force and A_0 is the nominal cross-section area perpendicular to the loading direction, Δl is the compressive displacement and l_0 is the initial gauge length. The ultimate compressive strength UCS_L is the first maximum stress the lattice can withstand before collapsing, the plateau stress σ_{pl} is either the mean stress between 20% and 30% or 40% compressive strain. The effective elastic modulus of lattices $\mathrm{E_L}$ is usually derived from the slope of the elastic region of the stress-strain curves[94]. The yield strength of the lattices $\sigma_{\mathrm{y-L}}$ is usually evaluated by using the 0.2% offset stress[95].

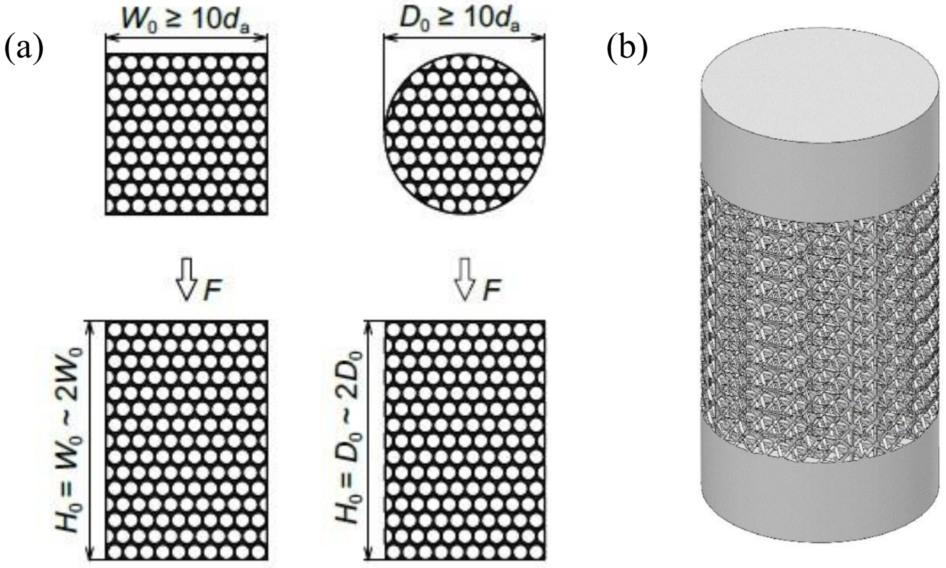

Fig. 2.7 Schematic illustration of the test specimen (a) prescribed geometry in ISO 13314[92] and (b) illustration of tested specimen with solid plates[93]

As shown in Fig. 2.8, Zhang et al.[96] have collected the experimental data obtained from different studies prior to 2017, where the porosity of human bone is calculated using the theoretical density of 1.99×10^3 kg·m^{-3}. The observations have confirmed that $\mathrm{UCS_L}$, $\sigma_{\mathrm{y-L}}$ and $\mathrm{E_L}$ increase with increasing $\bar{\rho}$. The EBPBF lattices exhibited higher $\mathrm{UCS_L}$ than that of cancellous bone while only few structures obtained comparable or higher $\mathrm{UCS_L}$ than that of cortical tibia. The highest $\mathrm{UCS_L}$ values of 196MPa and 163MPa were obtained for simple-cubic-cell-based lattices with relative densities of 0.37[59] and 0.50[49], respectively. The highest compressive strength values of approximately 160MPa were achieved by cubic ($\bar{\rho}$=0.37[59]–0.50[49]) and diamond lattices ($\bar{\rho}$=0.43[97]). For Young's modulus, the reported $\mathrm{E_L}$ values were much lower than that of cortical bone with similar density. It can be observed from Fig. 2.8 (a)–(b) that, at similar densities to cortical bones, only the simple cubic lattices exhibit comparable $\mathrm{UCS_L}$ and σ_{L} values to those of cortical bones.

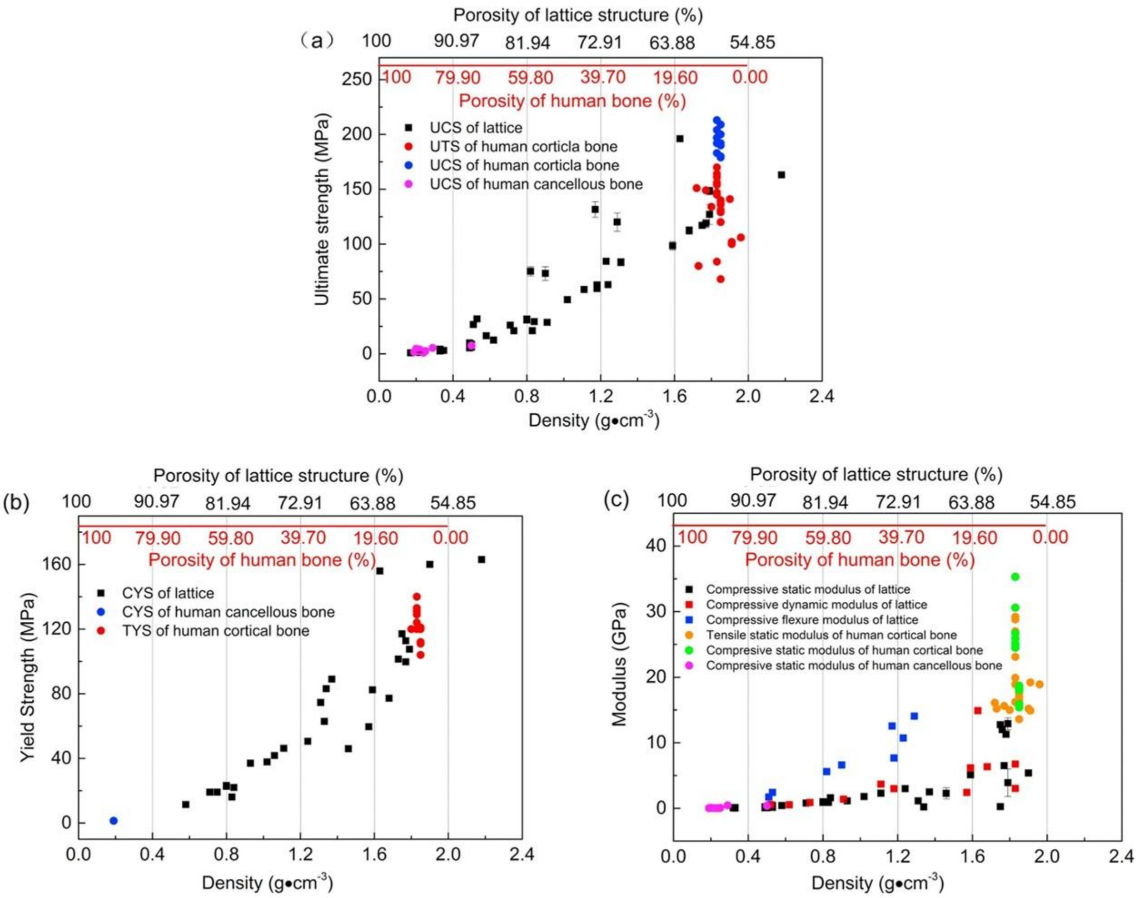

Fig. 2.8 Experimental data of (a) compressive and tensile ultimate strength, (b) compressive and tensile yield strength and (c) modulus vs density of EBPBF Ti6Al4V lattice structures and human bone[96]

As observed in Fig. 2.8(c) The variation in $\mathrm{E_L}$ values determined by different testing methods has been highlighted by Zhang et al.[96]. The authors indicated that the static and dynamic $\mathrm{E_L}$ were similar, whereas flexure modulus was substantially higher. The dynamic $\mathrm{E_L}$ is usually measured using resonant frequency and damping analyser (RFDA). During the dynamic tests, the measured specimen dissipates energy into vibration resulting in damping sine wave and the vibration modes for porous structures is given by:

$$E_L = \zeta \widetilde{m} f_r^2 \tag{2.8}$$

where ζ is a geometric function, $\widetilde{\mathrm{m}}$ is the mass of the specimen and $\mathrm{f_r}$ is the resonant frequency. The flexure modulus is determined by three- or four-point flexure testing, describing the effective stiffness of the tested lattice specimen when it subjects to a bending load. Then the static modulus of a lattice is measured by quasi-static compression test as previously discussed. However, this statement only considered the effects of relative density, neglecting the effects of other critical factors, such as the unit cell type. To clarify the influence on $\mathrm{E_L}$ of different testing methods, additional literature data of $\mathrm{E_L}$ have been collected alongside the data reviewed in Ref. [96] are listed in Table. 2.2 and plotted in Fig. 2.9. It can be observed that, for lattices with the same unit cell type and similar relative densities, the

E_L values determined by dynamic tests using damping analyser and flexural tests are higher than those obtained via uniaxial compression tests. In consistent with the compared results between dynamic and static measured E_L values reported by Li et al. 47], Xu et al.[98] further explained that the dynamic E_L values are more credible than those determined by compression tests. Since during compression tests, the specimens can be deformed either by slipping or local deformation at the loading points, which can typically result in underestimated E_L values. However, as shown in Fig. 2.9, the variation in E_L values may not only be resulted by the different testing methods, but also from the accuracy of the measured displacement. The plotted data of E_L values of diamond lattices obtained via compression testing with contactless digital image correlation (DIC) also provide a reliable measurement of the modulus.

Table. 2.2 Experimental data of quasi-static properties of Ti-alloy PBF lattice structures

Cell Type	$\bar{\rho}$	**E_L(GPa)**	**PBF**	**Testing Method**	**Ref**
SC-Like	0.12	0.58	E	Damping Analyser	[99]
G7	0.41	6.74	E	Damping Analyser	[99]
SC	0.49	2.92	E	Compression Test	[100]
SC	0.40	2.68	E	Compression Test	[100]
SC	0.30	2.13	E	Compression Test	[100]
SC	0.30	1.13	E	Compression Test	[101]
SC	0.37	14.90	E	Damping Analyser	[59]
G7	0.36	2.40	E	Damping Analyser	[59]
RD	0.38	6.30	E	Damping Analyser	[59]
RD	0.40	11.99	E	Flexure Test	[102]
RD	0.40	11.29	E	Flexure Test	[102]
RD	0.30	5.59	E	Flexure Test	[103]
RD	0.30	6.60	E	Flexure Test	[103]
RD	0.30	7.67	E	Flexure Test	[103]
RD	0.40	10.72	E	Flexure Test	[103]
RD	0.40	12.54	E	Flexure Test	[103]
RD	0.40	14.05	E	Flexure Test	[103]
DIA	0.29	3.00	E	Compression Test with Extensometer	[104]
DIA	0.36	5.10	E	Compression Test with Extensometer	[104]
DIA	0.40	6.50	E	Compression Test with Extensometer	[104]
DIA	0.31	2.48	E	Compression Test with Extensometer	[97]
DIA	0.43	5.38	E	Compression Test with Extensometer	[97]
BCC	0.24	0.46	L	Compression Test	[105]
BCC	0.15	0.21	L	Compression Test	[105]
BCC	0.30	1.10	E	Compression Test with Sensor	[68]
BCC	0.20	0.36	E	Compression Test with Sensor	[68]
BCC	0.10	0.08	E	Compression Test with Sensor	[68]
BCC	0.45	3.70	L	Compression Test	[106]
BCC	0.45	3.20	L	Compression Test	[106]
DIA	0.50	15.00	L	Compression Test with DIC	[107]
DIA	0.40	9.30	L	Compression Test with DIC	[107]
DIA	0.30	5.10	L	Compression Test with DIC	[107]

DIA	0.20	3.10	L	Compression Test with DIC	[107]
RD	0.39	4.38	L	Compression Test	[108]
SC	0.60	12.80	L	Compression Test	[109]
SC	0.50	8.30	L	Compression Test	[109]
SC	0.40	4.30	L	Compression Test	[109]
SC	0.11	0.65	E	Damping Analyser	[52]
SC	0.14	1.89	E	Damping Analyser	[52]
SC	0.16	2.24	E	Damping Analyser	[52]
SC	0.20	2.98	E	Damping Analyser	[52]
SC	0.36	15.42	E	Damping Analyser	[52]
RD	0.14	0.50	E	Damping Analyser	[52]
RD	0.16	0.93	E	Damping Analyser	[52]
RD	0.21	1.41	E	Damping Analyser	[52]
RD	0.27	3.00	E	Damping Analyser	[52]
RD	0.38	6.41	E	Damping Analyser	[52]

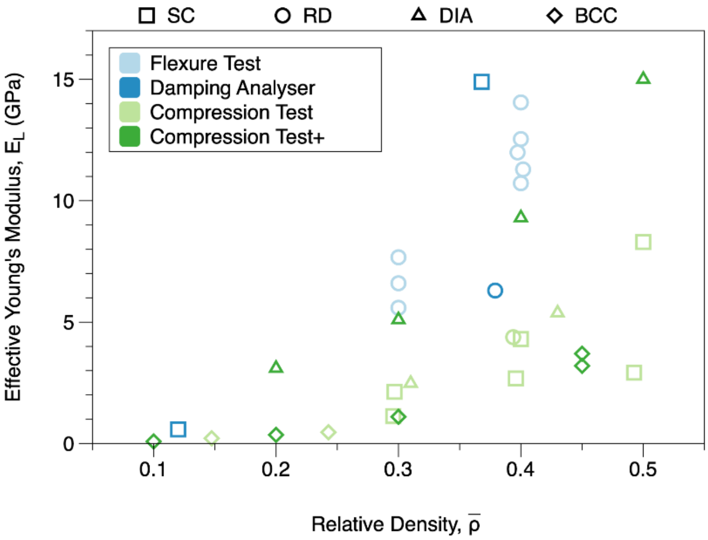

Fig. 2.9 E_L values vs $\bar{\rho}$ for different types of PBF lattices obtained using different testing methods

2.2.2. FEA-based Assessment of Compressive Responses

Advanced numerical modelling techniques are able to overcome the limitations of Gibson-Ashby's models. Finite element analysis (FEA) is widely employed to predict the mechanical behaviour of lattice structures, but the methodologies applied in FEA can vary significantly across the literature. FE models with 3D solid elements are capable to capture the details of geometry and then provide high accuracy in predicting mechanical behaviour, but it requires highest computational cost. Some authors modelled the geometrical imperfections by different methods, such as reconstructing using micro-CT[81] and defining the non-uniformity by a script[110], to represent the AM processed structures to capture the local defects and deformations. In addition, beam elements have been used to improve the computational efficiency of simulation of lattice structures, researchers modelled the lattices with either uniform or varied cross-sections[111,112]. It was suggested by Alomar et al.[55] that using beam elements for a lattice with a small aspect ratio may result in underestimated E_L. Furthermore, homogenisation techniques have also been employed in lattice simulations by replace the entire lattice structures with appropriate representative volume element (RVE)[113]. This approach simplifies the analysis by averaging the behaviour over a large scale, allowing efficient simulation but not be able to capture the local stress concentration. Dong et al.[114] have compared the experimental and numerical stiffness results for four different X-shape cell (BCC-like) lattices. The numerical results obtained using different FEA elements are shown in Fig. 2.10, indicating significant variation in stiffness values and the most accurate results were achieved by employing the fine solid elements.

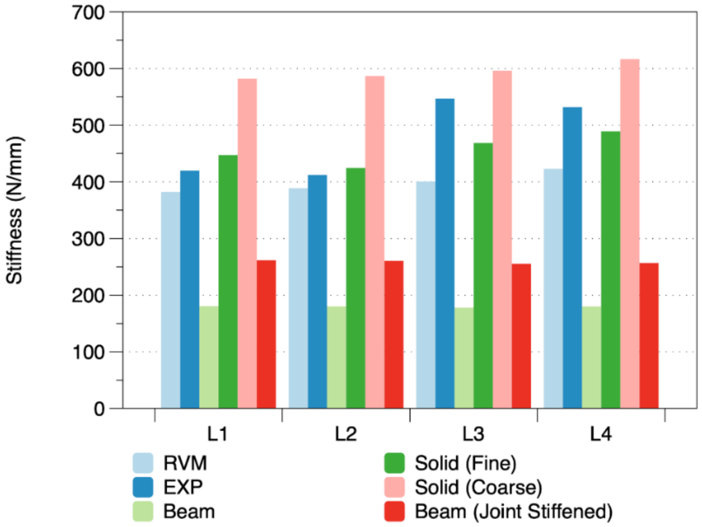

Fig. 2.10 Comparison of the experimental and numerical results of stiffness of four lattices[114]

Various boundary conditions have been used for compression tests of lattice structures, such as directly applying a displacement to the top nodes while fixing the bottom nodes[47,110,115] or introducing two shells in the model to represent the platens during experimental tests. The contact behaviour between the lattice and the platens has been addressed in different ways, including introducing a penalty factor to account for friction[57,116,117] as well as models with frictionless contact[83,118,119] or bonded contact[120].

Plasticity of base material of the lattice structures is usually considered in the FE models by introducing a bilinear-elastic-plastic model[121], directly using the stress-strain data[122] or using other material models such as Jonhson-Cook (J-C) failure model[47,117,123,124]. In this model, if an element exceeds the failure limit, it will be removed from the structure. The advantage of J-C failure model is that the maximum plastic strain at fracture with triaxiality can be considered. The failure initiation strain $\bar{\varepsilon}_0^{pl}$ in J-C model is described as:

$$\bar{\varepsilon}_0^{pl} = \left[D_1 + D_2 e^{(D_3 \sigma^*)}\right][1 + D_4 \ln(\dot{\varepsilon}^*)[1 + D_5 T] \tag{2.9}$$

where D_1, D_2, D_3. D_4 and D_5 are material constants, $\dot{\varepsilon}^*$ is the strain ratio of given strain rate to the reference strain, T is the temperature parameter and σ^* is the stress triaxiality defined by the hydrostatic stress σ_h and equivalent stress σ_q:

$$\sigma^* = \frac{\sigma_h}{\sigma_q} \tag{2.10}$$

The experimental simulation results of compressive properties of simple cubic and diamond lattices collected from literature are plotted in Fig. 2.11. The simulation results are categorised by whether the J-C failure model is considered for the properties of bulk Ti6Al4V. Despite considerable scatter across the collected data, it can be observed that the FEA-predicted properties effectively establish the quasi-static compressive properties of the lattices.

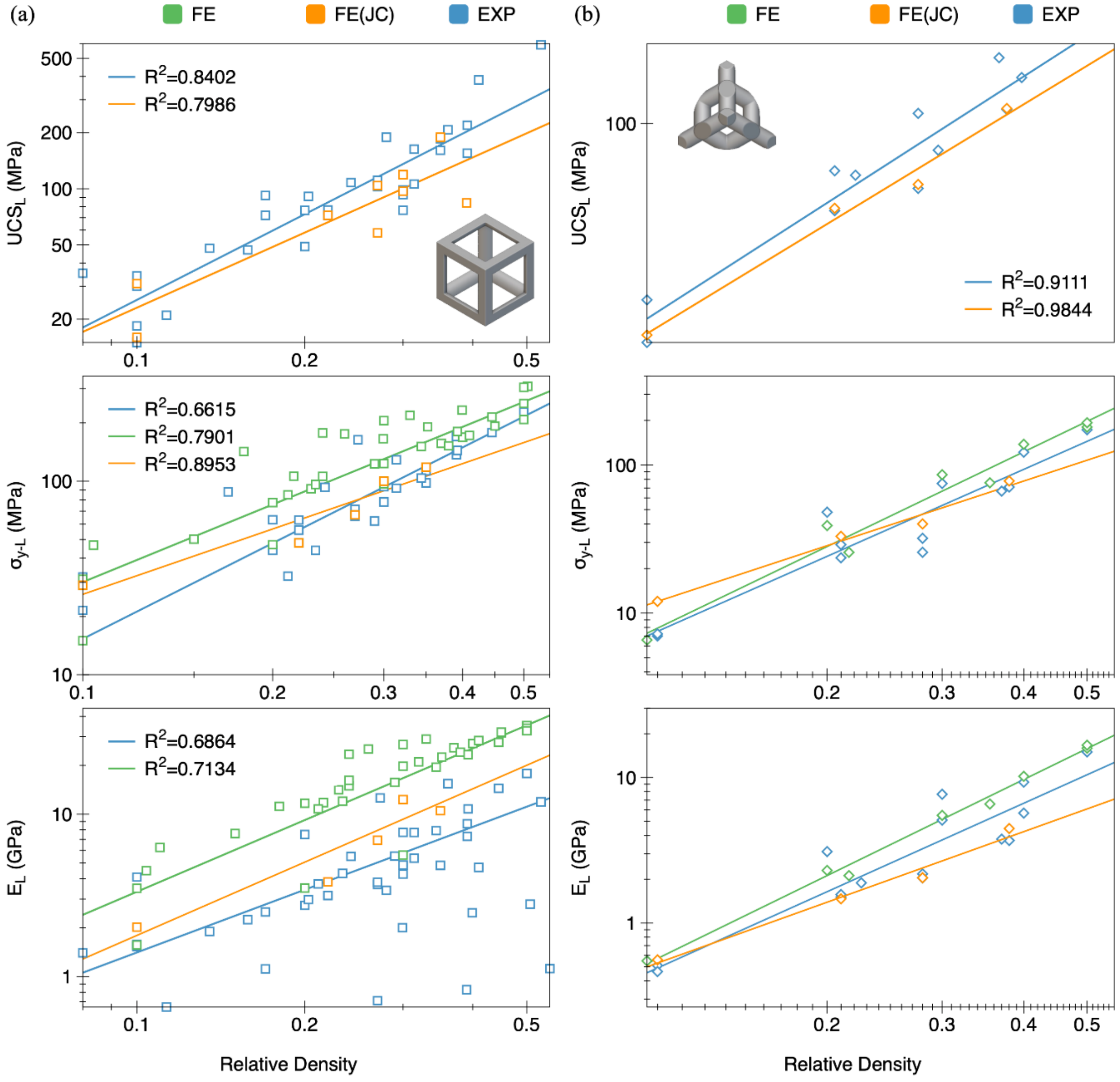

Fig. 2.11 FEA and experimental results of the compressive properties of (a) SC and (b)DIA lattices

2.2.3. Factors Affecting Quasi-Static Compressive Properties

For orthopaedic applications, the main objective of the studies is to replicate the mechanical properties of human bone as closely as possible. As highlighted in previous sections, the mechanical behaviour of lattice structures can be customized by adjusting their geometric design. Furthermore, the mechanical performance of PBF-processed materials can be influenced by both the printing process parameters and post-processing treatments. Therefore, this section offers an in-depth review of the factors that impact the quasi-static compressive properties of PBF-processed lattice structures.

2.2.3.1. Lattice Design

A comprehensive review conducted by Benedetti et al.[1] have examined the cell-topology dependant compressive properties of lattice structures. The data collected from published works are presented in Fig. 2.12. The trend is consistent with the Gibson-Ashby model, all these studies have validated the established relationship between $\bar{\rho}$ and the quasi-static mechanical properties of the lattices. The sheet-based lattices exhibit higher E_L and σ_{y-L} than the strut-based structures. Among the strut-based lattice, at similar $\bar{\rho}$, simple cubic lattice achieved highest E_L and σ_{y-L}.

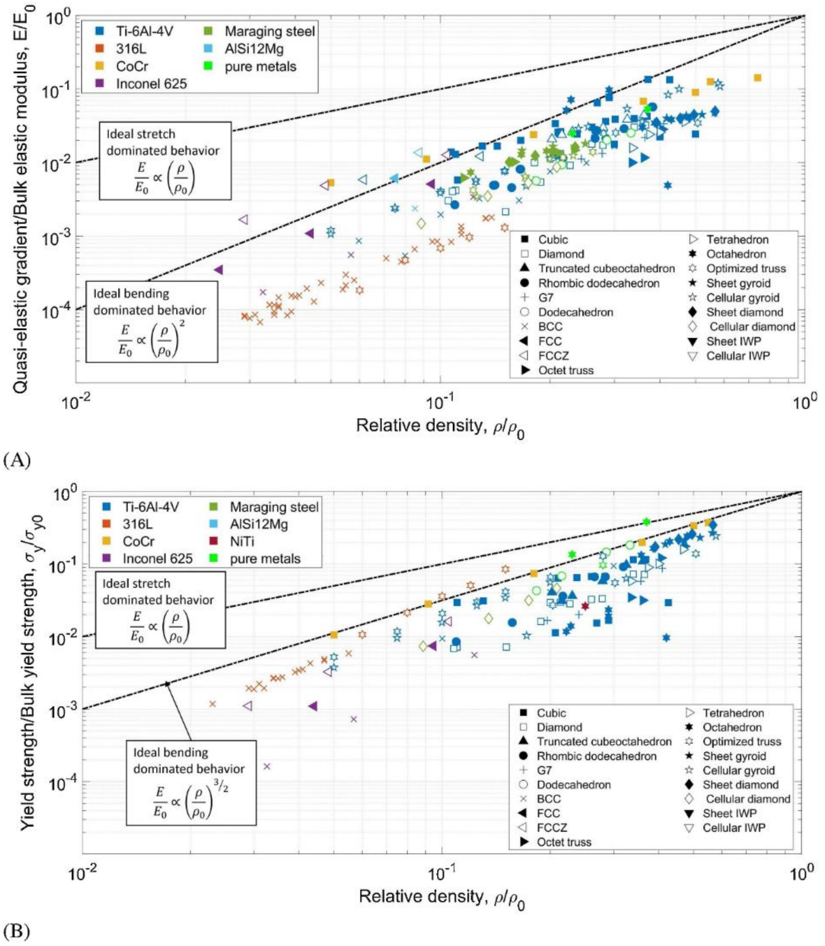

Fig. 2.12 (a) relative Young’s modulus and (b) relative yield strength as a function of relative density of different PBF lattice structures investigated in literature[1]

Li et al.[52] investigated the compressive behaviour of cubic, G7 and rhombic dodecahedron lattices fabricated by EBPBF with a varied porosity level of 58–88%, revealing that the modulus and strength of the lattices decreased in order of cubic, rhombic dodecahedron and G7. These cell-shape-dependant mechanical behaviours were characterised by the coupled mechanisms of buckling and bending deformation of struts. As shown in Fig. 2.13, a greater strut angle α led to a rise in bending component P_1, resulting in a lower modulus and compressive strength but a smoother plateau regime as illustrated in Fig. 2.14. All the lattices fractured by the formation of crush bands shown in Fig. 2.15. In cubic structure, the crush band was perpendicular to the loading direction, whereas in rhombic dodecahedron and G7 lattices, they were about 45º to the loading direction.

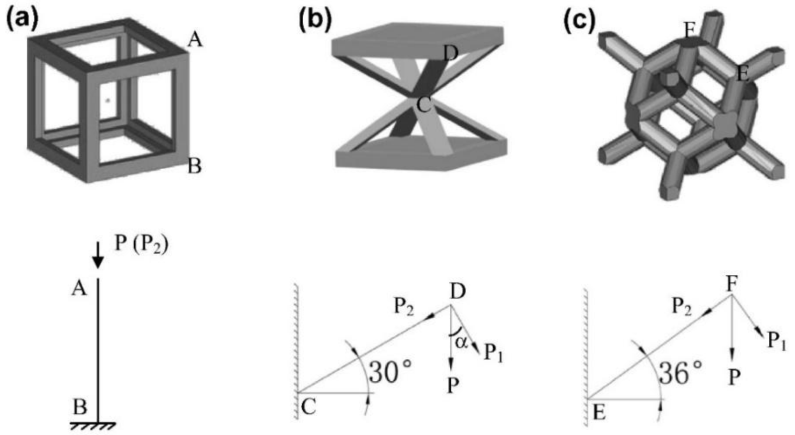

Fig. 2.13 Schematic illustration of bending P1 and buckling P2 components in (a) cubic, (b) G7 and (c) rhombic dodecahedron cells[52]

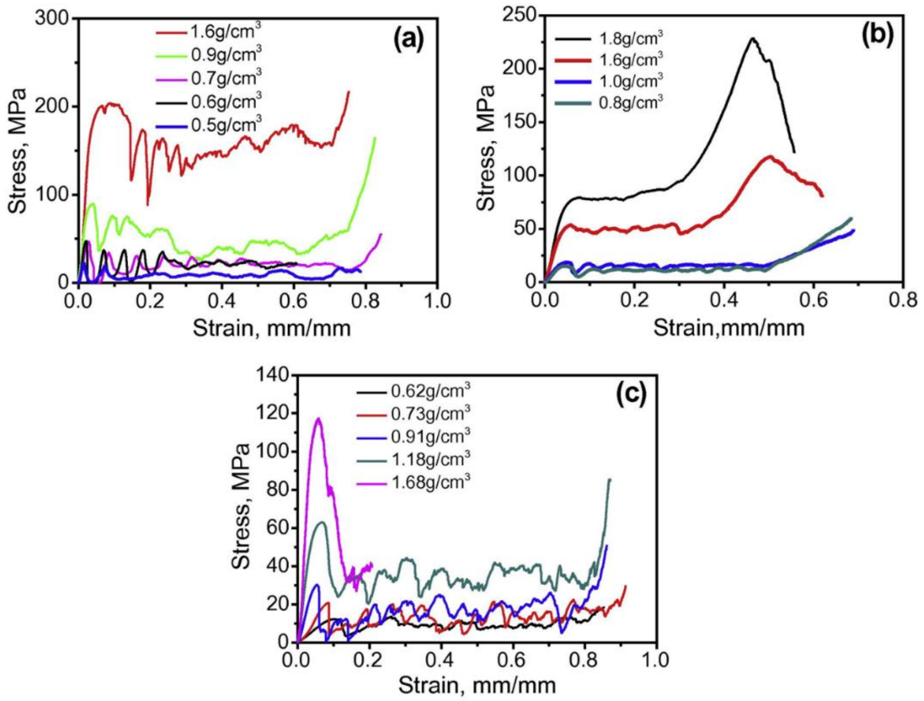

Fig. 2.14 Compressive stress-strain curves of the lattices with (a) SC, (b) G7 and (c) RD cells[52]

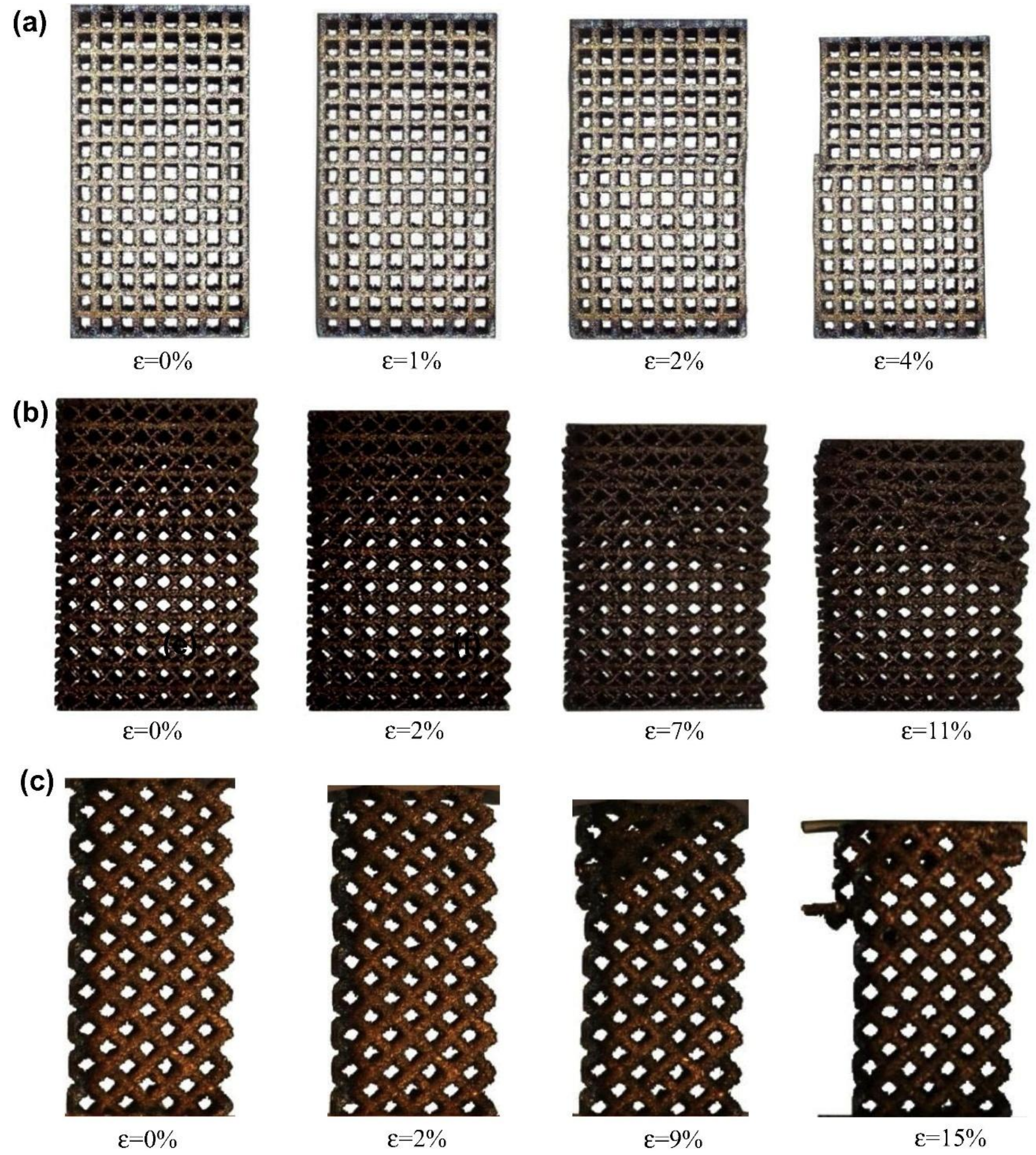

Fig. 2.15 Images of the lattices with (a) cubic, (b) G7 and (c) rhombic dodecahedron cells at different compressive strain levels during the quasi-static tests[52]

Further work done by Ahmadi et al.[48] have investigated the compressive properties of six different types of LPBF fabricated lattice structures with different relative densities, including simple cubic (SC), diamond (DIA), truncated cube (TC), truncated cuboctahedron (TCO), rhombic dodecahedron (RD), and rhombicuboctahedron (RCO). The experimental results of E_L are plotted in Fig. 2.16 (b), respectively, where the structures can be divided into a high-stiffness group (TC, SC, TCO and RCO) and a low-stiffness group (RD and DIA). When $\bar{\rho} > 0.2$, TC showed remarkably higher E_L compared to the other members of its group. The results of UCS_L are shown in Fig. 2.16 (c), where TC, SC and RCO structures demonstrated similar values of UCS_L. In addition, different failure mechanism was observed in the structures with vertical struts (TC, SC, and RCO), where failure of one vertical strut could result in the collapse of the entire lattice. Despite the authors described the sequential collapse initiated by the failure of a vertical strut, the definitive mechanical explanation for why the vertical strut is the initial site of failure was not provided.

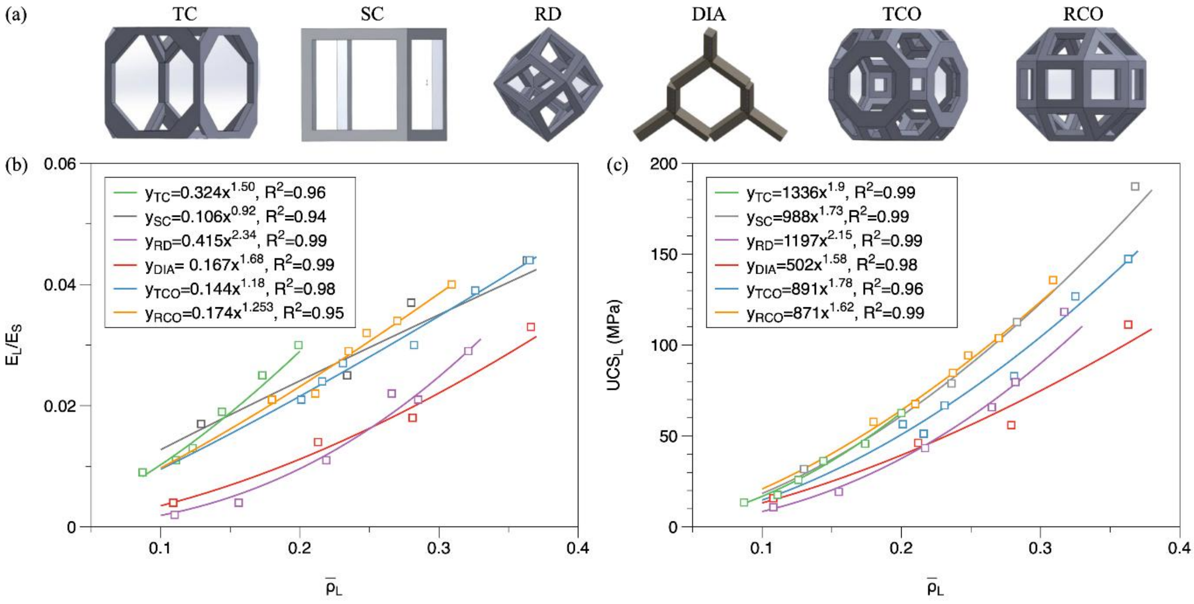

Fig. 2.16 The cell types and data collected from[48]: (a)Six different cell types (b) E_L/E_S and (c) UCS_L

Liu et al.[125] have investigated the compressive properties of the topologically optimised (TO) unit cells introduced by Challis et al.[126] and compared with SC and RD structures fabricated using LPBF with the same relative density of 20%. The stress-strain curves are presented in Fig. 2.17. In this study, SC and TO structures exhibited similar UCS_L, giving 56MPa and 58MPa respectively, while SC structure showed slighter higher E_L than TO lattice, giving 3.3GPa and 2.3GPa, respectively. However, different deformation strain values before failure of SC (~6%) and TO (~15%) structures was observed. In agreement with the previous studies[52,59], the authors concluded that the low ductility of SC structure was contributed by the buckling deformation of the vertical struts in SC cells. For TO structure, the presence of inclined struts at an angle of 45° to loading direction resulted in higher bending stress which contributed more to deformation. However, the uncertainties inherent in this work by Liu et al.[125] must be addressed. Specifically, the authors have utilised a relatively coarse powder size 45–106μm for the LPBF process. This powder size range should be typically used in EBPBF and might introduce uncertainty in resolution and surface finish of the printed component, potentially resulting in LoF defects in their LPBF processed lattices. Thus, this unique processing condition should be considered when comparing the reported mechanical properties to those from studies using conventional LPBF powder specifications.

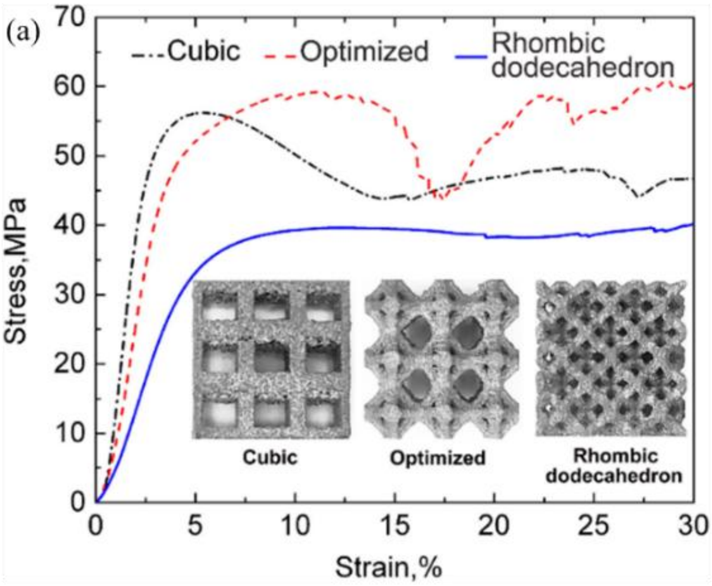

Fig. 2.17 Stress-strain curves for three different types of lattices[125]

2.2.3.2. Processing Parameters and Build Orientation

In LPBF processes, the most important processing parameters are laser power P, scanning speed v, layer thickness τ and hatch spacing h. The commonly used metric to optimise the LPBF processing parameters is volumetric energy density (VED), which can be described by[127–129]:

$$VED = \frac{P}{vh\tau} \tag{2.11}$$

Based on VED, another equation linear energy density (LED) proposed by Dai et al.[130] , which can be written as:

$$LED = \frac{P}{v} \tag{2.12}$$

As reviewed by Buhairi et al.[128] as VED increased, the internal porosity reduced and the smaller α' martensite size as well as larger columnar β grain are exhibited in the LPBF Ti6Al4V dense parts. For LPBF lattice structures, the effects of laser power and scanning speed on the geometrical features of BCC lattices have been investigated by Salem et al.[131]. The authors suggested that with optimised processing parameters, the geometrical accuracy could be improved and the internal porosity within the struts can be minimised. Additionally, the effects of using continuous laser beam (CLB) and pulsed-laser beam (PLB) scanning strategies on the compressive properties of LPBF Ti6Al4V diamond lattices were investigated by Karami et al.[132]. It has been reported that higher $\mathrm{E_L}$, $\sigma_{\mathrm{y-L}}$ and smoother plateau in the stress-strain curve was observed in the PLB specimens due to the finer microstructure.

For EBPBF process, the most common processing parameters are the acceleration voltage , the scanning strategy, the beam current, focus offset (FO), layer thickness, the scanning speed and the spot size[133]. Similar to Equation (2.11), the VED for EBPBF process is defined as[134,135]:

$$VED = \frac{UI}{vh\tau} \tag{2.13}$$

where U is the acceleration voltage, I is the beam current, v is the scanning speed, h is the hatching distance, and τ is the layer thickness. For Acram Q10 machine, the acceleration voltage is 60kV. The scanning speed by means of the speed function (SF) dynamically controls the beam current and scanning speed of electron beam during the process thus controls the melt pool size. The algorithm of SF is disclosed by the Acram company[136], therefore no information is available in the literature. The FO is the additional current provided by the electromagnetic lenses for the translation of the focal plane to its zero position. The spot size is controlled by the combination of focus offset and beam current. The scanning strategy is determined by the scanning process and the scanning mode. The scanning process includes a pre-heating step, a melting phase and a post-heating step. The scanning mode refers to the set of segments that the electron beam scans from point to point. The most commonly used mode is the hatching mode, where a number of parallel lines are connected by perpendicular lines.

Multiple studies have investigated the effects of EBPBF processing parameters on the surface properties of dense Ti6Al4V samples. Several studies[28,137,138] reported that larger molten pools corresponded to higher FO values. Prisco et al.[138] analysed the change in microstructure with varied LED, line offset and FO. It was reported that a coarser microstructure resulted from increasing LED and decreasing line offset. In contrast, the effects of FO on microstructure were found to be negligible. Regarding to surface roughness, multiple works[28,138,139] indicated that the surface roughness was increased with increasing LED and FO and decreasing line offset. For mechanical properties, Hrabe et al.[88] investigated the effects of SF on the tensile properties of dense Ti6Al4V specimens, reported a small change in UTS (+2%) and σ_y (+3%) while changing SF from 30 to 40. Similarly, Wang et al.[140] reported increased E and hardness with increasing SF from 20 to 50 and suggested the optimal mechanical properties could be achieved using an SF between 36 to 50.

For EBPBF lattice structures, the only available work published by Galati et al.[141] demonstrated the effects of variation in processing parameters on mechanical properties of EBPBF diamond lattice structures($\bar{\rho}$=0.20 and d_s=0.42mm). Two levels of beam current (2mA and 4mA), two levels of scanning speed (450mm/s and 750mm/s) and three levels of FO (0mA, 9mA and 15mA) were consisted in the design of experiment (DoE). As shown in Fig. 2.18, in all the cases, the measured values of $\bar{\rho}$ and d_s of all the specimens were over the nominal value of 0.20 and 0.42mm. The smallest deviation in strut size was exhibited at a I=2 mA, FO=0 mA and v=750 mm/s. As a consequence of the variation in strut size, the relative density of the built structures follows the strut thickness. The mechanical properties including E_L and UCS_L were strictly dependant on the geometrical features of the lattices.

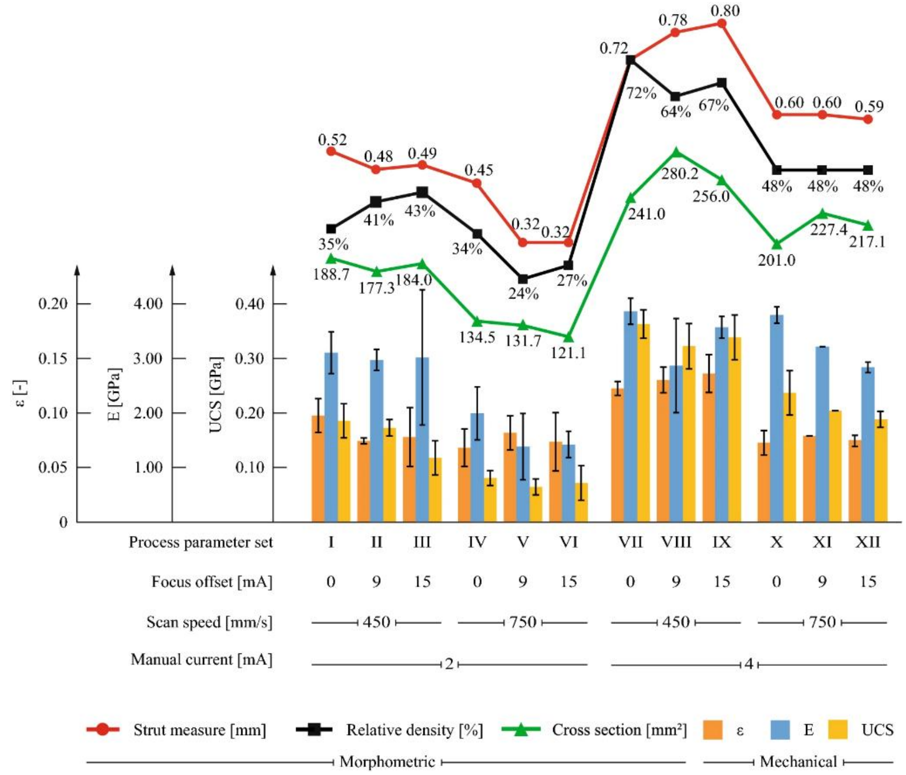

Fig. 2.18 Mechanical and morphometric properties of diamond lattices fabricated using different EBPBF parameters with the same nominal CAD geometry[141]

Build orientation (BD) refers to the positioning of a part relative to the build platform during fabrication, which affects the manufacturability, dimensional accuracy and the mechanical properties of the final products[142]. The angle between the building direction and the build platform is denoted as θ_{BD}. Numerous studies have examined the impact of BDs on mechanical properties, with most focusing on tensile behaviour of single thin strut or sub-structures of the lattices. The experimental results gathered from literature are summarised in Table. 2.3.

Hossain et al.[143] investigated the tensile properties of single struts fabricated using LPBF at θ_{BD}= 90º, 70º, 40º, and 20º. Their findings revealed a trend of increasing tensile strength with higher build angles, consistent with the results reported by Dong et al.[144] and Pehlivan et al.[145]. However, other studies have presented conflicting results. For instance, Barba et al.[146] reported that horizontally built specimens, with strut sizes ranging from 0.25 mm to 3 mm, exhibited slightly higher UTS and yield strength than vertically built ones. Additionally, Murchio et al.[147] observed the highest UTS in samples built at θ_{BD}=15º , further highlighting the variability in reported results.

For EBPBF built structures, Sepe et al.[148] conducted tensile tests on the single-strut specimens at a θ_{BD}= 0º, 45º and 90º to the building platform. It was reported that 45º specimens provided up to 11% higher stiffness and 15% higher UTS that the 90º ones (data of 0º specimens was considered not reliable due to defects). Additionally, there were unmelted powders found in the 0° specimens, which affected the surfaces and the cross-sections of the printed struts.

The apparent conflicting results in literature are driven by differences in stress calculation methods, scanning strategy and post-processing treatments. Murchio et al.[147] calculated stress using the minimal cross-sectional area along the gauge length of their heat treated specimens, the denser inner core of the single strut built at $\theta_{BD} = 15°$ retained high load-bearing capacity. In contrast, Hossain et al.[143] calculated stress using average diameter of their as-built struts, which penalised rougher and lower-angle struts by overestimating the true load-bearing area.

Table. 2.3 Studies on the effects of build orientation on tensile response of PBF specimens

Ref	AM Process & Material	Structure & Size, mm	E	UTS	σ_{y-L}
Hossain[143]	LPBF Ti6Al4V	Single strut 0.25–0.35	No clear trend	90° > 70°> 40°>20°	–
Barba[146]	LPBF Ti6Al4V	Single Strut 0.25–3.00	–	0°>90°	0°>90°
Murchio[147]	LPBF Ti6Al4V	Single Strut 0.60	0°>90°>15°>45°	15°≈0°>90°>45°	15°>0°≈90°>45°
Dong[144]	LPBF AlSi10Mg	Single Strut 1.00	90°>60°>45°>35.5°	90°>60°>45°>35.5°	90°>60°>45°>35.5°
Pehlivan[145]	LPBF CP-Ti	Single Strut 0.15–4.60	–	90°> 0°	90°> 0°
Sepe[148]	E-PBF Ti6Al4V	Single Strut 1.00–2.00	45°>90°	45°>90°	45°>90°

Only two studies specifically addressed static compressive properties. A summary of the studies on compressive performance is presented in Table. 2.4. Wahthle et al.[149] examined the static compressive performance of lattices with diamond unit cells built at BDs at θ_{BD}= 0°, 45° and 90°. The 90° and 0° specimens exhibited comparable mechanical properties, since the printed struts of the lattices were orientated identically at these two BDs. In contrast, the 45° specimen exhibited 35% lower E_L and UCS_L than the 90° specimen, since at θ_{BD}=45°, some struts were printed parallel to the build platform with low quality. Dallago et al.[150] investigated the compressive performance of LPBF Ti6Al4V simple-cubic lattices fabricated in vertical and horizontal orientations. The study reported 40% lower E_L, σ_{y-L} and UCS_Lin the horizontally built (0°) samples compared to the vertically built (90°) ones. This behaviour was attributed to significant irregularities in the struts and slight curvature of the specimens, which likely induced unintended bending forces during testing.

Table. 2.4 Studies on the effects of BD on static compressive response of PBF Ti6Al4V lattices.

Ref	AM	Cell	$\bar{\rho}_L$	d_s,mm	E_L	UCS_L	σ_{y-L}

[149]	LPBF	DIA	0.30	0.40	90° > 0°> 45°	90° > 0°> 45°	90° > 0°> 45°
[150]	LPBF	SC	0.07	0.67	90° > 0°	90° > 0°	90° > 0°

2.2.3.3. Geometrical Inaccuracies and Defects

As discussed in 2.1.2, PBF processed as-built surfaces of metallic components usually have relatively high surface roughness, considerable deviation between the as-designed geometry and other manufacturing defects. LPBF is prone to significant thermal distortion driven by the high residual stress, while the high temperature environment of EBPBF can minimise the residual stress and distortion[7]. Despite EBPBF process is typically associated with lower resolutions and higher surface roughness compared to LPBF processes due to the larger powder size and thicker powder layers used in EBPBF, EBPBF can offer superior dimensional stability and global geometrical accuracy for medium to thick parts[151].

The effects of these geometrical defects or imperfections on the mechanical properties of the PBF lattices have been widely studied in literature[152–155]. It was reported that the strut waviness and variation in strut thickness can greatly affect the compressive properties of PBF lattices due to the increased bending moment and the change in moment of inertia in the struts, respectively. Several studies[153–155] suggested that strut size variation would have a greater impact on the mechanical properties than the effect caused by strut waviness. The enhancement or reduction in strength depends on whether the as-built cross-sectional area is oversized or undersized corresponding to the nominal designed strut thickness. In addition, it was reported that by increasing the strut building angle, both the strut thickness variation[147,155] and waviness decreased[83,155].

For PBF dense parts, published works[156,157] suggested that the small pores were harmless to their mechanical performance. For small pores with a low total porosity (<0.1%), no significant effects were found on the tensile properties of the LPBF dense parts. However, several studies suggested that even small amounts of porosity can significantly affect the tensile performance of lattice structures due to the presence of thin struts or walls. Yan et al.[158] reported that by increasing the cell size of the gyroid lattice structures ($\bar{\rho}=0.15$) from 2mm to 8mm, the internal porosity increased from 0.5% to 10.4%, resulting in a reduction of 27% in E_L and of 36% σ_{y-L} in their LPBF lattices. A recent study conducted by Wares et al.[159] further confirmed the detrimental effects of the internal pores on the tensile properties of gyroid lattices.

For compressive properties, it has been reported by Strauss et al. [160] that the combined influence of internal porosity and strut size variation would change the relative density, thereby affecting the quasi-static compressive behaviour of PBF lattices. The maximum reduction in cross-sectional area of 44.29% was observed for the FCC lattice with a strut size of 0.5mm. However, Plessis et al.[157,161] reported that introducing a spherical 0.5mm pore inside a 0.8mm vertical strut of an LPBF SC cell lattice did not affect the compressive yield strength of the lattice. However, their FEA simulation showing in Fig. 2.19 suggested that all the pores larger than 0.1mm could act as the stress concentrator. The authors suggested that the discrepancy between their experimental and FEA predicted results was attribute to be the difference between the ideal strut conditions in FEA model and the as-built surfaces of the LPBF specimens. The authors concluded that this as-built rough surface creates higher stress concentrations than those predicted for a large 0.5mm internal pore, indicating that surface roughness was the more dominant factor affecting the quasi-static compressive properties of the lattice.

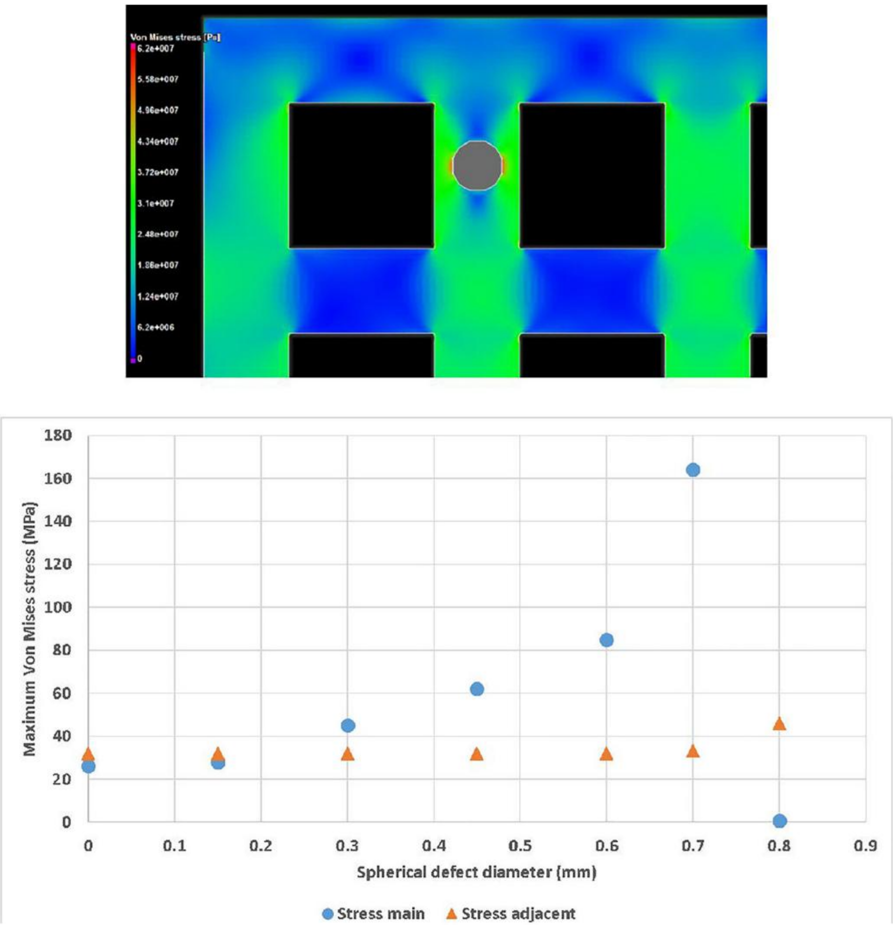

Fig. 2.19 FEA simulated maximum σ_{VM} with varying internal pore size on the load-bearing strut[157]

2.2.4. UCO-Dependant Quasi-static Properties

As reviewed in the last three sub-sections, the properties of EBPBF lattices have been studied intensively using compression tests covering the effects of various factors, such as lattice design, processing parameters and the geometrical imperfections, on the mechanical properties of lattices. However, the effects of UCOs with respect to the LD have not been considered in these studies. For a load-bearing implant after implantation, the compressive loading acting on it can be multi-directional, thus, the anisotropic properties of the lattices and the behaviour of the cells under loading need to be considered. Only limited studies have focused on investigating the influence of the unit cell orientation

(UCO) with respect to the loading direction on the mechanical performance of lattice structures. Choy et al.[67] compared the compressive properties of simple cubic and honeycomb lattices with two UCOs: [001] and [011]. Both of the [001] SC and honeycomb samples exhibited higher compressive strength and elastic modulus, attributed to the presence of vertical struts in the [001] orientation. Furthermore, the failure mechanisms differed between the orientations: [001] samples failed in a layer-by-layer manner, while [011] samples experienced abrupt shear failure along a shear plane approximately 45° to the loading direction.

Wauthle et al.[149] investigated diamond-based lattices with three different unit cell orientations. Their findings indicated that the mechanical properties could not be distinguished due to the isotropic nature of the diamond unit cell. However, later studies[162,163] reached different conclusions, highlighting a significant dependence of the mechanical properties of diamond lattices on cell orientation. This discrepancy can be attributed to the poor quality of the printed struts in Wauthle et al.'s investigation[149], where the highest strut density was below 97.5%, and large pores were observed in all specimens.

Soul et al.[163] confirmed the tensile behaviour of AlSi10Mg diamond lattices to be dependent on unit cell orientation (UCO), examining three orientations: [001], [011], and [111]. The [001] samples demonstrated a 20% higher ultimate tensile strength than the other orientations, while the [111] specimens showed the highest elastic modulus but lower ductility. Furthermore, Cutolo et al.[162] investigated the compressive response of diamond lattices with these three UCOs. Their experimental results for elastic modulus differed from those of Soul et al.[163], with the [011] samples exhibiting the highest elastic modulus. The variations in elastic modulus observed between the two studies can be attributed to differences in production and testing methods.

Table. 2.5 Studies on the effects of cell orientation on mechanical properties of PBF specimens

Material &AM	Cell Topology & Porosity	Unit Cell Orientation	Young's Modulus	Compressive Strength	Tensile Strength	Ref
Ti6Al4V LPBF	Cubic 41.7%–91.7%	[001] & [011]	[001]>[011]	[001]>[011]	–	[3]
Ti6Al4V LPBF	Honeycomb 23.6%–84.4%	[001] & [011]	[001]>[011]	[001]>[011]	–	[67]
Ti6Al4V LPBF	Diamond ~70%	[001], [011], [00−1]	[001]≈[011]≈[00−1]	[001]≈[011]≈[00−1]	–	[149]
AlSi10Mg LPBF	Diamond 66%	[001],[011],[111]	[111]>[011]>[001]	–	[001]>[011]≈[111]	[163]
Ti6Al4V	75%	[001],[011],[111]	[011]>[111]>[001]	[011]>[111]>[001]	–	[162]

The above reviewed studies revealed that, there still remains a lack of research effort of the investigation of the orientation-dependant effects of the compressive properties of lattice structures, thus the anisotropic behaviour of lattices is not well understood. Therefore, the combined effects of LD, UCO and the EBPBF defects of struts on the compressive behaviour of the lattices should be studied. These combined effects should be investigated using SC cell-based lattices, since each unique strut-LD relationship can be defined clearly and then the effects of various LD-UCO combinations can be defined.

2.3. Fatigue Properties of PBF Lattices and Orientation Effects

2.3.1. Experimental Evaluated Fatigue Behaviour of PBF-Lattices

Metal fatigue is the characteristic that describes the damage mechanism that structural components exposed to time-varying loads are prone to failure at stress levels below the ultimate strength of a given material. With an applied load above a certain threshold, the accumulated microscopic damage will result in initiation and propagation of cracks or other macroscopic damage, which leads to the final fatigue failure. Depending on the applied stress level, the fatigue life of a component can be classified in either high-cycle fatigue (HCF) and low-cycle fatigue (LCF), which is characterised by the presence or absence of plastic deformation[1].

For AMed bulk materials, the fatigue failures usually related to the localised factors within the material, such as defects associated with the PBF process, namely lack of fusion (LoF) defects and porosity.[164]. As a result, AMed materials generally exhibit lower fatigue strength, especially in high cycle fatigue (HCF) and shorter fatigue life compared to their counterparts manufactured using traditional methods[165]. For porous metallic structures, the typical qualitative plot of total strain versus the number of fatigue cycles is presented in Fig. 2.20(a), illustrating the three stages of the fatigue life. As described by Sedat et al.[166], Stage I is marked by progressive strain accumulation, primarily dominated by cyclic ratcheting. Based on the $\varepsilon - \mathrm{N}$ plot, the intensity of the ratcheting occurring during stage I can be quantified by the average ratcheting rate $\frac{\mathrm{d}\varepsilon}{\mathrm{dN}}$, in terms of the plastic strain accumulated during the fatigue process. It can be defined as the slope of the line fitting the mean strain up to $\mathrm{N_i}$[167]. Stage II features a long plateau, where the cracks initiate at critical locations, accompanied by a noticeable cumulative deformation rate. In the final stage, failure occurs abruptly, characterized by a sudden increase in strain due to the coalescence of multiple cracks. The number of cycles at damage initiation $\mathrm{N_i}$ is defined as the point where the strain amplitude shows a 1% increase over its initial constant value. The number of cycles to failure $\mathrm{N_f}$ is determined as the intersection between the ratcheting line and the line fitted to the final points of the mean strain before the test is terminated[167]. Under HCF conditions, the stress-life relationship can be described by Basquin equation as[168]:

$$\sigma = K' \cdot (N_f)^B \tag{2.14}$$

where σ is the applied stress, N_f is the number of cycles to failure, K' is the fatigue strength coefficient and B is the fatigue strength exponent. The effect of mean stress σ_m can be described by the curves presented in Fig. 2.20(b), the region below each curve indicates infinite life.

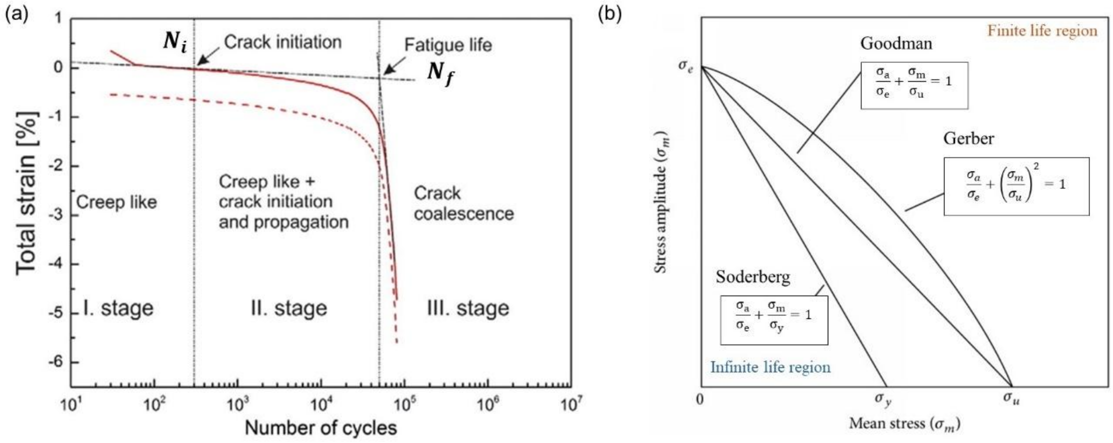

Fig. 2.20 (a)Typical strain-life curve of fatigue damage of porous metallic materials[166](b) illustration of mean stress equations[169]

The experimental data of fatigue properties of the PBF-processed lattice structures gathered from the literature is summarised in Table. 2.6, demonstrating the varied fatigue strength of PBF lattice. Most fatigue experiments on lattice structures have been conducted under uniaxial compression-compression, in accordance with the International Standard ISO 13314[92], outlined in Section 2.2.1, which specifies quasi-static mechanical testing for porous structures. The reviewed compression-compression tests were mostly conducted at a frequency of 10–30Hz and a load ratio (ratio of maximum to minimum load) of R=10. Fatigue tests are preceded by quasi-static tests to determine the yield stress, ultimate compressive strength and plateau stress. The maximum absolute global stress σ_{max} applied for the fatigue tests are typically within the range of 10–80% of the yield stress. The variation in σ_{max} values among the collected data can be attributed to various factors, such as lattice type, PBF process, heat treatment and relative densities.

For a better understanding of these collected data in Table. 2.6, σ_{max} values are plotted against $\bar{\rho}$ in Fig. 2.21, where the N_{RO} values of the plotted data points range from 10^6 to 10^7 cycles. It can be understood that the fatigue strengths of non-SC lattices are relatively low, giving σ_{max}=25MPa at $\bar{\rho}$=0.4, except for two notable exceptions. The first exception is the diamond-cell based lattice with [011]//LD UCO, which has exhibited a high σ_{max} of 80MPa at $N_{RO}=10^6$[170]. It has been suggested by the authors that the notably differences in σ_{max} between the [011]//LD diamond lattice and the other two orientated lattices were not only caused by the design of unit cells but also by the geometrical manufacturing deviations introduced by the PBF process. The second exception is the FCCm[95] and topologically optimised[171] lattices. It should be noted that these unit cells are the examination of the 3D models from the two studies suggests that both correspond to the same type of unit cell, namely the modified face-centred-cubic (FCCm) configuration. Thus, as shown in Fig. 2.21, for $N_{RO}=10^6$, the σ_{max} of FCCm lattices increases to 55MPa as $\bar{\rho}$ rises to 0.3. However, in both studies[95,171], it is has not been explicitly clarified that, compared to other non-SC lattices, why FCCm lattices might offer superior fatigue performance by either delaying the crack initiation or slowing down the crack growth.

Table. 2.6 Fatigue data collected from literature

Ref	**Cell**	**Porosity**	**R**	**f(Hz)**	**AM & Material**	N_{RO}	σ_f/σ_y	σ_f/σ_{pl}	σ_f/UCS
[95]	FCCm	0.63−0.88	10	15	LPBF (HIP) Ti6Al4V	1.0×10^6	0.25−0.29	−	0.18-0.23
[172]	Diamond	0.68	10	15	LPBF (AB, HT, HIP) Ti6Al4V	1.0×10^6	0.19−0.27	−	−
[173]	Diamond	0.63−0.66	10	15	LPBF (AB) Ti6Al4V	4.0×10^6	0.25−0.28	0.31−0.39	0.19−0.23
[174]	Diamond	0.66−0.89	10	15	LPBF (AB) Ti6Al4V	1.5×10^5	0.25−0.4	0.28−0.35	0.15−0.22
[170]	Diamond	0.75	10	30	LPBF (AB) Ti6Al4V	5.0×10^6	−	−	0.13−0.60
[23]	Diamond	0.60-0.83	10	15	EBPBF (AB) Ti6Al4V	1.0×10^6	0.15−0.25	−	−
[175]	RD	0.62−0.84	10	10	EBPBF(CE) Ti6Al4V	1.0×10^7	−	−	0.11−0.15
[176]	RD	0.68−0.91	10	10	EBPBF (AN) Ti2448 & Ti6Al4V	1.0×10^7	0.10-0.21	−	0.11−0.20
[177]	RD	0.72	10	10	LPBF (AB) CP-Ti	1.0×10^6	−	−	0.13
[59]	RD	0.62	10	10	EBPBF (AB) Ti6Al4V	1.0×10^7	−	0.23	0.16
[178]	RD$_m$	0.82−0.87	10	10	EBPBF (AB) Ti6Al4V	1.0×10^6	0.18−0.19	−	0.17−0.18
[59]	Cubic	0.63	10	10	EBPBF (AB) Ti6Al4V	1.0×10^7	−	0.67	0.54
[150]	Cubic	0.93	−1	120	LPBF (HT) Ti6Al4V	1.0×10^7	0.04−0.13	−	0.04−0.13
[179]	Cubic	0.72	10	10	EBPBF (AB &HT) Ti6Al4V	1.0×10^7	0.72−0.85	−	−
[180]	Cubic	0.50−0.70	10	30	EBPBF (AB) Ti6Al4V	1.0×10^7	1.00−1.30	−	−

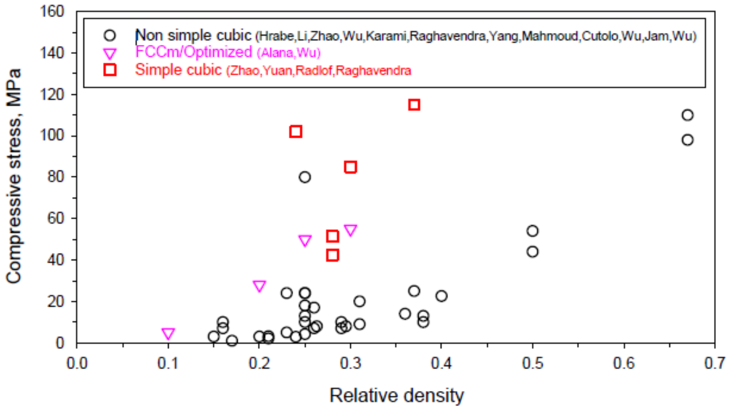

Fig. 2.21 Fatigue strength data vs relative density collected from literature

2.3.2. FEA-Based Assessment of Fatigue Performance of Lattices

Different approaches have been applied to predict the fatigue performance of lattice structures. Once the stress or strain distribution on the lattices is evaluated by FEA, the local stress and strain values can be considered as the input for fatigue assessment. The procedure of determining S-N curve of a lattice structure is described by Peng et al.[181], showing in Fig. 2.22. The maximum fatigue damage is modelled as a function of shear strain and the strain normal to the shear plane by Brown-Miller strain-life equation:

$$\frac{\Delta\gamma_{max}}{2} + \frac{\Delta\varepsilon_n}{2} = 1.65\frac{\dot{\sigma_f}}{E}\left(2N_f\right)^b + 1.75\dot{\varepsilon_f}\left(2N_f\right)^c \tag{2.15}$$

where $\Delta\gamma_{max}$ and $\Delta\varepsilon_n$ are the maximum range of the shear strain and normal strain, respectively. $\dot{\sigma_f}$ and $\dot{\varepsilon_f}$ are the coefficients of fatigue strength and fatigue ductility. The FEA calculated results were imported to the fatigue analysis software Fe-Safe for the prediction of fatigue life. The results confirmed that the fatigue life improved with increased $\bar{\rho}$ for all the investigated lattices (SC, SC-BCC, FCC and BCC) and the highest fatigue strength was exhibited by SC lattices. However, no experimental validation was conducted in this study. The predicted S-N curves of the lattices are presented in Fig. 2.23. A noticeable discrepancy is observed when comparing the fatigue limit ($N=10^7$) of SC lattice predicted by FEA ($\sigma_{max}/\sigma_{y-L}$ ≈0.7) with the experimental data as listed in Table. 2.6 ($\sigma_{max}/\sigma_{y-L}$≈0.5[179] or ≈1.1[180]), at a similar relative density level ($\bar{\rho}$≈0.3-35).

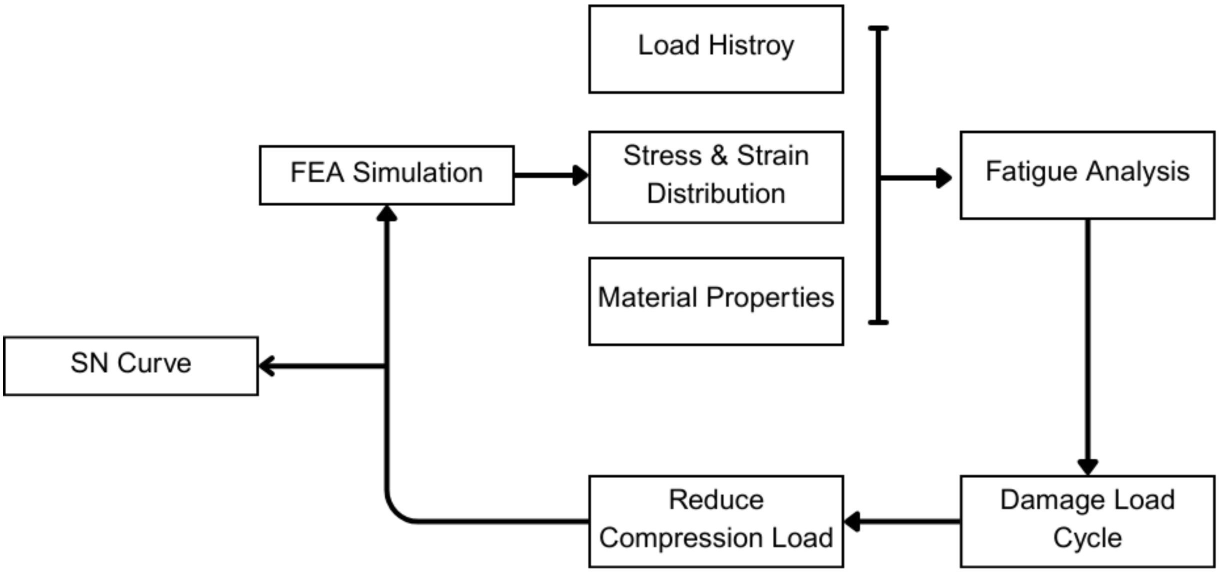

Fig. 2.22 Procedures of determining SN curve using FEA[181]

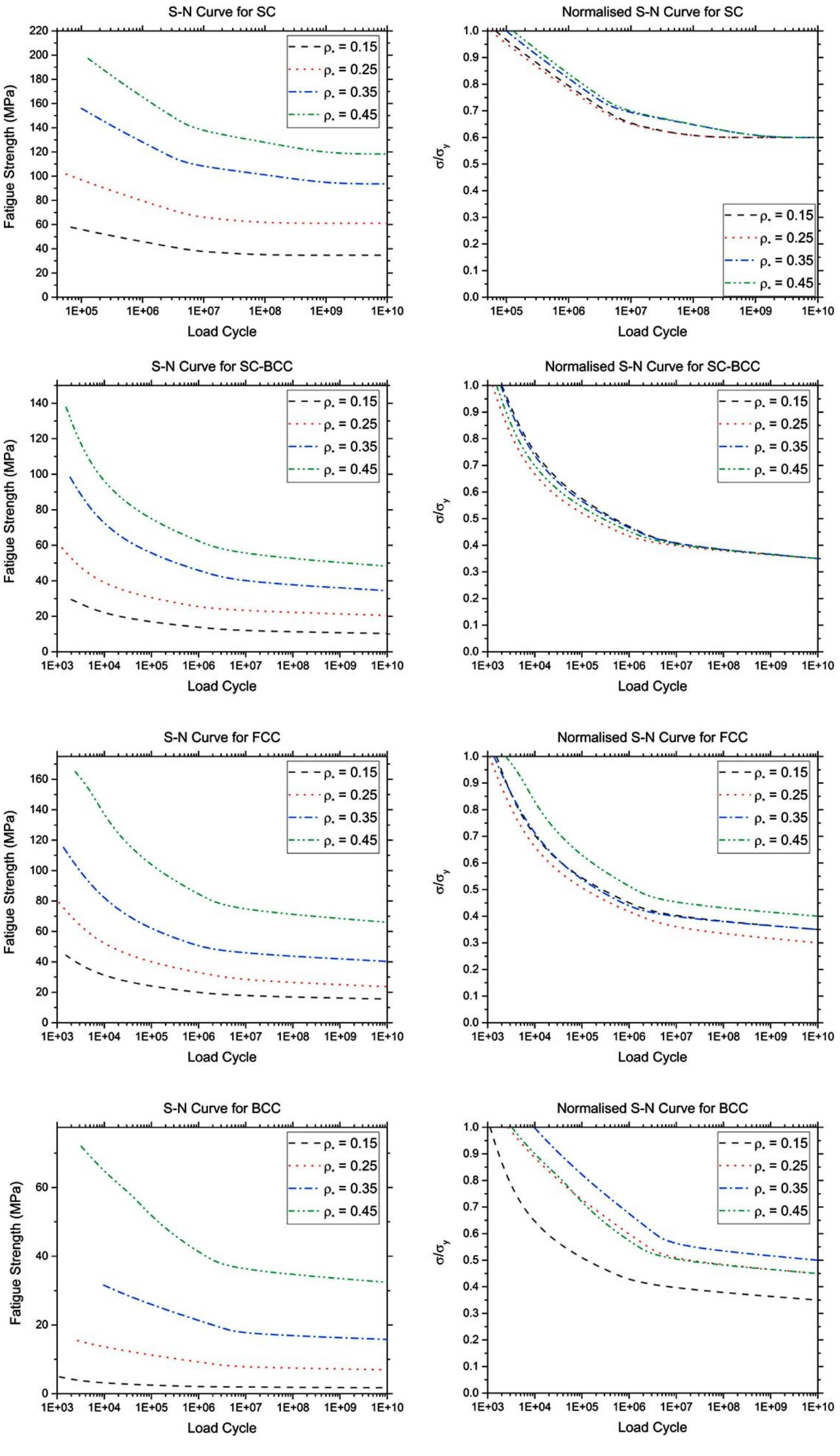

Fig. 2.23 S-N curve and normalised S-N curve of SC, SC-BCC, FCC and BCC lattice with different $\bar{\rho}$[181]

Hedayati et al.[182] analysed the fatigue performance of rhombic dodecahedron lattices with different porosity levels (66.4%–83.7%) by FE models using beam elements. Each of the FE simulation cycle represented a number of loading-unloading cycles Δn_i The stress concentrations were described by a single stress concentration factor K_f for each type of lattices to account for the effects of the strut irregularities and surface roughness of the PBF struts. The stress concentration factor K_f was used as a multiplier applied to the equivalent reversible stress σ_{rev} of each strut, representing the localised amplification of stress due to the geometrical imperfections. The damage accumulation D_i in each strut was described by the S-N curve of the parent material and Miner's rule[183], given by:

$$D_i = \sum_i \frac{\Delta n_i}{N_i} \tag{2.16}$$

where the equivalent reversible stress was calculated for each strut and then the life of the strut considering the imposed stress level was calculated. The elements with larger damage than the defined threshold or if the stresses exceeded σ_{y-S} were removed from the model. The simulation continued until 90% drops of E_L achieved. As shown in Fig. 2.24, comparing with the experimental results obtained in Ref. [51], the predicted results exhibited acceptable accuracy in low-stress regimes when applied stress level was lower than $0.6\sigma_{y-L}$. For high-stress regimes, the model predicted unrealistic short lives. It was suggested that alternative approaches should be used for the prediction in high-stress regimes.

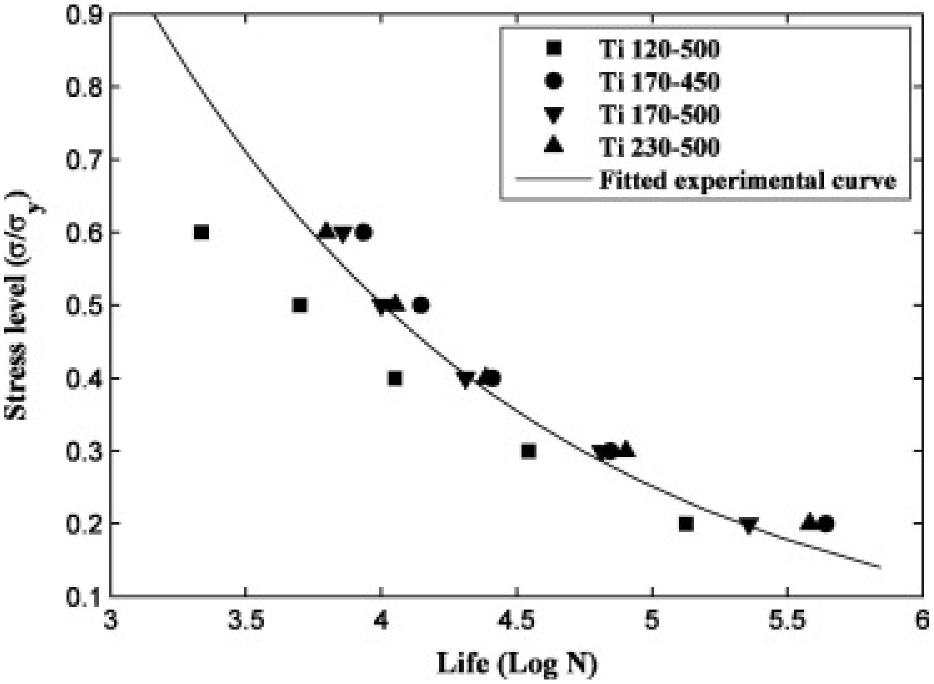

Fig. 2.24 FE predicted S-N data compared to the experimental S-N curve[182]

By neglecting the stiffness reduction due to damage, Zargarian et al.[184] predicted the fatigue behaviour of titanium lattices (diamond, rhombic dodecahedron and truncated cuboctahedron structures) using linear elastic FE simulations and implemented a failure-event based algorithm. Discontinuous damage process was considered, the strut with the lowest fatigue life was removed in each simulation cycle and the damage due to the failure of that strut was implemented in fatigue calculations using Miner's rule given in Eq.(2.16). The experimental validation suggested good agreement between the experimental and simulation results.

2.3.3. Factors Affecting Fatigue Behaviour

2.3.3.1. Lattice Design

It has been reported that the fatigue strength of a cellular porous structure is linearly related to the properties of the base material, which can be estimated from Gibson-Ashby model as described in Section 2.1[175,184]. As shown in Fig. 2.25, the S-N curves of rhombic dodecahedron[51,75,175,178] and diamond[23,173,174] lattices extracted from multiple studies confirmed that, lowering $\bar{\rho}$ can greatly shorten the fatigue life and reduce the fatigue strength of cellular lattice structures. The fatigue stresses are usually normalised by a quasi-static macroscopic property such as σ_{y-L}, σ_{pl-L} or UCS_L to account for different factors such as the varied relative density, microstructure, manufacturing defects in an implicit manner. As shown in Fig. 2.25, despite the curves are normalised with UCS_L, the data still demonstrates a decreasing trend with decreasing $\bar{\rho}$. As explained by Benedetti et al.[1], this is because that UCS_L, as a global mechanical response of the entire lattice structure, cannot capture the entire detrimental effects of the local damage phenomenon during the high-cycle fatigue. It can also be noticed that from the normalised curves, diamond lattices demonstrate slightly higher normalised fatigue strength than rhombic dodecahedron lattices at similar $\bar{\rho}$ levels, indicating that apart from relative densities, the fatigue strength of lattice structures is also significant affected by the cell topologies.

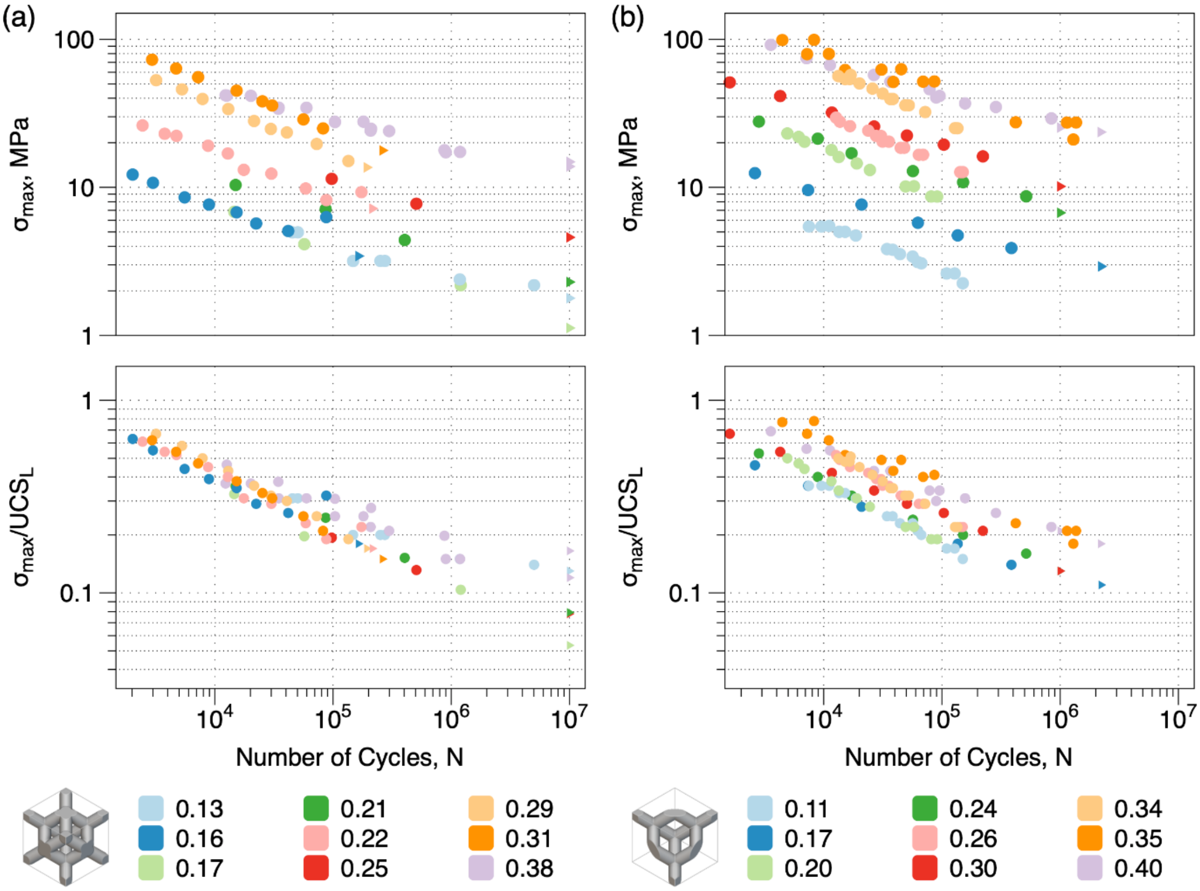

Fig. 2.25 S-N and normalised S-N curves of (a) rhombic dodecahedron[51,75,175,178] and (b) diamond Ti6Al4V lattices[23,173,174] extracted from literature

Benedetti et al.[1] reviewed the compression-compression fatigue properties of PBF lattices with different materials, cell topologies and relative densities at 5×10^6 cycles, the data collected from literature is plotted in Fig. 2.26. Simple-cubic-based lattices showed an exceptionally high compression stress when the load direction is parallel to their vertical struts. Yavari et al.[174] observed no fatigue damage in the LPBF SC lattice ($\bar{\rho}$=0.1~0.35) at 10^6 cycles even subject to a high load of $0.8\sigma_{y-L}$. A later study published by Zhao et al.[59] reported a fatigue strength of 75MPa(≈0.38UCS_L) of the EBPBF SC lattice($\bar{\rho}_L$≈0.37) at 10^7 cycles. It was reported by Li et al.[175] that cyclic ratcheting plays a dominated role in determination of the fatigue life of PBF lattices.

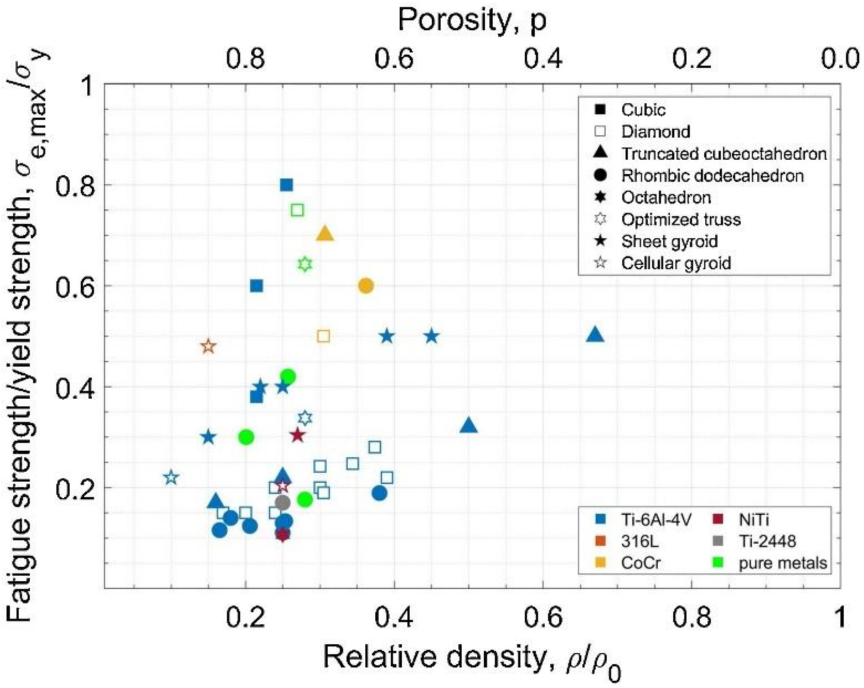

Fig. 2.26 Relative density vs fatigue strength of the PBF lattices (N=5×10^6 cycles)

In a later study conducted by Zhao et al. [59], the results of cyclic ratcheting and fatigue damage strain of the studied SC, G7 and RD lattices are presented in Fig. 2.27 (a-b), confirming that the cyclic ratcheting has been the main factor causing the fatigue failure. The authors have indicated that the cyclic ratcheting behaviour depends to the interaction between the bending and buckling deformation of the struts. As suggested by Fig. 2.27(c), the cyclic ratcheting rate $d\varepsilon/dN$ is greatly dependent on the cell topology and local geometry. The experimental suggested that the increasing the buckling component (illustrated in Fig. 2.13) to decrease $d\varepsilon/dN$ would be an effective way to enhance the fatigue strength of the PBF lattices.

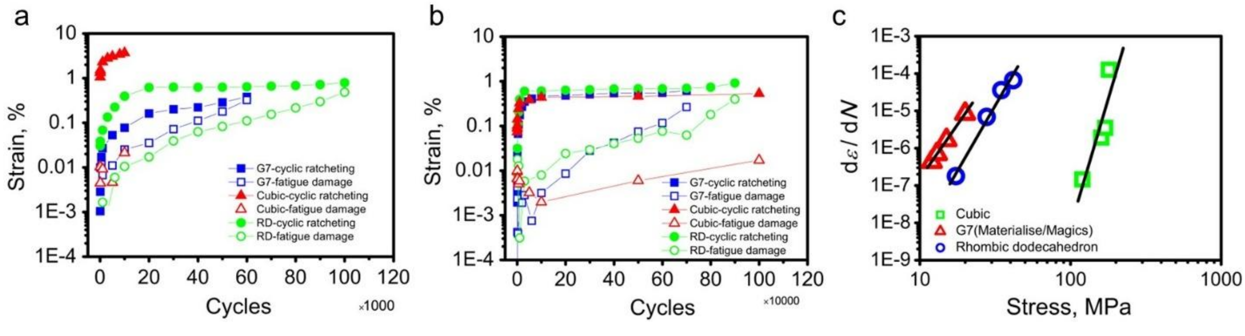

Fig. 2.27 The cyclic ratcheting and fatigue damage strains of the lattices with SC, G7 and RD cells in (a) L- (b) HFC region and (c) the effect of stress on the cyclic ratcheting rate of the meshes with different structures[59]

2.3.3.2. Building Direction

Since no published works were found specifically addressing the effects of BD on the compression-compression fatigue behaviour, a broader contextual review was conducted involving relevant studies on compression-tension and tension-tension fatigue performance. The majority of the available studies discussed the effects of BD on single strut sub-structures of the lattices, while only one study[150] was found discussing the effects of BD on fatigue properties of the entire lattice structures. The reported results of fatigue properties are summarised in Table. 2.7.

Table. 2.7 Fatigue properties of PBF built Ti6Al4V structures with different BDs

High Cycle Fatigue (HCF)								
Ref	AM	Structure	Test	d_s,mm	R	f(Hz)	N_{RO}	σ_f
[150]	LPBF	SC lattice	T–C	0.67	-1	120	10^7	90° > 0°
[147]	LPBF	Single strut	T–C	0.60	-1	200	10^7	45°>90°>15°>0°
[185]	LPBF	Strut–junction	T–C	0.67	-1	200	10^7	15°>0°>45°>90°
[186]	LPBF	Strut–junction	T–C	0.67	-1	200	10^7	15°>0°>45°>90°
Low Cycle Fatigue (LCF)								
Ref	AM	Structure	Test	d_s,mm	R	f(Hz)	N_f	σ_{max},MPa
[187]	E-PBF	Single strut	T	2.00	0.1	10	0°>45°>90°	290
[188]	LPBF	Single strut	T	1.30	0.1	30	75°>90°>60°–0°	400−700

For strut-junction structures, under HCF compression-tension fatigue tests ($R = -1$), both Murchio et al.[185] and De Biasi et al.[186] found that the highest fatigue strength (N_{RO}=10^7) was exhibited at $\theta_{BD} = 15°$ for LPBF strut-junction sub-structures. However, for single strut, Murchio et al.[147] reported that the highest static strength was obtained at $\theta_{BD} = 15°$, but the highest fatigue strength was achieved at $\theta_{BD} = 45°$. Under LCF tension-tension fatigue tests ($R = 0.1$), Persenot et al.[187] reported that the highest fatigue life ($R = 0.1$) were obtained at θ_{BD}=0° for EBPBF single strut, while Zhang et al.[188] found that the highest life at $\theta_{BD} = 75°$. The BD-dependent effect on surface roughness R_a, number of defects, and strut size deviations has been discussed in these studies.

On the other hands, for lattice structures, Dallago et al.[150] investigated the fatigue performance of SC lattices under fully reversed fatigue tests (R= -1 and f=120Hz). The 0° built samples demonstrated approximately 80% lower σ_f than the 90° specimens ($N_{RO} = 10^7$). The authors have concluded that the reduction in fatigue strength of the 0° samples was attributed to the high surface irregularities and strut thickness deviations resulting from the smaller angle of θ_{BD}.

In these studies, even though the greatest R_a values were often reported at lower θ_{BD}, some studies reported the opposite trend of increasing R_a with increasing θ_{BD}. Regardless of the R_a trend, fatigue crack initiation was almost always linked to these lower θ_{BD} induced high-roughness downward-facing surfaces or strut thickness deviations. This suggested that, even without specific data on the effect of BD on compression-compression fatigue performance, the reviewed works demonstrated that the fatigue life of PBF struts and lattices are strongly dominated by the BD-dependant geometric features.

2.3.3.3. Geometrical Imperfections and Defects

In the last section, as shown in Fig. 2.28, the effects of four different BDs on the fatigue strength have been investigated by Murchio et al.[147], concluding that the lower fatigue strength of the struts built at 0° and 15° was resulted by the poor surface texture and higher geometrical imperfections. In addition, the authors also evaluated the effect of porosity on the fatigue behaviour of the PBF single strut, the pore distribution is shown in Fig. 2.29. The authors highlighted the role of defects location, their statistical analysis revealed that there were fewer but larger (in terms of the square root of the projected area $\sqrt{\mathrm{Area}}$, Murakami parameter[189]) surface defects in the 90° specimens, indicating that the distribution of surface defects played a key role in the fatigue performance. It was reported in this study that the small pores were found to have little influence on the fatigue strength of the PBF built thin struts for all the specimens except for the 90° ones. The pores with considerable size were only observed on the fracture surfaces of the 90° samples, while sub-surface small pores were considered not affecting the fatigue strength and gas-holes were considered less detrimental on the fatigue behaviour of specimens due to the low stress intensity factor. Even though the 90° specimens exhibited largest defect size measured from the SEM image of the fracture surface, no direct evidence demonstrated that the failure of the 90° specimens resulted by the presence of pores. The authors considered that the facture of the 90° specimens under cyclic loading might be caused by a combined effect of rough surface and porosity, further investigation on determining the critical-killer defects should be conducted.

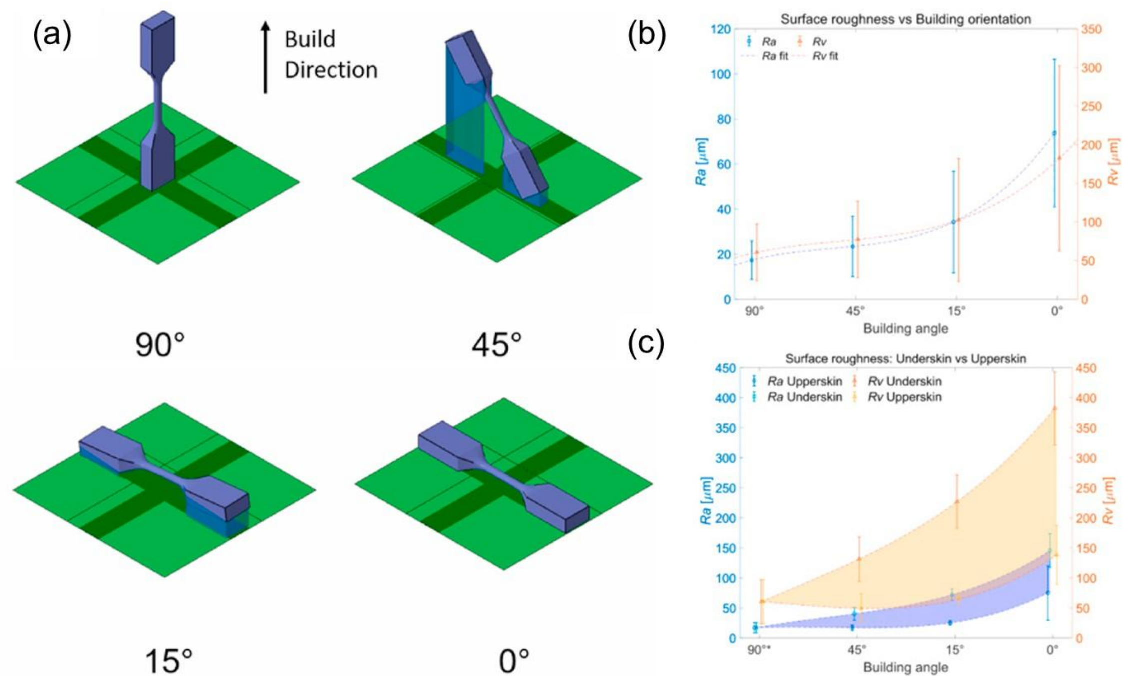

Fig. 2.28 (a) Illustration of the BDs (b) surface roughness measurement results of the struts and (c) the surface roughness measured at the upper skin and under skin of struts built at different BDs [147]

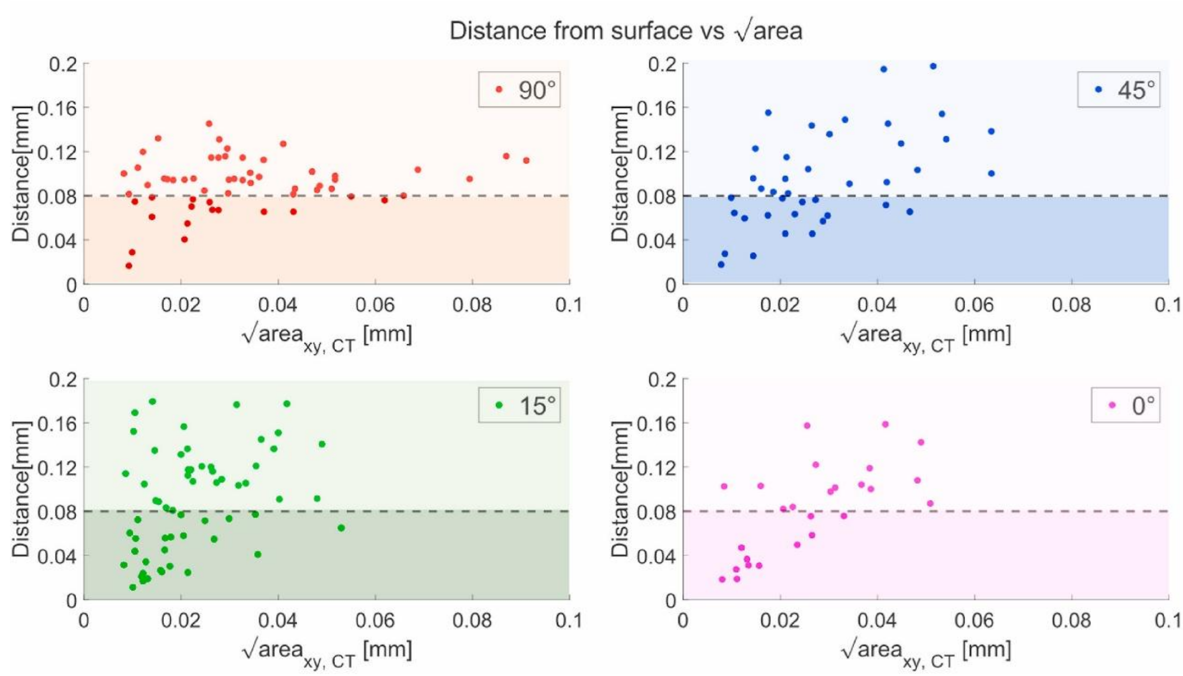

Fig. 2.29 Pore distance from surface vs √area scatter plots for the four specimens (the dashed line is the threshold used to classify the internal and surface pores) [147]

A lateral study conducted by the same authors[185] has investigated the fracture surfaces of the cyclic tested PBF sub-unital elements (struts with a node). As shown in Fig. 2.30, it was observed that the fracture initiation site was near the surface, where the geometrical imperfections such as notches or unmelted powders acted as stress raisers causing the nucleation of cracks. Specifically, the authors concluded that in 90° specimens, sufficiently large gas pores or lack-of-fusion (LoF) defects act as crack initiation sites and serve as dominant failure origins, thereby significantly reducing the fatigue strength. Although neither of these two studies[147,185] conducted a detailed analysis to elucidate the influence of defect location and size on the fatigue performance of thin struts or sub-unit elements, the observation of that cracks initiate from surface or near-surface defects is consistent with findings reported for PBF-fabricated bulk parts[190].

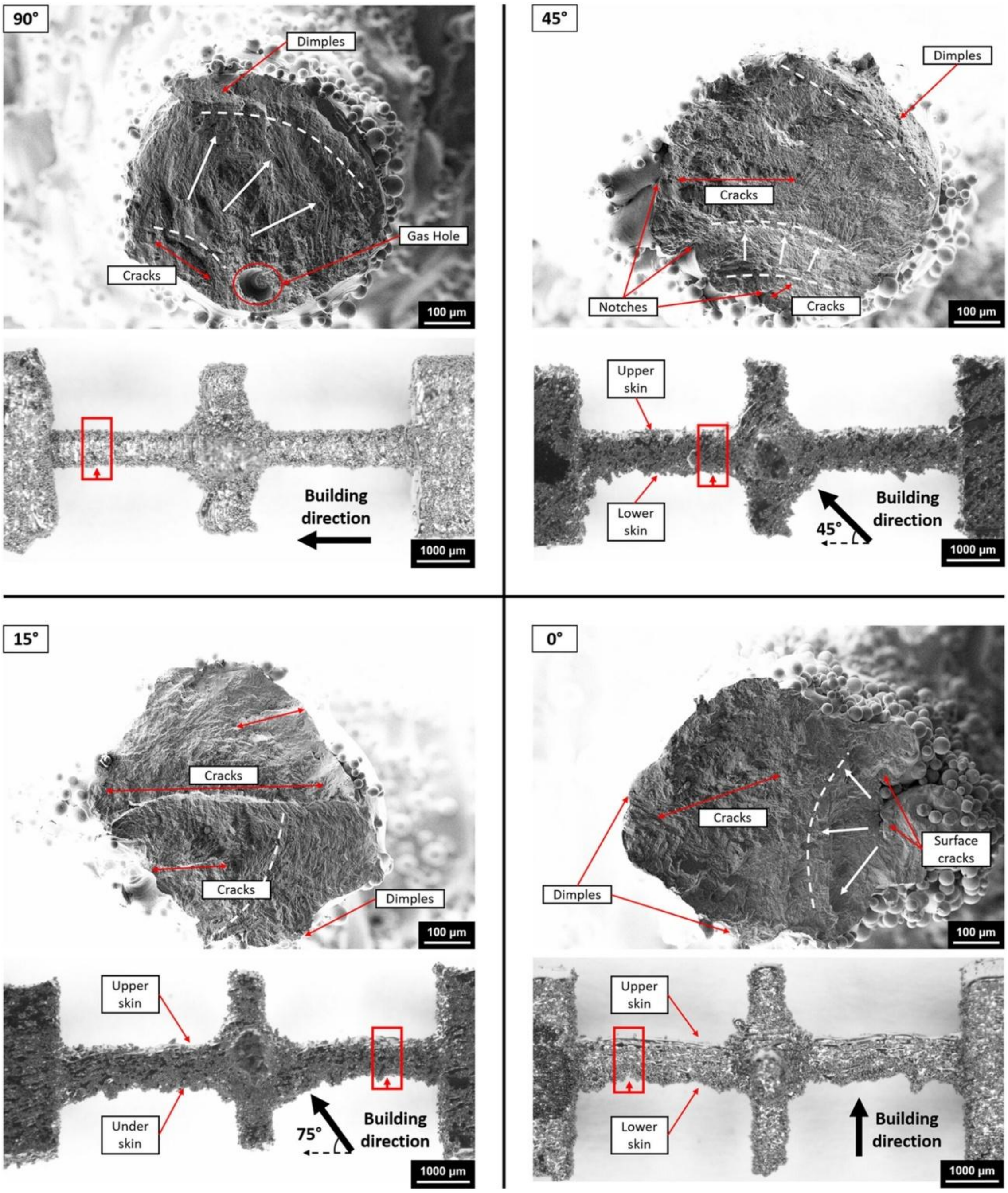

Fig. 2.30 SEM and microscopy images of the fatigue failed specimen built at four different BDs[185]

Tammas-Williams et al.[191] have investigated the effects of the proximity to the surface of the defects on the stress concentrations of EBPBF Ti6Al4V components, suggesting that the surface or near surface defects would be more detrimental to fatigue life than the internal ones. As shown in Fig. 2.31, regardless of the aspect ratio of the defect, a large increase in $\mathrm{K_t}$ can be seen while the pore is approaching to touch the surface when $\mathrm{d/D} \leq 1$ while for internal pores when $\mathrm{d/D} > 2$ the effect on $\mathrm{K_t}$ is negligible.

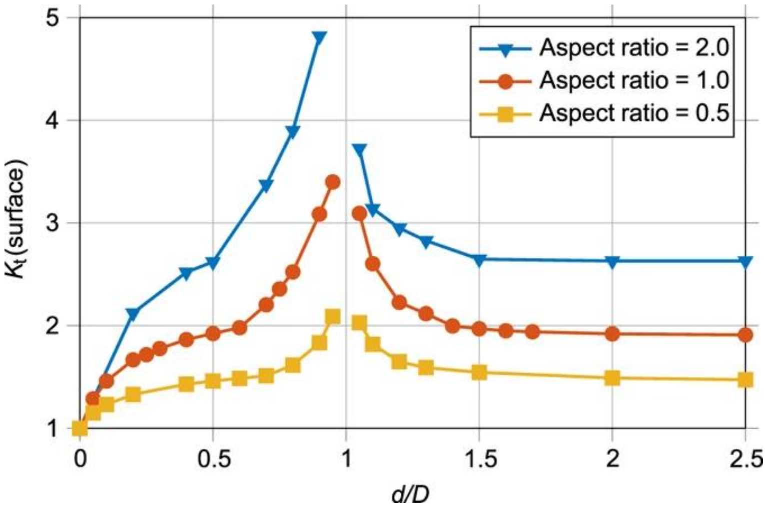

Fig. 2.31 The stress concentration $\mathrm{K_t}$ vs pores proximity to a free surface[191]

Based on Murakami's[189] $\sqrt{\mathrm{Area}}$ parameter, the stress intensity factor can be expressed by:

$$\Delta K = Y\Delta\sigma\sqrt{\pi\sqrt{area}} \tag{2.17}$$

where Y is equal to 0.65 for surface defects and 0.5 for internal defects. Furthermore, by using the threshold of stress intensity factor $\Delta\mathrm{K_{th}}$, the relationship between the fatigue stress range $\Delta\sigma_{\mathrm{th}}$ and the corresponding crack length a can be described by Kitagawa-Takahashi (K-T) diagram[192]. As shown in Fig. 2.32, EI-Haddad et al.[193] suggested a relationship between the fatigue stresses and crack length on the K-T diagram by:

$$\Delta\sigma_{\mathrm{th}} = \frac{\Delta K_{th,LC}}{Y\sqrt{\pi(a + a_0)}} \tag{2.18}$$

where $\Delta\mathrm{K_{th,LC}}$ is the $\Delta\mathrm{K_{th}}$ for long cracks, $\mathrm{a_0}$ is an intrinsic crack, which can be then calculated using the theoretical fatigue limit in ideal surface condition $\Delta\sigma_{\mathrm{f0}}$ by:

$$\mathrm{a_0} = \frac{1}{\pi}(\frac{\Delta K_{th}}{Y\Delta\sigma_{f0}}) \tag{2.19}$$

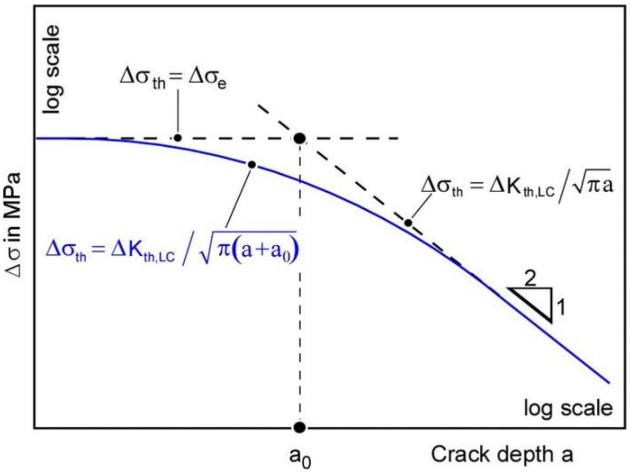

Fig. 2.32 K-T diagram obtained by the basic approach, by El-Haddad curve [194]

In addition, according to Murakami's approach, the effective length of the equivalent micro-notch is determined by the square root of the effective convex area of the defect A_{eff} as shown in Fig. 2.33. Pagliari et al.[195] analysed the fractured LPBF Ti6Al4V samples using this approach combined with K-T diagram. The authors considered the combined effects of surface roughness, surface defects and inner defects, these defects were converted into equivalent micro-notches. The effective notch length of the surface roughness was treated as a shallow defect has a length-to-width ratio greater than 10 as $\sqrt{\mathrm{Area}_{\mathrm{shallow}}} = \sqrt{10}\mathrm{R_v}$. However, considering surface roughness in the high-cycle fatigue region (N<10^7 cycles) might over-estimate the effective defect size and thus their detrimental effects of those defects on fatigue limit of their samples. As discussed in earlier studies[196–198], for almost all of the as-built PBF samples, the failure initiated from the critical locations on the surface and the most common failure mechanism from the surface are the LoF defects[199].

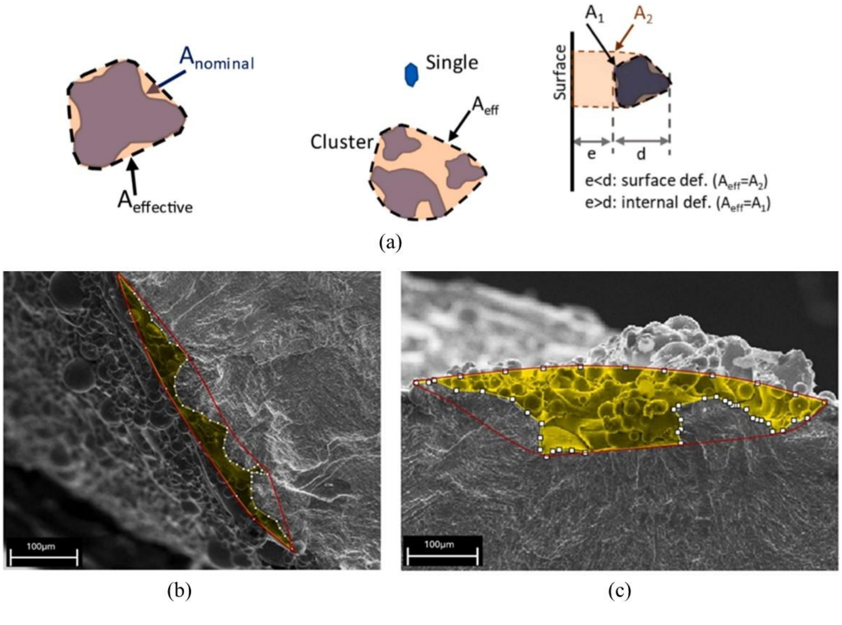

(a)

(b)

(c)

Fig. 2.33 Definition of the (a) defect size using Murakami's method and (b–c) the nominal area (yellow) and effect convex area (red) of the as-built samples[195]

2.3.4. UCO-Dependant Fatigue Properties

As reviewed in Section 2.2.3.3, Cutolo et al.[162] and Soul et al.[163] have investigated the effects of unit cell orientation (UCO) on the static mechanical properties of diamond-cell based lattice structures. For fatigue properties, a further study conducted by Cutolo et al.[170] investigated the compressive fatigue behaviour of the diamond lattices orientated in [001], [011] and [111] UCOs. The normalised SN curves obtained from [163,170] are presented Fig. 2.34.

Cutolo et al. investigated the compressive fatigue properties of the diamond lattices with UCOs of [001], [011] and [111] with respect to LD. [011]-orientated coupons process higher fatigue resistance (0.6UCS_L) at 5×10^6 cycles than the [001]- and [111]-orientated specimens. In contrast, Soul et al.[163] studied the tensile fatigue behaviour of the diamond lattices with the same UCOs. The [001]-orientated specimens exhibited slightly higher fatigue strength than the [001]- and [011]-orientated specimens at 10^7 cycles.

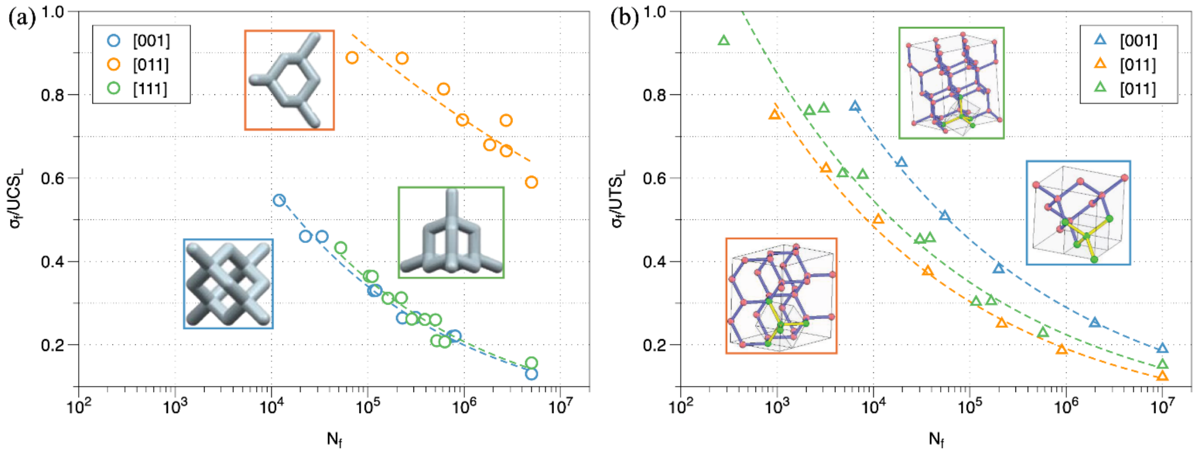

Fig. 2.34 Normalised SN curves of the (a) compress-compression[170] and (b) tension-tension fatigue tests[163]

Based on the limited data published in the literature, it can be concluded that there is a significant research gap concerning the orientation-dependent fatigue strength of PBF lattice structures. Specifically, as reviewed in 2.3.1, although SC cell-based lattices have demonstrated higher compressive fatigue strength than that of the non-SC lattices, the effect of LD respect to UCO of SC lattices on the compressive fatigue strength has not be significantly understood yet. This orientation-dependant effect must be considered for the practical applications such as load-bearing implant, where the actual compressive loading can be acted on the implant in different directions.

2.4. Comparison Between Solid and Porous Femoral Stems

2.4.1. Solid Femoral Stem Implants and Their Complications

Given the reviewed advantages of PBF in fabricating complex porous lattice structures, the subsequent review focuses on the potential of integrating the specific lattice concepts and their mechanical behaviour directly into the design of femoral stems. In general, depending on the anchorage to the bone, the femoral stem implants can be categorized into three types, including cemented, cementless or hybrid. The fixation of cemented implants is achieved by using bone cement, while the fixation of cementless ones relies on osseointegration[200]. The cementless femoral stem implant is usually covered by a roughened surface[201] or a porous coating[202] to enhance the initial stability. The coating can include plasma-sprayed hydroxyapatite (HA), plasma-sprayed titanium, titanium sintered beads and other types[203]. The implants can also be characterized by their size into conventional or short stem (length less than 120mm). The short stem aims to provide a stress distribution close to the native femur but can potentially resulted in reduced initial stability[204]. The main stem prosthesis offered by the global leading manufacturer are summarised in Table. 2.8. Taper-designed stems are designed to limit the stress-shielding by offering proximal load transfer and enhance the proximal fixation, but the high stiffness of the dense stem still directly related to stress shielding[205]. These stems are coated with plasma spraying, titanium sintered beads[206–211] or EBPBF fabricated porous surfaces[211], to offer enhanced bone ingrowth. However, the stability of the implant remains a challenge, the most common complications are dislocation, periprosthetic fracture, osteolysis, and aseptic loosening[8]. Thus, ongoing research and development efforts have been contributed to reduce the complications.

Table. 2.8 Commercially available femoral stem implants

Schematic	Key Features	Ref	Manufacturer
	▪ Ti6Al4V; ▪ Cementless; ▪ Size ranges from 94–118mm; ▪ Tapered in three planes; ▪ collared or collarless; ▪ 135º neck angle & 6 mm offset; ▪ proximal plasma spray coating & HA coating.	Z1™ [206]	Zimmer
	▪ Ti6Al4V; ▪ Cementless; ▪ Size ranges from 115–151mm; ▪ Macro-structure for increased bone contact surface; ▪ Rectangular cross-section with smoothed edges for rotational stability; ▪ Double layered coating: plasma sprayed Ti & TA coating.	Avenir®[207]	Zimmer
	▪ Ti-alloy; Cementless; ▪ Size ranges from 93–126mm; ▪ Size-specified curvature; ▪ 132º or 127º neck angle & varied offset lengths; ▪ HA coating over titanium plasma spray substrate.	Accolade® II[208]	Stryker
	▪ Ti6Al4V; ▪ Cementless; ▪ Size ranges from 93–117mm; ▪ Size-specified medial curvature; ▪ 132º neck angle & varied offset length from 30–38mm; ▪ HA coating.	Insignia®[209]	Stryker

	▪ CoCrMo; ▪ Cementless; ▪ Fully HA coated with macro texture 150µm; ▪ 130º neck angle	EMPHASYS™[210]	Depuy
	▪ Ti-alloy; ▪ Cementless; ▪ POROCOAT™ porous & UOFIX™ HA coatings; ▪ Collarless; ; ▪ 130º neck angle & offset ranges in 36–54mm	SUMMIT™[211]	Depuy
	▪ Ti-alloy; ▪ Cementless; ▪ Ti-Por® porous surface; ▪ EBM fabricated; ▪ 135º neck angle	Parva[212]	Adler Ortho

2.4.2. Porous Stems for Reduced Stress Shielding and Improved Stability

As briefly introduced in Section 1.1 and 2.4.1, the current dense femoral stems on market are considered much stiffer than the host bones, known as stress-shielding. This mismatch of stiffness can lead to long-term complications such as loosening. Thus, femoral stem designs incorporating porous structures have been proposed to minimise stiffness mismatch with the host bone. In addition, featuring porous structures in a femoral stem can promote the bone ingrowth inside the stem, which can enhance the long-term fixation of the implant.

The recent studies implementing porous structures for femoral stem are summarised in Table. 2.9, usually focus on specific Gruen zones (GZ) showing in Fig. 2.17(c), which used to define the specific anatomical regions around the implanted femur[213]. GZ 7 is considered as the critical area for implant failure due to bone resorption[214,215]. According to Huiske's strain-adaptive bone remodelling theory[216], the change of bone density can be described by:

$$\frac{d\rho}{dt} = \begin{cases} < 0, & S < (1-s)S_{ref} \\ = 0, & (1-s)S_{ref} < S < (1+s)S_{ref} \\ > 0, & S > (1+s)S_{ref} \end{cases} \tag{2.16}$$

where S is the strain energy density (SED) per unit bone mass ρ ($S = \frac{U}{\rho}$), S_{ref} is the SED in the intact bone and s is an empirical constant used to define the dead zone where no bone remodelling occurs, the value is usually set to be 0.75[39,216]. Then the mass fraction of the resorbed bone after the implantation m_r at local point p in the case of $\frac{d\rho}{dt} < 0$ can be obtained from[39]:

$$\tilde{m}_r(p) = \frac{1}{\tilde{M}}\int_V f(x)\rho dV \tag{2.17}$$

where $\tilde{M}$, ρ and V are the mass, density and volume of the intact bone, respectively. Additionally, $f(x)$ is defined as $f(S(p) - (1 - s)S_{ref}(p)$. Comparing to the solid stems, Abrabnejad[39] and Naghavi et al.[217] reported that the porous stems exhibited 40% and 50% lower m_r values in GZ7, repectively.

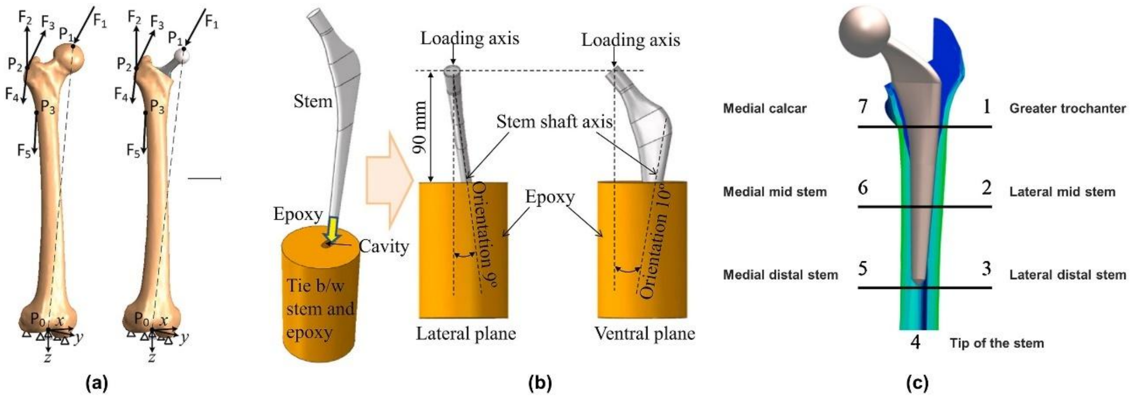

Fig. 2.17 Schematic illustrations of loading configurations (a) in-vivo[39] (b) ISO 7206-4[37] and Gruen zones

In addition, the initial stability of the cementless stems is achieved by the press-fit between the stem and the medullary cavity, which is affected by the relative micromotion between the implant and bone. It is suggested that the micro-motion should be controlled lower than 150μm to ensure the ingrowth of fibrous tissues[24,214,218,219]. In general, the micromotion at the stem-bone interface is negatively correlated with the stiffness of the stem, indicating a trade-off between stress shielding and micromotion. Alkhatib et al.[218] reported that micromotions increased from approximately 45μm to 147μm when $\overline{\rho}$ increased from 20% to 80%. Similar findings were reported by Wang et al.[220], suggesting that the porosity of the porous portion should be controlled lower than 50% to ensure the acceptable micromotions. Additionally, the interfacial micromotion can be controlled by tailoring the stiffness of different region of the stem[214,218,220].

As summarised in Table. 2.9, the performance of the porous stems has been analysed using experimental tests or FE simulations under different loading conditions, either setting up the in-vivo conditions or following the ISO 7206-4 settings. The majority of the published works have focused on the investigation of reducing the stiffness of the femoral stem implants, achieving 24%–90% reduction in stiffness. Based on the FEA results of the or experimental results, the level of stress shielding can by characterised by the ratio of stress change after the implantation using the equation[215,217,219,221,222]:

$$SSI = \frac{\sigma_{int} - \sigma_{stem}}{\sigma_{int}} \times 100\% \tag{2.20}$$

where σ_{int} and σ_{stem} is the stress value measured on the intact femur and on the implanted femur, respectively. Depending on the design of the stems, up to 80% lower SSI[219] has been reported with respect to the solid counterpart.

Table. 2.9 Summary of published works of porous femoral stems

Porous type	**Mat**	**Results**	**Set-up**
RD & holes[102]	Ti6Al4V	−65% in k	Compression
Holes[102]	Ti6Al4V	–20% in k	Compression
Graded SC[223]	CoCr	–64% in k	Cantilever
Pillar octahedron[214]	CoCr	–90% in k	3Ps bending
Stochastic (P=33%) [224]	Ti6Al4V	–47% in k	ISO 7206
DIA(P=58%)[225]	Ti6Al4V	–31% in k	ISO 7206
RD (P=40%)[226]	CoCr	–40% in k	Similar to ISO 7206
Graded Vintiles (P=0.4–0.7)[227]	Ti6Al4V	–62% in k	ISO 7206
Hybrid TMPS (P=56%–67%)[217]	Ti6Al4V	–24% in k, –74% in SSI, –40% in m_r	ISO 7206 / In-vivo
Nonhomogeneous auxetic [222]	Ti6Al4V	–38% in SSI	In-vivo FEA
Graded TMPS(P=20%–70%)[215]	Ti6Al4V	–14% in SSI	In-vivo FEA
Tetrahedron(P=70%) [39]	Ti	–70% in m_r	In-vivo + ISO 7206
BCC[228]	Ti6Al4V	–25% in SSI	In-vivo FEA
Stochastic [229]	Ti	–40% in k	ISO 7206
BCC(P=47%)[219]	Ti	–80% in SSI	In-vivo FEA

2.4.3. Fatigue Properties of Solid Femoral Stems

A femoral stem fracture after THA is a rare but serious complication, since the commercially available stems must fulfil the requirements for fatigue endurance specified in the international standard. Cook et al.[230] studied 13 failed THA cases involving different solid stems. Despite the fracture occurred at different locations as shown in Fig. 2.35, all the fractures were attributed due to fatigue failure. The risk factors for stem fracture can relate to implant positioning, surgical techniques, patient-related risk factors and also the implant characteristics[231].

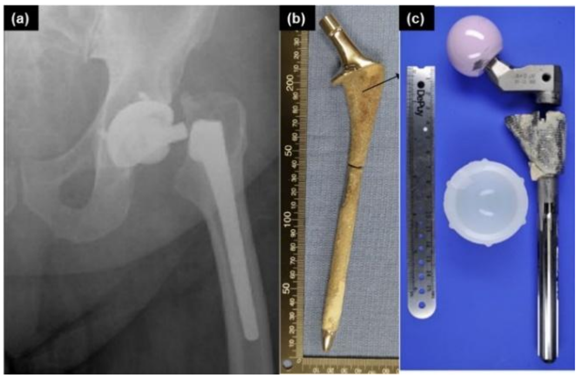

Fig. 2.35 Fracture at (a) neck[232] (b) mid-shaft and (c) proximal femoral sleeve-stem interface[230]

FE simulations have been utilised to predict the fatigue performance of solid stems with different fatigue criterions, such as Soderberg theory[37,233,234], Goodman theory[235–237] and Gerber theory. If the FEA calculated maximum stress at the concentration area is less than the fatigue strength of the material, the risk of fatigue fracture can be eliminated. As discussed in Section 2.3.1, the safe region is defined under the lines. The fatigue safety factor FSF can be calculated using the equations listed in Table. 2.10, in terms alternating stress σ_a, mean stress σ_m in one load cycle, as well as endurance limit σ_e, ultimate strength σ_u and yield strength σ_y of the material. As expected, all solid Ti6Al4V stems in the reviewed literature[233,235–239] exhibited a fatigue life greater than 5×10^6 cycles under ISO 7206-4 loading conditions.

Table. 2.10 Fatigue safety factor equations

Theory	Equation	Equation No.
Goodman	$\frac{1}{\mathrm{FSF}} = \frac{\sigma_a}{\sigma_e} + \frac{\sigma_m}{\sigma_u}$	(2.21)
Soderberg	$\frac{1}{\mathrm{FSF}} = \frac{\sigma_a}{\sigma_e} + \frac{\sigma_m}{\sigma_y}$	(2.22)
Gerber	$1 = \frac{\mathrm{FSF} \cdot \sigma_a}{\sigma_e} + \left(\frac{\mathrm{FSF} \cdot \sigma_m}{\sigma_u}\right)^2$	(2.23)

2.4.4. Fatigue Properties of PBF Porous Femoral Stems

The fatigue properties of porous femoral stems have been evaluated experimentally and numerically in literature. To date, only four studies[217,240–242] have been found experimentally evaluated the fatigue performance of the designed PBF porous stems under ISO 7206-4 configurations. As summarised in Table. 2.11, the two stems[240,241] with considerable solid portion and the other one with large fenestrations[242] satisfied the survival criterion of 5×10^6 cycles. However, these designs might not meet the design requirements for effective bone-ingrowth.

Wang et al.[240] have experimentally investigated the fatigue properties of EBM built custom short stems with four different lengths between the middle of lesser trochanter and the distal point of the stem (20, 40, 60 and 80mm). As shown in Fig. 2.36, 2mm-thick porous coating (average pore size ~0.65mm) on the stem surface. The results indicated the two stems with length shorter than 40mm successfully survived after 5 million cycles during the fatigue tests. Multiple crack fatigue initiation sites were observed in the fractured samples. The cracks initiated from the interface between the coating and substrate at the locations with maximum tensile stress. However, the cross-sectional image of the stem in Fig. 2.36(d) shows that a significant portion of the stem remains solid. It may still lead to stress shielding and limit the bone-ingrowth depth.

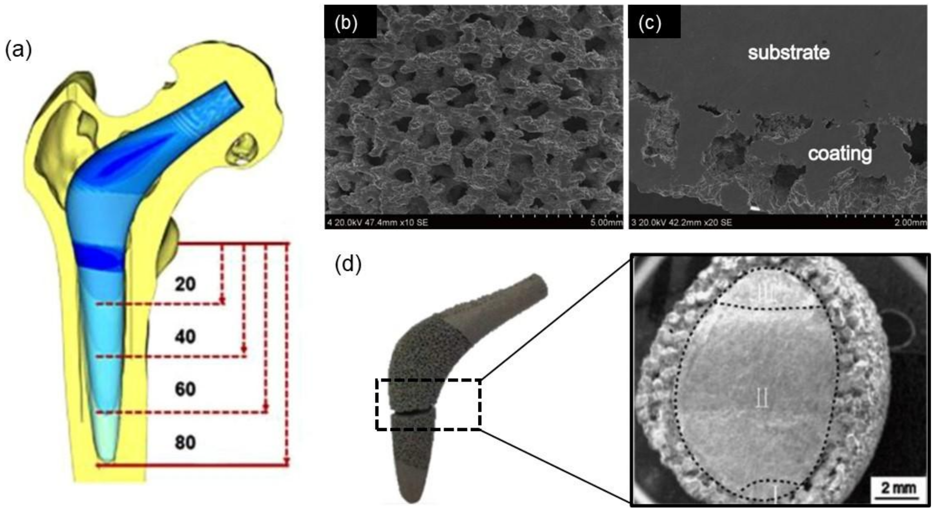

Fig. 2.36 (a) illustration of the designed lengths, (b) porous coating with trabecular structures (c) the cross-section of the porous coating on the stem and (d) fracture surface of the tested stem with a length of 60 mm[240]

Delikanli et al.[241] fabricated porous implants consisting of a porous outer region with semi-spherical pores and cylindrical channels and an inner region with a Kubisch Raumzentrierten (KRZ) type lattice structure with a porosity level of 78.3%. Two different pore sizes, 0.6mm (BG) and 0.3mm(KG) of the outer region at the surface were applied to the design. Then the fatigue performance of nine LPBF fabricated specimens, (three solid implants(T), three BG implants and three KG implants) and one machined specimen (O) were analysed under ISO 7206-4 loading conditions using. All specimens were found to survive after 5×10^6 cycles. Comparing to the solid counterparts, the porous stems achieved a mass reduction of approximately 16±1%, suggesting that the stems retained largely a largely solid portion. FEA models were also created with nine different surface pore size was modelled, ranging from 0.3mm to 1mm with 0.1mm increments, all of which exhibited infinite fatigue life.

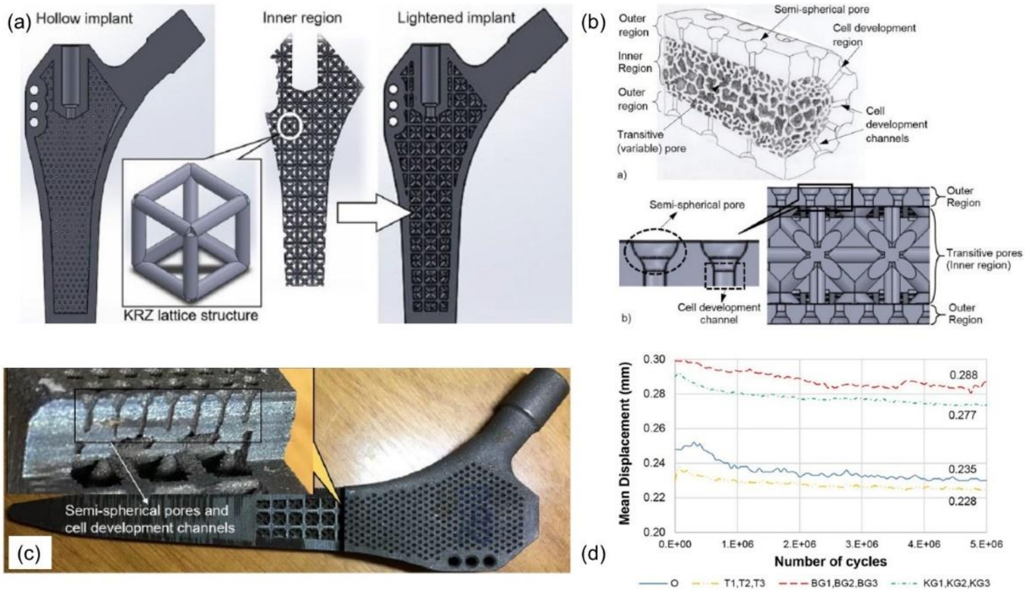

Fig. 2.37 Schematic illustration of cross-section of (a)the designed implant and (b) pore structure, (c) sectioned LPBF BG sample and (d) fatigue testing results[241]

Croitoru et al.[242] analysed the fatigue performance of the personalised LPBF stem with fenestrations using the Locati method. As illustrated in Fig. 2.38, the fatigue test started at 2300N until reaching 5 million cycles and then continued in consecutive steps with an increment of 500N every 1 million cycles until failure. The fenestrations were designed to mimic the structure of natural bone with a size of 2×2 mm and 6×6 mm based on the directions of the trochanteric patterns. Even though all of the stems survived at 5 million cycles, the fenestrations used in this study were exceeded the ideal range for promoting osseointegration, which may limit the bone-ingrowth into the fenestrated structures.

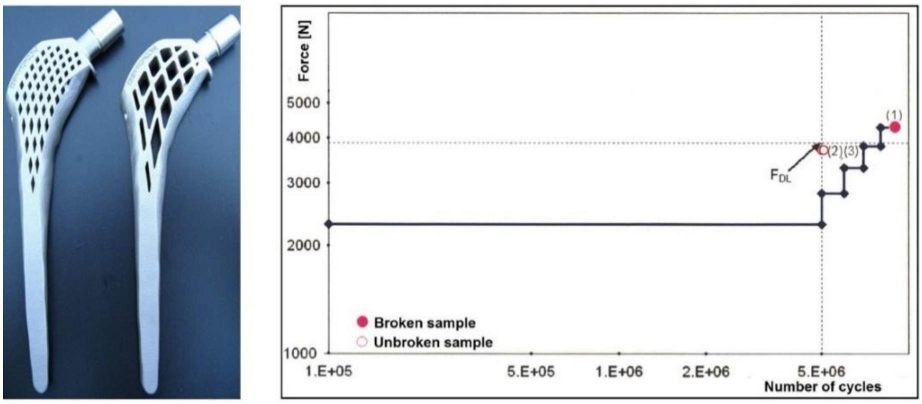

(a) (b)

Fig. 2.38 (a)The manufactured fenestrated femoral stems (b) Locati method for fatigue testing[242]

In contrast, the other design proposed by Naghavi et al.[217] featured ideal porous design for osseointegration but endured only about 10% of the fatigue life required in the ISO standard. As illustrated in Fig. 2.39, the stem featured TPMS lattices with ideal pore sizes (0.1–1mm) and sufficient porosity levels (56.4%–67.4%) for osseointegration. The FEA-predicted safety factor of fatigue greater was than 1 but the experimentally evaluated fatigue life was only 457,349 cycles.

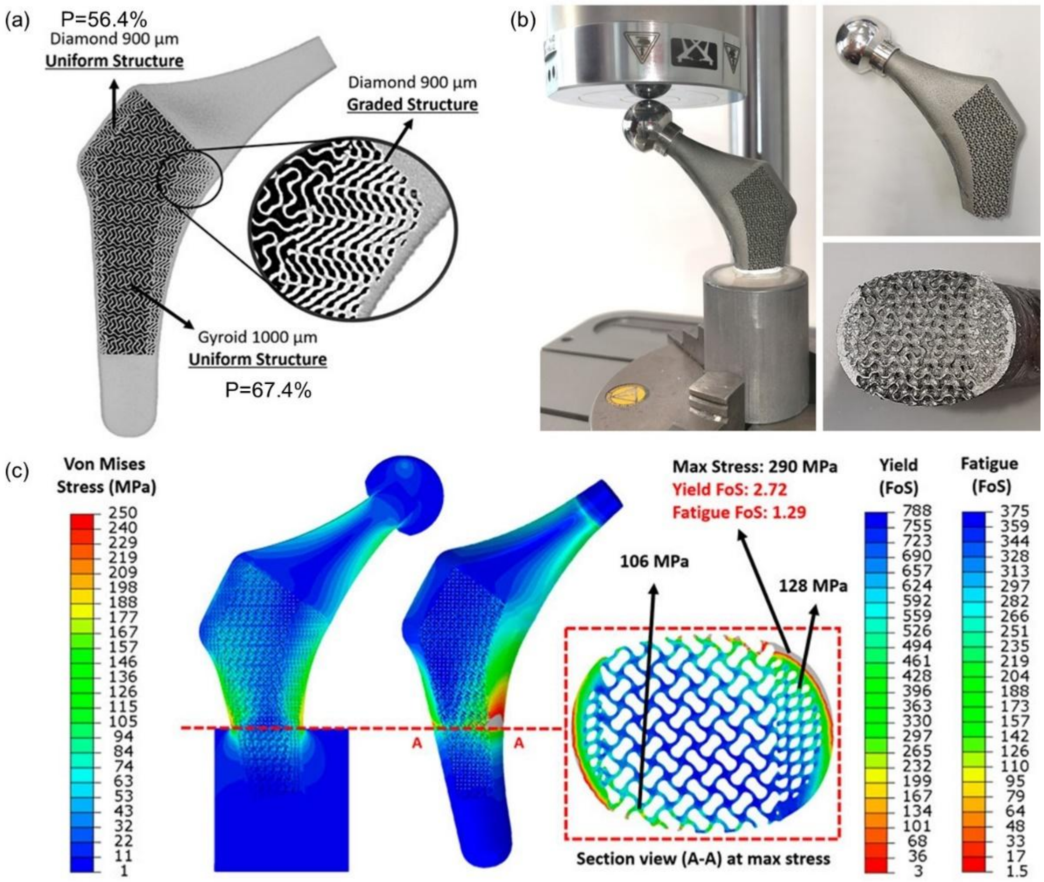

Fig. 2.39 (a) Cross-section of the porous stem (b) fatigue test set-up and fractured stem (c) FEA results[217]

Mehboob et al.[243] analysed the fatigue properties of the stems employing Soderberg equation as described in Eq.(2.22). The design envelope was developed by considering the effective stiffness of the stem, the $0.3\sigma_{y-L}$ of the BCC lattices with respect to the fatigue limit and the fatigue limit of the dense shell of 500 MPa. The overlapping area of the three design spaces was determined as the safety region for fatigue. However, no experimental validation was provided to confirm the fatigue design.

Table. 2.11 Experimental fatigue results of PBF Ti6Al4V porous femoral stems

Design	CT (mm)	Stem Length (mm)	AM	N_f(EXP)	N_f(FEA)
Customised short stems with 2mm-thick porous coating (pore size ~ 0.65mm) [240]	–	20 & 40	EBPBF	>5×10^6	–
	–	60	EBPBF	1.59×10^6(AB) 2.11×10^6(HIP)	–
	–	80	EBPBF	3.94×10^5(AB) 2.34×10^6(HIP)	–
Porous-shell (0.3 mm or 0.6mm pores) outer region combined with a KRZ-lattice inner region, overall solid portion ~84%[241]	160	–	LPBF	>5×10^6	>5×10^6

Personalized implants with fenestrated design (2×2 mm & 6×6 mm fenestrations) [242]	–	–	LPBF	>5×10^6	–
1mm-thick solid shell & hybrid TPMS lattices with porosity level higher than 50% [217]	113	79	LPBF	4.57×10^5	>5×10^6
Dense shell with internal BCC lattice structures (within identified design space)[243]	–	–	–	–	>5×10^6

2.5. Summary of Knowledge Gaps and Research Questions

The above review has shown that PBF can readily fabricate the complex lattice structures with suitable geometrical properties for orthopaedic implants. However, to date, there is no practical clinical applications reported using the PBF porous stems with a sufficient porosity level. Since there is a trade-off between increased porosity and fatigue endurance limit of the lattices.

The existing challenge is to improve the fatigue strength of the PBF lattices while maintaining a sufficient porosity level. The above review has suggested that SC lattices exhibit both higher compressive static and fatigue strength than other non-SC strut-based structures. However, the effects of UCO with respect to LD on their mechanical properties has not been investigated in detail. Therefore, the anisotropic behaviour of the SC lattices has not been fully understood. Despite few studies has discussed the UCO-dependant mechanical behaviour of lattices, the reviewed literature has not provided consistent results.

In addition, the majority of the studies on PBF porous stems have focused on reducing stress shielding, while only few researchers investigated the fatigue behaviour of the porous stems. Two studies have reported that their PBF built porous stem can meet the requirements of surviving 5×10^6 fatigue cycles as specified in ISO 7206-4[42]. However, large solid regions have been presented in those designs. Extensive solid regions, especially along the stem surface, can limit the bone-ingrowth, thus affect the implant's long-term performance.

Considering the summarised knowledge gaps above, the following research questions are addressed:

RQ1. Under quasi-static compressive loading, how does the combination of UCO and LD (-BD) affect the effective compressive strength and modulus and how do the stress distribution within unit cells and strut quality contribute to crack propagation and the resulting strength of the lattices?

RQ2. Under cyclic compressive loading, how does the combined effect of UCO and LD affect the fatigue performance of the lattices? Specifically, how does the stress distribution within each unit cell contribute to the crack initiation and what is the crack growth mechanism that leads to final failure, thus defining the overall fatigue strength of the structures?

RQ3. For the exploratory study on porous femoral stems, with optimal-UCO lattice incorporated in fully porous stems, what is the fatigue life and critical stress level that would contribute to the fatigue strength? Furthermore, is a topologically optimised solid-reinforced porous stem suitable for meeting the relevant ISO standard, and what is the primary source and underlying mechanism of failure that may compromise this suitability?

3. Design of Study

This chapter details the comprehensive methodology employed to achieve the research objectives, including the design, fabrication, testing, examination and analysis of the EBPBF Ti6Al4V lattice structures and the final porous femoral stems. The study first establishes the orientation-dependent mechanical properties of SC lattices with varied UCOs then applied orthopaedic design. The research utilised an approach across both the fundamental lattice structures and the final stems, encompassing quasi-static and cyclic compressive testing, FEA modelling, examination, and analysis.

3.1. Design and EBPBF of the Lattice Specimens

As illustrated in Fig. 3.1, simple cubic lattices with three different unit cell orientations (UCOs), including [001], [011] and [111] were designed to investigate the effects of UCOs with respect to loading directions (LDs) on the static and cyclic compressive properties. The build plane of the EBPBF machine (i.e., x-y plane) was fixed for all the three designs, maintaining the building direction (BD) during EBPBF to be parallel to the loading direction (i.e., z-axis) in both quasi-static and fatigue tests. The [001] orientation was obtained with unit cell coordinate system (x', y', z') parallel to global coordinate system (x, y, z). The [011] orientation was obtained by rotating about global x-axis of 45º with respect to the x-y plane. In [111] orientation the angles with respect to x'-z' and x'-y' plane to the global x-y plane were both equal to 54.7º. For all these specimens with different UCOs, the cell size was fixed at 1.1mm×1.1mm×1.1mm and the strut size was fixed at 0.5mm, resulting in the same unit cell relative density $\bar{\rho}_C$ of 35.4%.

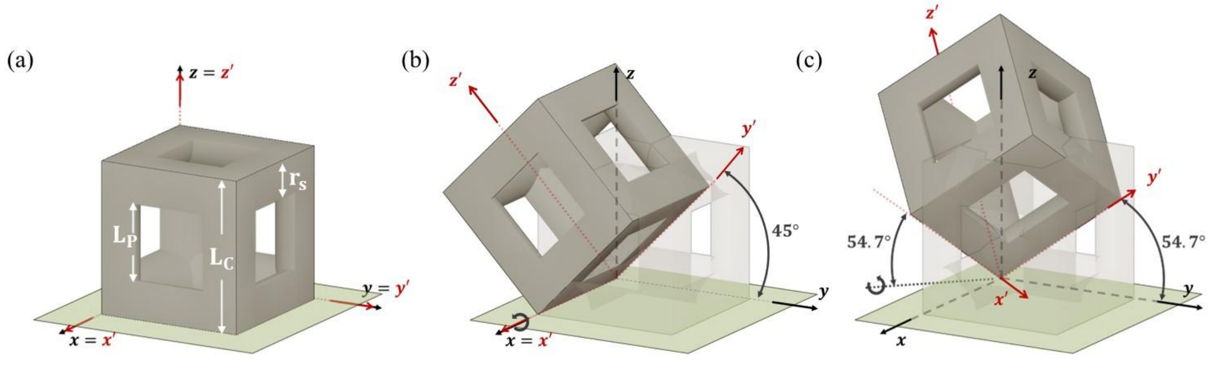

[001] [011] [111]

Fig. 3.1 Illustration of SC lattices with different UCOs: (a) [001], (b) [011] and (c) [111]

SC unit cells (L_c=1.1mm, d_s=2r_s=0.5mm) with three different UCOs, [001], [011] and [111] was used for the generation of the lattice structures. As specified in ISO 13314:2011[4], the diameter of the cylindrical D sample shall be at least 10 times of the pore size and no less than 10mm and the sample height H to diameter ratio $\frac{H}{D}$ shall be between 1 to 2. As shown in Fig. 3.2, each sandwich-like EBPBF lattice specimen consists of two solid ends and a lattice portion in between. The geometry of the solid ends can be considered as a conical frustum and an attached circular disk. The conical frustum portion possesses two circular face diameters of D_{End}=15mm and D=10mm, with a corresponding height of h_1=4.5mm. The attached circular disk has a diameter of D=10mm and a height of h_2=2mm. The lattices used in this study were cylinders with a heigh H of 20 mm and a diameter D of 10 mm. The process of trimming the lattices within the cylinder resulted in the final relative densities of the cylindrical samples $\bar{\rho}$ were slightly above the theoretical value $\bar{\rho}_c$, giving approximately $\bar{\rho}$=0.36 for all the cylinder samples with different UCOs. In addition, solid ends were built together with the lattices to ensure the parallelism and planarity of the contact surface between the specimens and the test machine.

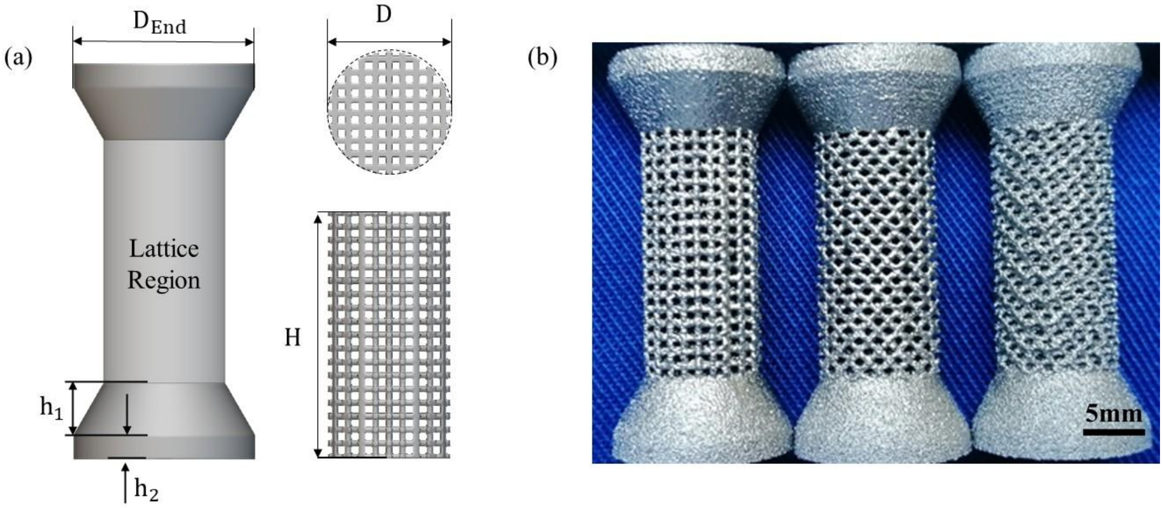

Fig. 3.2 (a) Schematic illustration of the lattice and (b) the as-built specimens of [001], [011] and [111] lattices

The lattice samples were printed layer-by-layer using Arcam Q10plus EBM machine (Fig. 3.3) using the Ti6Al4V grade 5 powder with a layer thickness of 50μm. The specimens were built using the standard Acram EBM parameter control theme. The NET theme developed by Acram was applied for the fabrication of the lattice portion and the standard theme was used to print the solid portion of the specimens. The NET theme is designed for small and fine features. The unmelted power was removed from the specimens using the powder recovery station and no post-process heat treatments were applied on the printed specimens.

Fig. 3.3 Arcam Q10plus EBPBF machine[244]

3.2. FEA Simulation of Lattice Structures

The sandwich-like geometry was composed of the solid top plate, the lattice, and the solid bottom plate. The simulations have been conducted using the implicit solvers in ANSYS Mechanical. The lattice CAD models utilized for the FEA represented idealised, as-designed geometries. Therefore, as-built geometrical imperfections resulting from the EBPBF process were not incorporated into the simulations. According to literature[47,121], the mechanical response of a lattice structures can be well predicted using a finite number of unit cells. Hence, the sensitivity analysis of the number of cells is conducted by evaluating the resulting effective mechanical properties and the localised peak stress values

As the solid ends were printed together with the lattice body, which means no physical interface where sliding can occur, the contact between the plates and the lattice structure was set as bonded[59].To evaluate the robustness of the selected bonded contact condition, additional FEA models were developed with frictional platen contact to compare the variation in resulted E_L and σ_{y-L}. The mesh convergency study was conducted to determine the appropriate mesh size for the simulations by evaluating the key macroscopic properties, including E_L and σ_{y-L}, as well as the localised peak stress values. The boundary conditions were applied to the solid plates, the bottom plated is fixed and the axial displacement is applied to the upper plate. The material properties of Ti6Al4V used in simulations are presented in Table. 3.1.

Table. 3.1 Material properties for Ti6Al4V used in simulations

E (GPa)	**ρ(kg/m^3)**	**ν**	**σ_y (MPa)**	**E_T(MPa)**
120	4430	0.323	1001	1332

Additionally, as reviewed in Section 2.1, the process-induced geometry imperfections in PBF-fabricated lattices will lead to deviations from bulk material properties. To justify the utilisation of bulk data and bound the potential effects of these deviations on the mechanical response of the lattice structures, a parametric sensitivity analysis has been conducted. The E and σ_y values listed in Table. 3.1 were used as the baseline parameters and independently varied by approximately 15%.

The stress and strain are calculated by:

$$\sigma = \frac{F}{A_0} \tag{3.1}$$

and

$$\varepsilon = \frac{\Delta l}{l_0} \tag{3.2}$$

where F is the reaction force at the bottom plate and A_0 is the apparent cross-section area of the specimen, Δl is the displacement of the top plate and l_0 is the length of the lattice specimen.

3.3. Quasi-Static and Cyclic Testing of Lattice Samples

Quasi-static compression tests were conducted at a crosshead speed of 1.2 mm/min using Tinius Olsen H50KS testing system with a load cell of 50 kN as shown in Fig. 3.4. The load and cross-head displacement data was recorded force each test and then the corresponding stress and strain values were calculated using Eq.(3.1) and Eq. (3.2), respectively. The majority of the tests were terminated manually when a sudden drop of recorded force occurred or when the fracture collapse of the specimen was observed. In addition, several tests were intentionally terminated within the plastic region before the final collapse occurred. The quasi-elastic gradient and the 0.2% compressive offset stress specified in ISO 13314: 2011[92] were considered as the effective Young's modulus $\mathrm{E_L}$ and yield strength $\sigma_{\mathrm{y-L}}$of the lattices. $\mathrm{E_L}$ was determined by the slope of linear region of the stress-strain curve and $\sigma_{\mathrm{y-L}}$ was taken as the stress value at the intersection point between the 0.2%-strain offset linear line and the curve. In addition, the apparent plastic strain ε_{p} is determined at the ultimate compression strength $\mathrm{UCS_L}$ by:

$$\varepsilon_p = \varepsilon_{total} - \varepsilon_{elastic} = \varepsilon_{total} - \frac{UCS_L}{E_L} \tag{3.3}$$

(a) (b)

Fig. 3.4 Quasi-static compression test of a lattice sample

As shown in Fig. 3.5, compression-compression fatigue tests were performed on MTS Landmark Servo-hydraulic Test System with a load cell of 25kN. All tests were conducted in an ambient laboratory environment at a room temperature of 25 ± 3 °C and a relative humidity of approximately 80%.The lattice specimens were subjected to axial force-controlled, constant sinusoidal amplitude loads as shown in Fig. 3.6(a), with a loading ratio R of 10 and a test frequency f of 20 Hz. The magnitude of the maximum applied load $|-\sigma_{\mathrm{min}}|$, i.e., the minimum applied load in compression, was calculated based on the quasi-static tested results. The tests were terminated when the 5×10^6 cycles (based on the fatigue requirement specified in ISO 7206-4 for femoral stems) reached or when a sudden change in peak-peak displacement $\Delta \mathrm{d_p}(\mathrm{N_t})$ was detected. As illustrated in Fig. 3.6(b), the test will be terminated once the detected crosshead $\mathrm{L_p}(\mathrm{N_t})$ reaches a threshold that described by:

$$L_p(N_t) = \begin{cases} L_{P,max}(N_i) + m\Delta D_p(N_i), & Upper\ limit \\ L_{P,min}(N_i) - m\Delta D_p(N_i), & Lower\ limit \end{cases} \tag{3.4}$$

where $\mathrm{N_i}$ denotes the reference cycle at which the system is considered to have reached a stabilized state, with $\mathrm{N_i}$ =1000 in this thesis and m is the tolerance percentage. The tolerance value m corresponded to the threshold amount of sudden increase in displacement detected during the test, where a higher value of m typically correlated with a more complete fracture of the specimen before the test was terminated. During the fatigue tests, the load and crosshead displacement data were continuously recorded. Then the effective Young's modulus under the cyclic loading is calculated by the change in apparent stress $\Delta\sigma$ and the change in apparent strain $\Delta\varepsilon$ within each cycle, where $\Delta\sigma$ and $\Delta\varepsilon$ are obtained using the recorded load and displacement values with Eq. (3.1) and Eq. (3.2), respectively.

(a) (b)

Fig. 3.5 Set-up of the fatigue tests: (a) Landmark Servo-hydraulic Test System and (b) [001]//LD lattice under compressive cyclic loading

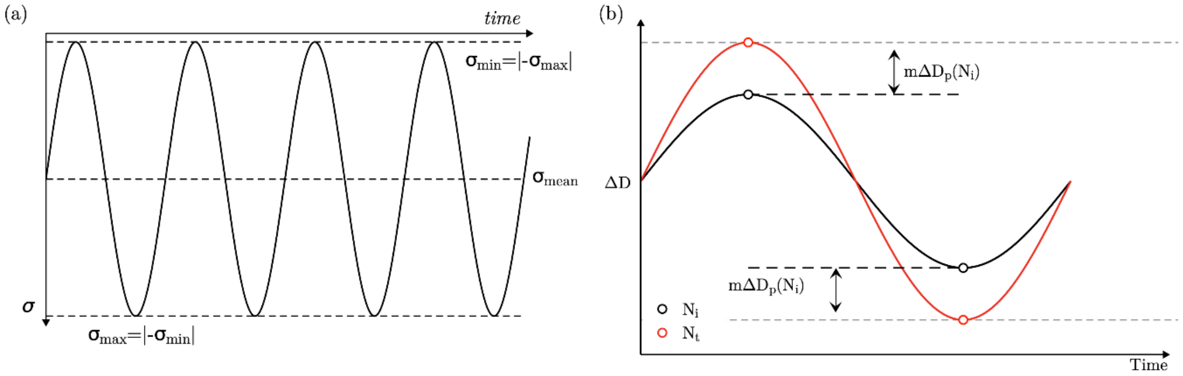

Fig. 3.6 (a) constant amplitude cyclic loading (b) illustration of the test termination criteria

To address the fatigue performance of each UCO configuration, S-N curves were derived. The S-N curve is linear in the logarithmic scale and described in a power-law equation, known as Basquin relation[245]:

$$\sigma_a = \sigma_f'(2N_f)^B \tag{3.5}$$

where σ_a is the applied stress amplitude, N_f is the number of cycles to failure, σ_f' is the fatigue strength coefficient and B is the fatigue strength exponent. As the compression-compression fatigue tests were conducted using a constant stress ratio R=10, σ_{max} is directly proportional to σ_a, then the equation can be reformulated using a modified fatigue strength coefficient C and expressed as:

$$\sigma_{max} = C(N_f)^B \tag{3.6}$$

In addition, the fatigue tests usually contained several run-out points without failure. To evaluate the fatigue data, the Maximum Likelihood Estimation (MLE) method was utilised. This technique calculates the probability of definitive failures while giving proper statistical weight to the exact survival times of the run-out specimens.

3.4. Design, EBPBF and Fatigue Testing of the Porous Femoral Stems

The design approach undertaken to develop the porous femoral stem that meets desired fatigue strength and bone in-growth properties is illustrated in Fig. 3.7. Section 3.4.1 defines the baseline geometry of the femoral stem, followed by Section 3.4.2, discusses the conducted FEA models in accordance with ASTM F2996-13 to simulate the mechanical response under ISO 7206-4 loading. The approach utilised to define the optimal UCO that exhibits the load bearing abilities is described in 3.4.3, where a multi-objective genetic algorithm (MOGA) was employed to perform response surface optimisation. These optimised points were subsequently validated through additional FEA simulations and fatigue testing. Based on the test outcomes, further topological optimisations were carried out to define the solid reinforcement portion in the stem, leading to the final design of the porous femoral stem.

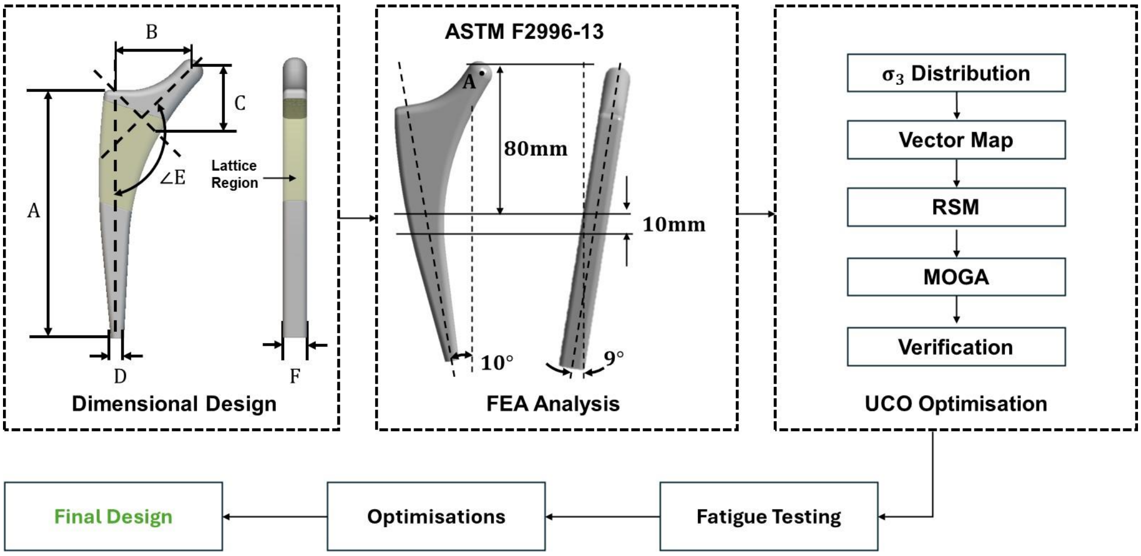

Fig. 3.7 Design process of the porous femoral stem

3.4.1. Geometry of the Designed Femoral Stem

As presented in Table. 3.2, the geometry of the stem is designed based on the commercially available product CORAIL® (Johnson & Johnson DePuySynthes). The designed femoral stem can be divided into three parts, including neck, proximal unpotting part and distal embedded part under ISO 7206-4 configuration. As briefly discussed in Section 2.4.4, only four studies analysed the fatigue performance of PBF porous femoral stems. Despite Wang et al.[240] and Delikanli et al.[241] reported the PBF stems survived after 5 million cycles. The designs proposed in these two studies remained highly dense.

To obtain sufficient porosity level and pore size for bone-ingrowth, a stem features fully porous region is designed. The lattice region was constructed within the proximal unpotting part. Simple cubic cells were used to generate the lattice structures, to improve the efficiency of the powder removal procedure, the cell size and strut thickness set to be 2.2 mm and 1 mm to achieve a relative density of 36%.

Table. 3.2 Dimension of the designed stem and the commercially available stem referring to Fig. 3.7

	L_A(mm)	L_B(mm)	L_C(mm)	∠E(°)	L_F(mm)
CORAIL® (Size 9)	130	36	38.5	135	8
This Study	122	36	38.5	135	12

3.4.2. FEA Modelling

The FEA models of the femoral stem were constructed based on ASTM F2996-13[246], where the applied loading $F_y = 2300N$ and the orientation of the stem were guided by ISO 7206-4, where the load in the FEA model was applied to the end of the rounded face of the hip stem trunnion to produce the worst-case head offset. The femoral stem was firstly cut at a distance of 80 mm from the centre of head as described in the ISO standard, this cut presented the potting level and defined the RoI above this cut. A second cut was made 10 mm below the potting level, all the surfaces distal to the second cut were constrained in all directions. As stated in ASTM F2996, constraining the stem in this manner would not significantly affect the identification of worst-case stress conditions in the RoI. The femoral stem was meshed using SOLID 187 elements and a mesh sensitivity analysis was conducted, determining a final mesh size of 0.1 mm. The material properties of Ti6Al4V were applied as listed in Table. 3.1.

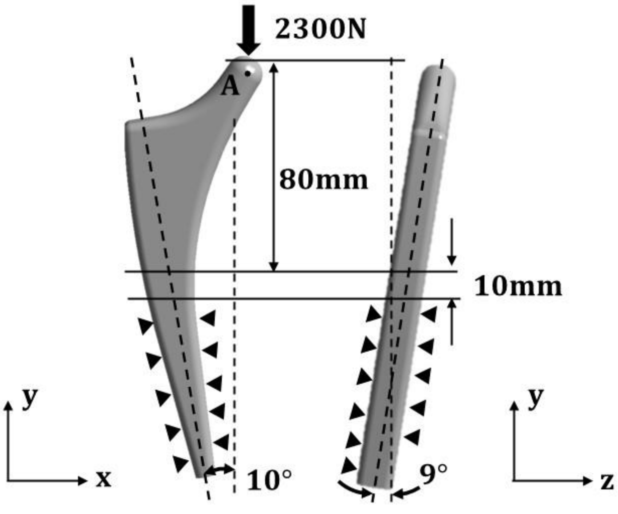

Fig. 3.8 Load application and boundary condition for the femoral stem simulation based on ASTM F2996[246]

3.4.3. Unit Cell Orientation Optimisation

Based on the experimental and simulation results of the quasi-static compressive properties of the lattices with varied UCOs. The [001]//LD lattice demonstrated the most favourable compressive performance. Thus, the optimal UCO of the lattice used in the femoral stem design should align with the principal compressive stress distribution on the stem. To determine the UCO to maximum the compressive load bearing ability of the lattice structure, response surface optimisation was conducted stem with orientated SC lattice structures using ANSYS static implicit solver. To improve the computational efficiency, the boundary conditions for the optimisation were simplified as described in ASTM F2996-13[246], where the stems were loaded in the ISO 7206-44 manner. As shown in Fig. 3.9, the hip stem was constrained in all directions on all the surfaces distal to the position 10mm below the potting surface specified in ISO 7206-4. Then the embedding resin was not included in the optimisation FE models. In addition, the lattices were meshed using BEAM188 elements. The axial direct forces F_{axial} and the bending moments M_b on the struts, as well as the overall displacement of the porous stem in the loading direction were estimated. Only the rotation θ with respect to loading direction (global y-axis in FEA as shown in Fig. 3.9) was considered in the UCO optimisation, the local x' axis of the unit cell is set to be parallel to the stem surface.

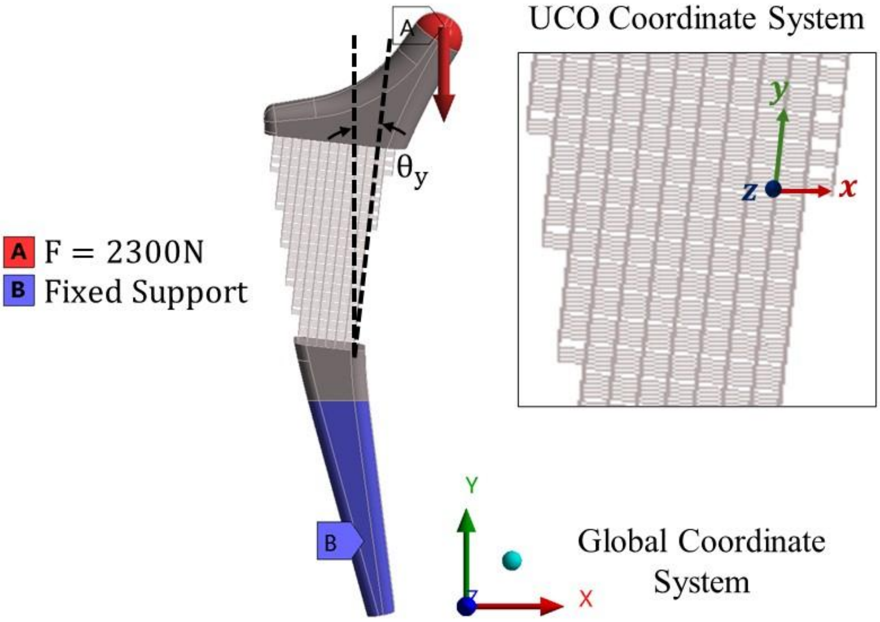

Fig. 3.9 FEA model for UCO optimisation

To determine the design range of the θ_y, a preliminary FE model of the fully solid stem was conducted using the same boundary conditions as described in Fig. 3.8. Then solid stem was meshed using SOLID187 elements, and the vector principal stresses were evaluated. Then vector maps were computed using a python code to determine the direction vector of the principal axes of σ_3 and imported to nTop to analyse the angle $\theta_{\sigma 3}$ between of σ_3 and the loading direction. Then the design range of θ was determined as between 0° and 13° using the minimum and maximum values of θ_3 in the compressive stresses concentrated area where $\sigma_3 < -100$ Mpa.

Design of experiment was carried out in using the toolbox in ANSYS based on the optimal space filling method, central composite design (CCD) samples were generated. The statistical analysis was carried out to investigate the effects θ on the objective functions. When all the design points were solved, response surface methodology (RSM) was applied to obtain a surrogate model approximating the real model, describing the relationship between the input variable θ and the output parameters. In this study, Kriging response surface model was constructed and multi-objective genetic algorithm (MOGA) was applied to determine the optimal value of θ. The three output parameters to be optimised were the directional displacement of the stem at the selected point A along the loading direction δL_y, the percentage of beam elements of the load-bearing struts under compression P_c and under minimal bending moment P_b, i.e. $F_y(\theta_i) < 0N$ and $M_b < 20N \cdot mm$, respectively. To maximise the compressive load bearing ability of the struts, he multi-objective optimisation can be written as:

$$y = Maximise(f_{F_y}(\theta_i), f_{P_c}(\theta_i), -f_{P_b}(\theta_i) \tag{3.7}$$

Once the optimised UCO is found, the stem would be trimmed at the plane normal to the X-Z plane showing in Fig. 3.9 of the UCO coordinate system to ensure better connectivity between the lattice and the solid portions.

3.4.4. Sample Preparation by EBPBF and Fatigue Testing

The fatigue tests of the porous femoral stems were designed based on the ISO 7206-4 configuration with a compressive load of 2300N applied. Given the resource limitations, the test rig was simplified for this exploratory study. Similar to the test set up shown in Fig. 3.10 [102,247], where the dense solid end of the porous stems were fixed using mechanical vices for axial compression test, the proposed test configuration introduced a solid gripper printed together with the unpotting portion of the stem. The drawing shown in Fig. 3.11, illustrates this simplified configuration, aligning the unpotted portion of the stem by a ventral angle of 10° and a lateral-medial angle of 9°. The gripper locates at the potting plane to define a unpotted length of 80 mm from the centre of the femoral head. This simplification was based on the assumption and the findings reported in literature[217] that failure would consistently initiate near the potting surface rather than in the embedded portion. In addition, this simplification should not significantly affect the identification of worst-case stress conditions in the region of interest (RoI), in this study, the designed porous region, which will be discussed in Section 6.1.2.

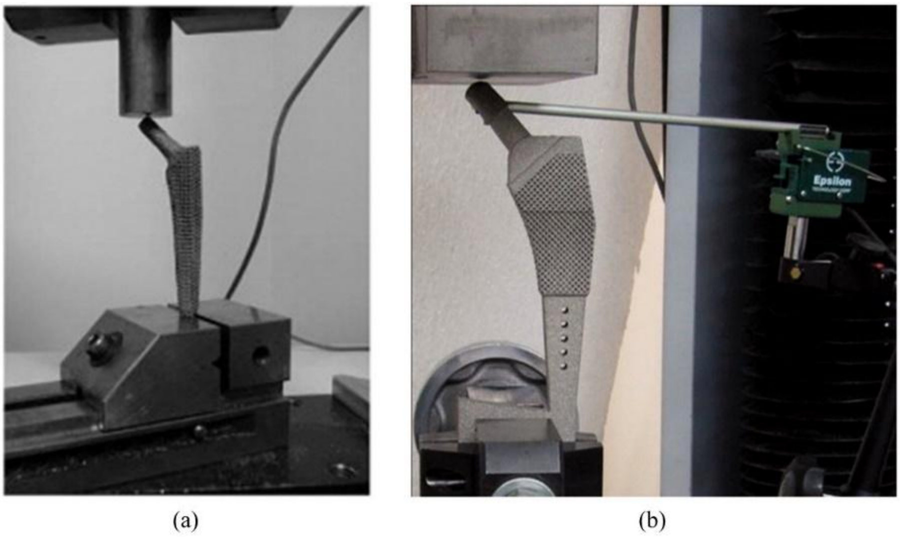

Fig. 3.10 Quasi-static test setup of porous femoral stems in (a) Ref[102] (b) Ref[247]

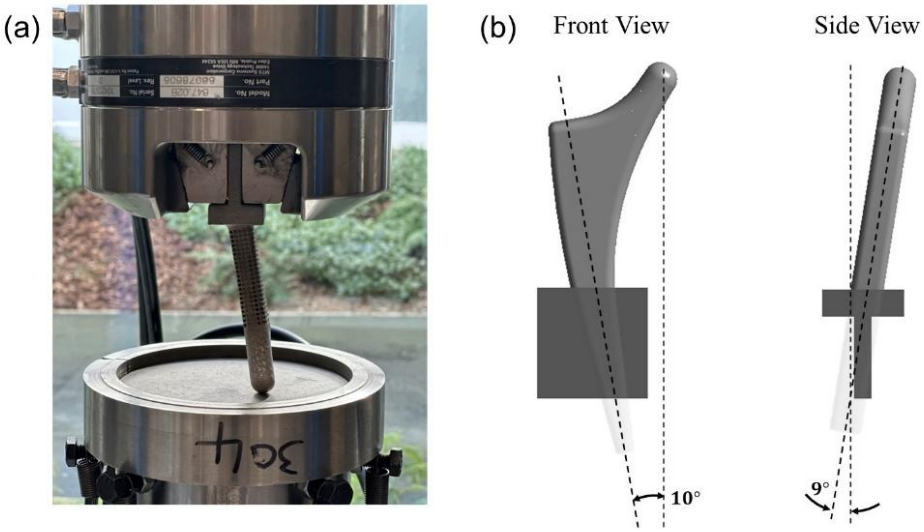

Fig. 3.11 (a) Fatigue testing setup (b) the schematic illustration of the simplified configuration

3.4.5. Estimation of the Relative Density of the EBPBF Fatigue Samples

In literature, the relative density $\bar{\rho}$ of the as-built EBPBF lattices was usually estimated using either Archimedes method[67] or Micro-CT[248]. However, because the fabricated lattices consisted of interconnected open-cell structures, the traditional Archimedes method exhibited inherent limitations for estimating relative density. The measuring liquid can readily infiltrate these open spaces, which prevents an accurate measurement of the solid volume and consequently leads to an inaccurate calculation of the $\bar{\rho}$. In contrast, micro-CT can theoretically isolate the lattice volume computationally, but it has been considered resource-intensive for this work. Thus, to estimate the relative density $\bar{\rho}$ of the as-built EBPBF lattices, the mass of eleven specimens with different UCOs has been measured. As shown in Fig. 3.2, a lattice specimen a central lattice portion placed in between a bottom and top solid end. The nominal mass of a specimen m=10.59g is the given by the total mass of the lattice portion and the two solid ends, by:

$$m = m_L + 2m_{End} \tag{3.8}$$

where the mass of the lattice portion m_L=2.51g can be calculated using the volume of the cylinder portion. It can be written as:

$$m_L = \bar{\rho} V_L \cdot \rho_s = \bar{\rho}(\frac{\pi D^2}{4} H) \cdot \rho_s \tag{3.9}$$

where $\bar{\rho}$=0.36 is the relative density of the lattice portion, V_L is the apparent volume of the cylinder region and ρ_s=4430kg/m^3 is the density of bulk Ti6Al4V. The nominal mass of the solid ends of approximately $2m_{End}$ =8.08g has been calculated using the density of Ti6Al4V (4430kg/m^3). The volume of a solid end V_{End}= 913mm^3 is determined by the sum of the volume of a conical frustum $V_{Frustum}$=560mm^3 and the volume of a circular disk V_{disk}=353mm^3, by:

$$V_{End} = V_{Frustum} + V_{Disk} = \left\{\frac{1}{3}\pi h_1 \left[\left(\frac{D}{2}\right)^2 + D \cdot D_{End} + \left(\frac{D_{End}}{2}\right)^2\right]\right\} + \frac{\pi D^2 h_2}{4} \tag{3.10}$$

The averaged results for all the specimens with different UCOs are listed in The estimated values of relative density were found slightly lower than the nominal value of $\bar{\rho}$=0.36 using the method described in 3.4.5, but the variation is considered acceptable for the investigation of the fatigue strength of the designed . Assuming that mass of each solid ends is equal to the nominal value of $2m_{End}$ =8.08g, the relative density of the lattice portion is then estimated by:

$$\bar{\rho}_{Estimated} = \frac{m_{Measured} - 2m_{End}}{m_L} \tag{3.11}$$

3.4.6. Topology Optimisation of the Porous Femoral Stems

As illustrated in Fig. 3.12, the proximal lattice region was selected as the design domain for topology optimisation (TO). TO has been performed using the software nTop 5.29, which is a cutting-edge engineering tool specifically designed for integrating design, simulation, topology optimisation within a single environment[249]. The workflow of the TO process is presented in Fig. 3.12, the region of interest (RoI) for performing TO in nTop was selected as the entire unpotting region. Then the design domain was meshed using SOLID elements with a mesh size of 1.1 mm. The Young's modulus and Poisson's ratio of Ti6Al4V were given in Table. 3.1. The stem is positioned in ISO 7206-4 configuration using ASTM F2996 boundary conditions the same as described in Section 3.4.2. Therefore, the embedded part of the stem was not included in the optimisation to save computational cost.

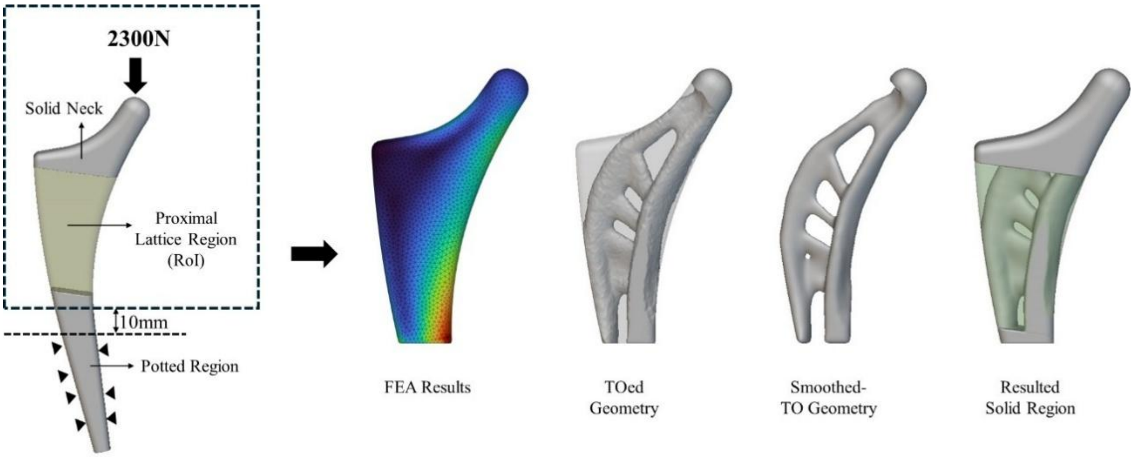

Fig. 3.12 Topology optimisation workflow

The topology optimisation was performed based on the density of each element of the FE model, employing solid isotropic material with penalisation (SIMP) method, where the density was forced to approach zero (representing a void) or one (representing solid material). The SIMP method changes the stiffness of each element per interaction and the penalised Young's modulus of an element based on its design variable x_i can be written as:

$$E_i(x_i) = E_{min} + x_i^p(E_0 - E_{min}) \tag{3.12}$$

where $\mathrm{E_{min}}$ is the minimal Young's modulus, $\mathrm{E_0}$ is the Young's modulus of the material and p is the penalisation factor. The design variable of each element was adjusted incrementally based on the sensitivity to its compliance with respect to the design variable. The design objectives were to reduce the volume of the unpotting region (RoI) and ensure the maximum stress in the optimised geometry remained below the selected threshold, which can be written as:

$$\text{Minimise:} f(x) = \sigma_{max} \tag{3.13}$$

while subject to the constraints of:

$$\begin{cases} g_1(x) = V_{ROI}(x) < V_{Target} \\ g_2(x) = \sigma_{max}(x) < \sigma_{Allowable} \end{cases} \tag{3.14}$$

3.5. Examination and Analysis of the EBPBF Specimens

3.5.1. Morphological Examination of the EBPBF Lattice Specimens

Morphological features of the as-built and mechanical tested lattice specimens and fractured femoral stems were examined using Hitachi SU-70 scanning electron microscope (SEM) with an acceleration voltage of 15 kV. The strut sizes of the lattice specimens were estimated using the imaging analysis tool

ImageJ and customised Python code. The process of the strut size analysis is illustrated in Fig. 3.13, the SEM images were converted into binary image then the distances between the black pixels are measured in Python with the process as shown in Fig. 3.14.

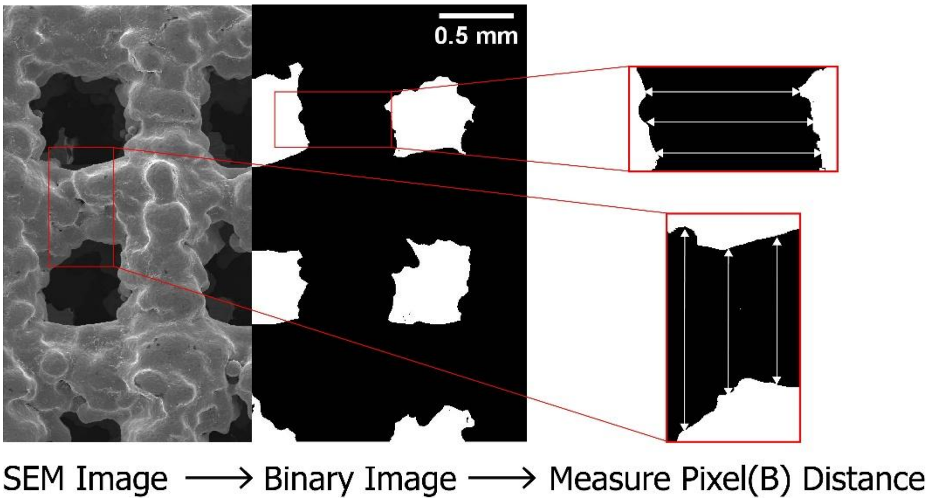

Fig. 3.13 Strut size estimation process

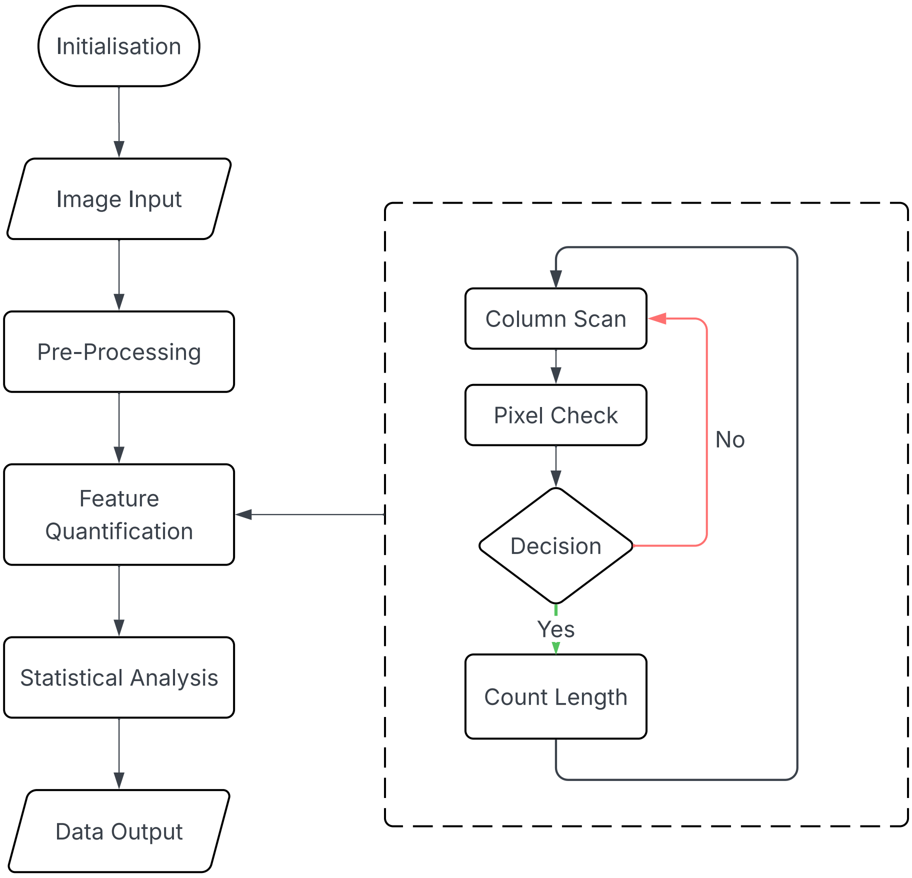

Fig. 3.14 Flow chart for the illustration of the pixel measurement process in Python

3.5.2. Defect Analysis and X-ray CT Examination of the Stem Specimens

For the EBPBF femoral stems, the fracture surfaces of the failed specimens were examined using both optical microscope OLYMPUS SZX9 and SEM (Hitachi SU-70) with an acceleration voltage of 15kV. The defect size on the fracture surface was measured from the SEM image using ImageJ. The boundary of the defect was manually traced in ImageJ, and the effective area of the defect is defined as the fitted convex area as illustrated in Fig. 2.33(a) and the effective defect length $\sqrt{\mathrm{Area}}$ was determined.

To perform the analysis using K-T approach, the stress concentration factor threshold $\Delta \mathrm{K}_{\mathrm{th}}$ was determined by the fatigue crack growth (FCG) tests using EBPBF built Ti6Al4V standard compact tension (CT) specimens with crack growth direction normal to BD. This particular crack growth direction was chosen as it is similar to the crack direction observed in the tested stem samples. The pre-cracking was initiated using a $\mathrm{K}_{\mathrm{max,0}}$ of 12.6MPa$\sqrt{\mathrm{m}}$, and was reduced to a final $\mathrm{K}_{\mathrm{max}}$ of 9MPa$\sqrt{\mathrm{m}}$ at a constant loading ratio of R=0.1 and a frequency of f=20Hz, until the calculated crack length of more than 1mm was detected. Then the FCG tests were performed with decreasing ΔK(9.5–0.95 MPa$\sqrt{\mathrm{m}}$) at room temperature with constant loading ratio (R=0.1 and f=20Hz). As the crack grew, the applied load was continuously reduced to achieve a normalised K-gradient of -0.12 mm^{-1}. The results of the three FCG tests are plotted in Fig. 3.15, yielding stress intensity threshold values $\Delta\ \mathrm{K}_{\mathrm{th}}$ of 4.7, 4.9, and 5.3 MPa$\sqrt{\mathrm{m}}$.

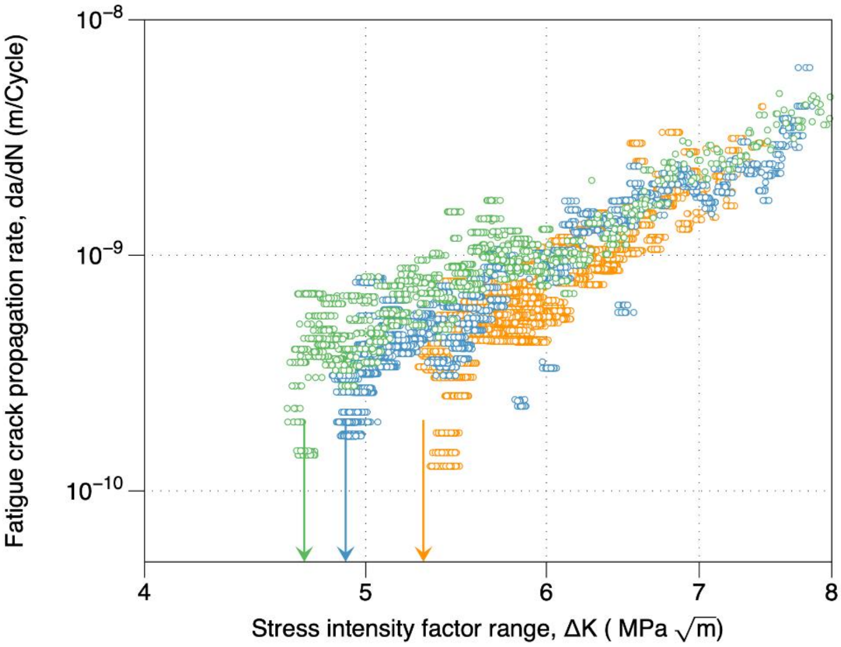

Fig. 3.15 the results of fatigue crack growth (FCG) for EBPBF fabricated Ti6Al4V CT specimen with stress ratio of R=0.1,yielding stress intensity threshold values $\Delta\ \mathrm{K}_{\mathrm{th}}$ of 4.7, 4.9, and 5.3 MPa$\sqrt{\mathrm{m}}$

The process of the defect analysis of the run-out femoral specimens is illustrated in Fig. 3.16. X-ray CT computed tomography was used for the defect characterisation of the cyclic tested femoral stem specimens. The XCT scanner Skyscan1172 with a voxel size of 9.76μm was used with a source voltage of 100kV and a source current of 100μA. The reconstruction of the XCT images was performed using the software NRecon 2.2.0.6, then a series of grey-scale images obtained from the XCT scanning. For further analysis, the XCT data has been converted into binary images in Image J. To address the sensitivity of the segmentation, the threshold values were adjusted using a baseline of 60% (±5%) to evaluate the robustness of the measured $\sqrt{Area}$ and the resulting defect count. Following proper segmentation, binary image stacks containing the information of the defects were obtained. The subsequent analysis has been performed in MATLAB to investigate the distribution of the defects on the scanned objects. Considering the typical LoF defect size in EBPBF built Ti6Al4V parts is generally between 0.005mm^2 to 0.165mm^2[250]. Considering the resolution of the XCT and the reasonable defect size, the defects were filtered based on their cross-section area size, those with an area less than 100μm^2 (one voxel cross-section) and greater than 165000μm^2 were eliminated from the subsequent analysis. Then the measured defects have been classified into surface- and internal defects using the categorising method described in 2.3.3.3.

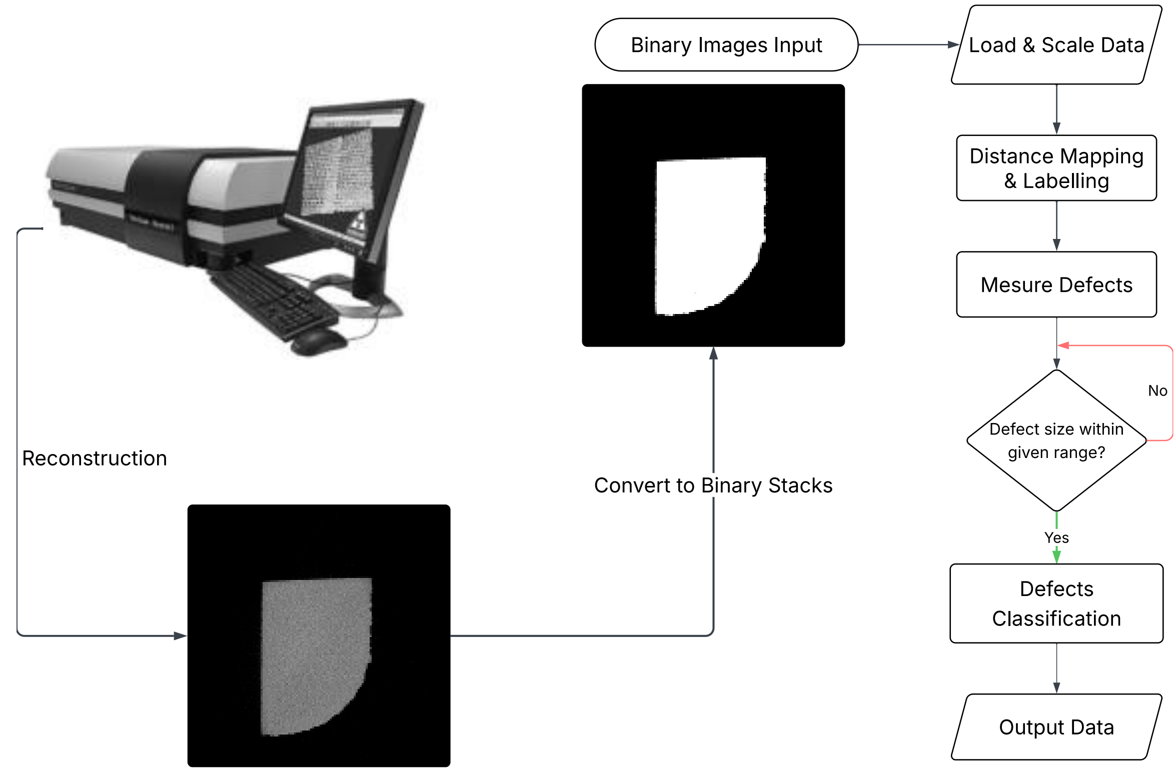

Fig. 3.16 Defect analysis process

The surface roughness of the run-out specimens has also been estimated using the XCT results, following the methodology described in Fig. 3.17. The surface roughness at the tension concentration region of the specimen has been analysed using the each 2D slice within the area of interest (AOI) independently. The AOI was determined based on the stress distribution across the stem specimens, ensuring that only the tension concentrated region would be taken into consideration. The 2D edge profile for each slice was detected by systematically scanning each column of pixels within the AOI to identify the last pixel of the object. Then a smooth mathematical curve was used to fit the detected edge profile, the roughness was estimated as the collection of distance from the actual edge points to the smoothed curve. The examples of the detected AOI and the fitted profile are presented in Fig. 3.18. Then the maximum valley depth R_v was determined, demonstrating the single largest deviation between the ideal surface and the actual edge profile.

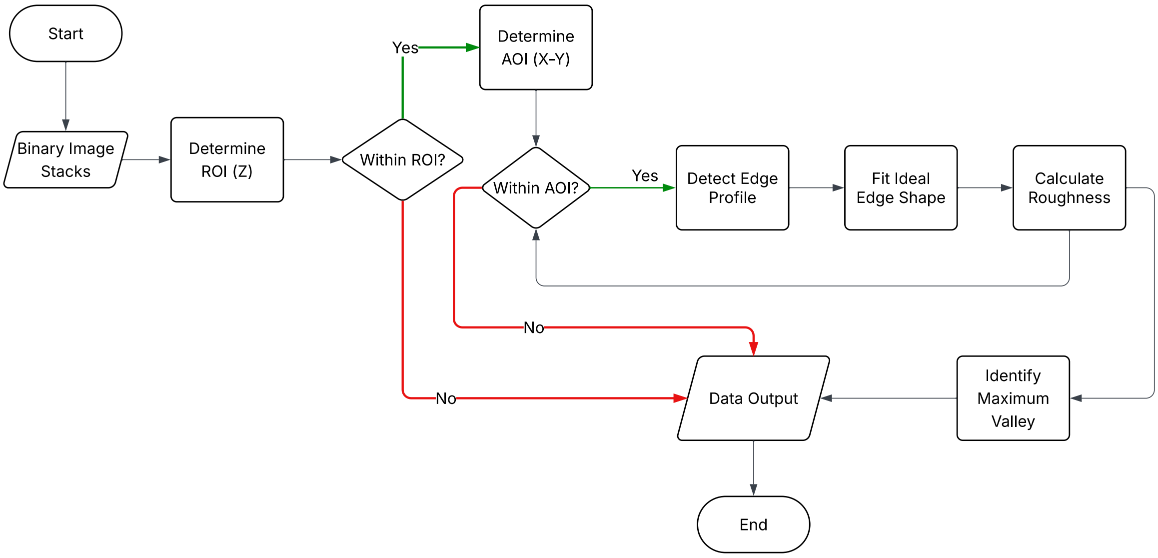

Fig. 3.17 Roughness measurement process

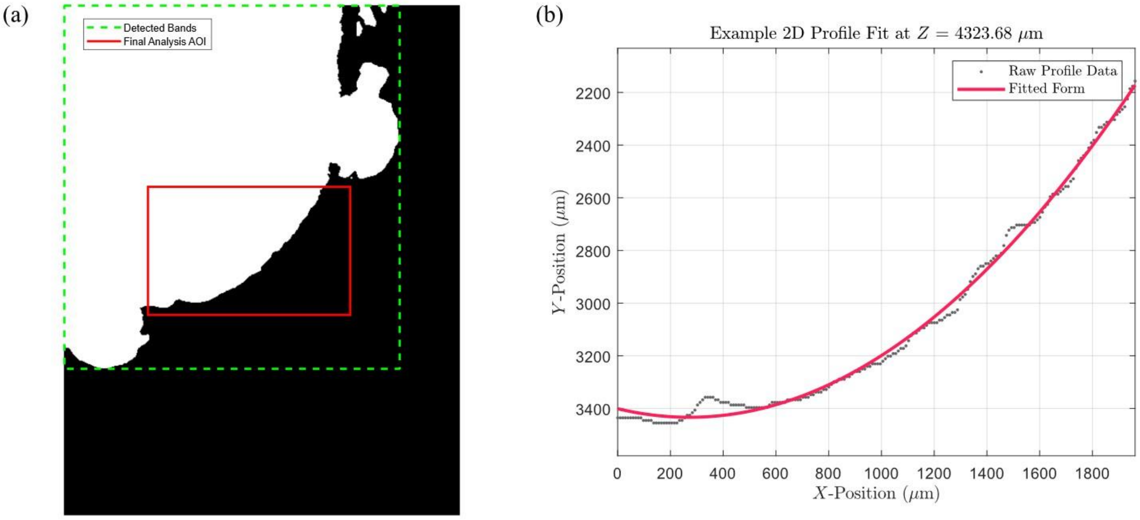

Fig. 3.18 Examples of the (a) determined AOI and (b) the detected raw edge with fitted ideal shape

4. Orientation-dependent Quasi-static Behaviour

To understand the mechanical anisotropy of the EBPBF lattice structures, this chapter studies the combined effects of loading direction (LD), unit cell orientation (UCO) and strut irregularity of the EBPBF lattices on the mechanical behaviour have been studied. In this chapter, the UCO dependant values of Young's modulus, compressive strength, failure strain under quasi-static compression will first be evaluated. Subsequently, due to the difficulty in achieving an accurate experimental determination of the modulus of lattices, a theoretical consideration of the modulus of [001]//LD will be addressed. The FEA predicted stress distribution will then be presented to aid the understanding of the fracture paths and thus the strength values are obtained.

4.1. Stress-strain Response and Mechanical Performance

4.1.1. Stress-strain Curves and Quasi-Static Properties

The stress-strain curves obtained from the experimental tests are presented in Fig. 4.1, an initial small plateau can be observed in each curve until the stress level reaching $\sigma \approx 10\mathrm{MPa}$. It is considered resulting by the small movement between the solid plates and the lattice structure. For [001] and [111] specimens, two separate runs were performed using specimens printed from two different batches. In each FEA simulation predicted curve, the stress initially increases steeply with increasing strain until yielding, then the stress continues to increase gradually until ε=3%. The failure of the lattice was not predicted by FEA. As shown in Fig. 4.1, the majority of the derived curves from $\mathrm{EXP_A}$ and $\mathrm{EXP_B}$ are aligned well, while only one curve for each group of specimens demonstrated slightly different trend. The quasi-elastic gradient and compressive offset stress specified in ISO 13314: 2011[92] were considered as the effective Young's modulus $\mathrm{E_L}$ and yield strength $\sigma_{\mathrm{y-L}}$ of the lattices. $\mathrm{E_L}$ was determined by the slope of linear region of the stress-strain curve and $\sigma_{\mathrm{y-L}}$ was taken as the stress value at the intersection point between the 0.2%-strain offset linear line and the curve. In addition, the apparent plastic strain ε_{p} is determined at the ultimate compression strength $\mathrm{UCS_L}$ by:

$$\varepsilon_p = \varepsilon_{total} - \varepsilon_{elastic} = \varepsilon_{total} - \frac{UCS_L}{E_L} \tag{4.1}$$

A manually interrupt test was performed for each group of the specimens after passing the elastic region. For interrupt [001]//LD samples, all the other tests were also manually interrupt once UCS was reached and the loading level started to decrease. There was no fracture but only distortion can be observed in the tested [001]//LD samples. For [011]//LD and [111]//LD samples, apart from the interrupt tests, the sudden drops in the stress-strain curves indicate the collapsing of the specimens. There were fractured struts could be observed in the tested [011]//LD and [111]//LD samples. The increased in loading level after first rapid drop in the stress-strain curves for [011]//LD and [111]//LD samples indicated that the upper portion of the fractured specimen collapsed on the lower portion, thus further compression resulted in the increasing compressive stress.

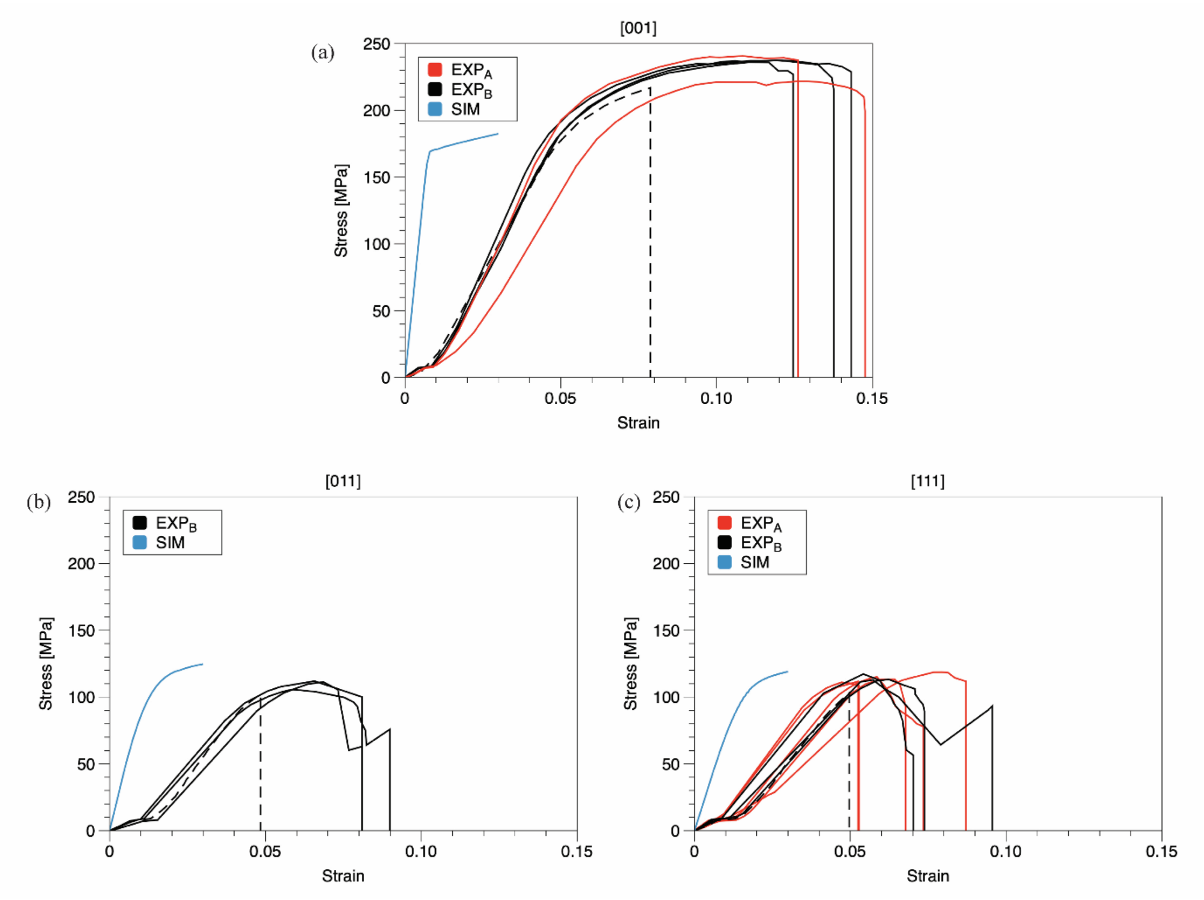

Fig. 4.1 Stress-strain curves obtained by FE simulation and experimental tests for: (a) [001]//LD, (b) [011]//LD and (c) [111]//LD samples (the dashed lines indicate the interrupt tests)

The compressive properties of the lattices with three different UCOs determined by experimental tests and simulations are given in Table. 4.1. Even though the tested lattices had the same strut size and relative density, their experimentally determined E_L, σ_{y-L} and UCS_L decreased in the order of [001]//LD, [111]//LD and [011]//LD orientation. In both experimental tests and FEA models, [011]//LD and [111]//LD samples obtained comparable values of E_L and σ_{y-L}. However, the [001]//LD specimens exhibit much higher values of the compressive strength, indicating the anisotropic behaviour of the SC structures. Since only bi-linear material properties have been considered in FEA models, UCS_L and ε_p was not estimated by simulations.

Table. 4.1 Quasi-static compressive properties obtained from experimental testing (± standard error) and FEA simulations. Note: Data from interrupted tests were excluded from these calculations.

UCO	**EXP (n)**	**E_L(GPa)**		**σ_{y-L}(MPa)**		**UCS_L(MPa)**	**ε_p**
		EXP	FEA	EXP	FEA	EXP	EXP

[001]	5	4.9±0.2	23	182±2	172	235±3	0.063±0.004
[011]	3	3.0±0.1	9	92±1	103	109±2	0.019±0.002
[111]	7	3.1±0.1	7	97±2	98	112±1	0.012±0.001

As presented Table. 4.2, the cell-orientation-dependent quasi-static compressive properties of SC lattice structures have been reported and compared with each other. The experimental data of $\sigma_{y-L[001]}$ and $UCS_{L[001]}$ are approximately twice than the values of [011]//LD and [111]//LD samples. The experimentally determined $E_{L[001]}$ is 1.6 times higher than that of either $E_{L[011]}$ and $E_{L[111]}$. From the FEA simulations, $E_{L[001]}$ is 2.6 and 3.3 times higher than that of $E_{L[011]}$ and $E_{L[111]}$, respectively. The experimentally determined E_L values across all the three groups of samples with varied UCOs are considerably lower than the values predicted by FEA simulations. Further validation and explanation will be provided in the following section. In contrast, the experimental and simulation results of σ_{y-L} values are reasonably comparable. [011]//LD and [111]//LD samples demonstrated comparable values of σ_{y-L} and UCS_Lin experimental results. The simulation predicted E_L and σ_{y-L} values of [011]//LD and [111]//LD lattices exhibit 30% and 10% difference, respectively. The plastic strain $\varepsilon_{P[001]}$ represents the plastic strain before the distortion of [001] lattice while $\varepsilon_{P[011]}$ and $\varepsilon_{P[111]}$ describe the plastic strain before the collapsing of these samples.

Table. 4.2 Comparison of the compressive properties of the lattices

[uvw]/[uvw]	$\frac{E_{L[uvw]}}{E_{L[uvw]}}$		$\frac{\sigma_{y-L[uvw]}}{\sigma_{y-L[uvw]}}$		$\frac{UCS_{L[uvw]}}{UCS_{L[uvw]}}$	$\frac{\varepsilon_{P[uvw]}}{\varepsilon_{P[uvw]}}$
	EXP	FEM	EXP	FEM	EXP	EXP
[001]/[011]	1.6	2.6	2.2	1.7	2.2	3.3
[001]/[111]	1.6	3.3	2.1	1.8	2.1	5.3
[011]/[111]	1.0	1.3	1.0	1.1	1.0	1.6

4.1.2. Validation and Verification of Experimental and FE Results

To verify and validate the experimental and FEA results, data for PBF fabricated SC lattices with $\bar{\rho}$ of in the range of between 0.28 and 0.40 has been collected from literature. The experimental results of effective Young's modulus of PBF fabricated SC lattices are listed in Table. 4.3. The experimental determined E_L in this research is comparable to those reported in literature[47,49,100,109] obtained by conducting axial compression tests. All the experimental results of E_L are considerably lower than the values determined using damping analyser[52,59] and LVDT[251]. The measured discrepancy, wherein the static E_L is less than the dynamic E_L, agree with the findings for bulk materials[252]. In addition, as the primary focus of this study was to investigate the strength and failure mechanisms of the lattices with different UCO rather than to establish the absolute E_L values. It can be observed in Fig. 4.1, even though the platen seatings could distort the initial linear-elastic slope, those seating adjustments would be fully resolved by the time that the structure reached macroscopic yielding. Thus, the measurements for strength values in this study should remain robust and were unaffected by the initial compliance. Therefore, despite the lower E_L values determined by compression tests using crosshead displacement has been understood, it is a widely established approach in literature for characterising varied lattice structures [48,67,109].

Table. 4.3 Experimental data of effective Young's modulus of simple cubic lattices collected from literature

E_L (GPa)	$\bar{\rho}$	d_s(mm)	AM	Testing Method	Ref
14.8	0.37*	~ 0.50	EBPBF	Damping analyser	[59]
~14	0.36*	~ 0.50	EBPBF	Damping analyser	[52]
2.9	0.39	0.80	EBPBF	Axial compression tests	[49]
2.7	0.31	0.80	EBPBF	Axial compression tests	[100]
13.4	0.24	0.50	LPBF	LVDT	[251]
4.8	0.35	0.72	LPBF	Axial compression tests	[47]
3.8	0.28	0.80	LPBF	Axial compression tests	[67]
4.3	0.40	0.60	LPBF	Axial compression tests	[109]
4.9	0.35	0.50	EBPBF	Axial compression tests	This Work

The mesh sensitivity analysis has been performed with five different mesh size values (0.25mm, 0.20mm, 0.15mm, 0.10mm and 0.09mm). The apparent compressive stress values calculated by the reaction force at the fixed plate were taken to determine the mesh size. As shown in Fig. 4.2(a), convergence was found between the mesh size of 0.10mm and 0.09mm. Therefore, the mesh size of 0.10mm was set for the FE models to save the computational cost. However, the resulted σ_1 values indicated that the mathematical convergence could not be achieved at the selected mesh size of 0.10mm. Because the intersections of the lattices in FEA were modelled as idealised sharp corners, these geometrical features would generate pure stress singularities where the theoretical stress approaches infinity. As the mesh was refined, the calculated stress values approached the theoretical singularity, causing the peak stress to increase unboundedly rather than stabilise at a finite plateau. This divergence demonstrates that mathematical convergence of the peak σ_1 value is impossible without physically modifying the idealised CAD geometry. Therefore, this study adopted the widely used approach found in the literature, utilising the macroscopic response of the lattices to verify mesh independence.

In addition, as suggested by multiple authors[47,181,218,253], the mechanical properties of a lattice can be well predicted by simulating a finite number of unique cells, rather than the whole structure. Hence, the effect of the number of unit cells was estimated by modelling 1, 8, 27, 64, 125 and the full size (the actual size of the PBF samples) lattices. As the results of estimated results of $\mathrm{E_L}$ and $\sigma_{\mathrm{y-L}}$ shown in Fig. 4.2(b), it was concluded that 3×3×3 lattice (27 cells) would be sufficient to predict the properties of an infinite structure.

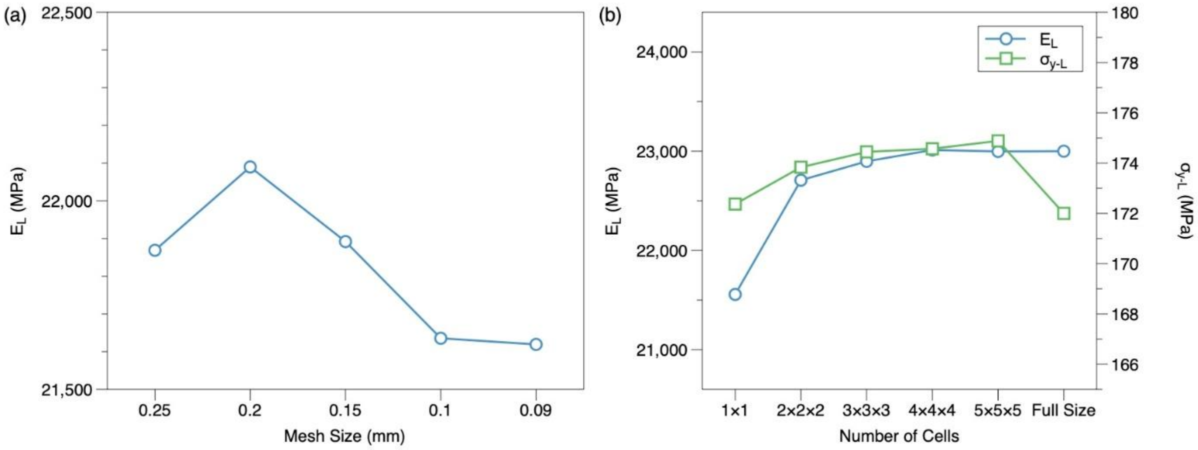

Fig. 4.2 The sensitivity analysis of the (a) Mesh size and (b) cell numbers

To justify the use of the bi-linear material properties and bound the potential effects on the global effective mechanical properties and the localised stress hot-spots using 3×3×3 [001]//LD lattice. The results of the sensitivity analysis of material properties are presented in Table. 4.4. As the baseline input parameters varied by approximately ±15%, the macroscopic lattice response of $\mathrm{E_L}$ and $\sigma_{\mathrm{y-L}}$ scaled highly predictably with the varied inputs. The variation of bulk E primarily affect the maximum magnitude of σ_1, while the maximum σ_{VM} values exhibited much lower sensitivity. In contrast, the bulk σ_{y} demonstrated more pronounced influence on $\sigma_{\mathrm{VM,max}}$ values. Additionally, despite the variation in exact location of the maximum stress were observed, the overall stress distribution pattern and critical regions remained unchanged.

Table. 4.4 Sensitivity report of the material properties with 15% variation in the input bulk E and σ_{y}

Inputs		**Output Results**							
E(GPa)	σ_{y}(MPa)	$\mathrm{E_L}$(GPa)	$\Delta\mathrm{E_L}$(%)	$\sigma_{\mathrm{y-L}}$(MPa)	$\Delta\sigma_{\mathrm{y-L}}$(%)	$\sigma_{\mathrm{VM,max}}$ (MPa)	Δ(%)	$\sigma_{\mathrm{1,max}}$(MPa)	Δ(%)
120	1001	20.3	-	165	-	1074	-	546	-
104	1001	17.2	–15	165	0	1040	–3.2	503	–7.8
138	1001	23.3	+15	165	0	1071	–0.3	587	+7.5
120	850	20.3	0	164	–15	907	–15.6	503	–7.7
120	1151	20.3	0	189	+15	1211	+12.8	583	+6.8

To justify the bonded contact condition, frictional contact at the interfaces between the end plates and with varying frictional coefficients (0.1–0.3) has been introduced. The stress-strain curves are plotted in Fig. 4.3, the results suggested that allowing lateral slip introducing artificial structural compliance, which lowered the initial E_L. However, the macroscopic σ_{y-L} remained robust. It indicated that despite the initial modulus is sensitive to the contact conditions, the ultimate load-bearing capacity and the yielding mechanism of the lattices are dictated by the cellular architecture rather than contact conditions.

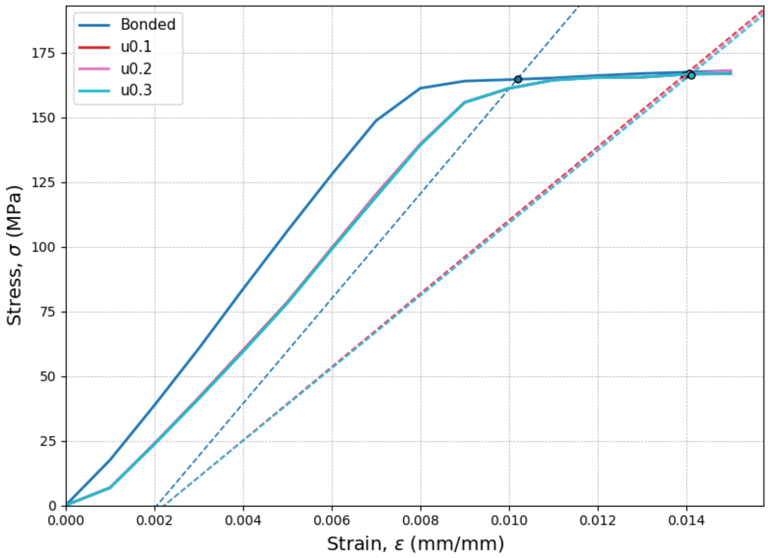

Fig. 4.3 FEA simulated Stress-strain curves based on [001]//LD 3×3×3 lattices with varied contact conditions

FE models are validated by comparing with the reported simulation results of E_L in literature, as presented in Fig. 4.4. The values of E_L of cubic lattices with different $\bar{\rho}$ obtained from the present simulation models agree with other published works[38,121,254,255]. Thus, the simulation predicted $E_{L[001]}$ for $\bar{\rho} = 0.35$ could be reviewed as reasonable.

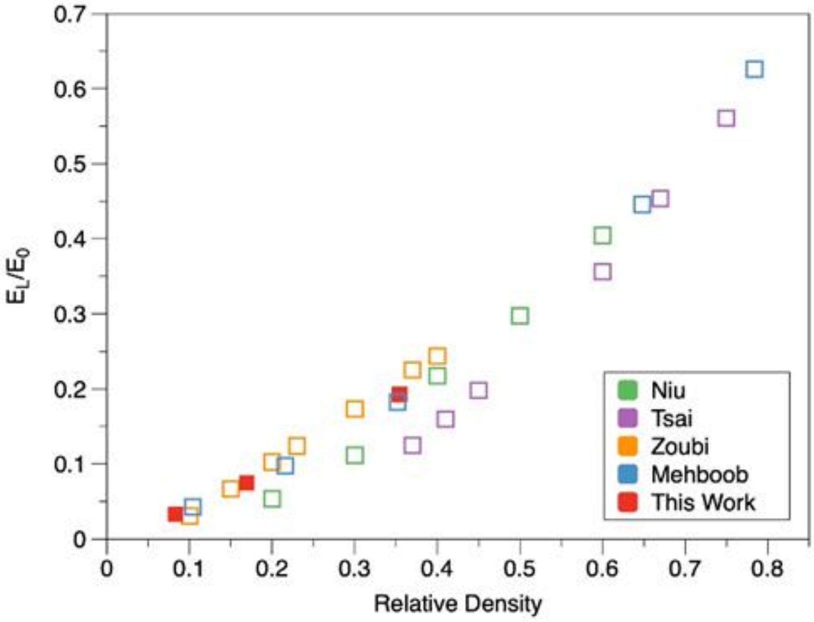

Fig. 4.4 Comparisonof FEA predicted results of E_L/E_S of [001]//LD SC lattice structures with different relative densities against data collected from literature [38,121,254,255]

4.1.3. Further Discussion on the Properties of [001]//LD Lattices

An analytical model is proposed for the further understanding of the compression behaviour of the [001]//LD samples. Square cross-section of the struts is considered in the analytical model instead of circular cross-section for simplification. In this case, the relative density of a [001]//LD SC cell can be calculated by:

$$\bar{\rho}_C = \frac{V_s}{V_c} = \frac{4d_s^2 L_c + 8d_s^2 L_p}{L_c^3} \tag{4.2}$$

where the $\mathrm{d_s}$ is the strut size, $\mathrm{L_c}$ is the cell size and $\mathrm{L_P}$ is the pore size. In the case of fully solid, the relationship between the geometrical parameters can be described by:

$$\begin{cases} L_p = 0 \\ d_s = L_c \end{cases} \rightarrow \bar{\rho}_c = 1 \tag{4.3}$$

Then the compressive response can be described by:

$$F = \frac{\delta L}{L_c} \times E L_c^2 \tag{4.4}$$

where δL is the compressive displacement and F is the applied load. Given the relative density in the present research is 0.36, substituting the value into Eq.(4.2), the ratio of $\mathrm{L_c/d_s}$ can be solved, equalling to 2.9315, which is independent to cell size. Then,

$$L_C = 2d_s + L_p = 4.931 d_s \tag{4.5}$$

In the case of uniaxial compression F is applied on the [001] simple cubic unit cell, assuming that the vertical struts with a length of $\mathrm{L_c}$ deforms uniformly without the constraint of the horizontal struts. Then the force F in Eq.(4.4) can be proportionally reduced to keep the same $\mathrm{\delta L/L_c}$ ratio to derive the effective Young's modulus of the unit cell $\mathrm{E_C}$ can then be derived from, meaning that:

$$\frac{F \times (\frac{4d_s^2}{L_c^2})}{L_c^2} = \frac{\frac{\delta L}{L_c} \times E \times L_c^2 \times \frac{4d_s^2}{L_c^2}}{L_c^2} = \frac{\delta L}{L_c} \times E_c \tag{4.6}$$

Then,

$$E_C = \frac{4E \times d_s^2}{L_c^2} = \frac{4 \times 120GPa \times d_s^2}{(4.931 d_s)^2} = 19.7GPa \tag{4.7}$$

To verify the analytical model, as illustrated in FEA simulations of a full unit cell with $\bar{\rho} = 0.36$ and a unit cell with vertical struts only with the same L_C and d_s have been conducted. For the vertical-struts-only cell, the simulation has indicated the effective modulus of $E_{L[001]}$=19.7 GPa, which equals to the results obtained from the analytical model discussed above using Eq.(4.5)–(4.7). For the full unit cell, the horizontal struts are included in the FEA model, exhibiting an effective modulus of $E_{L[001]}$=21.8GPa, which is slightly higher than that obtained from the vertical-struts-only model and slightly lower than the value predicted for the full-size lattice ($E_{L[001]}$=23GPa) listed in Table. 4.1. Comparing to the vertical-strut-only cell, the presence of horizontal struts in the full-unit-cell model resists the compressive strain of the $(L_c - L_p)$ portion, thus the slightly lower strain results in a higher E_L value.

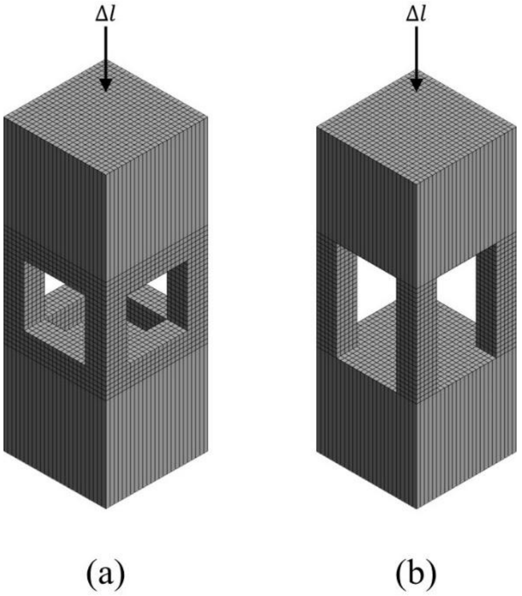

Fig. 4.5 FEA models for two different load supporting conditions of a unit cell to determine $E_{L[001]}$: (a) a full unit cell and (b) a unit cell only contains four vertical struts

4.2. FEA Estimated Cell-orientation Dependant Stress Distribution

The FE simulations predicted stress distribution of von-mises stress σ_V and maximum principal stress σ_1 of the [001]//LD, [011]//LD and [111]//LD samples under compressive loadings are presented in Fig. 4.6. The indicated loading for each sample represents the loading levels near the yielding point of each respective structure. The corresponding loads for these three lattices are $F_{y[001]} = -13277.2\text{N}$, $F_{y[011]} = -7591.6\text{N}$ and $F_{y[111]} = -7950\text{N}$, indicating the corresponding stress values of approximately 170MPa, 97MPa and 102MPa, respectively. These values were considered in agreement with the experimentally determined apparent stress values at yielding as presented in Fig. 4.1. The σ_y of bulk Ti6Al4V (1001 MPa) indicates the local yielding in the specimens. It can be observed from Fig. 4.6, σ_V is distributed evenly in the vertical struts which are parallel to LD and the majority of the stress is compressive in the [001]//LD sample. In [011]//LD and [111]//LD samples, the distribution of σ_V is not even, consisting of both compressive and tensile stress.

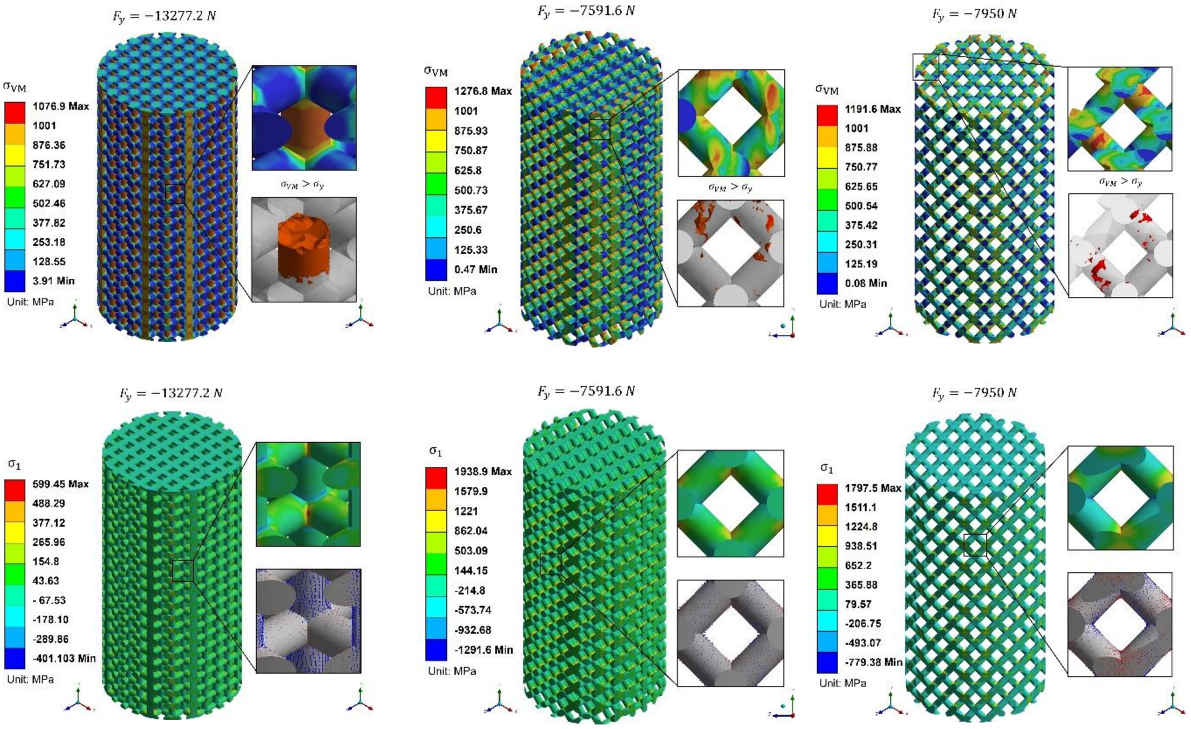

(a) (b) (c)

Fig. 4.6 Stress distribution of Von-Mises stress σ_{VM}(top row) and maximum principal stress σ_1(bottom row) on (a) [001]- (b) [011]- and (c) [111]-orientated specimens

To further verify that using a smaller number of unit cells can well predict the behaviour of an infinite structure, the stress distribution in the 3×3×3 lattice structures are presented in Fig. 4.7. The extreme values of σ_{VM} and σ_1 are slightly varied from the ones predicted using the full-size cylinder structures. The smallest variation in maximum and minimum stress values is observed in [001]//LD lattices while up to approximately 20% differences are noticed in [011]//LD and [111]//LD lattices. The variations in the stress values were contributed by the edge effects. Rather than the global, homogenised, or averaged properties like E_L and σ_{y-L}, these stress values are point-specific and sensitive to the geometries and boundary conditions. Comparing to 3×3×3 models, the full-size cylinder models contained more free struts at the boundaries, which were hardly bear external loads during the entire compression process and exhibited varied stress values. This finding agrees with the observation that reported by Sun et al. [256]. However, the 3×3×3 models predicted the same stress distribution patterns, the critical stress-concentration locations and the relative comparisons of the three types of lattices with different UCOs. Thus, he 3×3×3 models were considered sufficient for the subsequent analysis, balancing the computational efficiency with the overall accuracy of the simulation models.

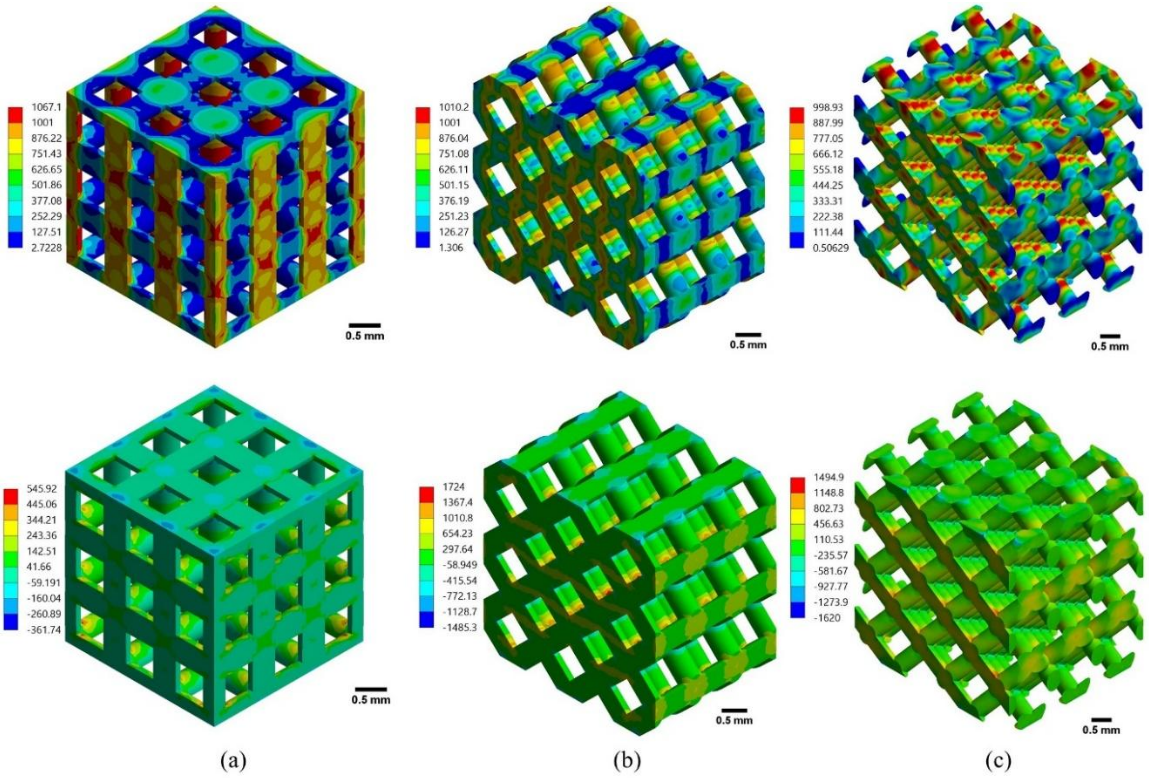

Fig. 4.7 Stress distribution in MPa of σ_{VM}(upper row) and σ_1(lower row) for (a) [001]//LD, (b)[011]//LD and (c) 111//LD with 3×3×3 cells under the loading conditions of $\sigma_{\mathrm{y-L}}$ of each structure

It is important to note that, as established in Section 3.2, all FEA models utilised in this study were based strictly on nominal as-designed CAD geometries. Consequently, the simulations did not incorporate the as-built geometrical imperfections inherent to the EBPBF process. While this idealisation means the actual localised peak stresses in the fabricated lattices are expected to deviate from the FEA-predicted values, the computational approach remains fully robust for predicting macroscopic responses and evaluating the relative mechanical performance across different UCOs.

4.3. Fracture and Deformation Behaviour

4.3.1. Deformation and Failure Modes

The photographs of the quasi-static tested samples with their corresponding stress-strain curves are presented in Fig. 4.8. The stress-strain curve of the [001]//LD specimen shows a long plateau region after the initial linear elastic deformation, followed by a slightly drop in stress upon reaching $\mathrm{UCS_L}$ before the test termination. The tested specimen is distorted due to the fracture of the vertical struts parallel to the LD, exhibiting a crash band almost perpendicular to LD. Both the [011]//LD and [111]//LD specimens also experienced the initial linear region, stress drop after $\mathrm{UCS_L}$, followed by a densification region characterised by a rapid increase in stress. However, the [011]//LD specimen exhibits a slightly smoother hardening response, whereas the [111]//LD specimen demonstrates a rapid stress drop following UCS_L. These [011]//LD and [111]//LD samples also fractured due to the formation of the crush band in an angle of approximately 45° and 36° with respect to LD, respectively.

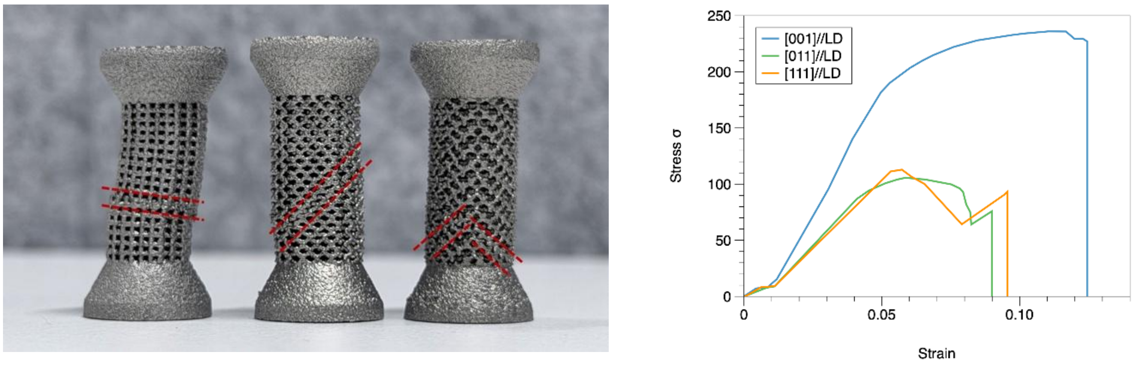

(a)

(b)

Fig. 4.8 Quasi-static tested (a) [001]//LD(left), [011]//LD(mid) and [111]//LD(right) samples and (b) their corresponding stress-strain curves

Further observations were revealed by the SEM images of the samples from the interrupted tests shown in Fig. 4.9–Fig. 4.11. As shown in the stress-strain curves in Fig. 4.1, all the interrupted tests were terminated slightly after the apparent yielding point of the tested lattices. For all the specimens from the interrupt tests, no noticeable global distortion or fractured struts are evident. In [001]//LD specimen, as revealed in the higher-magnification images, even though unmelted powders and unconnected struts are presented, no micro-cracks are detected on the strut surfaces. However, in both [011]//LD and [111]//LD specimens, micro-cracks are observed at the locations near the nodes of each unit cell although the global plastic strain is only at approximately 0.003%

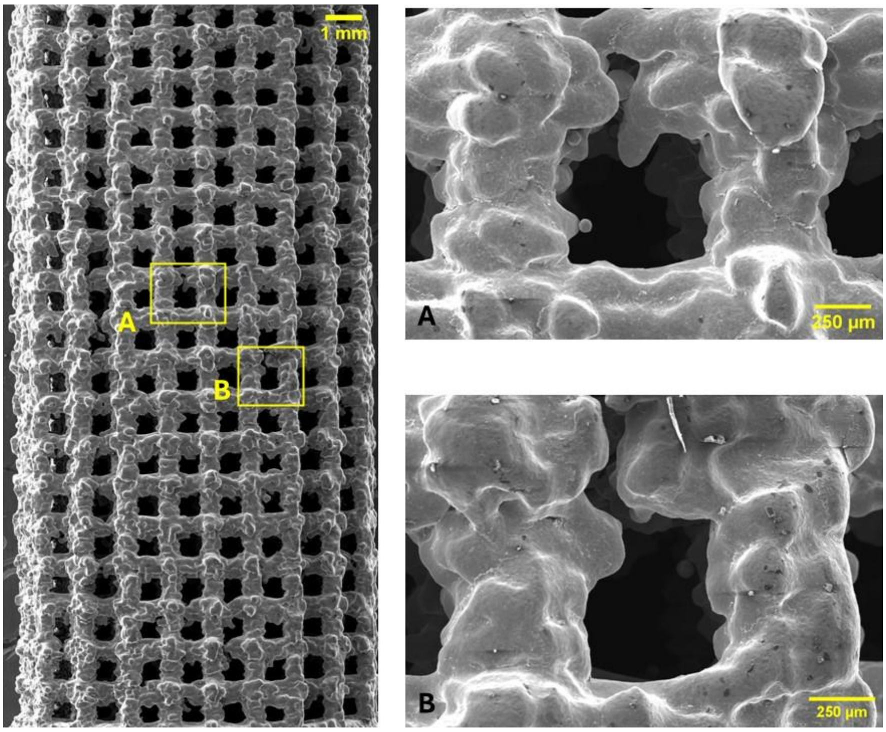

Fig. 4.9 SEM images of the [001]//LD sample from the interrupted test showing that no micro-cracks can be observed on the strut surfaces

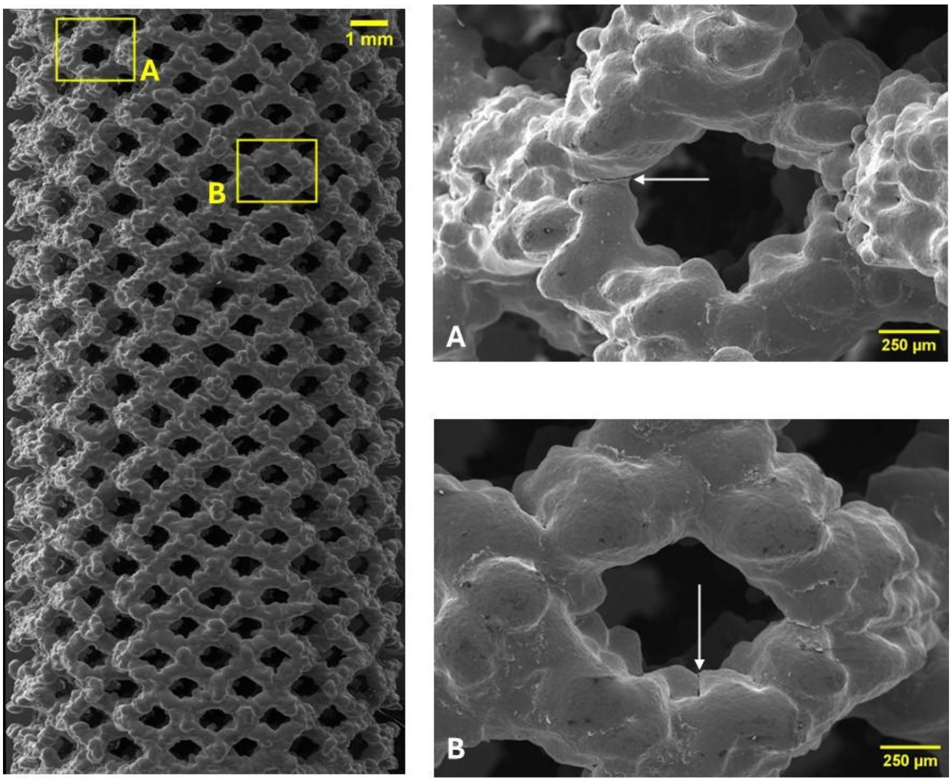

Fig. 4.10 SEM images of the [011]//LD sample from the interrupted test illustrating the presence of micro-cracks

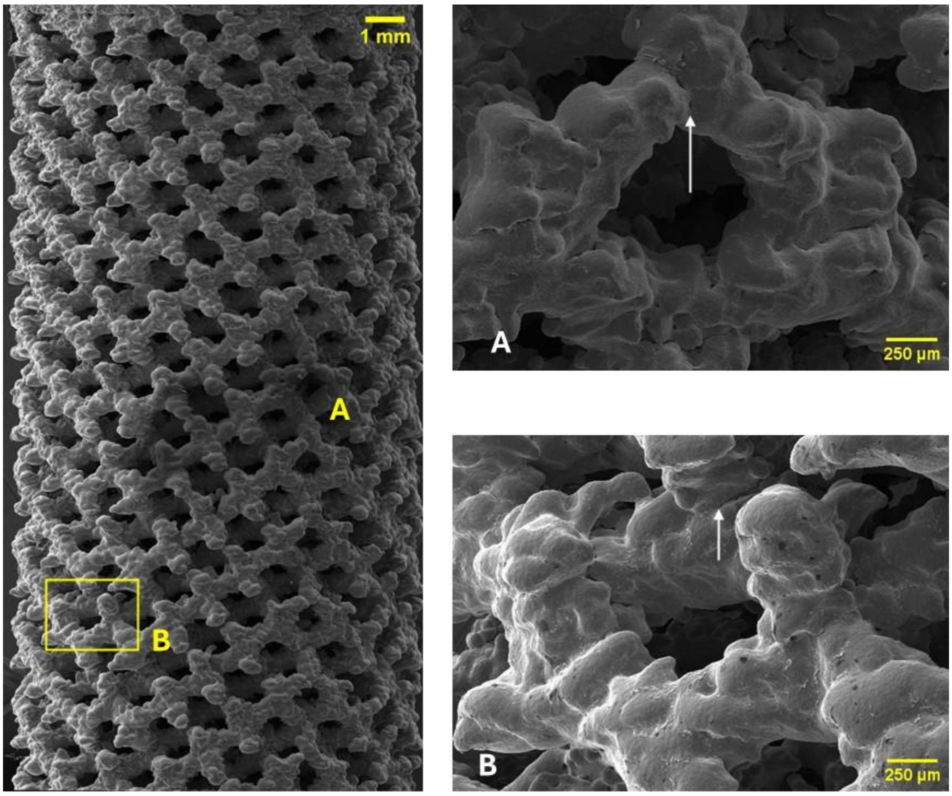

Fig. 4.11 SEM images of the [111]//LD sample from the interrupted test showing the presence of micro-cracks

More SEM images of the as-built and tested [011]//LD and [111]-orientated samples are presented in Fig. 4.12 and Fig. 4.13. Fracture paths with angles of approximately 45º and 36º were observed in the fractured [011]//LD and [111]//LD samples, respectively. The shear fracture of struts can be clearly seen in the higher magnification images in Fig. 4.12(b) and Fig. 4.13(b). As discussed, high values of σ_1 has reached locally in the struts where yielding of the lattices occurred. In addition, the irregularities in the forms of sharp protrusions, deep recesses and undercuts can readily increase the local stress concentration. Thus, those highly irregular struts fractured with at low ε_p(<0.02). Comparing to [111]-oriented samples ($\varepsilon_{p[111]} = 0.012$), the [011]-orientated samples demonstrated a significantly higher ε_p, giving $\varepsilon_{p[011]} = 0.019$, even though the FEA results suggested similar local stress concentration levels. In [111]-orientated samples, all the sturts supported the loads equally while in [011]-orientated samples, only two out of three sturts primarily bore the loads. Therefore, the reason of lower $\varepsilon_{p[111]}$ might resulted by a higher probability of strut defects assisted crack growth and fracturing.

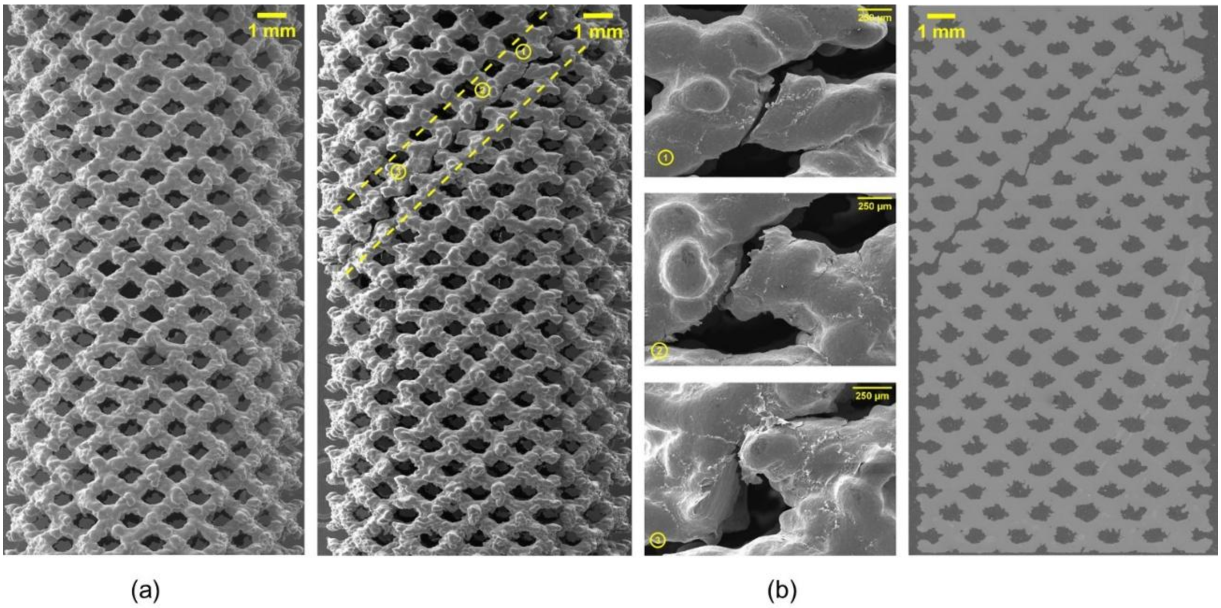

Fig. 4.12 SEM images of (a) as-built and (b) tested [011]-orientated sample showing the fracturing path of struts as indicated by the dotted lines in the left image, higher magnification images at the three fractured locations (mid images) and the cross-section of the sample clearly showing the fracture path (right image)

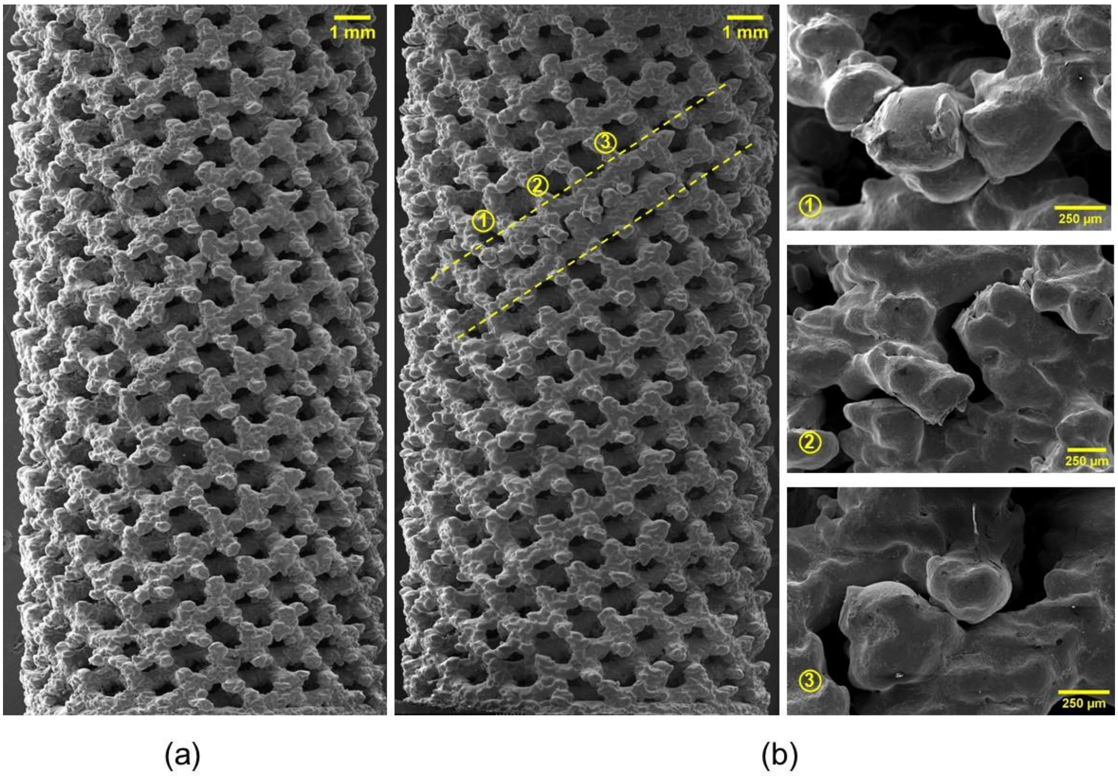

Fig. 4.13 SEM images of (a)as-built and (b) tested [111]-orientated sample with the fracture path (dotted line) and higher magnification images (right) detail the fractured locations.

4.3.2. The Effects of Strut Surface on the Quasi-static Behaviour

The highly irregular struts of the PBF fabricated lattices can be statistically demonstrated by measuring the size of the struts. For each UCO, two samples have been measured and the measured results are plotted in Fig. 4.14. The strut contributed by sharp protrusions, deep recesses and undercuts can be observed in the SEM images shown in the prior sections. The shown morphological features of the printed struts are consistent with the high values of standard deviation with the wide ranges in measured size. The calculated standard error of the mean strut size is considered to be minimal (only ~1%), indicating that a sufficient large number of sampling point has been used for the calculation. All the calculated values of the mean strut size are higher than the nominal designed strut size of 0.5mm. This is in agreement with the findings reported in other studies[47,59,257], where larger strut size of EBPBF lattices than designed size is found. The horizontal struts in [001]//LD specimens exhibited greater average thickness than the vertical struts and the inclined struts in [011]//LD and [111]//LD specimens, which is in consistent with the findings reported by Suard et al.[85] for the EBPBF Ti6Al4V thin struts printed with different BDs. However, all the struts expect for the horizontal ones exhibited smaller size than he designed ones in Ref. [85], which is different from the measured data in this work.

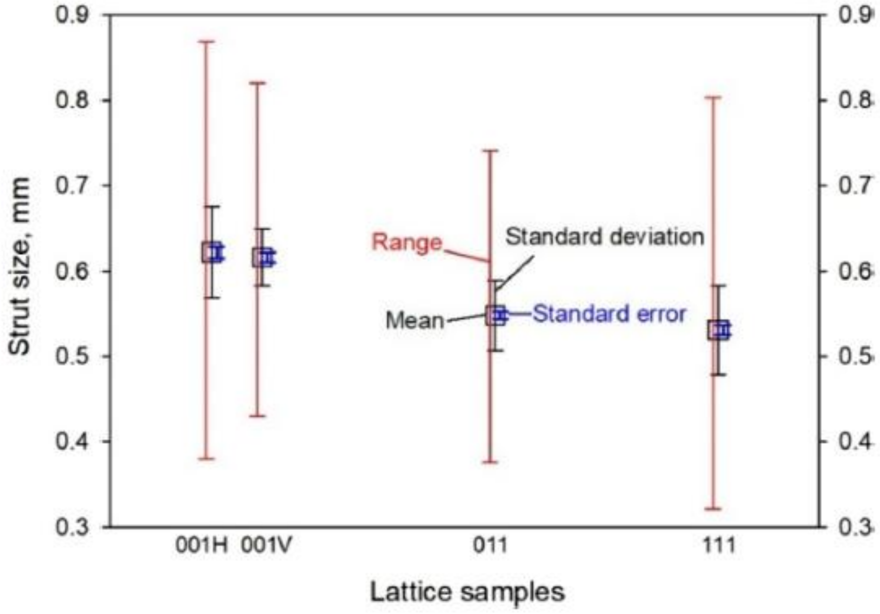

Fig. 4.14 Strut size measurement results of the lattices with different UCOs, including the mean, standard deviation, standard error, and range values of strut sizes

5. Orientation-dependent Fatigue Behaviour

Following by the understanding of the orientation-dependent mechanical behaviour of SC lattices under quasi-static compressive loading presented in last chapter, this chapter focus on the orientation effect on strength and fracture behaviour of the lattices under cyclic loading. Firstly, the considerably weakened structures with UCO deviates from [001]//LD will be discussed in detail. Associated with this, the fracture paths that are indicative of the fatigue strength of the lattices will be presented. Subsequently, the local cell fracture plane and direction along with the global fracture path for each [uvw]//LD lattice structure will be characterised. These facture characteristics also indicate how readily the fracture may progress through the lattice structures. Furthermore, the examination and observation of crack initiation sites together with the FEA predicted stress concentration locations in each cell will be illustrated to advance the understanding of the reason the non-[001]//LD structures exhibit reduced fatigue strength. The illustration will detail how the crack growth mechanism and crack path within each cell, showing the deviation and progression of the fracture, ultimately lead to the fracture of the entire lattice structure. Finally, the findings obtained from this work will be utilised to provide an explanation for why all the non-SC lattice structures reported in literature exhibited weak strength under cyclic loading.

5.1. Fatigue Tested Results

5.1.1. Displacement vs Cycle Curves and Evolution of Young's Modulus

The estimated values of relative density were found slightly lower than the nominal value of $\bar{\rho}=0.36$ using the method described in 3.4.5, but the variation is considered acceptable for the investigation of the fatigue strength of the designed lattices. The semi-log scale peak-peak displacement ΔD_p vs cycle N curves of the three types of lattice structures with different UCOs are presented in Fig. 5.1. Except for all the run-out samples and the 230MPa-[001]//LD sample, the test curves indicate that, ΔD_p remain constant with minimal strain accumulation over a wide cycle range. Then towards the end of each test, an initial gradual increase in ΔD_p is followed by a rapid rise that led to the test termination. Varying the tolerance value m from 92% to 150% did not significantly affect the N values but influenced the final accumulated damage. The 230MPa-[001]//LD sample demonstrated a distinct test curve, with a gradual increase in ΔD_p from the early stage and the test was terminated once the tolerance limit was reached. For [011]//LD and [111]//LD samples, the rapid increase in ΔD_p prior to the test termination was more pronounced. Higher tolerance values (m=135%–150%) were used for these two groups of orientated samples to allow more complete fracture and to facilitate examination of the fracture features.

Table. 5.1 Summary of the measured mass and the estimated relative density of the lattice specimens

UCO	**[001]//LD**	**[011]//LD**	**[111]//LD**
$m_{Measured}$ (g)	10.26±0.05	10.17±0.05	10.36±0.06
$\bar{\rho}_{Estimated}$	0.313	0.300	0.327

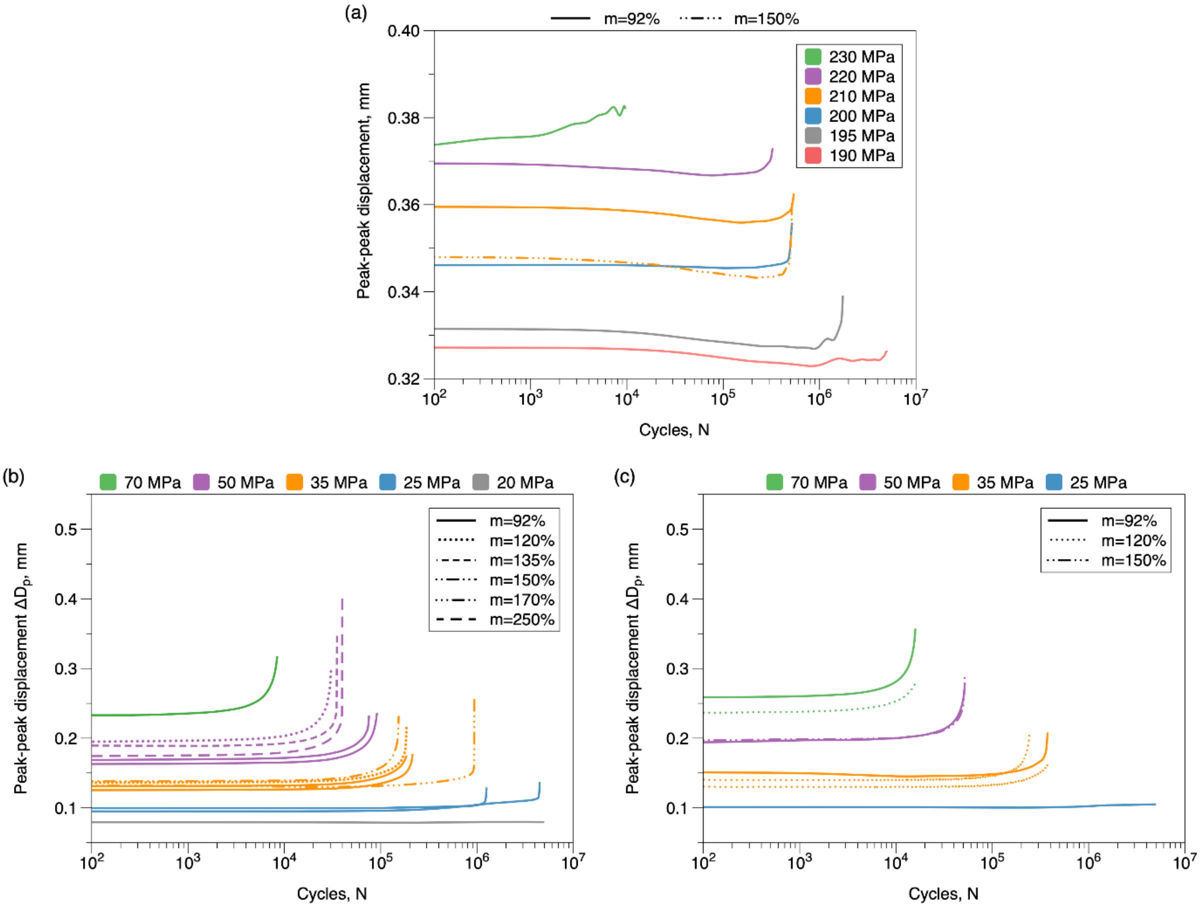

Fig. 5.1 Peak-peak displacement vs cycle curves for (a) [001]//LD, (b) [011]//LD and (c) [111]//LD samples

The reduction in effective Young's modulus E_L of the lattice structures during the cyclic loading is a progressive degradation process. As suggested by Alana et al.[95], degradation of the macroscale E_L can be considered as the result of damage, failure or local plastic deformation in the struts. For the tested SC lattices, the evolution of E_L during the fatigue tests is presented in Fig. 5.2. It can be observed that for all lattices, high stress levels result in more significant reduction in E_L from the initial stage. Specifically, for 230MPa-[001]//LD sample, rapid drop in E_L starts at 2×10^3 cycles, indicating possible immediate damage at the beginning of the test. The dramatic reduction in E_L under high stress level aligns with the short fatigue life of the 230MPa-[001]//LD sample shown in Fig. 5.1(a). In contrast, the ΔE_L-N curves under lower stress levels exhibit stabilised E_L values persist over a wide range of fatigue cycles prior to the final failure. For all the [001]//LD lattices apart from the 230MPa-[001]// sample, gradually increasing trend in E_L before the final rapid drop is observed, indicating the micro-gaps or imperfections may be progressively closed and compacted during the cyclic compressive loading.

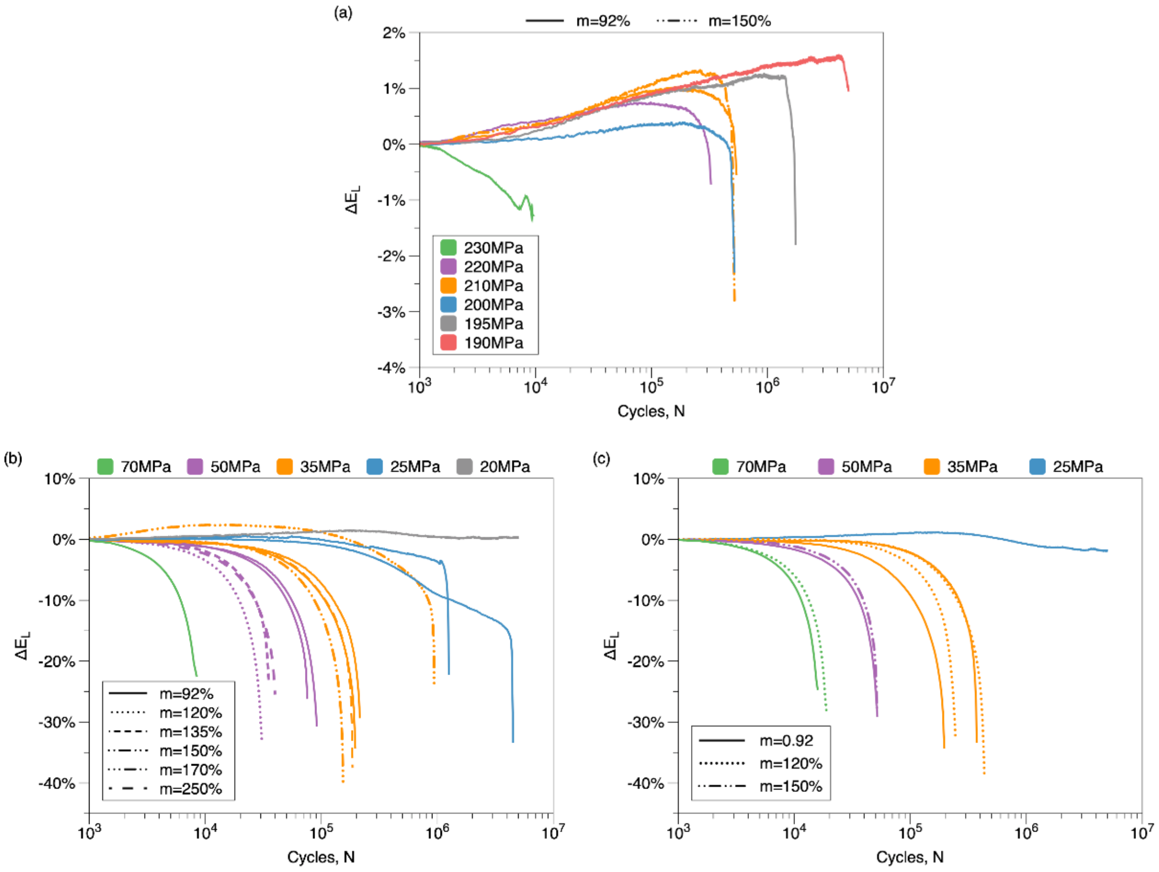

Fig. 5.2 Change of effective Young's modulus under different stress level and m values of (a) [001]//LD, (b)[011]//LD and (c) [111]//LD lattices during the fatigue tests(R=10, f=20Hz)

5.1.2. S-N Curves

The S-N data of the tested three different cell-oriented lattice structures is summarised in

Table. 5.2 and plotted in Fig. 5.3 in the form of the maximum compression stress $\sigma_{\max} = |-\sigma_{\min}|$ against the cycle number N. A total of 8, 13 and 4 specimens were tested for [001]//LD, [011]//LD and [111]//LD lattices, respectively. As presented in

Table. 5.2, small sample size was utilised in the fatigue tests. It should be noted that the primary objective of this fatigue testing was exploratory research aimed at identifying the underlying effects of UCO on fatigue mechanisms. Since the goal was broad preliminary S-N mapping, rather than establishing industrial design allowable, the limited available specimens were tested across a wide range of stress levels. Considering the required fatigue life of femoral stem implants specified in the international standard[42], the run-out samples are defined the tested samples reach a maximum number of cycles of 5×10^6 without failure. To correctly account for the run-out data without failure, the experimental data was fitted to the modified Basquin equation (3.8) using MLE. The resulting S-N curves and the corresponding 95% prediction intervals are presented in Fig. 5.3. The obtained coefficients and exponents are annotated with coefficients of determination (R^2). For non-[001]//LD structures, the fitted curves exhibit steep negative slopes, which clearly indicates the strongly dependence of N on the applied stress levels. In comparison, for [001]//LD lattices, the dependence between the applied stress levels and the fatigue life is weak, characterising by a significantly flatter slope (B=-0.03).

Table. 5.2 Summary of S-N data for the tested lattices

UCO	**Tested stress levels, σ_{max} (MPa) [Sample size, n]**	**Total Specimens**
[001]//LD	230 [1], 220 [1], 210 [1], 200 [1], 200 [1], 195 [1], 190 [1], 170 [1]	8
[011]//LD	70 [1], 50 [5], 35 [4], 25 [2], 20 [1]	13
[111]//LD	70 [1], 50 [1], 35 [1], 25 [1]	4

In addition, the quasi-static ultimate compression strength UCS_L of the lattice structures are also plotted in Fig. 5.3 for the evaluation of the effects of cyclic loading on the fatigue strength. Compared to [011]//LD and [111]//LD samples, the [001]//LD samples exhibited higher strength values. For [001]//LD samples, compared to $UCS_{L[001]}$, the stress σ_{max} only dropped by 2% and 17% as N increased to 10^4 and 10^6, respectively. For both [011]//LD and [111]//LD samples, σ_{max} decreased from UCS_L by approximately 56% and 374% for N=10^4 and N=10^6, respectively. It can also be observed that, the listed stress ratio in Table. 5.3 of $\sigma_{UCS[001]}/\sigma_{UCS[011]}$ (or $\sigma_{USCO[001]}/\sigma_{USC[111]}$) is only 2.2 but $\sigma_{max[001]}/\sigma_{max[011]}$ (or $\sigma_{max[001]}/\sigma_{max[111]}$) is 3.3 at N=$10^4$ and 8.7 at N=10^6. This finding indicates that, the cyclic loading demonstrated a significantly more adverse effects on the fatigue strength of the non-[001]//LD lattices than that of the [001]//LD samples.

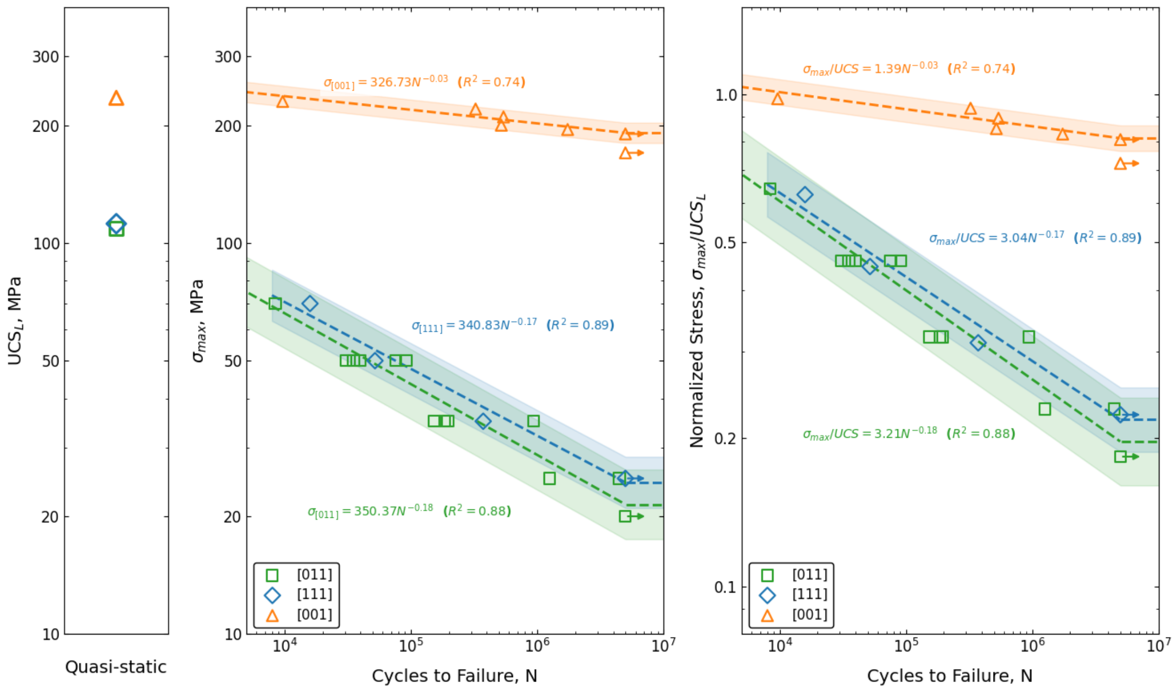

Fig. 5.3 S-N data, maximum applied stress ($\sigma_{max} = |-\sigma_{min}|$ with R=10) plotted against cycle number N with corresponding quasi-static USC$_L$ values for [001]//LD, [011]//LD and [111]//LD lattice structures

Table. 5.3 Comparison of strength values for the lattices under quasi-static and fatigue tests

[uvw]/[uvw]	**Stress Ratio**	**$N=10^4$**	**$N=10^6$**
[001]/[001]	USC$_L$/σ_{max}	235/230=1.02	235/201=1.17
[011]/[011]	USC$_L$/σ_{max}	109/70=1.56	109/23=4.74
[001]/[011]	$\sigma_{max}/\sigma_{max}$	230/70=3.3	201/23=8.7
[011]/[111]	$\sigma_{max}/\sigma_{max}$	70/70=1	23/22≈1

As shown in Fig. 5.4, to interpret the fatigue scatter probabilistically, a two-parameter Weibull survival distribution was fitted to the replicate data using MLE. Due to the small sample size, only the data sets obtained at stress levels of 50 MPa (n=5) and 35 MPa (n=4) were analysed. It can be observed that decreasing stress level from 50MPa to 35MPa significantly increased the characteristic life α from 6.2×10^4 cycles to 4.0×10^5 cycles. In addition, the Weibull shape parameter β also reveals a distinct shift from 2.45 (at 50MPa) to 1.25 (at 35MPa). This quantifies the well-known phenomenon that as applied stress decreases toward the fatigue limit, the statistical scatter in fatigue life inherently increases.

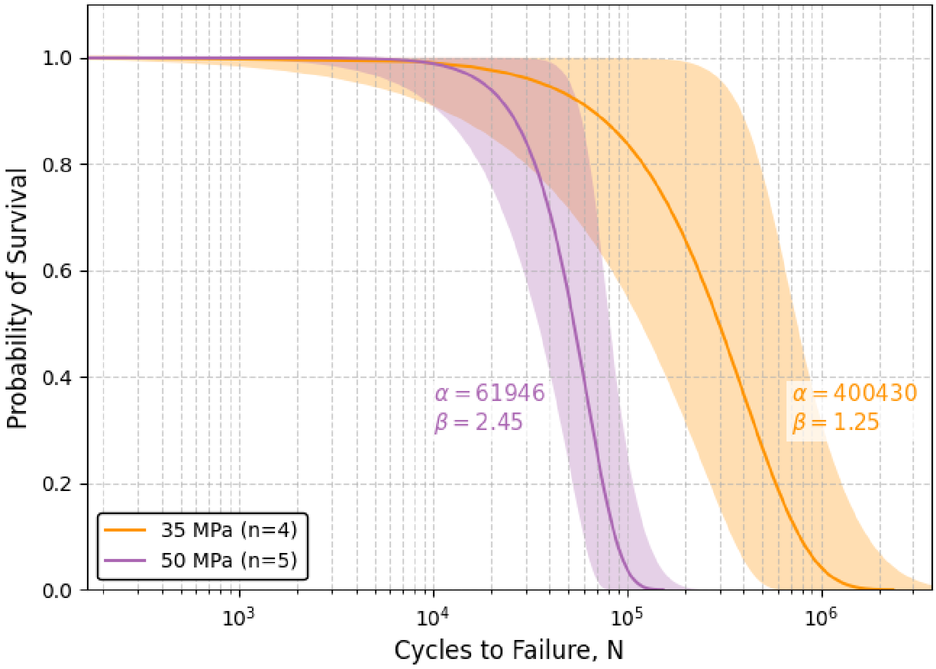

Fig. 5.4 Probability of survival plot for [011]//LD lattices tested under 50MPa (α=6.2×10^4 cycles, β=2.45) and 35MPa (α=4.0×10^5 cycles, β=1.25) with 95% confidence bands

5.2. Orientation-dependant Fracture Directions and Planes

For the evaluation and discussion of the orientation effects on the fatigue strength of the lattices, the various directions are defined as illustrated in Fig. 5.5. For non-[001]//LD samples, the failure occurred due to shearing fracture with the fracture plane (FP) forming between the top and bottom portions of a fractured sample. The fracture direction (FD), loading direction (LD) and the specific front view direction (FVD_S) are also illustrated in Fig. 5.5, where the FVD_S is defined such ∠FVD_S/LD=90° and also ∠FVD_S/FD=90°. The photographs of the fractured samples have been taken from the defined FVD_S, allowing the shear angle α relative to LD (*α*=∠FD/LD) can be measured directly from the photograph and the corresponding Miller index (h, k and l) of FP can be determined.

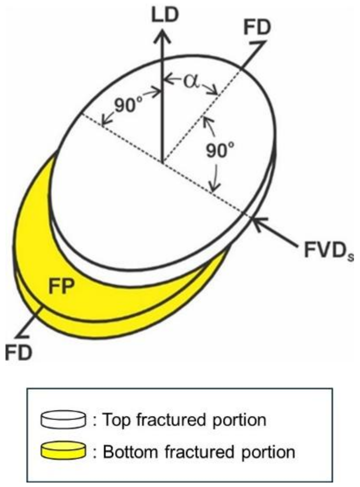

Fig. 5.5 Schematic illustration of the fractured sample (FP: fracture plane, FL: fracture direction, FVDs: specific front view direction and α: the angle between LD and FD.

The photographs taken from the (100) front view of the as-built and quasi-static tested [001]//LD samples are shown in Fig. 5.6, where the yellow square indicating the area corresponding to four cells in (100) view of the as-built sample. As shown in Fig. 5.6 (b), viewing from the 45° angle from the front view, the FP of (001) of the quasi-static tested [001]//LD sample is annotated by the red arrow. The upper portion above FD was slightly dislocated rightward after collapse, consistent with observations reported in the literature[52,117,251]. From the 45° view, slightly sideway displacement of the upper portion has been observed. Thus, FD in this fractured (001) is parallel to the 45° viewing direction and FD is [110].

The fatigue tested [001]//LD samples are presented in Fig. 5.6(c), slightly distortion or bending but without fracture is observed under the highest stress level when σ_{max}=230MPa=0.98 UCS_L this behaviour is similar to that observed in the quasi-static tested samples showing in Fig. 5.6(a-b). The slight bending of the sample tested at σ_{max}= 230MPa is likely to be a gradual process, as suggested by the ΔD_p-N curve shown in Fig. 5.1(a). The gradual deformation led to a continuous increase in ΔD_p until it reached the tolerance threshold resulting in test termination and sample failure. For the sample tested at σ_{max}=220MPa=0.94 UCS_L, difference failure behaviour can be observed in both Fig. 5.1(a) and Fig. 5.6(c). No gradual increase in ΔD_p over a wide range of cycles in this sample but a rapid jump associated with the final failure of the sample, thus no corresponding high degree of distortion was observed in the failed sample. For all the other [001]//LD samples tested at a stress level below 220MPa, except for the run-out one, the final rapid increase in ΔD_p was observed and the level of distortion remained negligible. However, fractured struts were captured in the 190MPa and 200MPa samples.

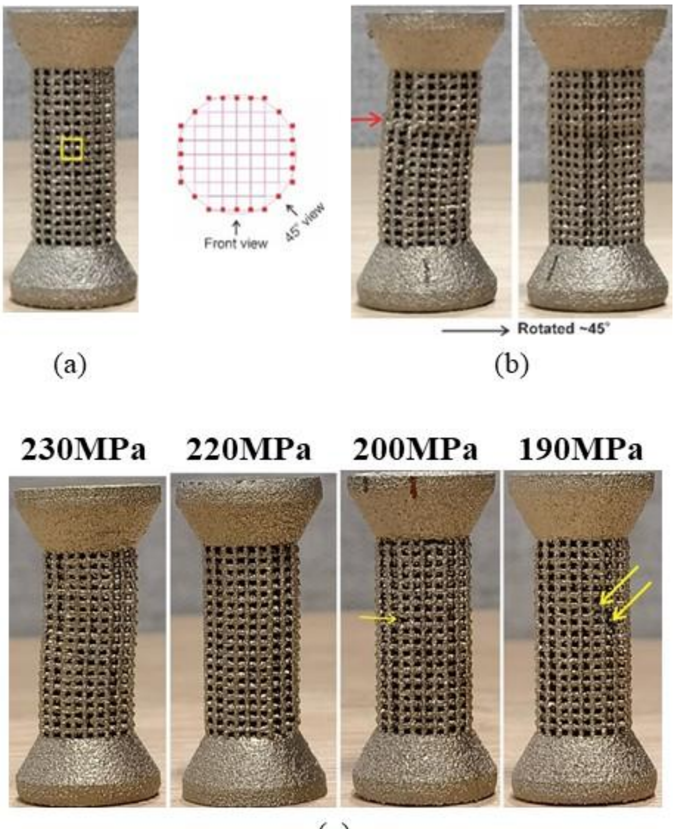

(a) (b)

(c)

Fig. 5.6 Photographs of the SC [001]//LD lattices: (a) as-built sample showing a cross-section normal to LD, the outer nodes are highlighted in in red and the yellow square presents four unit cells, (b) quasi-static sample with fracture path (red arrow) and (c) fatigue tested (m=92%) samples with broken cells (pointing by yellow arrows)

For the quasi-static [011]//LD sample as shown in Fig. 5.7(b) with FVDs=[100], FP is identified as (001) with FD=[010] and α=45°. Thus, fracturing and subsequent collapse caused a slight slip of the upper portion in (001) plane along [010] direction prior to the test termination. For the fatigue-tested [011]//LD samples with m=92% presenting in Fig. 5.7(c), no significant macroscopic deformation was observed, while fractured struts were captured in the tested samples, as indicated by the yellow arrows.

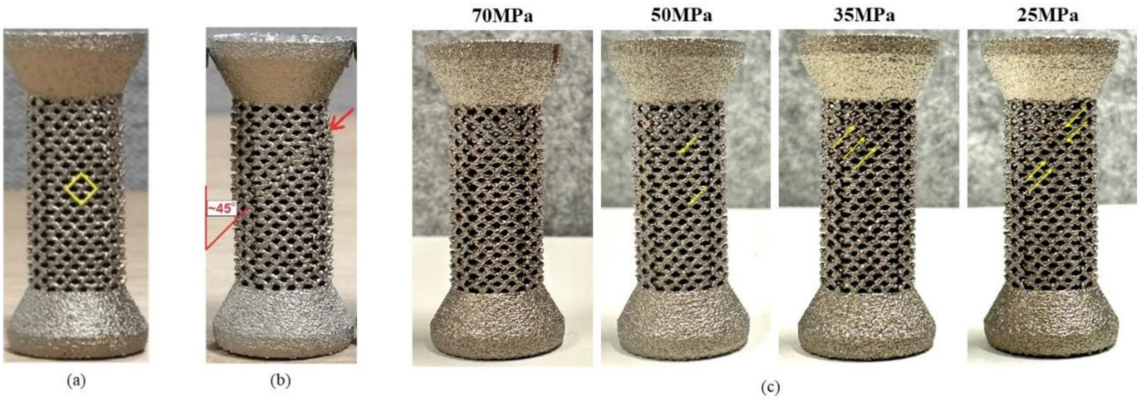

(a) (b) (c)

Fig. 5.7 Photographs of the [011]//LD SC lattices: (a) as-built sample with four unit cells highlighted by the yellow rectangle, (b) quasi-static sample showing the angle between FD and LD and (c) fatigue tested samples with broken cells highlighted by the yellow arrows

For the quasi-static tested [111]//LD sample as shown in Fig. 5.8(b), images 1–4 are presented showing the sample viewed from different FVDs. Image 1 was taken at the FVDs with α≈36°, where the outlined four-cell area of (110) from the as-built sample was superimposed on to Image 1 of the tested sample and fit well. The long edge of the outlined rectangular is in $[1\bar{1}0]$, parallel to FD. In other words, a line parallel to the long edge lies within the FP and the short edge of the rectangular is along [001], which is normal to the FP. Then, FP can be identified as (001). Images 2–4 were captured from viewing angles obtained by rotating the sample clockwise in 45° increments relative to Image 1. In Image 4, vertical dislocation of the sample is evident, indicating a shear fracture along $[1\bar{1}0]$ in (001), a feature also visible in Image 1 and 2. The photographs of the fatigue tested [111]//LD samples with m=92% are show in Fig. 5.8(c). These images were captured from the view angle the same as that used for Image 3 in Fig. 5.8(b). No significant deformation of fracture can be observed from those photographs and it is also difficult to identify if there are any cracks exhibited locally on the struts of these [111]//LD fatigue samples. Thus, further examinations will be conducted using SEM in the following sections.

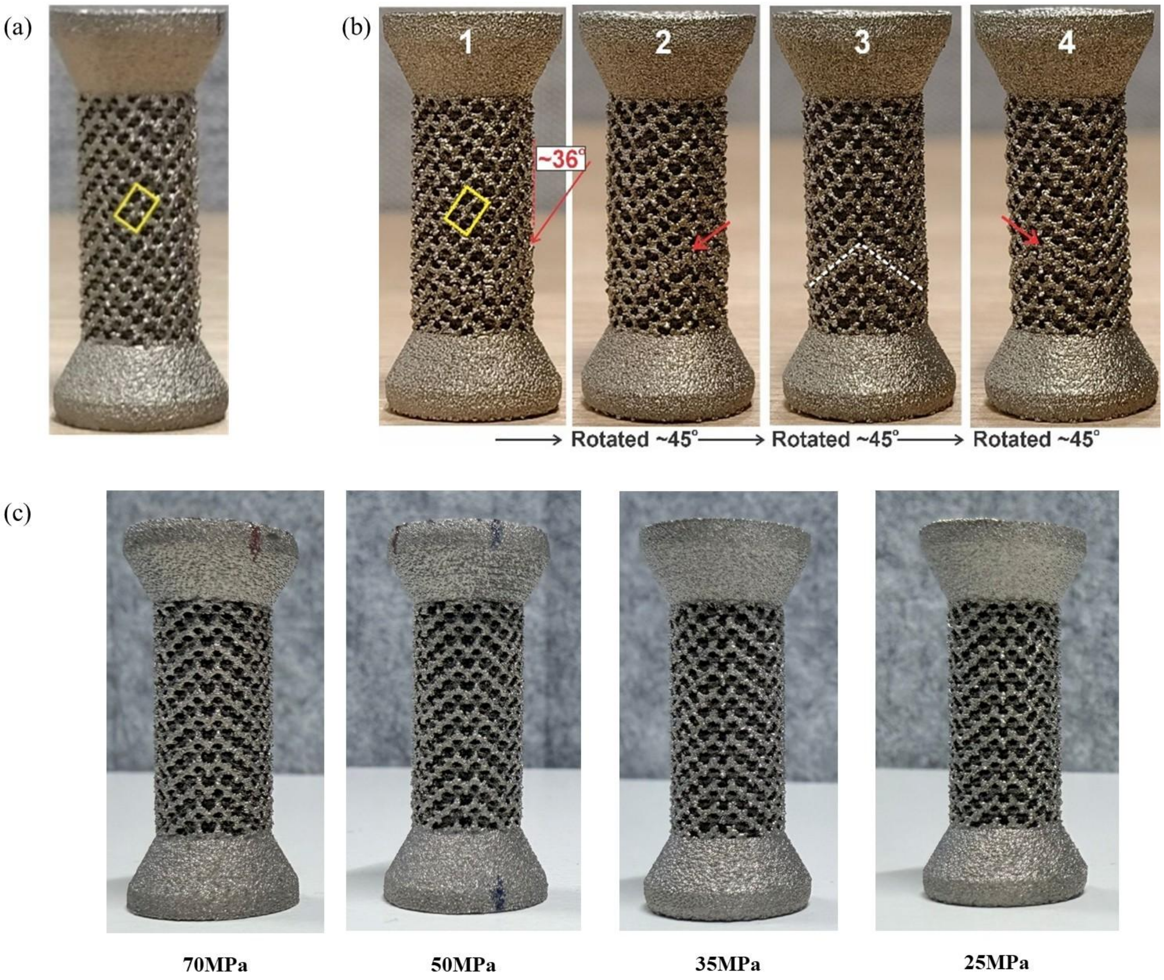

Fig. 5.8 Photographs of the [111]//LD SC lattice: (a) as-built sample with four unit cells highlighted by the yellow rectangle, (b) quasi-static sample showing the angle between FD and LD at different viewing directions and (c) fatigue tested(m=92%) samples

To obtain more completely fractured samples and enable better visual examination of the failed samples, additional fatigue tests were conducted using higher m values. As shown in Fig. 5.9, the use of higher m values did not induce collapse of [001]//LD sample but resulted in more pronounced bending. However, the higher m values caused completely fracture in [011]//LD and [111]//LD samples, giving a clear view of FDs and FDs in these samples. Despite Fig. 5.1 has suggested that varying m values has limited effects on fatigue life and using m=92% has successfully led to sample failure with FP moving along FD, the resulted change in $\Delta \mathrm{D_p}$ was insufficient to produce the completely fractured samples.

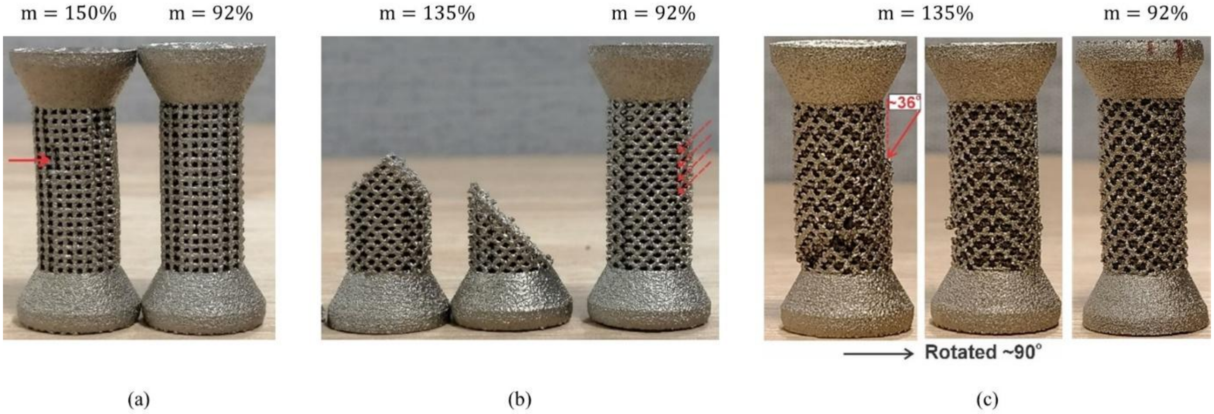

Fig. 5.9 Photographs of the fatigue tested samples with different m values: (a) [001]//LD (210MPa) samples with red arrow pointing the broken or fall out cells, (b) [011]//LD (50MPa) samples with red arrows pointing the cells with shared deformation and (c) [111]//LD (50MPa) samples with a fracture plane in 36° to LD

From the fractured pieces of [011]//LD sample tested with m=150%, it can be clearly seen that the FP is (001) and FD is either [010] or $[0\bar{1}0]$, forming an angle of 45° with respect to LD, consistent with the identified FP and FD observed in the quasi-static [011]//LD samples. For the [111]//LD sample tested with m=150% as shown in Fig. 5.9(c) from the FVD$_\mathrm{S}$ view, FD is approximately 36° with respect to LD. The identified FD of fatigue tested [111]//LD matches that of the quasi-static [111]//LD samples. However, the location of the FPs differs between the quasi-static and fatigue samples, indicating the fracturing occurred in different (001) layers. Rotating the fractured [111]//LD sample by 90° from FVDs view, the obtained image in the middle column in Fig. 5.9(c) shows vertical dislocation, which is similar to Image 3 in Fig. 5.8(b). It also confirmed that in the fatigue tested [111]//LD samples, FP is (001) and FD is $[1\bar{1}0]$. The identified results of the geometrical fracture features with varied UCOs are summarised in Table. 5.4.

Table. 5.4 Identified FPs, FDs and α of the lattices with varied UCOs

Sample	**FP-FD**	**α (∠FD/LD)**
[001]//LD	(001)-[110]	90°
[011]//LD	(001)-$[0\bar{1}0]$	45°

[111]//LD	(001)-[1$\bar{1}$0]	35.3°

5.3. Crack Initiation and Growth

5.3.1. Crack Initiation Observed on the Surfaces of the Tested Samples

The SEM images of the quasi-static and cyclic tested [001]//LD samples are presented in Fig. 5.10, including four rows of horizontal struts, while only partial struts from the top and bottom rows are shown in the images. In Fig. 5.10(a), the quasi-static sample only exhibits two rows of visible pores, since the vertical struts in the middle row were collapsed resulting in the closure of pores. It can also be observed that the top two rows of vertical struts are misaligned with those in the bottom two rows due to the dislocation sideways of the upper portion of the fractured sample. As previously discussed in 5.2, the collapsing and subsequent sliding in (001) and along [110] resulted in the upper portion of the fractured quasi-static [001]//LD sample to displace by $\frac{1}{2}\sqrt{2}a_{cell}$ and $\frac{1}{2}a_{cell}$ along the 45° viewing direction and FVDs, respectively. It is worth noting that, there were no microcracks observed in the cells shown in Fig. 5.10 either above or below the FP (001). The SEM image of the fatigue-tested [001]//LD sample at σ_{max}=210MPa is shown in Fig. 5.10(b), revealing that neither significant distortion nor complete planar fracture can be observed. However, as annotated by the red arrows Fig. 5.10(b), the cracks were well initiated locally at the horizontal struts and one of the struts was fully fractured. As seen in Fig. 5.1(a), the rapid increase in ΔD_p should be the result of a sudden change in displacement within a small number of cycles. It is possible that, when a horizontal strut is fractured, the adjacent vertical struts then effectively behave as longer columns, making them more prone to buckling. As a result, the compression or buckling of these vertical struts can occur more readily, causing the tolerance threshold to be reached and the termination of the test.

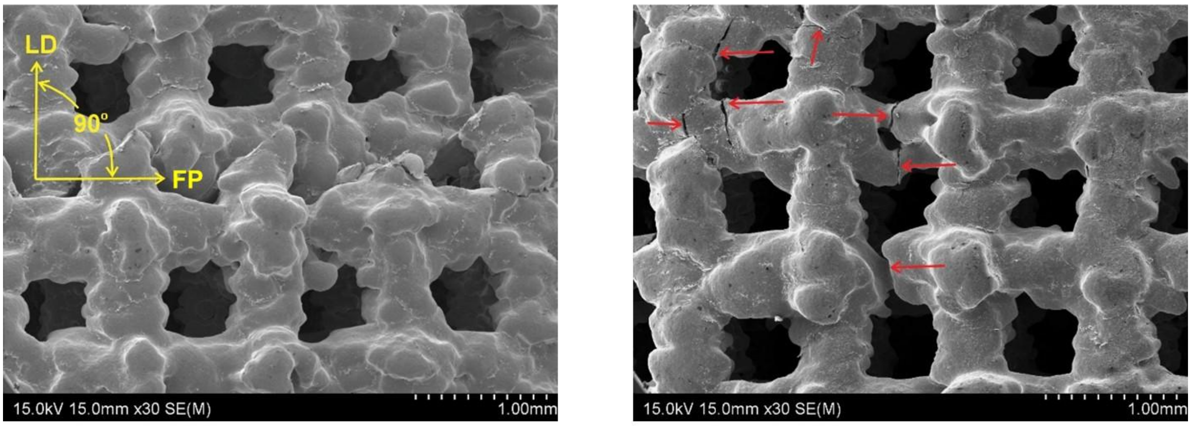

(a)

(b)

Fig. 5.10 SEM images of [001]//LD samples: (a) quasi-static tested and (b) cyclically tested at 210MPa (m=92%)

The examination of [011]//LD samples revealed that the struts fractured in (001) along [100]. Since [011] is parallel to LD in [011]//LD samples, the angle between the [011] and the (001) FP is 45°, which is the same as the angle between [011] and LD. Similar to the quasi-static tested [001]//LD sample, no cracks can be observed in the quasi-static [011]//LD sample shown in Fig. 5.11(a). However, clear differences can be seen in the fatigue-tested samples in Fig. 5.11(b), where a large number of small cracks are presented, particularly at the critical locations annotated by the arrows. It can be clearly observed that, the cracks initiation occurred at or near the top or bottom nodes of each cell, rather than at the right or left nodes. However, it can also be observed that the crack propagation tends to deviate from its initial path, and the cracks can grow straight downwards or upwards for a short distance. An example can be seen in Fig. 5.11(b), the crack outlined at the bottom corner of Cell 1 propagates toward the right corner of Cell 2.

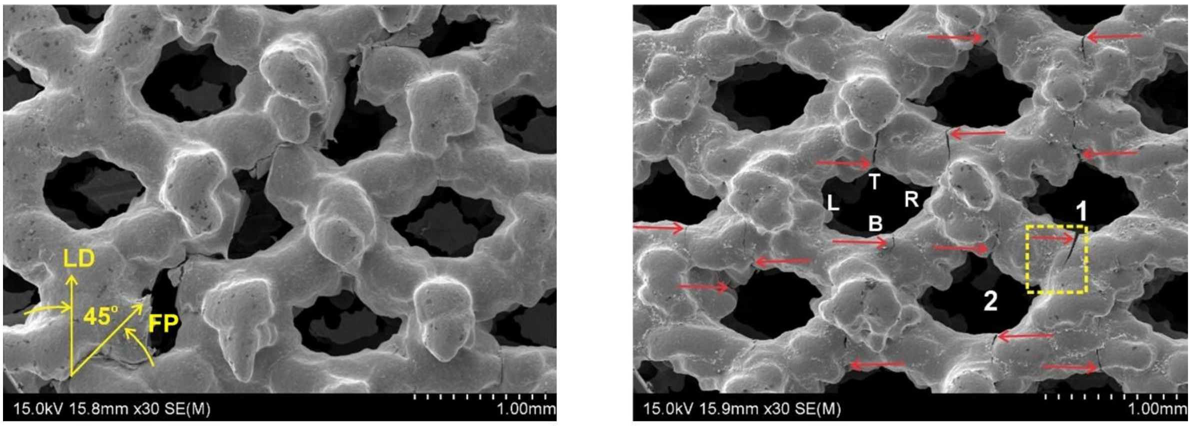

(a)

(b)

Fig. 5.11 SEM images of [011]//LD samples: (a) quasi-static tested and (b) cyclically tested at 50MPa (m=92%)

The SEM image of the quasi-static tested [111]//LD sample shown in Fig. 5.12(a) was taken from the same viewing direction as that of Image 2 in Fig. 5.8(b). Consistent with the observations made for the other two orientated quasi-static samples, no microcracks are found adjacent to the main macrocrack. For the fatigue-tested [111]//LD sample presented in Fig. 5.12(b), the crack initiation sites are similar to those observed in [011]//LD fatigue samples, with small cracks initiated at the top and bottom corners of the cells. This unique feature, in which the crack initiation occurs preferentially at the top and bottom nodes of a cell in the non-[001]//LD sample, may explain the reduced fatigue strength of these lattices under cyclic loading. In [00]//LD samples, no such critical locations within a cell appear to promote the crack initiation when σ_{max} is not significantly high. As a result, the effect of cyclic loading on the compressive strength of [001]//LD samples is limited.

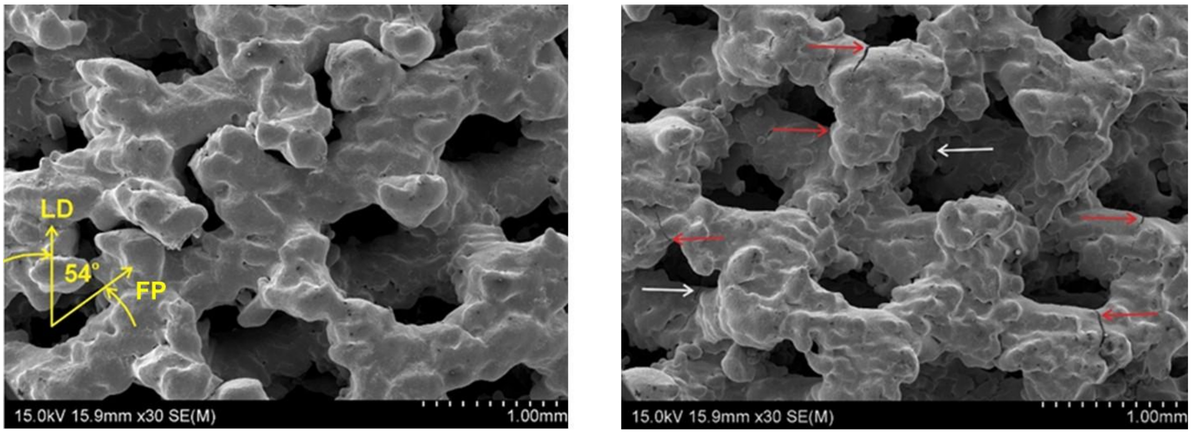

(a) (b)

Fig. 5.12 SEM images of [111]//LD samples: (a) quasi-static tested and (b) cyclically tested at 50MPa (m=92%)

5.3.2. Crack Initiation and Growth Observed inside the Struts

Further examinations have been conducted by sectioning the fatigue-tested samples to observe the internal crack paths inside the struts. The cross-sectional images of the [001]//LD and [011]//LD samples are shown in Fig. 5.13 and Fig. 5.14, respectively. For [111]//LD samples, sampling could not be done to view the cross-sectioned struts in a metallographic plane normal to FP with LD included in. However, since both the quai-static and fatigue strengths of [011]//LD samples are comparable with those of [111]//LD samples, and the crack initiation sites are similar in these samples, then the examination of sectioned [011]//LD samples is considered sufficient for revealing the internal crack paths. No cracks are found away from the FPs in the quasi-static tested [001]//LD and [011]//LD samples at the cross-sectional surface of each sample. For fatigue-tested [001]//LD sample, microcracks are observed even though the tested sample was not fully fractured or collapsed.

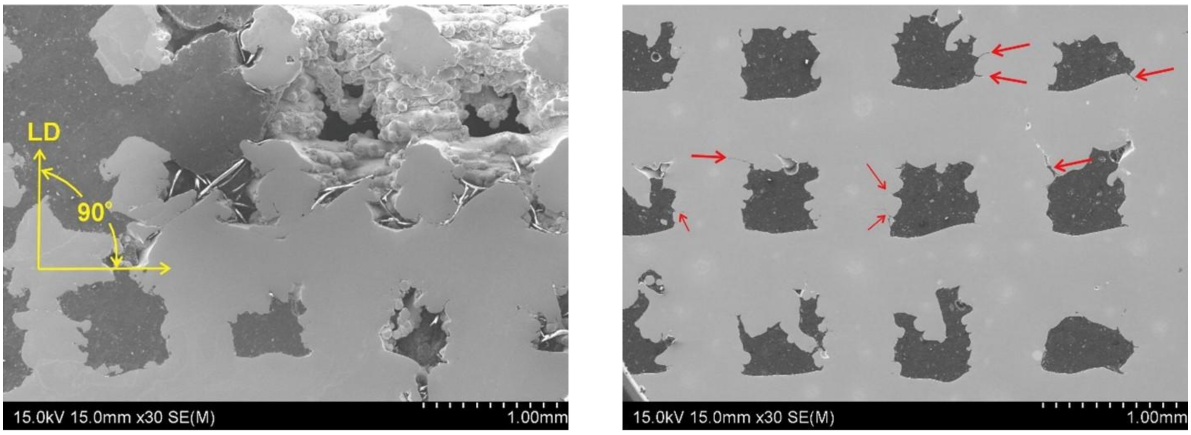

(a) (b)

Fig. 5.13 Cross-sectional images of [001]//LD samples: (a) quasi-static tested and (b) fatigue tested at 210MPa with micro-cracks pointed by red arrows

At the cross-section surfaces of the fatigue tested [011]//LD samples, the crack initiation sites at the top and bottom nodes and the crack paths can be clearly seen in Fig. 5.14(b)–(c) under varied stress level with $\sigma_{\max}$=70MPa ($N \approx 10^4$) and $\sigma_{\max}$=35MPa ($N \approx 10^6$), respectively. The red arrows in the images indicate the crack tips, showing each crack exhibiting deviation in its growth direction. As seen in Fig. 5.14(c), the initiated crack at location T of Cell 1 grows towards location L of Cell 2, rather than propagates upwards through the node to Cell 5. This behaviour is considered reasonable, since a node is relatively much thicker than a strut. As the cracks propagating in the deviated direction, each crack grows through a strut on the side surface to the next cell in an angle of 45°. The T cracks propagated sequentially following the order Cell 1 → Cell 2 → Cell 3 → Cell 4, while the B cracks in Cell 2 and Cell 4 grew toward Cell 1 and Cell 3, respectively. Notably, the B crack in Cell 3 propagated in two directions, growing towards both Cell 2 as well as Cell 6. The growth of the cracks from Cell 1 to Cell 4 leads to a relative movement Δd as indicated in Fig. 5.14(c), once $\sum \Delta d \times \cos 45^\circ$ reaches the tolerance limit, the test is terminated. Increasing m value allows a higher Δd and when m value is sufficient high, the sample fractures completely into two separate pieces. Then the FP is through the node in each cell along a (001) plane.

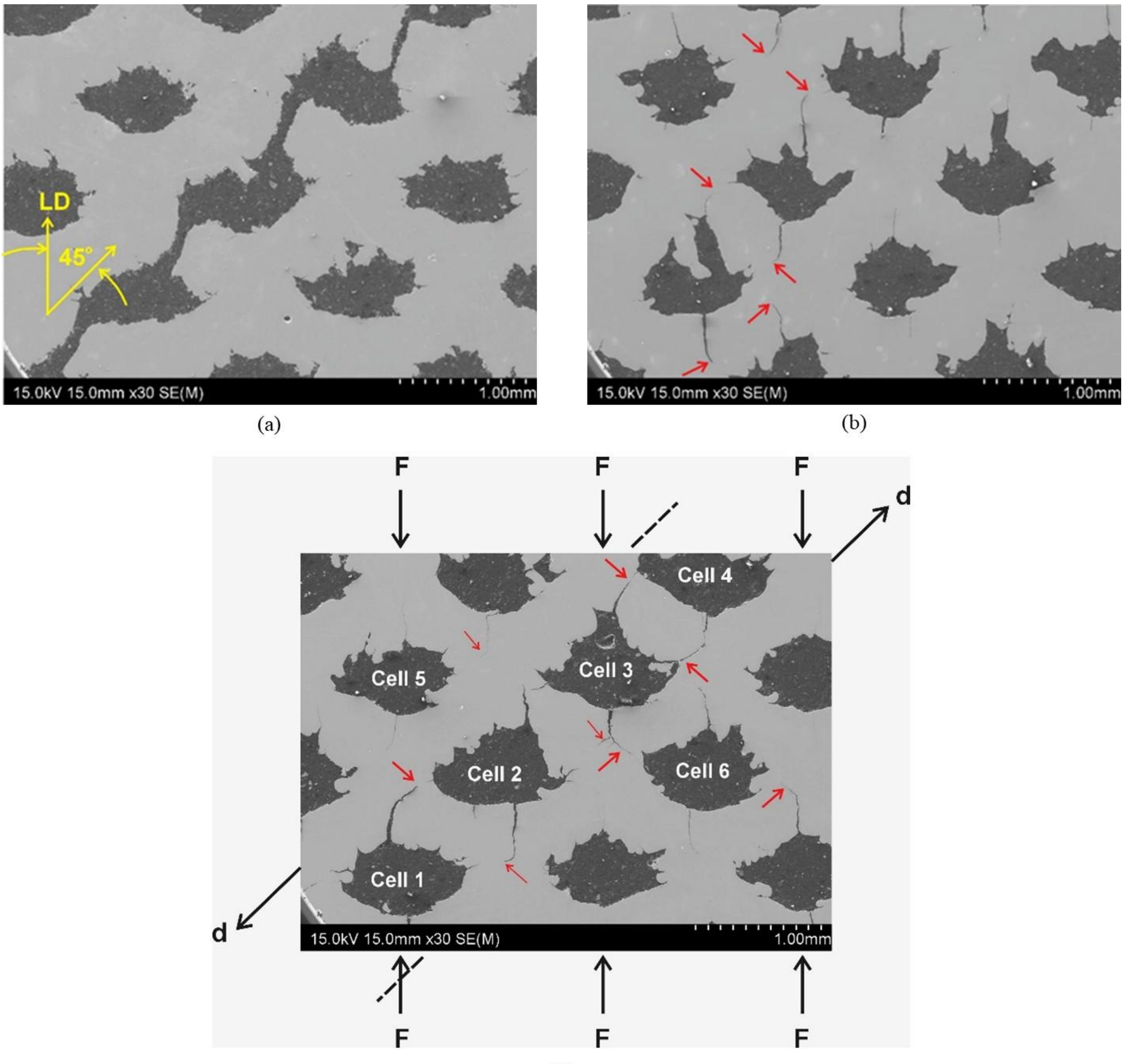

(a)

(b)

(c)

Fig. 5.14 Cross-sectional images of [011]//LD samples: (a) quasi-static tested sample showing no micro-cracks distant to the main crack path, (b) fatigue-tested at 70MPa and (c) fatigue-tested at 35 MPa, the LD and possible shear displacement are indicated. Note: micro-cracks pointed by the red arrows in (b) and (c)

The fracture surface of a completely fractured [011]//LD fatigue-tested sample has been examined and the SEM fractography images are presented in Fig. 5.15. At the viewing direction which is normal to the FP(100), where the unit cells appear to be square on the fractured surface. The planar fracture has been resulted by the fracture of all the nodes on or near that plane. As can be seen in the high-magnification images, the appearance of Node 1 and Node 2 are similar, consisting of two sections, indicating two-stage failure. The higher-magnification images of Location a and Location b at Node 1 are also presented. At Location a, the apparently flat planar crack suggests that the crack propagated smoothly in a single direction until reaching Location b, where the crack growth direction subsequently changed. This change in crack growth direction observed is consistent with the findings summarised from the cross-sectional images of the sample. Extra-higher-magnification images taken at Location a and b indicates that Location a is the crack initiation site. The red dotted line in the lower-left image represents the crack initiation front, suggesting a predominantly brittle fracture model with minimal shear dimple formation. Subsequently, the crack propagated to Location b, where the stage transmission occurred. The boundary between the two stages is indicates by the white dotted line in the lower-right image. Beyond this boundary and following the change in crack-growth direction, the fracture surface exhibits ductile characteristics with the presence of shear dimples. It is suggested that fatigue crack growth proceeded predominantly in Stage I and sudden fracture occurred in stage II. In stage II, once the remaining unfractured load-bearing area in the struts adjacent to the node after Stage I can no longer support the applied stress σ_{max}, rapid fracture of the strut occurs.

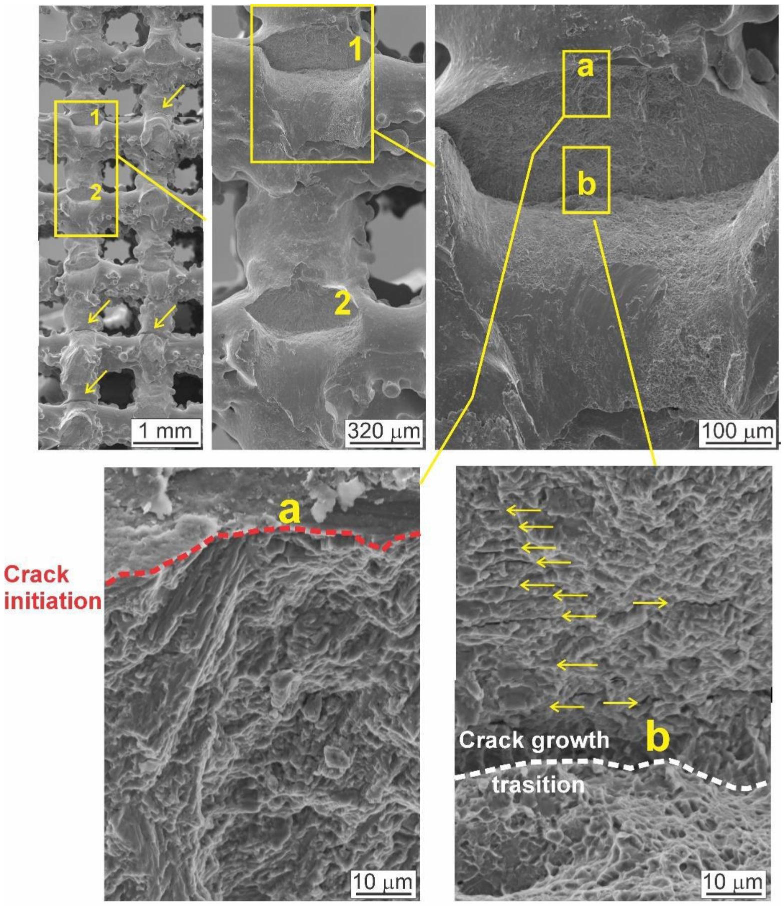

Fig. 5.15 SEM fractography of the fatigue tested sample [011]//LD sample shown in Fig. 5.9 (b) with viewing direction normal to FP(100), the arrows point to the micro cracks and the crack initiation front and the crack growth transition front are illustrated by the dashed curves

To understand the sensitivity of location to crack initiation, the stress distributions are estimated by FEA models using as-designed nominal geometries. As discussed in Section 4.2, although the FEA-predicted localised stress values may deviate from those in the as-fabricated geometries, the simulations remain highly robust for evaluating macroscopic mechanical behaviour and global stress distribution patterns. To reduce the computational cost and eliminate the effects of trimmed free struts at the boundaries as discussed in Section 4.2, 3×3×3-cell structures were modelled for the analysis. In the FEA models, the corresponding stress $\sigma_{\max}$ for $N=10^6$ has been applied to the lattice to identify the high-tension concentrated locations for the understanding of crack-initiation conditions. The corresponding applied stress values for [001]//LD, [011]//LD and [111]//LD lattices are 200MPa, 35 MPa and 35 MPa, respectively. The stress distributions of both σ_1 and σ_3 are presented in Fig. 5.16. For the three groups of specimens under the loading of $\sigma_{\max}(N = 10^6)$, high tensile stress (>500MPa) concentrated at the upper and lower corner of each cell in the [011]//LD and [111]//LD specimens.

At 10^6 cycles, the values of $\sigma_{\max}$ are close to the fatigue limits for HCF. As understood in literature[258], stress concentration factor is considered as the primary determinant for crack initiation under cyclic loading and the fatigue limit defined the stress threshold below which crack initiation at the notch root does not occur. The nodal locations of the lattices can be effectively considered as notches, thus the highly concentrated σ_1 at the bottom and top corners of each cell in [011]//LD and [111]//LD lattices has resulted in well-initiated cracks at the corners after 10^6 cycles at a stress level of σ_{max}=35MPa (approximately 50%–60% of σ_{y-L}). For [001]//LD specimen, even under σ_{max}=200MPa (>$\sigma_{y-L[001]}$), the maximum magnitude of positive σ_1 only has only reached about 500MPa, thus the effect of compressive cyclic loading on the fatigue strength of [001]//LD specimen is limited.

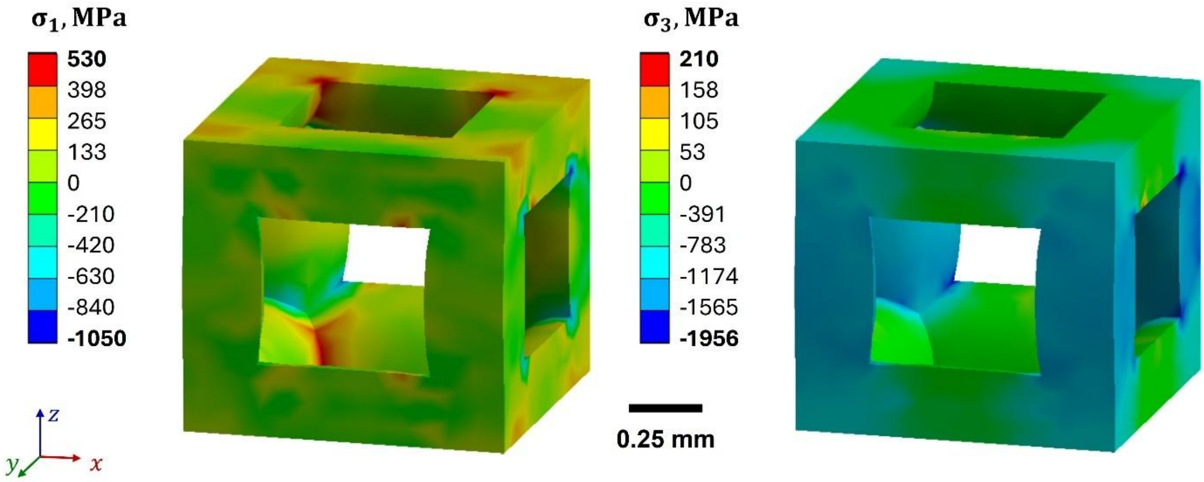

(a)

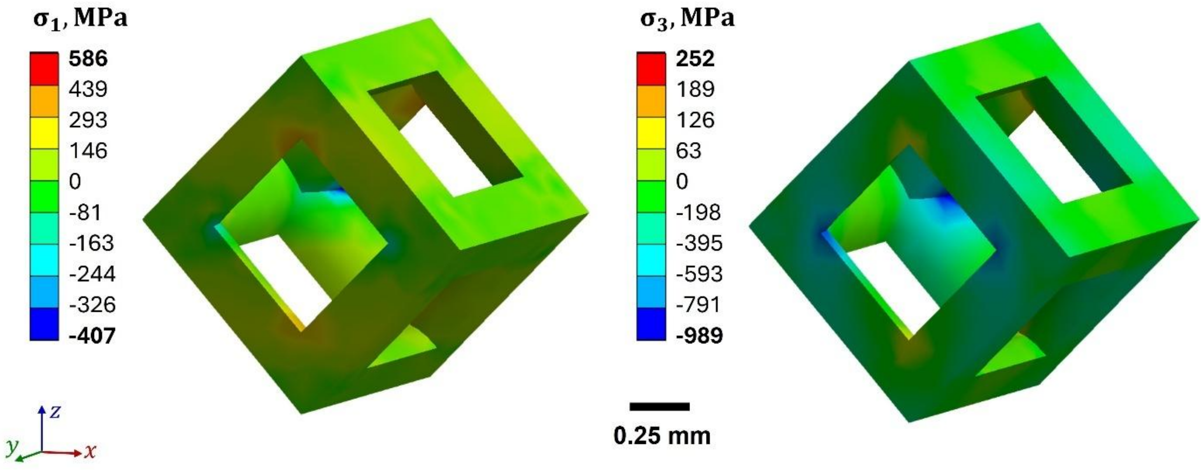

(b)

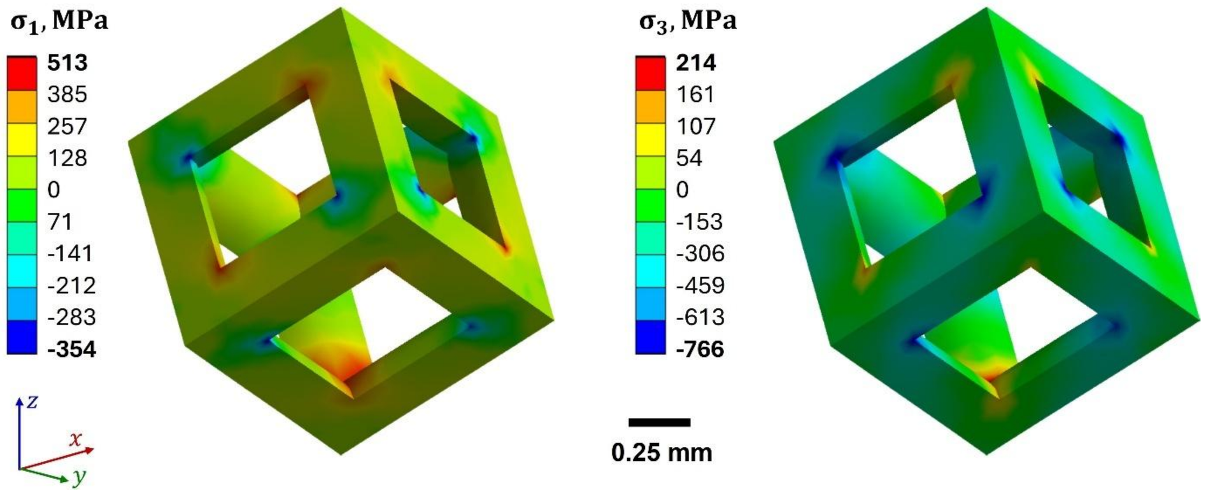

(c)

Fig. 5.16 Stress distribution of maximum- σ_1 and minimum principal stress σ_3 for (a) [001]//LD, (b) [011]//LD and (c) [111]//LD lattice structures under the applied stress level corresponding to the fatigue stress level σ_{max} at N=10^6 cycles obtained from the 3×3×3-cell FEA models

5.4. Further Discussion on the Fatigue Strength of PBF Lattices

Comparing to the data of all the non-SC lattices plotted in Fig. 2.21, SC lattices demonstrated generally higher fatigue strength values, even though the available data is limited and highly scattered. The role of crack initiation locations in the fatigue strength of PBF lattices identified in previous sections can be used to explain the literature data presented in Fig. 2.21. Therefore, S-N data along with the quasi-static UCS_L values of PBF lattices ($0.3< \bar{\rho} <0.4$) are plotted in Fig. 5.17. A single trend line has been fitted for [011]//LD and [111]//LD SC lattices in the present research since both the fatigue strengths and UCS_L values of these two orientated lattices are comparable. Compared to all the other fatigue strength values reported in literature, the fatigue strengths values obtained in this research are significantly higher within the given range of $\bar{\rho}$.

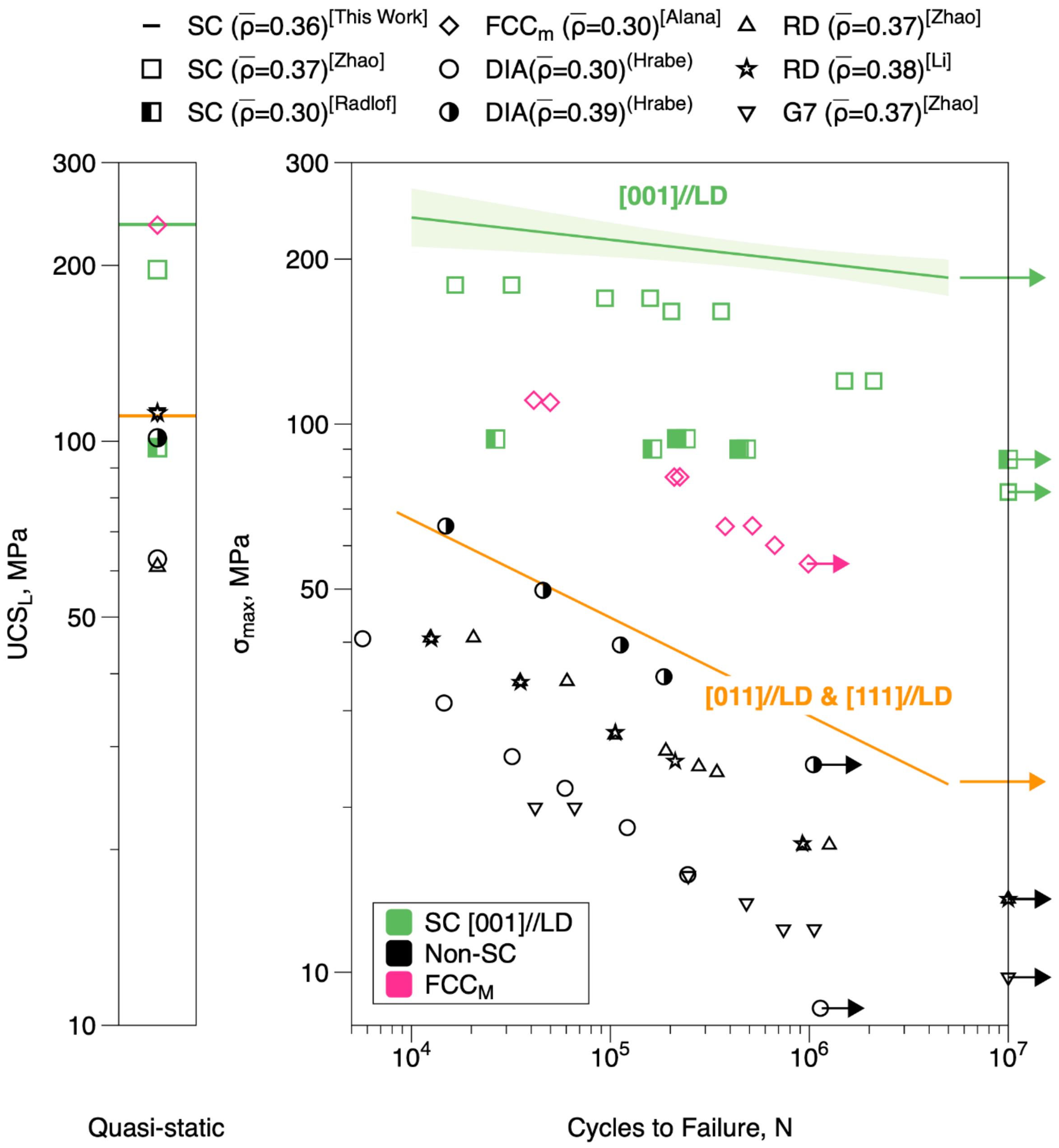

Fig. 5.17 Compression-compression fatigue (R=10) data. SN curves show the fatigue data obtained in this work versus values collected from the literature, alongside the UCS$_L$ data for various lattice structures.

For [001]//LD SC samples, compared to the data obtained in this research, the lower strength values reported by Zhao et al.[59] and Radlof[180] are attributed to the deviation between the designed and measured relative densities. The stated $\bar{\rho}$=36.8% was measured from the as-built samples in Zhao et al's work[59]. From the reported design strut size (0.5mm) and cell size (1.43mm) measured from the provided images, the calculated designed relative density of their SC lattice is 28%, notably lower than that used in this research ($\bar{\rho}$=35%). The properties of the [011]//LD SC lattice reported by Radlof et al.[180] were based on a stated $\bar{\rho}$ of 30%. However, based on the given strut size of 0.6mm and a cell size of 1.2mm, the nominal designed $\bar{\rho}$ is calculated to be 26%, which is lower than the stated value of 30%

and slightly lower than the value used by Zhao et al.[59]. However, the reason for the notably lower quasi-static strength and fatigue strength values across the high-cycle range, for similar $\bar{\rho}$, reported by Radlof et al.[180] compared with those reported by Zhao et al[59], remains unclear.

All the non-SC structures expect for FCCm lattices in literature exhibited lower quai-static and fatigue strengths than those of the non-[001]//LD lattices in this research. For these non-SC structures, it is suggested that the presence of inclined struts introduces localised stress concentrations, even at low $\sigma_{\max}$. Thus, considering the effects of stress concentration on fatigue strength, the load-bearing mechanism in these non-SC lattices may be similar to that observed in non-[001]//LD SC structures. The influence of relative density on the fatigue strength can also be observed in Fig. 5.17, where the strength values for $\bar{\rho}$=40% reported by Hrabe et al.[23] are comparable to those obtained in this research and significantly higher than the values for lattices with $\bar{\rho}$=30%.

Alaña et al.[95] has designed the FCCm lattices to avoid the manufacturing problems associated with fabricating horizontal struts. The FCCm lattices exhibited higher strength values than other non-SC structures. As illustrated in Alaña et al.'s work, all struts in each cell support the load in an angle of 45° with respect to LD with four struts joining at a single node. In this research, as illustrated in Fig. 3.1, 4 out of 12 struts in a [001]//LD cell effectively support the load parallel to LD. In each [011]//LD and [111]//LD SC cell, 8 struts orientated at 45° to LD and 12 oriented at 54.7° to LD, respectively, effectively contributed to load supporting. In addition, the FEA predicted yield strength $\sigma_{y-\mathrm{FCCm}}$ is 175MPa of FCCm lattice for $\bar{\rho} = 30\%$, which is comparable to the values of $\sigma_{y[001]}$=172MPa predicted for [001]//LD lattices in 4.1.1. However, as shown in Fig. 5.17, the fatigue strength of FCCm lattice drops steeply with increasing fatigue cycle number. It can be attributed the stress concentration at the T and B locations within the FCCm cells, which is favourable for crack initiation and consequently resulted in the rapid decreased in $\sigma_{\max}$ under cyclic loading.

The observed location-dependent crack initiation cites also indicated the effect of surface quality of EBPBF parts on fatigue limits. The cross-section samples shown in Fig. 5.13 and Fig. 5.14 have been presented with building direction (BD) pointing upwards, thus the bottom surfaces or nodes shown in the figures are the upper skin surfaces during the EBPBF process. Then it can be seen that the upper skin surfaces are considerably smoother than the other side surfaces. Since the side surfaces contain partially melted powder whereas the upper skin surfaces are the solidified surfaces and are free of powder particles. While the high roughness of side surfaces in PBF parts is known to affect the fatigue strength, the evidence shown in Fig. 5.11(b), Fig. 5.12(b) and Fig. 5.14(b)–(c) has demonstrated that the crack initiation cites are primarily T and B locations within cells, with the B locations are observed to be as readily as the T locations for fatigue crack initiation. This suggests that stress concentration is the dominant factor affecting the fatigue strength of lattice structures, while the surface roughness only exhibit limited effects.

6. Fatigue Performance of the EBPBF Stems

Following on the understanding of the orientation-dependant static and fatigue behaviours of the lattice structures discussed in the last two chapters, an attempt has been made to investigate the fatigue behaviour of the porous femoral stems in this chapter. A preliminary study on femoral stem design included the selection of optimal UCO used in the design of fully porous (FP) stem along with the FEA models and experimental testing. The experimental and FEA results have indicated the low fatigue life of the fully porous stems. Thus, the stem was then subsequently re-designed and modified through the incorporation of topological optimisation, providing a solid reinforcement while maintaining a highly porous structure. In the final stem design, surface lattice portion was increased ensuring a fully porous surface to promote bone ingrowth, and four stem specimens were fabricated using EBPBF. The four EBPBF built specimens were fatigue tested. Two specimens failed without reaching the target fatigue life of 5×10^6 cycles as specified in IOS 7206-4, while another two achieved fatigue life well beyond the required life. Fractography examination has been conducted on the failed specimens. For the run-out samples, a detailed assessment was performed using X-ray micro-CT analysis coupled with K-T diagram analysis, revealing the dependence of fatigue life on the presence of lack of fusion (LoF) defects. Finally, the synthesis of findings and analysis from this work will be utilised to discuss and explain the approach required for the design, manufacturing and quality check of highly porous EBPBF femoral stems to ensure the compliance with the relevant international standards.

6.1. Results of the Preliminary Study on Porous Femoral Stem Design

6.1.1. Optimised UCO

As presented in Fig. 6.1, the FEA results suggested that stress concentration was observed near the potting level, with the highest stress values located in the medial region. It can also be observed that, the medial region was predominantly subjected to compression, indicating a higher concentration of σ_3, while the lateral region experienced tension, reflecting by the elevated σ_1 values. The observed distribution of tensile and compressive stresses was consistent with the findings reported in literature[217]. As discussed in Chapter 5, [001]//LD SC lattices exhibited highest compression-compression fatigue strength comparing with other non-[001]//LD samples. To maximise the load-bearing ability of [001]//LD lattices under compression, the optimal UCO was then determined using multi-objective genetic algorithm (MOGA) for response surface (RS) optimisation as described in 3.4.3. under the configurations illustrated in Fig. 3.8, the vector principal stresses in the compression concentrated region with $\sigma_3 < -100\text{MPa}$ was extracted, the vectors of the principal axes of σ_3 were computed using a Python code. Then the computed vector map was imported into nTop for visualisation. As illustrated in Fig. 6.2, the angles θ_y between the axes of σ_3 and the loading direction were in the range approximately between 0° and 13°, which was then defined as the designed range of θ_y for the UCO optimisation.

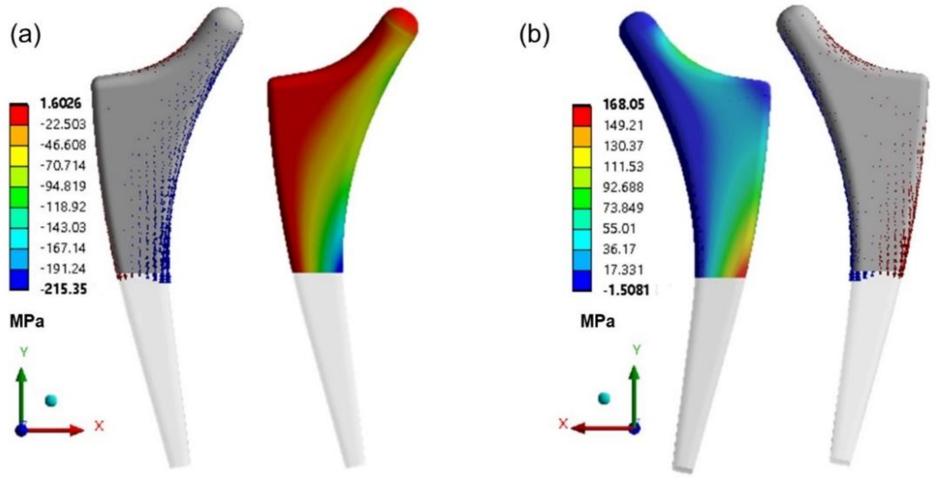

Fig. 6.1 Principal stress distribution in the unpotted region of the solid stem: (a) minimum principal stress σ_3 (b) maximum principal stress σ_1

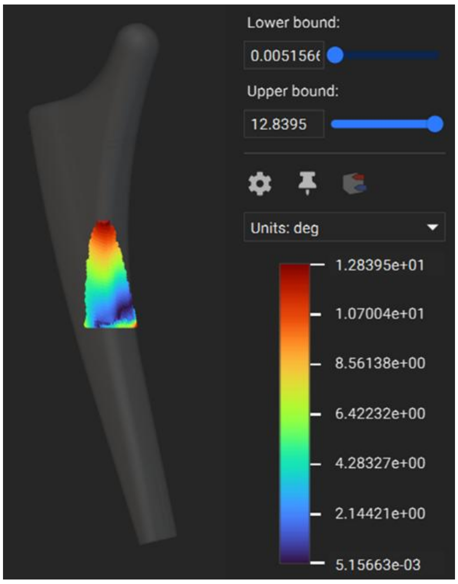
Lower bound: 0.005156(

Upper bound: 12.8395

Units: deg

Fig. 6.2 Point map illustrates the distribution of θ_y within the region where $\sigma_3 <$ -100 MPa in the unpotted region of the solid stem

The design of experiment (DOE) matrix and the 2D response plots are shown in Table. 6.1 and Fig. 6.3, respectively, based on the FEA model under the loading configurations as shown in Fig. 3.8. The higher P_c suggested that a greater number of struts are under compression with negative stress magnitude. The lower P_b indicated that fewer load-bearing struts were subjected to bending moments higher than 20N · m. Moreover, as discussed in Chapter 4, [001]//LD lattice exhibited higher E_L than non-[001]//LD lattices. As suggested by the 2D response results, there is a trade-off between the output objective parameters. More clearly, it can be found from Fig. 6.4, the objective of maximisation of P_c and δL_y is compete with the aim of minimising P_b. Thus, the MOGA was applied to obtain the suitable value of θ with optimal overall performance. Three candidate points with similar performance listed in Table. 6.2 were selected MOGA and the validation was carried out by the FEA tool ANSYS Mechanical. By taking consideration of all the output objective parameters, $\theta = 7.7°$ has been selected as the optimal UCO. As both minimal $|\delta L_y|$ and lowest P_b were obtained at this UCO.

Table. 6.1 Design points for UCO optimisation

Design Points	θ, º	P_c,%	P_b,%	δL_y, mm
1	-6.5	0.492	0.219	-1.2439
2	-1.3	0.541	0.248	-1.1659
3	-3.9	0.523	0.249	-1.326
4	-9.1	0.470	0.212	-1.246
5	-11.7	0.457	0.227	-1.3549
6	-7.8	0.482	0.223	-1.2948
7	-5.2	0.515	0.232	-1.2815

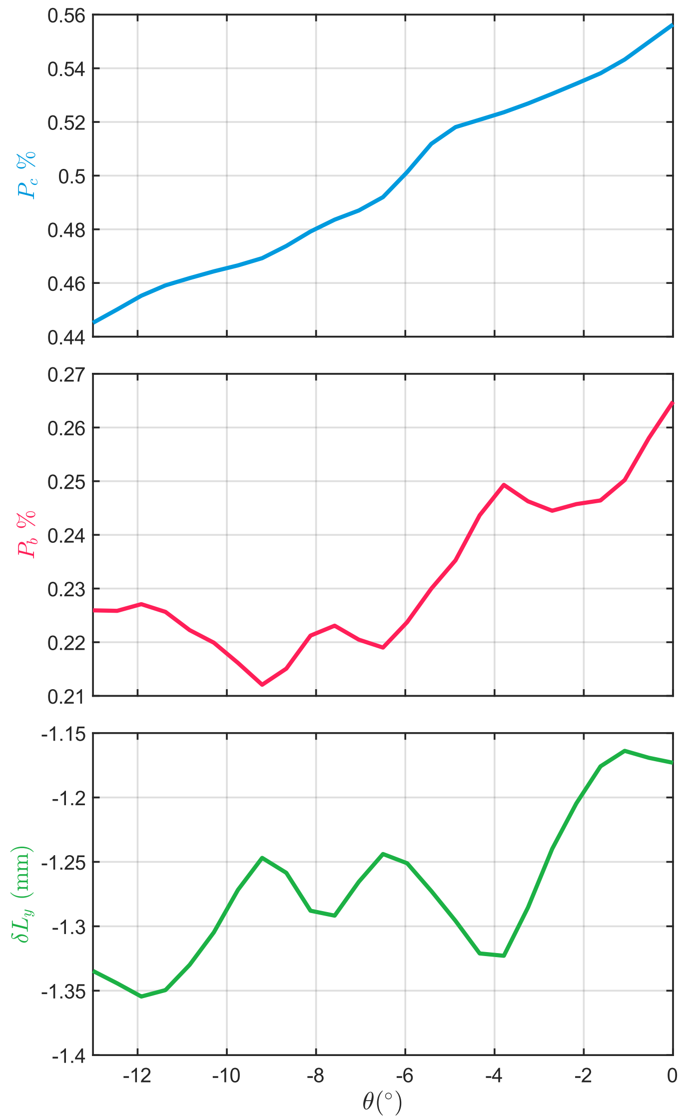

Fig. 6.3 Response plots illustrating the effect of θ on the objective parameters including P_c, P_b and δL_y

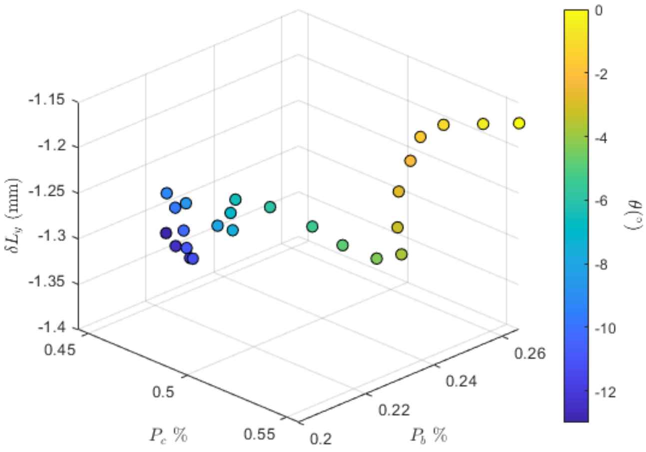

Fig. 6.4 3D trade-off plots between the input variable θ and the output objective parameters (P_c, P_b and δL_y)

Table. 6.2 Candidate design points selected by MOGA with FEA verified results

Candidate Points	θ, °	P_c,%	P_b,%	δL_y, mm
1	-5.9	0.504	0.215	-1.2171
2	-6.7	0.492	0.211	-1.2033
3	-7.7	0.487	0.200	-1.1764

6.1.2. Verification of the Simplified Test Configuration

FEA models have been created under ASTM F2996-13 and simplified configurations as shown in Fig. 3.8 and Fig. 3.11 with applied force of 2300N, respectively. The stress distributions in the designed RoI under the two configurations are shown in Fig. 6.5. The comparison of the two configurations revealed minor differences in localised stress concentrations. The simplified configuration resulted in a slightly lowered maximum σ_1 value of 4 MPa, dropping from 152MPa to 148Mpa at the lateral side and increased maximum value of σ_{VM} of 58 MPa from 211MPa to 269MPa at the medial side. However, these stress variations were only found to be in small local regions, and the overall stress distribution remained largely unchanged. Specifically, for the lateral hot-spot, a variation of only 3% in the peak stress values of σ_1 was obtained. Given the minimal impact on the global stress distribution, the simplified configuration was considered as a valid and acceptable representation for the purpose of this preliminary study.

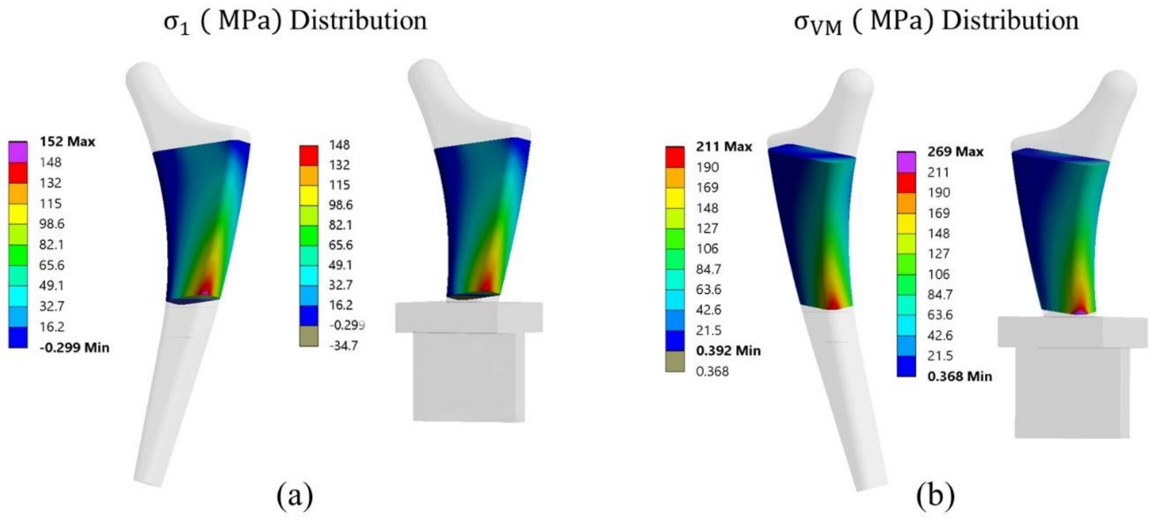

Fig. 6.5 Comparison of the stress distribution of (a) maximum principal stress and (b) Von-mises stress on the designed porous region of the stem under ASTM and simplified configurations

6.1.3. Fatigue Behaviour of the Fully Porous Stem with Optimised UCO

The femoral stem specimens with simplified configuration have been built using EBPBF as shown in Fig. 6.6. The design of the FP stem consists of a close-cell SC shell and an open-cell SC lattice with optimised UCO. The EBPBF fabricated samples were tested under the loading conditions specified in ISO 7206-4 configurations, the peak-peak displacement vs cycle curves are presented in Fig. 6.7(a).

The specimens exhibited a fatigue life of only approximately 1×10^5 cycles, which is less than 2% of the required 5×10^6 cycles as specified in the international standard.

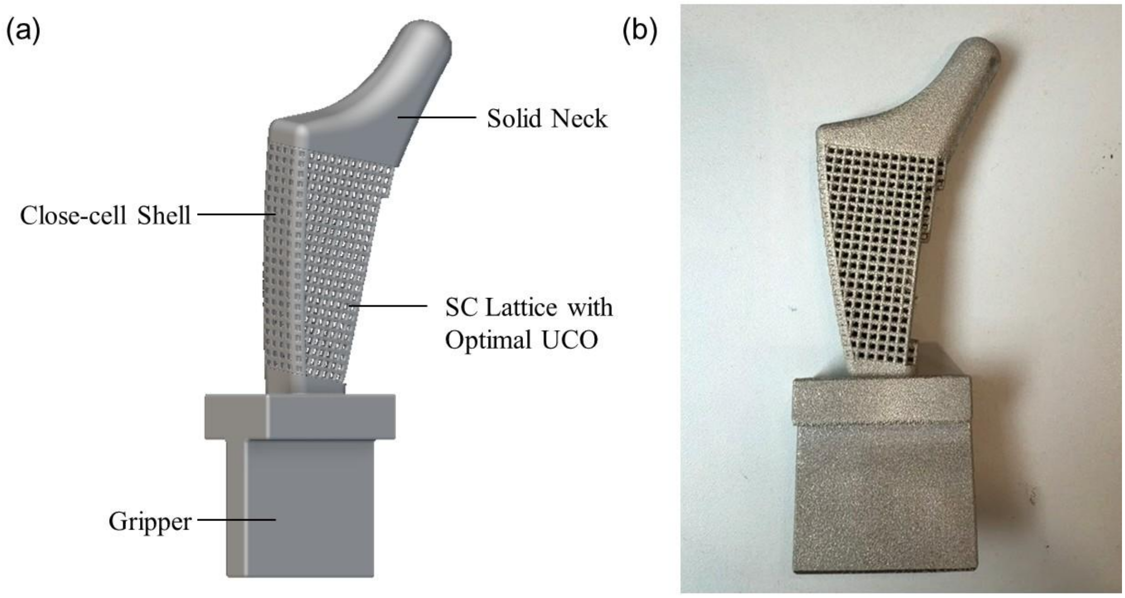

Fig. 6.6 (a) CAD designed and (b) EBPBF fabricated FP stem specimen

As shown in Fig. 6.8, the fatigue fracture occurred at the tension concentrated area while no obvious damage was observed in the compression site. Compared to the fatigue life of porous stems reported in published works[217,240], this SC-cell-based porous stem here demonstrates approximately 80% shorter fatigue life. The shorter N_f of the proposed porous stem could be attributed to several key differences in the design and geometry of the stem. The proposed porous stem exhibited significant longer stem length L_A, up to 15% greater than those in the published works and lower the porosity level at the fracture surface ($\overline{P}_{fs} \leq 25\%$ in the published works[217,240]).

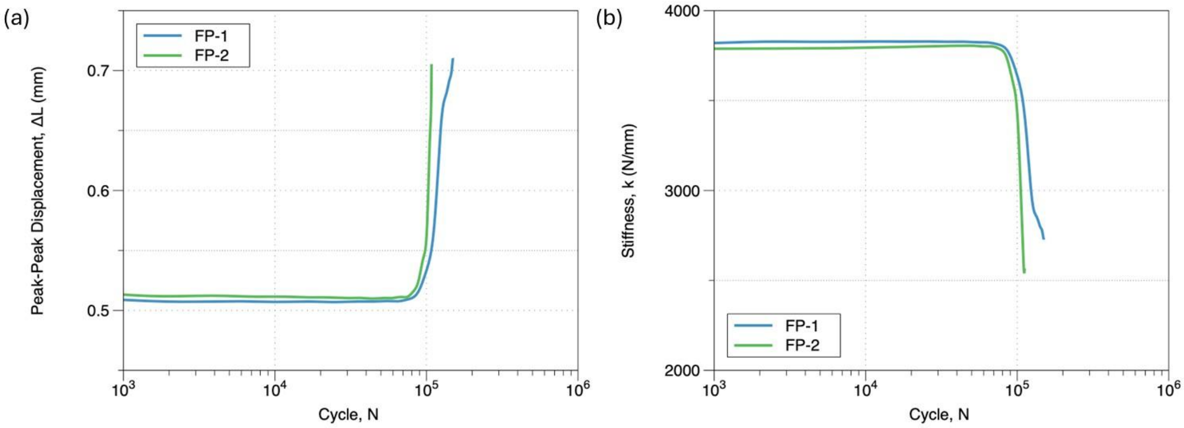

Fig. 6.7 Fatigue tests results of the fully porous design (a) Peak-Peak displacement and (b) stiffness vs cycles.

(a) (b) (c)

Fig. 6.8 (a-b) the porous femoral stem specimen during the fatigue test (c) fractured sample, the white arrow indicates the crack initiation location at the lateral side of the stem.

The FEA estimated stress distribution provides evidence that suggests at the short fatigue life of the F femoral stem. The stress distribution of σ_1 is shown in Fig. 6.9. With a load of 2300N being applied to the FP stem under the simplified configuration, the positive stresses of σ_1 are concentrated within the lateral side, with a maximum value of 866MPa exhibited at the corner of the close-cell shell. Across the medial region, negative values of σ_1 were estimated. The highest value of σ_1 reaches approximately 86% of the yield strength (σ_y=1001MPa) and 44% higher than the endurance limit (σ_N=600 MPa at 10^7 cycles[156]) of the EBPBF Ti6Al4V without defects. The FEA results have suggested that the FP stems are likely far away from suitable and further modifications are then required.

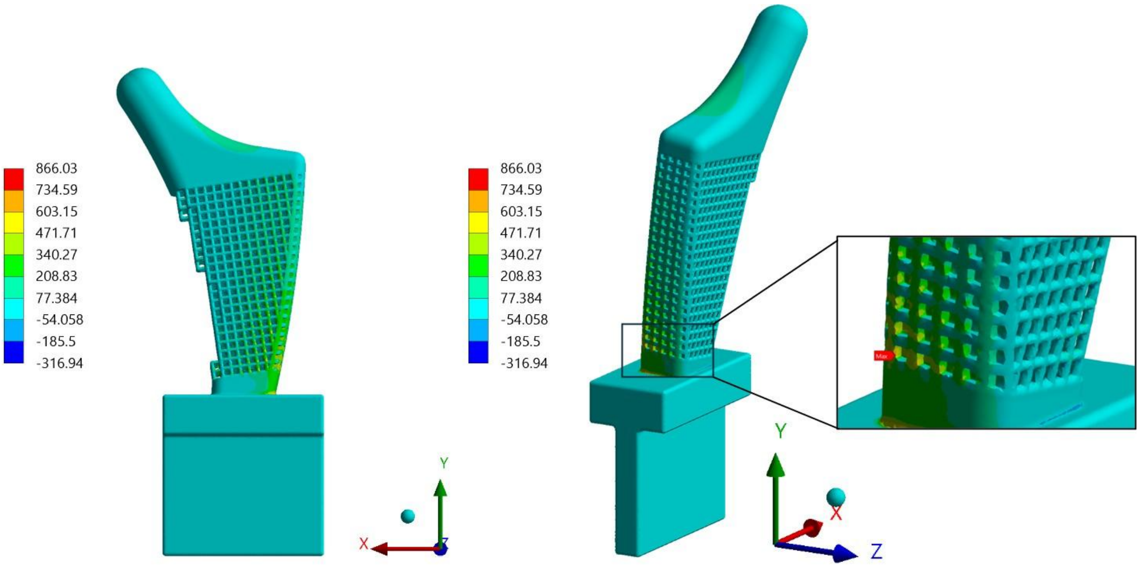

Fig. 6.9 Maximum principal stress σ_1 distribution on the fully porous stem under the simplified configuration with a load of F=2300N

6.2. Fatigue Performance of the Topologically Optimised Porous Stem

The results obtained in Section 6.1 suggested that, the concentrated tension distributed on the close-cell shell led to the fracture of the stem. Therefore, the design of the stem needs to be modified with reinforcement at the tension site. In the literature reviewed in 2.4.4, dense shells have been used in the lateral sides of the lattice as reinforcement. But the fatigue results in literature listed in Table. 2.11 have suggested that even with solid shell at both the lateral and medial sides, the porous femoral stem could still exhibit much lower fatigue life than the required 5×10^6 cycles. Thus, as described below, topological optimisation was conducted to define the region of reinforcement while maintaining sufficient porous volume for sufficient osseointegration features.

6.2.1. Topologically Optimised Solid Core

As described in 3.4.5, the optimisation was carried out in nTop with an objective to minimise the response stress and reduce the volume in the unpotting region by 80%. The design objectives were to reduce the volume of the unpotting region and ensure the maximum stress in the optimised geometry remained below the given threshold. In this case, the stress threshold of 580MPa was selected based on the simulation results obtained in Fig. 5.16. This value indicates the highest σ_1 in the non-[001] lattices under the loading corresponding to the fatigue limit at 1×10^6 cycles. Then the optimisation performed 250 interactions based on the stress distribution following the process described in 3.4.6, created a lightweighted form of the stem with reduced volume of solid core. The resulted geometry of the solid core is shown in Fig. 6.10, the smoothed TOed geometry achieved 72% reduced volume comparing to the dense RoI. Then a Boolean subtraction was applied within the RoI to extract the lattice region while the neck and the distal regions remained solid. The lattice region is illustrated by the translucent green body in Fig. 6.10. After the Boolean subtraction, the solid core within the objective region exhibited 53% reduction when compared against the fully dense version. Subsequently, the lattice with optimised UCO was filled into the extracted region, the final TOed stem achieved 21% lower volume comparing to that of its fully dense counterpart. Based on the optimised geometry, the TOed stem specimens shown in Fig. 6.11 have been fabricated using EBPBF.

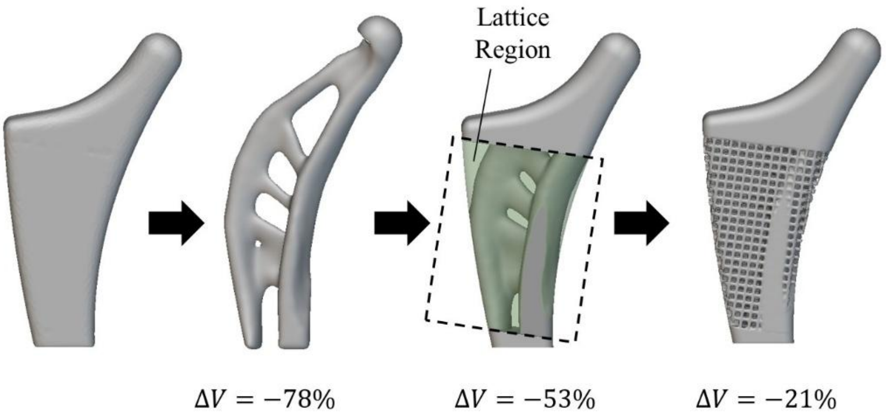

Fig. 6.10 Topology optimisation result showing the volume reduction process from the solid stem to the final TOed stem

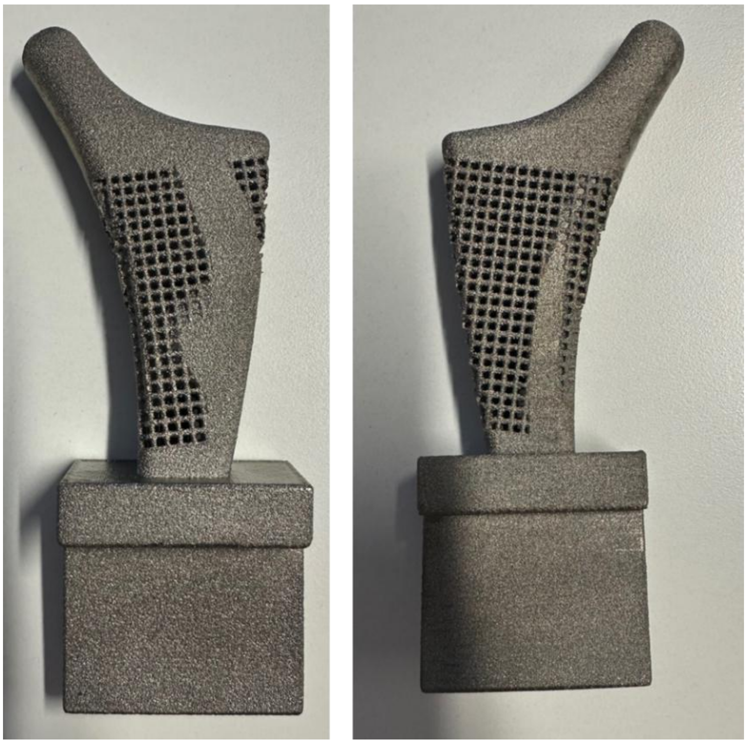

Fig. 6.11 EBPBF built TOed Porous stem

6.2.2. Fatigue Performance the TOed Porous Stem

The fatigue testing results for the TOed porous stem demonstrated an infinite fatigue life, all the tested samples ran out at 10^7 cycles under the simplified configurations with loading conditions as specified in ISO 7206-4. As shown in Fig. 6.12, the displacement curves obtained during fatigue testing indicate that both the peak-peak displacement and effective stiffness of the stem remained unchanged throughout the duration of the test. The fatigue testing results agreed with the findings observed from simulation. The FE simulation estimated stress distribution of σ_1 suggested that the highest σ_1 exhibited in the RoI was only ~238 MPa, indicating that this Toed stem should be able to satisfy the ISO requirements of fatigue limit.

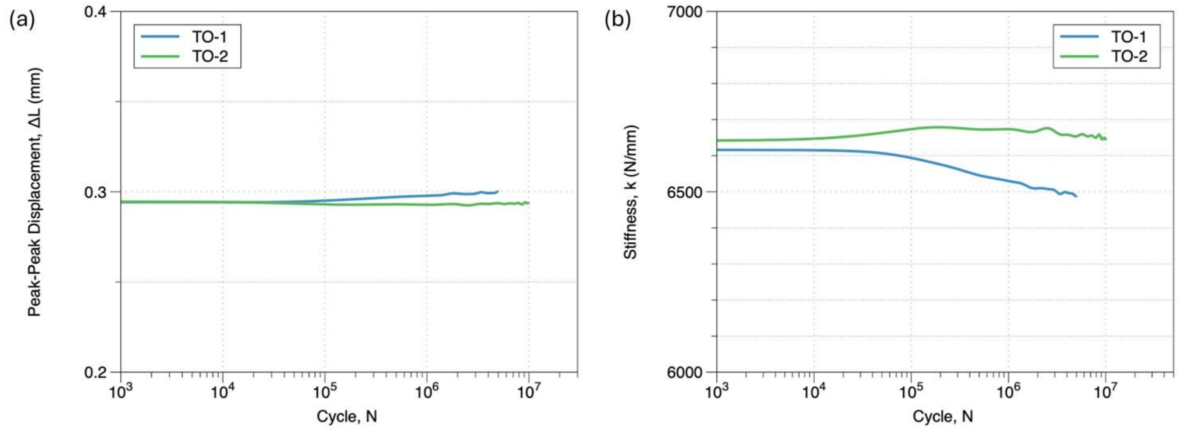

Fig. 6.12 Fatigue testing results of the topologically optimised samples: (a) peak-peak displacement vs cycle curves and (b) stiffness vs cycle curves

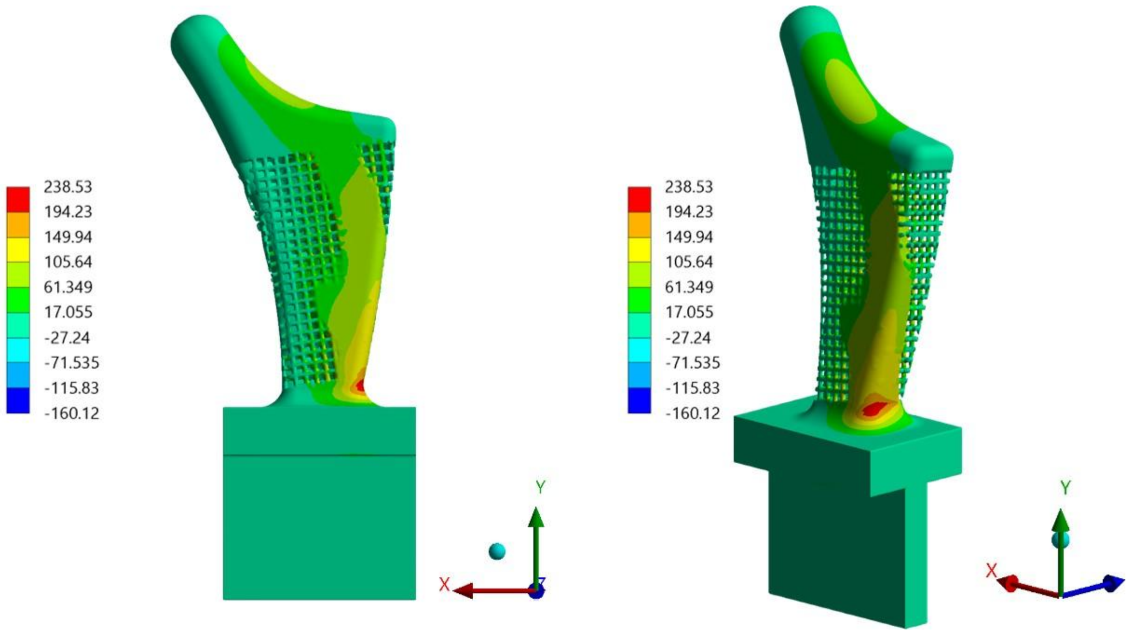

Fig. 6.13 Maximum principal stress σ_1 distribution on the topologically optimised (TOed) stem under the simplified configuration with a load of F=2300N

6.3. Fatigue Performance of the Solid Reinforcement with Lattice Stems

6.3.1. Further Topological Optimisation Results

The successful achievement of an infinite fatigue life in the TOed stem discussed in Section 6.2 indicates a potential for further geometric optimisation with increased surface porosity by employing an additional lattice layer on the surface to enhance bone ingrowth. The further optimisation can be achieved by further increasing surface porosity to provide enhanced bone in-growth properties. Therefore, an additional topological optimisation was conducted to obtain the Solid Reinforcement with

Lattice (SR-L) stem. To enable the inclusion of an extra layer of struts, the design space was decreased in thickness by 0.7 then TO was applied using the same objectives and constrains. The EBPBF fabricated SR-L specimen and the further optimised geometry of the solid core is shown in Fig. 6.14.

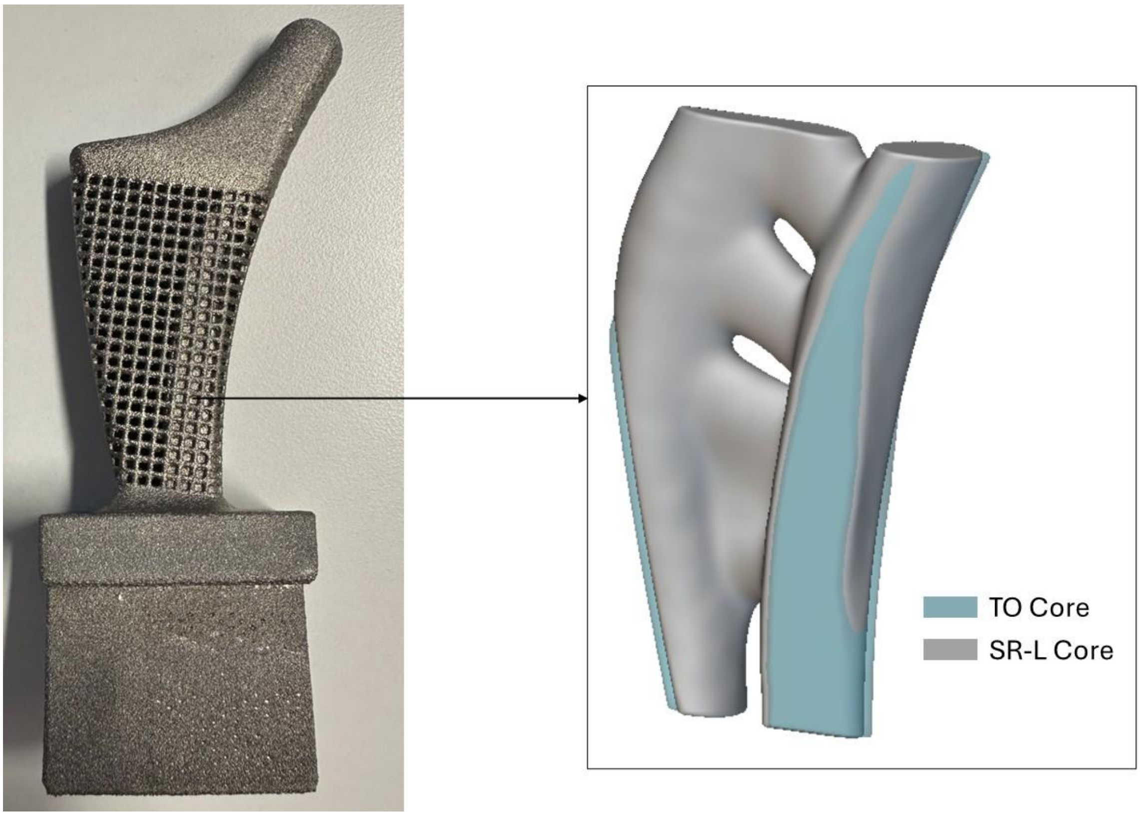

Fig. 6.14 EBPBF SR-L femoral stem with a porous lattice layer on the surface of the solid portion and the comparison between the TO and SR-L solid cores

6.3.2. Fatigue Performance and FEA Predicted Stress Distribution

From two separate batches, a total of four specimens were tested. The fatigue testing results are presented in Fig. 6.15, showing that two of the four tested specimens achieved runout at 10^7 cycles while the other two failed at approximately 1.41×10^6 and 1.78×10^6 cycles. The fatigue lives of the failed stems reached up to 36% of the required 5×10^6 cycles by the international standard. However, the FEA predicted distribution of σ_1 is shown in Fig. 6.16, the maximum value of σ_1 was increased to 434 MPa. The predicated maximum σ_1 is only 72% of the fatigue strength of EBPBF Ti6Al4V parts (approximately 600 MPa at 1×10^7 cycles[156]). Thus, the predicted stress distribution suggested that the designed porous stem should be capable of withstanding the ISO-7206 loading conditions and achieve an infinite fatigue life. To determine the cause of reduced fatigue life of the failed stem specimens, the fracture surfaces have been examined using SEM in the next section.

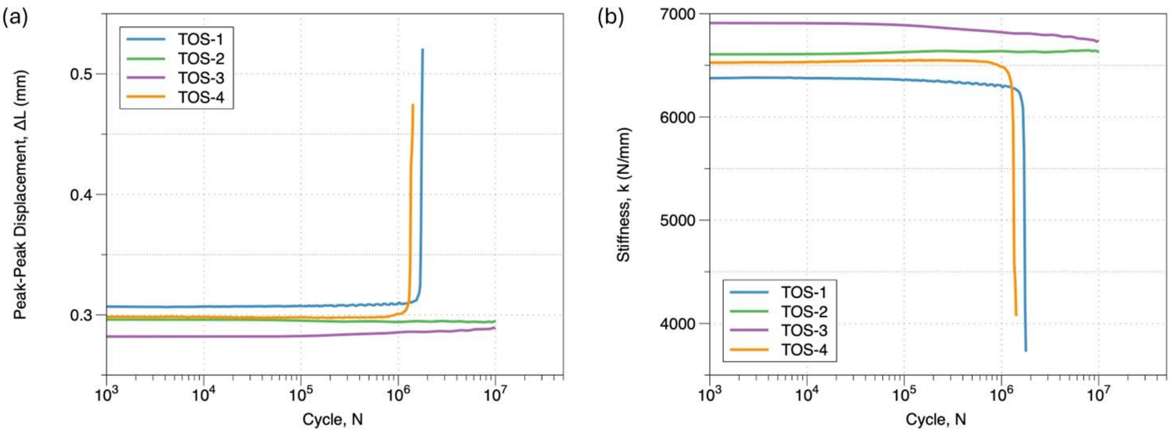

Fig. 6.15 Fatigue testing results of the SR-L stems: (a) peak-peak displacement vs cycle curves and (b) stiffness vs cycle curves

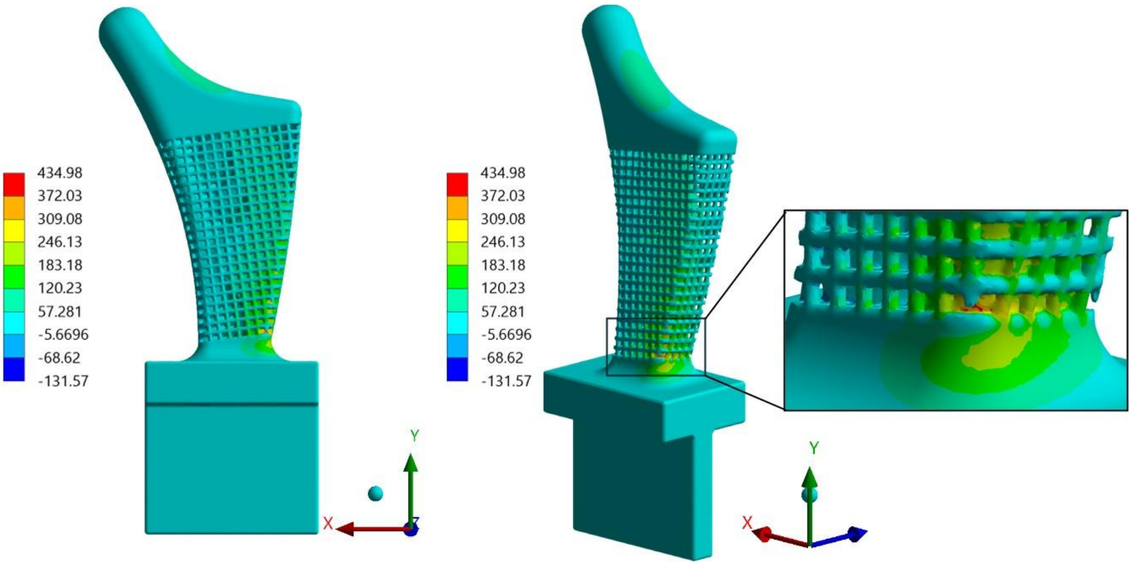

Fig. 6.16 Maximum principal stress σ_1 distribution on SR-L samples under the simplified configuration with a load if F=2300N

6.3.3. Fracture Mechanics Analysis and Kitagawa-Takahashi Diagrams

As shown in Fig. 6.17, the cracks initiated in the failed specimens at the tension concentrated area illustrated in Fig. 6.18 with the high σ_1 values. To identify the reason of the largely variation in fatigue results, the fracture surfaces shown in Fig. 6.17 of the failed samples have been examined under SEM. As presented in Fig. 6.20 , the examination of the fracture surface of the SR-L-1 specimen has revealed that, no large defects are observed at the crack initiation site but a LoF defect is identified at the surface of a strut near the high-tension region. In contrast, a LoF defect were observed in the SR-L-4 at the tension-concentration region. Both of the examined fracture surfaces exhibited identical surface irregularities, a characteristic commonly observed in parts fabricated using the EBPBF process. Even though rough surface and internal defects are observed, the crack initiation sites have been found located from the surface LoF defects in both failed specimens rather than originating from rough surfaces topography or internal defects. This is in agreement with the reviewed findings suggested by Tammas-Williams et al.[191] in 2.3.3.3, it has been widely found in the machined and polished PBF test pieces, the originally internal defects were exposed at the test piece surfaces, the shorter lives were found to be associated with cracks initiated from the pores located near the surface of the test pieces. Thus, surface-exposed LoF defects have been considered as the critical detrimental factor limiting fatigue lives.

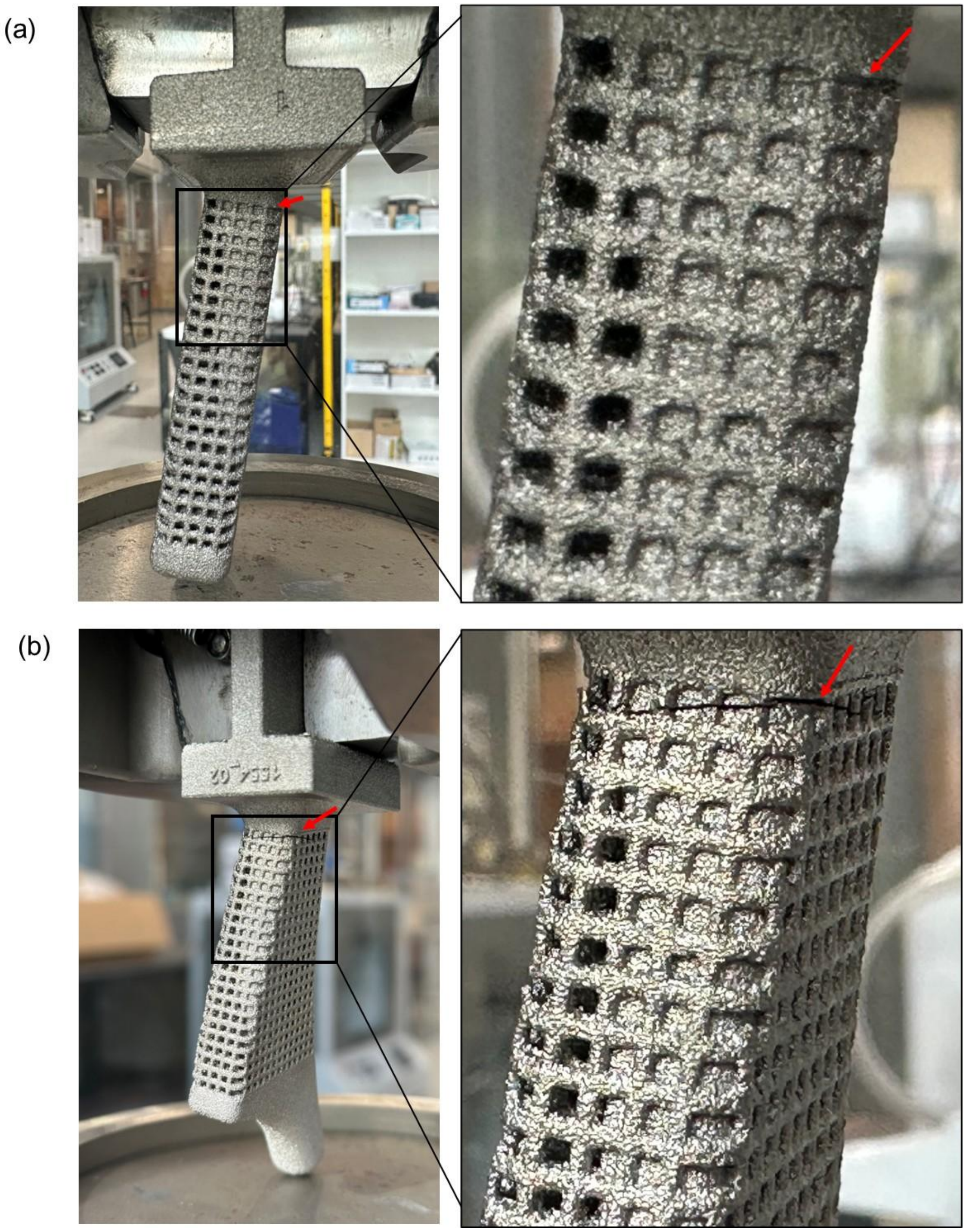

Fig. 6.17 Failed specimens (a) SR-L-1 (b) SR-L-4 during the fatigue tests (the red arrows point to the cracks)

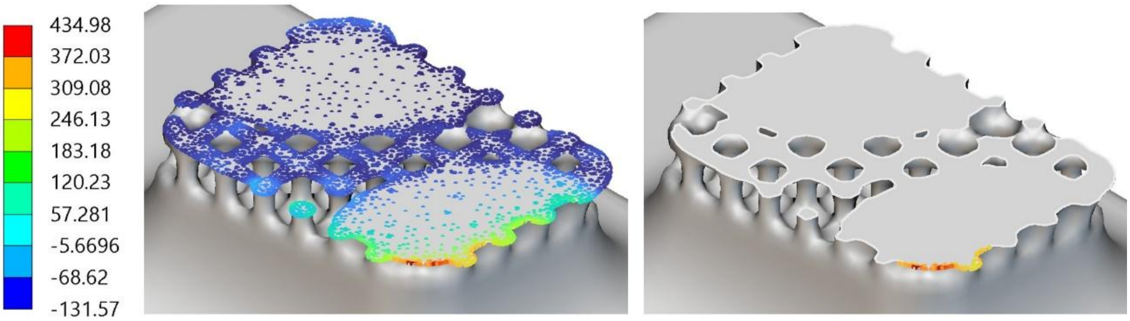

Fig. 6.18 Stress distribution of σ_1 (MPa) on the fracture surface and the region with σ_1>250MPa

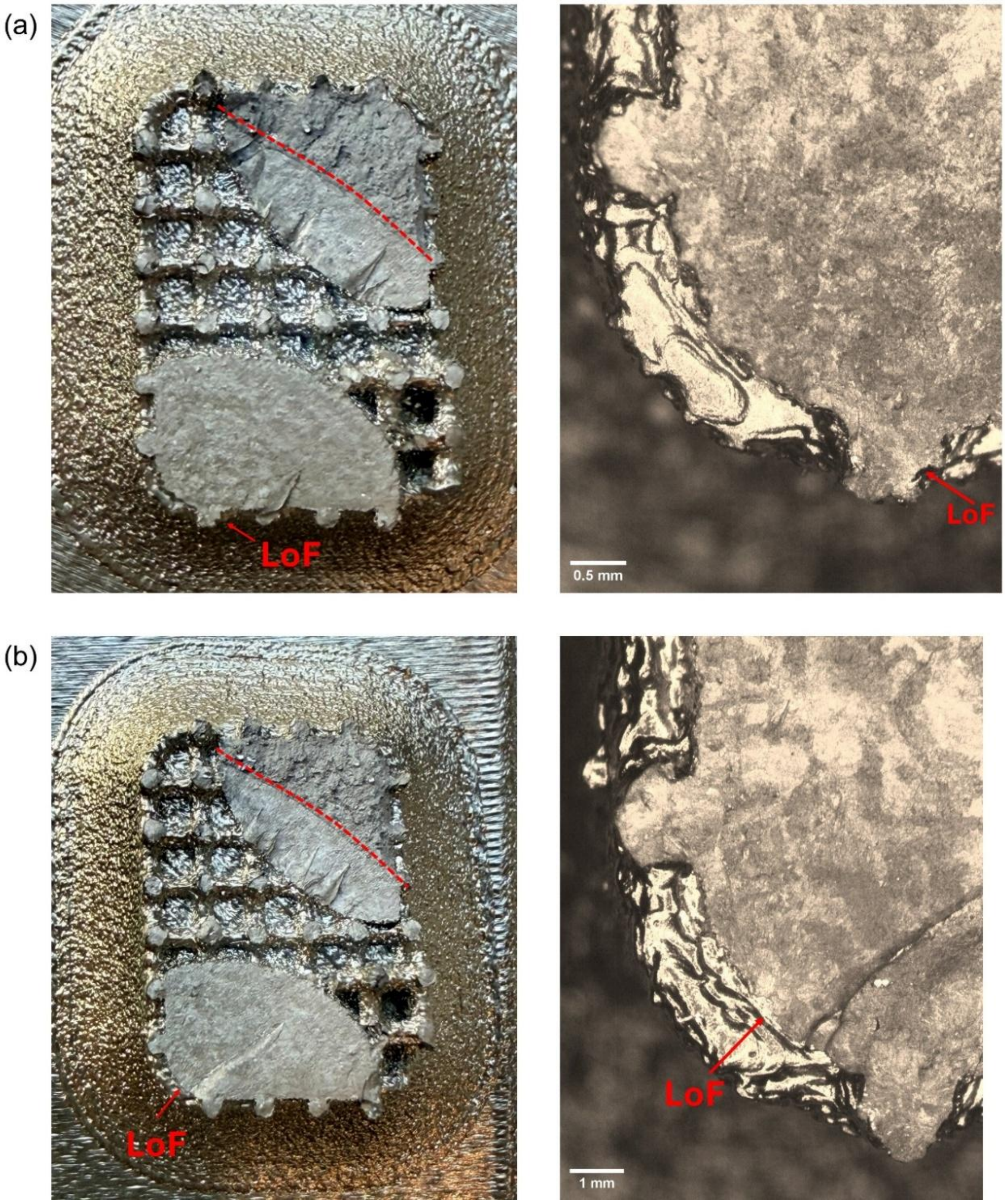

Fig. 6.19 Fracture surface of the failed stem specimens: (a) SR-L-1 and (b)SR-L-4, the LoF defects are pointed by red arrows

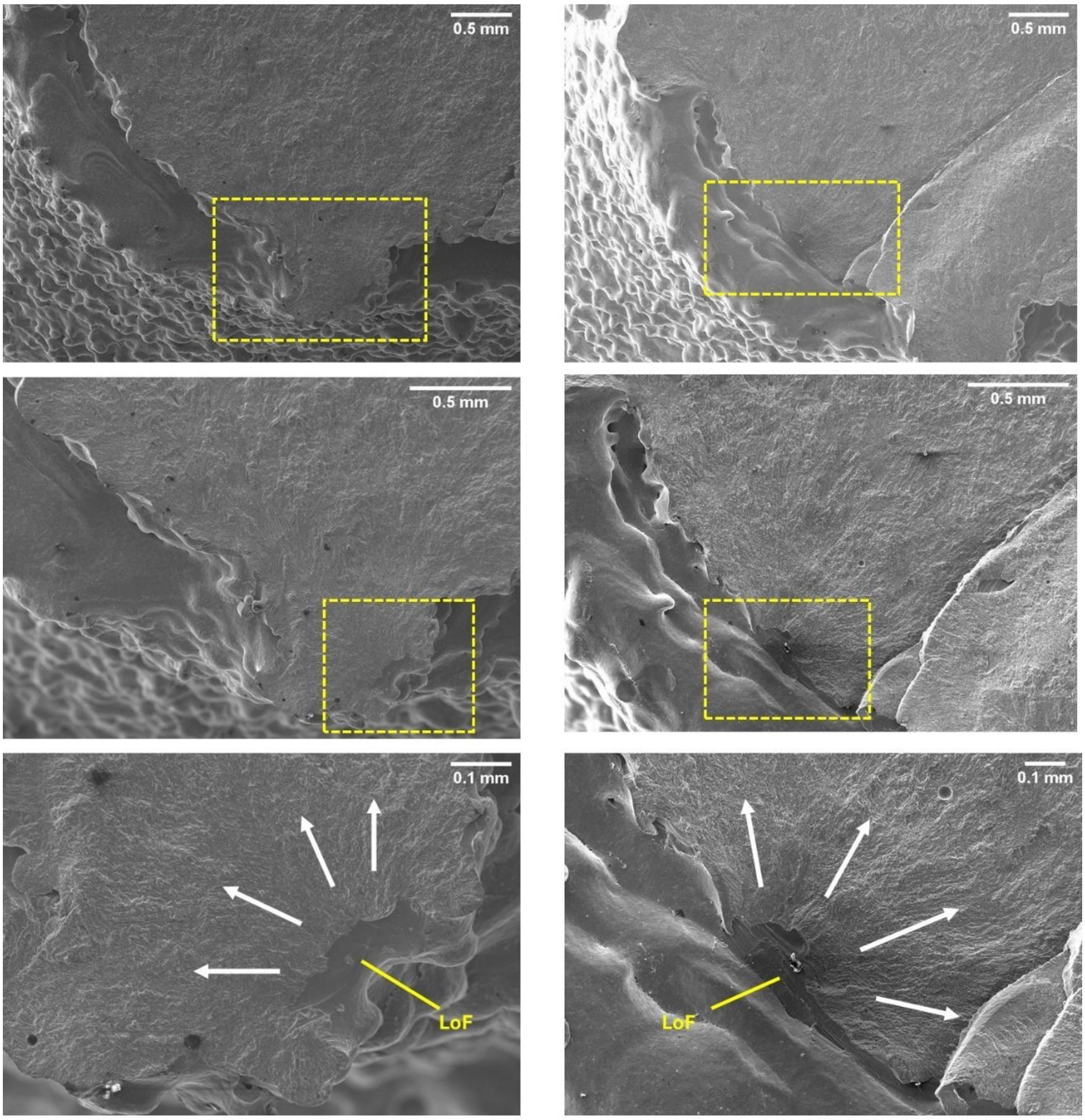

(a) (b)

Fig. 6.20 SEM image of the fracture surfaces of (a)SR-L-1 and (b)SR-L-4 stem specimens taken at the locations of LoF defects as shown in Fig. 6.17

To further confirm the effects of the observed LoF defects on the shortened fatigue lives, Kitagawa-Takahashi diagram approach has been applied for further analysis. The location the fracture plane is estimated using the measurement from the microscope images, as shown in Fig. 6.21. The measured fracture plane from each specimen showing in Fig. 6.21 is approximately 6.42 mm above the upper surface of the gripper. This observation is consistent with the FEA predicted results as presented in Fig. 6.16, where the maximum σ_1 is predicted at a location of 6.46 mm above the gripper. At the highest σ_1 concentrated region, the other principal stresses, σ_2 and σ_3, are found to be significantly smaller than σ_1, confirming a state of near-uniaxial tension. Thus, the stress distribution at the cross-sectional plane exhibiting maximum σ_1 has been obtained for the further analysis.

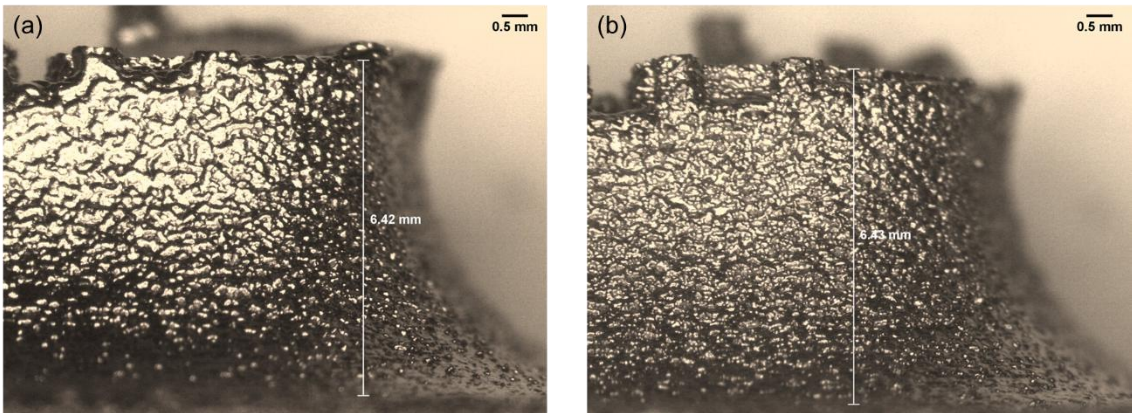

Fig. 6.21 Microscope images of the fractured (a) SR-L-1 and (b) SR-L-4 specimens

The LoF defect size were measured using the Murakami's approach as illustrated in Fig. 2.33, the measured LoF effective defect areas are 0.035 mm^2 and 0.087 mm^2, giving the effect defect size $\sqrt{\text{Area}}$ of 188μm and 295μm for SR-L-1 and SR-L-4 specimens, respectively. It needs to be addressed that the measured defect size might be overestimated. Therefore, the uncertainty associated with the defect size measurement will be discussed soon.

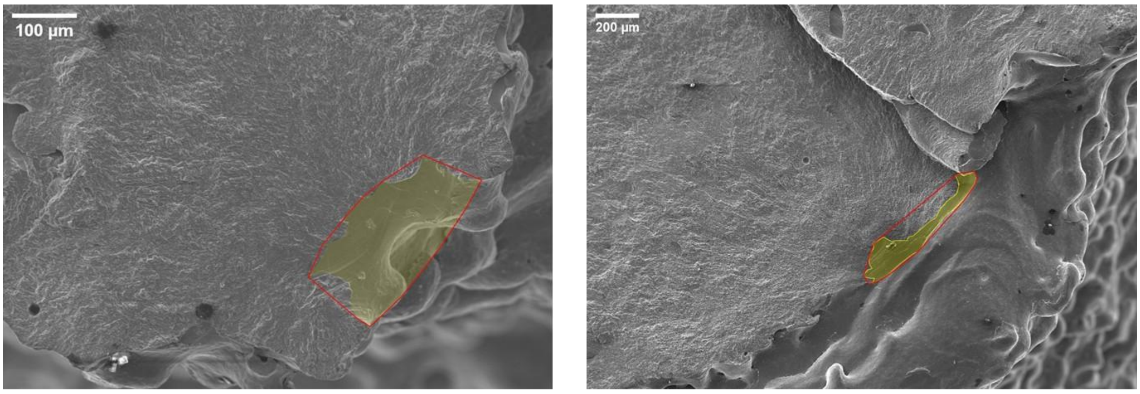

(a) (b)

Fig. 6.22 Determination of nominal area (yellow area) and convex effective area (red line) for defects in the failed specimens (a) SR-L-1 and (b) SR-L-4

As shown in Fig. 6.23, K-T diagram is plotted based on the FEA-predicted stress distribution on the fracture surfaces of the failed specimens and the measured defect sizes. The location of LoF defects varied between the two failed specimens. In SR-L-1, the defect is found on a surface sturt subjected to an FEA-predicted σ_1 of 282MPa. In comparison, the LoF defect in SR-L-4 was located at a site on the solid portion which exhibiting significantly higher σ_1 of 434MPa. The threshold values of stress intensity factor for EBPBF Ti6Al4V parts $\Delta K_{\text{th,EB}} = 5.3\ \text{MPa} \cdot \sqrt{\text{m}}$ (unpublished data, 2025) as described in 3.5.1, have been applied for the calculation of a_0. For LPBF specimens, $\Delta K_{\text{th,L}} = 3.48\ \text{MPa} \cdot \sqrt{\text{m}}$ was considered[195]. The ideal fatigue limit for defects-free EBPBF and LPBF Ti6Al4V component has been obtained from literature, giving $\sigma_{\text{max,EB}}$ =600 MPa[156] and thus $\Delta\sigma_{\text{th,EB}}$= 540 MPa and $\Delta\sigma_{th,L}$ =500 MPa (R=0.1) for as-built LPBF Ti6Al4V without defects[259], respectively. Although the femoral stem specimens were tested under global compression-compression conditions (R=10), the applied global compression to the steam head induced a macroscopic bending moment. This bending generated a highly localised tensile stress field on the lateral side of the stem. As the global compressive load oscillated, the local tensile stress on the lateral side simultaneously oscillated in a tension-tension manner. Therefore, the actual local stress ratio at the critical tension-concentrated region is positive, closely approximating the R=0.1 condition in the FCG tests. For this reason, utilising the ΔK_{th} threshold values derived from the standard CT specimens tested at R=0.1 was considered mechanical valid.

In Fig. 6.23, the plotted data point of SR-L-4 lies far above the El-Haddad curve, while SR-L-1 lies within the safe region but near the threshold. The plotted K-T diagram suggests that the LoF defect in SR-L-4 is expected to be more detrimental to the fatigue life of the specimen than that in SR-L-1, resulting in a shorter fatigue life of SR-L-4. This agrees with the experimentally determined longer fatigue live exhibited by SR-L-1. Conversely, this finding is inconsistent with the data collected from literature for LPBF[195,260,261] and EBPBF[262] Ti6Al4V specimens shown in Fig. 6.23, which generally suggests that the plotted data further away from the El-Haddad curve correlates with a shorter fatigue life. However, for SR-L-1, the plotted data suggests an infinite fatigue life, this prediction does not agree with the experimental outcomes from the fatigue testing. In addition, one of the LPBF data reported by Pagliari et al.[195] also fall into the safe region but exhibited a short fatigue life (N_f=24,652 cycles).

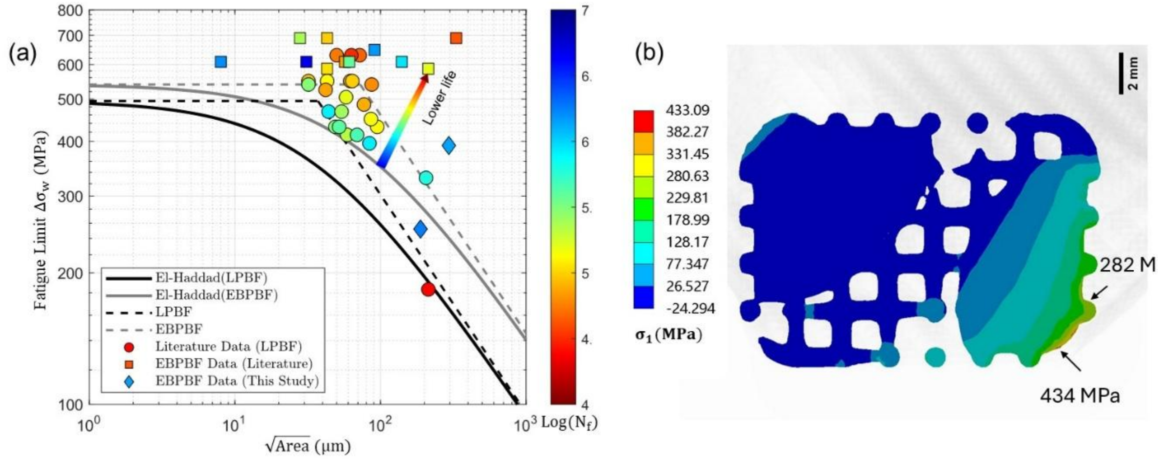

Fig. 6.23 (a) The K-T diagram for the measured LoF on the fracture surface of the EBPBF(ΔK_{th}=5.3MPa$\sqrt{m}$) stem specimens comparing against LPBF (ΔK_{th}=3.483MPa$\sqrt{m}$) literature data[195,260–262] and (b)the stress distribution of σ_1 on the fracture surface

To clarify that, the source of uncertainties in the plotted K-T diagram need to be considered. Firstly, the stress level of σ_{max}= 600MPa derived from the S-N curve on the EBPBF specimens defined the fatigue limit control regime. The obtained data from the cited work[156] exhibited considerable scatter and the results could also subject to specimen-to-specimen variation. Secondly, since the local stress level at the defect site has been predicted by FEA, the difference between the nominal CAD model and the as-built geometry would lead to uncertainty in the final stress value. Furthermore, the unpublished data of ΔK_{th} has been experimentally determined for EBPBF Ti6Al4V using the standard compact tension samples. However, there are limited data of ΔK_{th} of the as-fabricated EBPBF Ti6Al4V (R=0.1) reported in the literature is within the range of 4.0[263,264] – 6.5[265] $\mathrm{MPa}\cdot\sqrt{\mathrm{m}}$. The variation in ΔK_{th} for both EB- and LPBF parts would result in uncertainty in the final predicted safe region in the K-T diagram. To access the sensitivity of K-T analysis to varied ΔK_{th} values, a further analysis was conducted using additional experimentally determined ΔK_{th} values of 4.7 and 4.9 $\mathrm{MPa}\sqrt{\mathrm{m}}$. As shown in Fig. 6.24, with the additional lower ΔK_{th} values, the El-Haddad curves shift downward and to the left. The critical defect ($\sqrt{\mathrm{Area}}$ =295μm) detected in SR-L-4 still resides well within the expected failure regime. However, for the smaller defect ($\sqrt{\mathrm{Area}}$ =188μm) in SR-L-1, when the lowest ΔK_{th} is applied, the safety region is narrowed, bringing the defect size much closer to the critical a_0. In addition, the effective defect size has been determined using the measured 2D area from the fracture surface rather than the actual 3D shape. Thus, the variation between measured projected 2D area and the true cross-sectional area should be expected. The manually traced boundary of the defects could also introduce random measurement error in the results of $\sqrt{\mathrm{Area}}$.

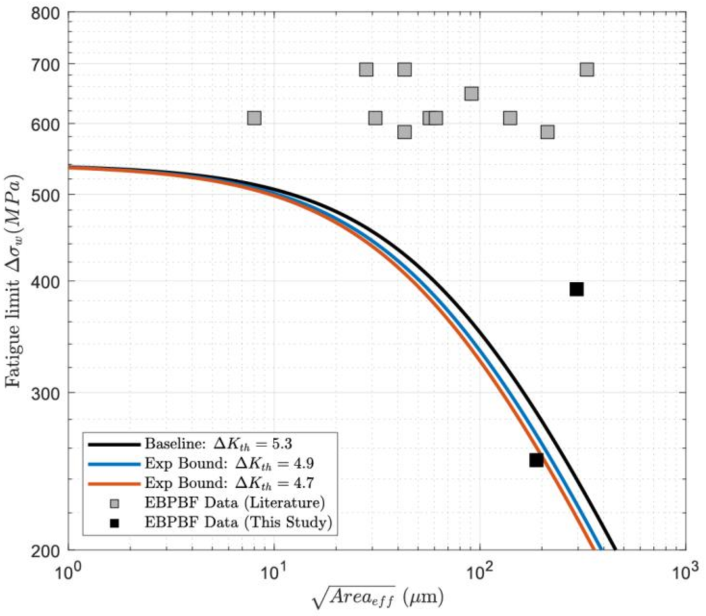

Fig. 6.24 K-T diagram for EBPBF data obtained from literature and this study using experimentally determined stress intensity threshold values ΔK_{th}=4.7, 4.9 and 5.3 $\mathrm{MPa}\sqrt{\mathrm{m}}$

For the two run-out specimens, as shown in Fig. 6.22, the tension-concentrated regions have been sectioned from the specimens approximately 2 mm above the gripper surface for the examination using micro-CT with a resolution of 9.758μm. Then the RoI for defects analysis has been defined by the stress distribution at the cross-sectional plane of maximum σ_1 shown in Fig. 6.17(c) with σ_1>250MPa, which is located 6.42 mm above the gripper surface. This corresponds to a position of approximately 4.42 mm above the bottom surface of the sectioned portions. As expected, the as-built EBPBF parts exhibit high surface roughness and CT-scanned image stacks have been analysed in MATLAB to reveal the distribution of the defects.

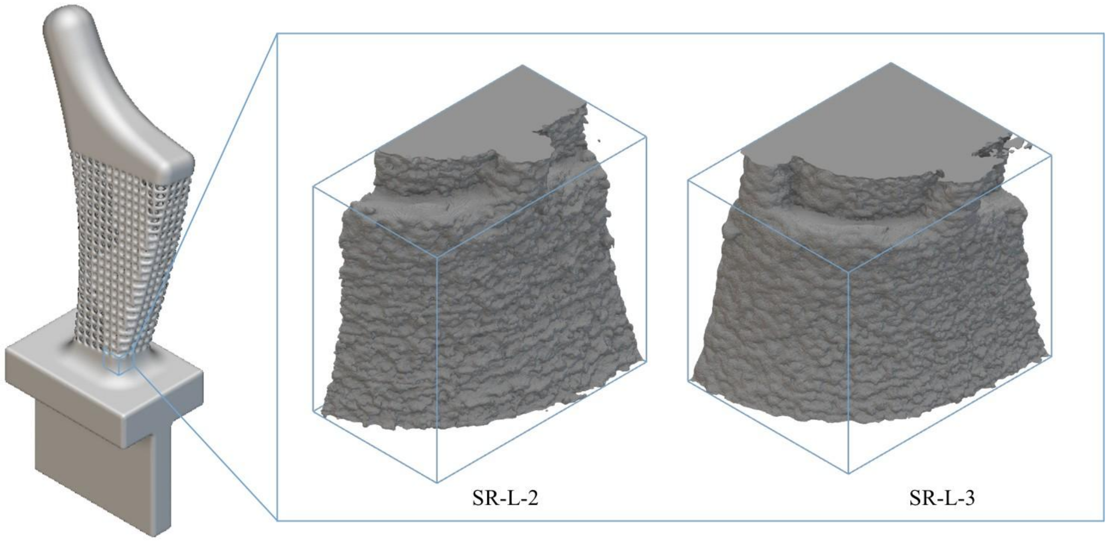

Fig. 6.25 Illustration of the sectioned region for micro-CT scanning and the reconstructed 3D models

The distributions of the defects in the two run-out specimens are shown in Fig. 6.26, where the defects are classified as internal and surface defects based on the criteria described in Fig. 2.33 (c). In summary, 15 and 5 defects have been identified within the RoI of SR-L-2 and SR-L-3, respectively. Further statistical analysis is presented in Fig. 6.29, the maximum effective defect size $\sqrt{\text{Area}}$ measured for SR-L-2 and SR-L-3 is 50μm and 42 μm, respectively. Thus, it can be concluded that there are no surface defects with significant size existed within the high-stress region in the two run-out specimens.

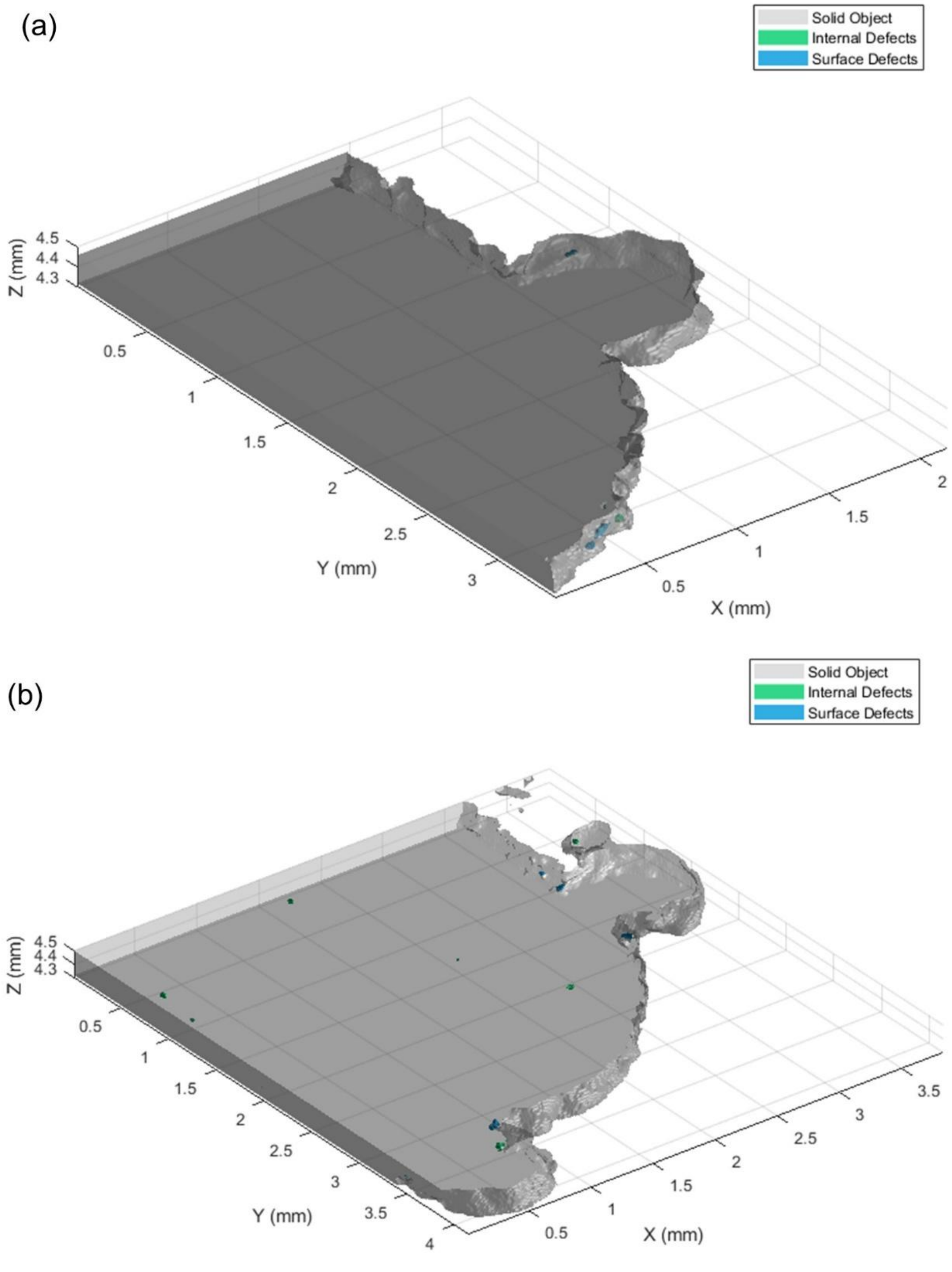

Fig. 6.26 Distribution of the defects detected by micro-CT scanning in the run-out stem samples: (a) SR-L-2 and (b) SR-L-3

To evaluate the robustness of the defect characterisation, a segmentation sensitivity analysis has been conducted. The global grayscale threshold used to isolate pores within the AOI was varied by ±5% from the nominal value. The results of the analysis shown in Fig. 6.27 revealed no significant deviation in either the total defect count or the critical defect size. This stability is attributed to the high contrast gradient present at the boundaries of the physical defects. Since the transition between the solid material and the internal voids is sharply defined in the tomographic reconstructions, minor fluctuations in the segmentation threshold do not artificially dilate or erode the measured geometries. Consequently, the derived $\sqrt{\mathrm{Area}}$ values are highly reliable, ensuring that the placement of these critical defects relative to the El Haddad transition length a_0 on the K-T diagram is mathematically robust and independent of subjective segmentation choices.

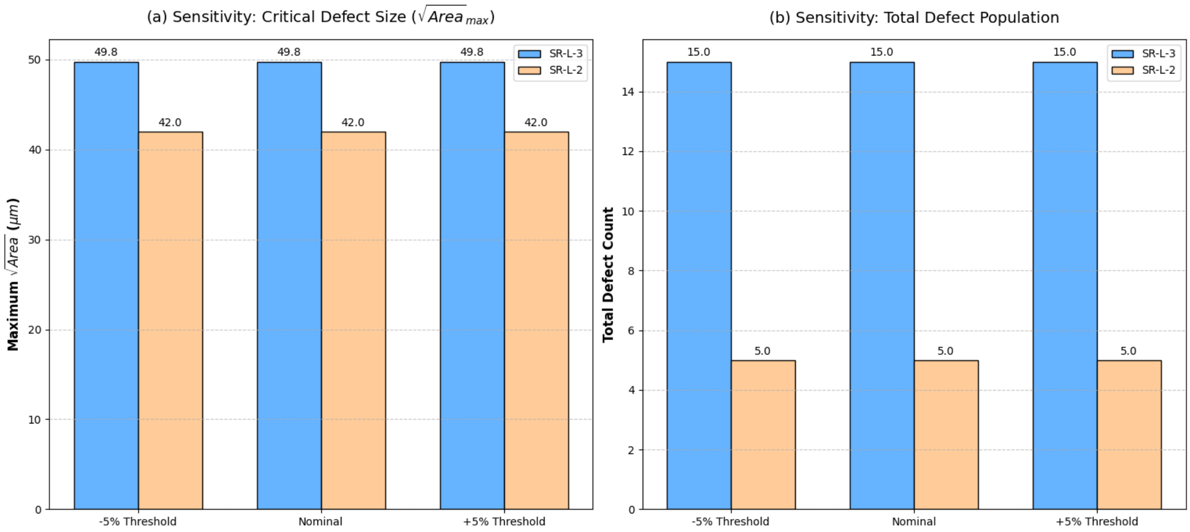

Fig. 6.27 Results of segmentation sensitivity of grey-scale threshold analysis on (a) critical defect size $\sqrt{\mathrm{Area}_{\mathrm{max}}}$ and (b) total defect population in the AOI

As shown in Fig. 6.28, the surface roughness R_v at the tension-concentrated region of the run-out SR-L-2 and SR-L-3 specimens were measured using the X-CT scanning results by the method described in 3.5.2, giving maximum R_v of approximately 80μm and 60μm, respectively. Following the approach suggested by Pagliari et al.[195], considering the surface roughness of R_v as micro-notch using the relationship $\sqrt{\mathrm{Area}_{\mathrm{Shallow}}} = \sqrt{10}R_v$, the calculated results yields an effective micro-notch length of 252μm and 189 μm for SR-L-2 and SR-L-3, respectively. As Pagliari et al.[195] suggested, the crack nucleation is contributed by the combined influence of roughness and surface defects, this suggestion implies that specimen SR-L-2 and SR-L-3 should have failed rather than run out at 10^7 cycles. The finding obtained from the examination of the run-out specimens suggests that the effects of surface roughness of EBPBF parts on the fatigue life are limited, while the most detrimental factor on fatigue life is surface LoF defects. Only the surface LoF defects should be considered as micro-cracks for the crack initiation. In contrast, surface roughness should not constitute a micro-crack. The fatigue cracks must first initiate within the rough surface before it can propagate and lead to fatigue failure.

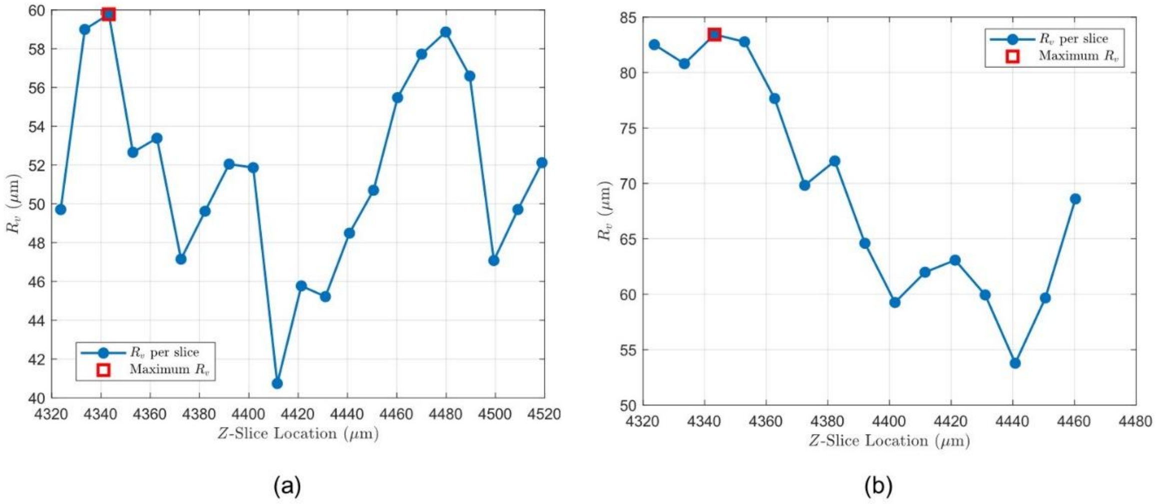

Fig. 6.28 The surface roughness R_v values measured from (a) SR-L-2 and (b) SR-L-3 specimens within the tension concentrated region

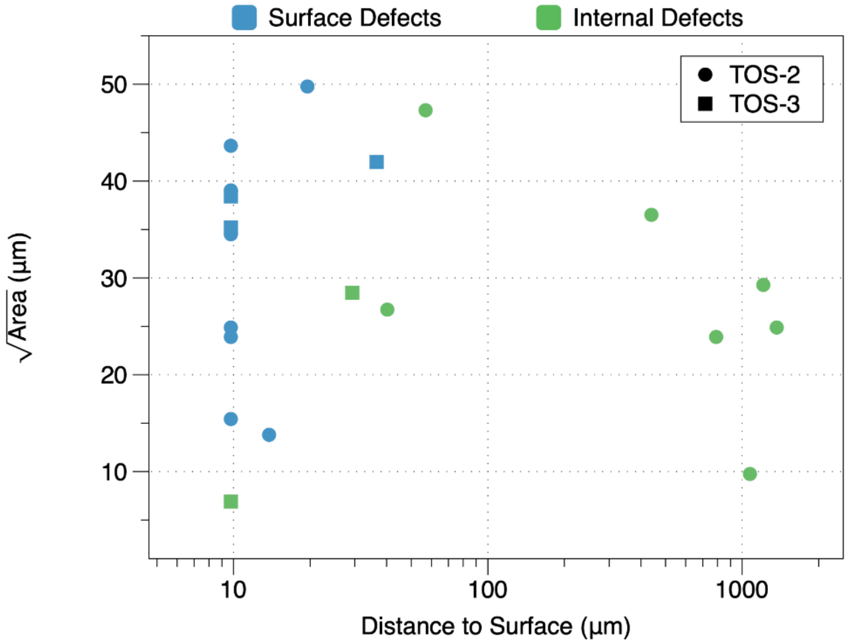

Fig. 6.29 Effective defect size vs distance to surface obtained from the mirco-CT scanning results of the run-out femoral stem samples

Based on the above analysis, it can be concluded that the LoF defects located in the high-stress-concentration locations were identified as the critical defects in the two failed EBPBF stem specimens. The presence of LoF defects acted as the key detriment factor resulting in the shorter fatigue life (up to 1.78×10^6 cycles). However, the obtained fatigue performance was not significantly distant from the required 5×10^6 cycles as specified in ISO 7206-4. In contrast, for the run-out specimens, even though rough surface was presented, the absence of LoF defects at the critical locations allowed them to exhibited fatigue lives far beyond the required 5×10^6 cycles. This further supported that the presence of LoF defects in the critical locations was the main detrimental factor leading to a shorter fatigue life.

Therefore, to ensure the quality of EBPBF porous femoral stems, X-ray micro-CT can be applied to the as-fabricated components to eliminate or screen out those containing LoF defects at critical locations. In addition, given that the current LoF-free run-out specimens exhibited a fatigue life (1×10^7 cycles) significantly longer than the required 5×10^6 cycles, coupled with micro-CT screening, the design of porous stem can be further optimised to significantly reduce the solid portion and increase the porous lattice portion.

7. Conclusions and Recommendations

In Chapter 4 Orientation-dependent Quasi-static Behaviour, the orientation-dependant quasi-static compressive behaviour of the three different lattices, including [001]//LD, [011]//LD and [111]//LD, has been analysed. The FEA predicted and experimentally determined yield strength σ_{y-L} values for all the SC lattices are generally comparable. Therefore, the effects of EBPBF process induced strut irregularities and defects on σ_{y-L} are negligible. Both the FEA predicted and experimentally determined results have indicated that the values of effective Young's modulus of [001]//LD lattices is considerably higher than those of [011]//LD and [111]//LD lattices. However, the experimentally determined E_L values are considerably lower than those predicted by FEA models, despite the compression-tests-determined values are widely reported in published works.

The yield strength σ_{y-L}, the ultimate compressive strength UCS_L and failure strain ε_p are found to be strongly dependant on the combined effects of LD and UCO. The experimentally determined σ_{y-L} and ε_p of [001]//LD structure are found to be 1.8–2.0 times and 4–6 times higher those of [011]//LD and [111]//LD lattices. This agrees with the FEA predicted results. In [011]//LD and [111]//LD lattices, stress concentration has resulted in local yielding and deformation when the applied load was only 57% and 60%, respectively, of the yielding point of [001]//LD lattice. The FEA simulations have illustrated high maximum principal stress σ_1 concentrated locally in the form of tension in the [011]//LD and [111]//LD lattices. This observation is consistent with the finding that micro-notches readily serve as crack propagation locations, resulting in the fracture of struts in the entire plane under low plastic strain values in the [011]//LD and [111]//LD lattices.

In Chapter 5 Orientation-dependent Fatigue Behaviour, the combined effects of LD and UCO on the compressive fatigue behaviour(R=10) of the EBPBF SC lattices have been studied. When the lattices were cyclically tested to 5×10^6 cycles, the fatigue strength of [001]//LD lattice decreased moderately from the quasi-static testing obtained UCS_L=235MPa to the run-out value of σ_{max} of approximately $0.8\,UCS_L$=190MPa. In contrast, the fatigue strength of [011]//LD or [111]//LD lattice decreased dramatically as the fatigue cycles increased. The fatigue strength of [011]//LD and [111]//LD lattices decreased from their UCS_L≈110MPa to approximately $0.63UCS_L$=70MPa and $0.23UCS_L$=25MPa when the fatigue life cycle reached 1×10^4 and 5×10^6, respectively. The findings in Chapter 5 suggest that for the optimal macroscopic compressive fatigue strength, SC lattice structures should be orientated in the [001]//LD UCO.

The low fatigue strength of non-[001]//LD lattices has been found to be related to the crack initiation and growth at the high-tension concentrated locations at the top and bottom nodes in each unit cell. In [001]//LD lattices, no such tension-concentrated locations were presented, thus, high fatigue strength was exhibited. In these non-[001]//LD lattices, once the crack was initiated and grown for a short distance within the nodes, each crack propagated sideways to the left or right, towards the adjacent cells. This mechanism resulted in the lattice fracturing along (001). For [001]//LD lattices, no complete fracture occurred, while the termination of the tests was contributed by the slightly local compressive movement during the high-cycle fatigue test at high stress level. It has also been found that all the available data reported in literature suggested low high-cycle fatigue strength of non-[001]//LD lattices, giving $\sigma_{\max} \leq$25MPa, indicating the same failure mechanism as that has been identified of the non-[001]//LD lattices in this thesis has been exhibited. In complex components, where non-[001]//LD orientations are geometrically unavoidable, the design of the component should target a local peak stress ratio of $\sigma_{max}/\sigma_{y-L} \lesssim 0.2$. Otherwise, alternative topological modifications should be introduced to artificially lower the localised stress concentrations at the nodes.

In Chapter 6 Fatigue Performance of the EBPBF Stem, the three different types of femoral stems, including FP, TOed and SR-L, have been designed, fabricated and tested. The UCO-optimised SC-lattice ($\bar{\rho} = 0.36$) based FP stem with close-cell shell exhibited short fatigue life of only approximately 10^5 cycles, which is less than 1% of the required 5×10^6 cycles. The FEA predicted stress distribution verified the poor fatigue performance by showing the highest σ_1 exhibited on the FP stem reaches approximately 86% of the yield strength of the alloy.

The validity of the solid-reinforced lattice (SR-L) stem was suggested by the fatigue testing results along with the post-test analysis. The fatigue results of four SR-L stem samples under the simplified configuration demonstrated that two of them failed at 1.78×10^6 and 1.47×10^6 cycles and the other two reached ran-out (1×10^7 cycles). The post-test examination has confirmed that the failure of the two samples with fatigue life not meeting the required 5×10^6 cycles has been attributed to the common PBF defect in the form of LoF observed in the tension concentration region.

The defect analysis following the Kitagawa-Takahashi (K-T) diagram approach has indicated that the effect of surface LoFs on the fatigue life can be predicted based on the linear fracture mechanics that K-T approach is based on. Further analysis using X-CT on the two run-out samples has demonstrated that no LoF defects with size exceed the threshold a_0 in the tension concentrated region, which also confirmed that the surface roughness of EBPBF components is tolerable to fatigue damages.

However, several experimental and computational limitations must be acknowledged. Firstly, the fatigue testes were conducted under uniaxial high-frequency spectra in an ambient environment. In this case, the potential detrimental, synergistic effects of corrosion or fretting were not considered. For in-vivo orthopaedic application, the performance of the porous EBPBF stem under more complicated loading conditions should be addressed. In addition, the current unit cell topological focus was restricted to simple cubic structures. Moving forward, a key area of future work should be extended to more complex structures, such as TPMS and FGLs.

Followed by the findings of this work, future research should address the following challenges to further advance the understanding and applications of EBPBF lattice structures:

- Even though the orientation-dependent fatigue behaviour of SC lattices has been understood in this work, an in-depth quantitative analysis of the fatigue damage process within the lattices should be conducted. The relative portion of the fatigue crack initiation phase versus the crack propagation phase within the total fatigue life should be determined, the relationship between fatigue cyclic loading, crack size, crack path and lattice geometry should be further investigated. Furthermore, the effects of the initiated crack on the mechanical properties of the lattice, such as changes in E_L and cyclic ratcheting rate should also be investigated.
- The testing and analysis of the four SR-L stem samples have shown that the current design and EBPBF can readily produce the femoral stems with sufficient fatigue strength satisfying the required 5×10^6 cycles by the ISO standard. Since the defect size up to a_0 can be detected using X-CT technology and thus the defected stems can be screened out. The LoF defects at the lateral tension zones should be screened for the accurately predicting fatigue life and preventing fatigue failure. In addition, the two run-out samples with no large defects greater than a_0 strongly suggest that the fraction of the solid-reinforced portion can be further reduced while still maintaining a fatigue life slightly higher than 5×10^6 cycles.

Data Availability Statement

The raw data and computational scripts supporting the findings of this thesis, including stress-strain data, S-N data, finite element meshes, boundary conditions, and XCT image stacks, are archived internally and are available from the author upon reasonable request.

References

1. Benedetti, M., du Plessis, A., Ritchie, R. O., Dallago, M., Razavi, N., & Berto, F. (2021). Architected cellular materials: A review on their mechanical properties towards fatigue-tolerant design and fabrication. *Materials Science and Engineering: R: Reports*, *144*, 100606. https://doi.org/10.1016/j.mser.2021.100606

2. Lin, Z., Dadbakhsh, S., & Rashid, A. (2022). Developing processing windows for powder pre-heating in electron beam melting. *Journal of Manufacturing Processes*, *83*, 180–191. https://doi.org/10.1016/j.jmapro.2022.08.063

3. Berghaus, M., Florian, S., Solanki, K., Zinn, C., Wang, H., Butz, B., Apmann, H., & von Hehl, A. (2025). Effect of high laser scanning speed on microstructure and mechanical properties of additively manufactured 316L. *Progress in Additive Manufacturing*, *10*(2), 1119–1132. https://doi.org/10.1007/s40964-024-00693-y

4. Jiao, M., Long, H., Xiao, B., Liang, X., & Lin, F. (2024). Electron Beam Powder Bed Fusion Additive Manufacturing: A Comprehensive Review and its Development in China. *Additive Manufacturing Frontiers*, *3*(4), 200177. https://doi.org/10.1016/j.amf.2024.200177

5. Soni, N., Renna, G., & Leo, P. (2024). Advancements in Metal Processing Additive Technologies: Selective Laser Melting (SLM). *Metals*, *14*(9), 1081. https://doi.org/10.3390/met14091081

6. Roudnicka, M., Misurak, M., & Vojtech, D. (2019). Differences in the Response of Additively Manufactured Titanium Alloy to Heat Treatment—Comparison between SLM and EBM. *Manufacturing Technology*, *19*(4), 668–673. https://doi.org/10.21062/ujep/353.2019/a/1213-2489/MT/19/4/668

7. Chastand, V., Quaegebeur, P., Maia, W., & Charkaluk, E. (2018). Comparative study of fatigue properties of Ti-6Al-4V specimens built by electron beam melting (EBM) and selective laser melting (SLM). *Materials Characterization*, *143*, 76–81. https://doi.org/10.1016/J.MATCHAR.2018.03.028

8. Dias, J. M., da Silva, F. S. C. P., Gasik, M., Miranda, M. G. M., & Bartolomeu, F. J. F. (2024). Unveiling additively manufactured cellular structures in hip implants: A comprehensive review. *The International Journal of Advanced Manufacturing Technology*, *130*(9–10), 4073–4122. https://doi.org/10.1007/s00170-023-12769-0

9. Wang, C., Tan, X., Liu, E., & Tor, S. B. (2018). Process parameter optimization and mechanical properties for additively manufactured stainless steel 316L parts by selective electron beam melting. *Materials & Design*, *147*, 157–166. https://doi.org/10.1016/j.matdes.2018.03.035

10. Köhnen, P., Haase, C., Bültmann, J., Ziegler, S., Schleifenbaum, J. H., & Bleck, W. (2018). Mechanical properties and deformation behavior of additively manufactured lattice structures of stainless steel. *Materials & Design*, *145*, 205–217. https://doi.org/10.1016/j.matdes.2018.02.062

11. Gümrük, R., Mines, R. A. W., & Karadeniz, S. (2013). Static mechanical behaviours of stainless steel micro-lattice structures under different loading conditions. *Materials Science and Engineering: A*, *586*, 392–406. https://doi.org/10.1016/j.msea.2013.07.070

12. Dzogbewu, T. C., & de Beer, D. J. (2024). Additive manufacturing of NiTi shape memory alloy and its industrial applications. *Heliyon*, *10*(1). https://doi.org/10.1016/j.heliyon.2023.e23369

13. He, M., Xiang, Z., Yi, J., Ni, Y., & Wang, S. (2022). A comparison of dislocation cellular patterns generated in Inconel 718 alloy and pure Ni fabricated by laser powder bed fusion. *Vacuum*, *199*. https://doi.org/10.1016/j.vacuum.2022.110974

14. Daram, P., Hiroto, T., & Watanabe, M. (2023). Microstructure and phase evolution of functionally graded multi-materials of Ni–Ti alloy fabricated by laser powder bed fusion process. *Journal of Materials Research and Technology*, *23*. https://doi.org/10.1016/j.jmrt.2023.02.151

15. Manfredi, D., & Bidulský, R. (2017). Laser powder bed fusion of aluminum alloys. *Acta Metallurgica Slovaca*, *23*(3). https://doi.org/10.12776/ams.v23i3.988

16. Mertens, R., Baert, L., Vanmeensel, K., & Van Hooreweder, B. (2021). Laser powder bed fusion of high strength aluminum. *Material Design and Processing Communications*, *3*(5). https://doi.org/10.1002/mdp2.161

17. Aversa, A., Marchese, G., Saboori, A., Bassini, E., Manfredi, D., Biamino, S., Ugues, D., Fino, P., & Lombardi, M. (2019). New aluminum alloys specifically designed for laser powder bed fusion: A review. *Materials*, *12*(7). https://doi.org/10.3390/ma12071007

18. Chen, W., Yang, J., Kong, H., Helou, M., Zhang, D., Zhao, J., Jia, W., Liu, Q., He, P., & Li, X. (2021). Fatigue behaviour and biocompatibility of additively manufactured bioactive tantalum graded lattice structures for load-bearing orthopaedic applications. *Materials Science and Engineering: C*, *130*, 112461. https://doi.org/10.1016/j.msec.2021.112461

19. Guo, Y., Chen, C., Tan, L., Wang, Q., Pan, Y., Zhu, H., Zhou, K., & Wu, C. (2022). The role of pore structures on the fatigue properties of additively manufactured porous tantalum scaffolds produced by electron beam powder bed fusion. *Journal of Materials Research and Technology*, *19*, 3461–3473. https://doi.org/10.1016/j.jmrt.2022.06.096

20. Lei, P., Qian, H., Zhang, T., Lei, T., Hu, Y., Chen, C., & Zhou, K. (2022). Porous tantalum structure integrated on Ti6Al4V base by Laser Powder Bed Fusion for enhanced bony-ingrowth

implants: In vitro and in vivo validation. *Bioactive Materials*, *7*, 3–13. https://doi.org/10.1016/J.BIOACTMAT.2021.05.025

21. Pałka, K., & Pokrowiecki, R. (2018). Porous Titanium Implants: A Review. *Advanced Engineering Materials*, *20*(5). https://doi.org/10.1002/adem.201700648

22. Refai, K., Montemurro, M., Brugger, C., & Saintier, N. (2019). *Mechanics of Advanced Materials and Structures Determination of the effective elastic properties of titanium lattice structures Determination of the effective elastic properties of titanium lattice structures*. https://doi.org/10.1080/15376494.2018.1536816

23. Hrabe, N. W., Heinl, P., Flinn, B., Körner, C., & Bordia, R. K. (2011). Compression-compression fatigue of selective electron beam melted cellular titanium (Ti-6Al-4V). *Journal of Biomedical Materials Research Part B: Applied Biomaterials*, *99B*(2), 313–320. https://doi.org/10.1002/jbm.b.31901

24. Liu, B., Wang, H., Zhang, N., Zhang, M., & Cheng, C.-K. (2021). Femoral Stems With Porous Lattice Structures: A Review. *Frontiers in Bioengineering and Biotechnology*, *9*. https://doi.org/10.3389/fbioe.2021.772539

25. Galati, M., Saboori, A., Biamino, S., Calignano, F., Lombardi, M., Marchiandi, G., Minetola, P., Fino, P., & Iuliano, L. (2020). Ti-6Al-4V lattice structures produced by EBM: Heat treatment and mechanical properties. *Procedia CIRP*, *88*, 411–416. https://doi.org/10.1016/j.procir.2020.05.071

26. Murr, L. E. (2020). Global trends in the development of complex, personalized, biomedical, surgical implant devices using 3D printing/additive manufacturing: A review. *MEDICAL DEVICES & SENSORS*, *3*(6). https://doi.org/10.1002/mds3.10126

27. Safdar, A., Wei, L. Y., Snis, A., & Lai, Z. (2012). Evaluation of microstructural development in electron beam melted Ti-6Al-4V. *Materials Characterization*, *65*, 8–15. https://doi.org/10.1016/J.MATCHAR.2011.12.008

28. Majumdar, T., Bazin, T., Ribeiro, E. M. C., Frith, J. E., & Birbilis, N. (2019). Understanding the effects of PBF process parameter interplay on Ti-6Al-4V surface properties. *PLOS ONE*, *14*(8), e0221198. https://doi.org/10.1371/JOURNAL.PONE.0221198

29. Lee, W., Hyun, Y. T., Won, J. W., & Yoon, J. (2024). Numerical simulation for β/α transformation of Ti–6Al–4V alloy using a lattice Boltzmann—Cellular automata method. *Journal of Materials Research and Technology*, *32*, 1416–1425. https://doi.org/10.1016/J.JMRT.2024.07.235

30. Liu, S., & Shin, Y. C. (2019). Additive manufacturing of Ti6Al4V alloy: A review. *Materials & Design*, *164*, 107552. https://doi.org/10.1016/J.MATDES.2018.107552

31. Galarraga, H., Warren, R. J., Lados, D. A., Dehoff, R. R., Kirka, M. M., & Nandwana, P. (2017). Effects of heat treatments on microstructure and properties of Ti-6Al-4V ELI alloy fabricated by electron beam melting (EBM). *Materials Science and Engineering: A*, *685*, 417–428. https://doi.org/10.1016/j.msea.2017.01.019

32. Bin Abdullah, M. S., Bol, E., Kelley, G., Doyle, C., Schleusener, R., Mojib, M., Chen, X., Arola, D., & Ramulu, M. (2023). Microstructure and microhardness of electron beam melted Ti–6Al–4V components with differential thickness in initial deposition layers. *Journal of Materials Research and Technology*, *26*, 6493–6507. https://doi.org/10.1016/J.JMRT.2023.09.010

33. Eshawish, N., Malinov, S., Sha, W., & Walls, P. (2021). Microstructure and Mechanical Properties of Ti-6Al-4V Manufactured by Selective Laser Melting after Stress Relieving, Hot Isostatic Pressing Treatment, and Post-Heat Treatment. *Journal of Materials Engineering and Performance*, *30*(7), 5290–5296. https://doi.org/10.1007/S11665-021-05753-W/FIGURES/6

34. Del Guercio, G., Galati, M., Saboori, A., Fino, P., & Iuliano, L. (2020). Microstructure and Mechanical Performance of Ti–6Al–4V Lattice Structures Manufactured via Electron Beam Melting (EBM): A Review. *Acta Metallurgica Sinica (English Letters)*, *33*(2), 183–203. https://doi.org/10.1007/s40195-020-00998-1

35. Smith, M., Guan, Z., & Cantwell, W. J. (2013). Finite element modelling of the compressive response of lattice structures manufactured using the selective laser melting technique. *International Journal of Mechanical Sciences*, *67*, 28–41. https://doi.org/10.1016/j.ijmecsci.2012.12.004

36. Cheng, X. Y., Li, S. J., Murr, L. E., Zhang, Z. B., Hao, Y. L., Yang, R., Medina, F., & Wicker, R. B. (2012). Compression deformation behavior of Ti–6Al–4V alloy with cellular structures fabricated by electron beam melting. *Journal of the Mechanical Behavior of Biomedical Materials*, *16*(1), 153–162. https://doi.org/10.1016/j.jmbbm.2012.10.005

37. Mehboob, H., Tarlochan, F., Mehboob, A., Chang, S.-H., Ramesh, S., Harun, W. S. W., & Kadirgama, K. (2020). A novel design, analysis and 3D printing of Ti-6Al-4V alloy bio-inspired porous femoral stem. *Journal of Materials Science: Materials in Medicine*, *31*(9), 78. https://doi.org/10.1007/s10856-020-06420-7

38. Al Zoubi, N. F., Tarlochan, F., & Mehboob, H. (2022). Mechanical and Fatigue Behavior of Cellular Structure Ti-6Al-4V Alloy Femoral Stems: A Finite Element Analysis. *Applied Sciences*, *12*(9), 4197. https://doi.org/10.3390/app12094197

39. Arabnejad, S., Johnston, B., Tanzer, M., & Pasini, D. (2017). Fully porous 3D printed titanium femoral stem to reduce stress-shielding following total hip arthroplasty. *Journal of Orthopaedic Research*, *35*(8), 1774–1783. https://doi.org/10.1002/jor.23445

40. Jin, Y., Li, J., Fan, H., Du, J., & He, Y. (2025). Biomechanics and Mechanobiology of Additively Manufactured Porous Load-Bearing Bone Implants. *Small (Weinheim an Der Bergstrasse, Germany)*, e2409955. https://doi.org/10.1002/SMLL.202409955;CSUBTYPE:STRING:AHEAD

41. Bezuidenhout, M. B., Dimitrov, D. M., Van Staden, A. D., Oosthuizen, G. A., & Dicks, L. M. T. (2015). Titanium-Based Hip Stems with Drug Delivery Functionality through Additive Manufacturing. *BioMed Research International*, *2015*(1), 134093. https://doi.org/10.1155/2015/134093

42. BSI Standards Publication. (2016, April 30). *BS ISO 7206-4:2010+A1:2016 Implants for surgery. Partial and total hip joint prostheses*. BSI British Standards. https://doi.org/10.3403/30083053

43. Guo, L., Ataollah Naghavi, S., Wang, Z., Nath Varma, S., Han, Z., Yao, Z., Wang, L., Wang, L., & Liu, C. (2022). On the design evolution of hip implants: A review. *Materials & Design*, *216*, 110552. https://doi.org/10.1016/j.matdes.2022.110552

44. Ashby MF , Author, Evans A , Author, Fleck NA , Author, Gibson LJ , Author, Hutchinson JW , Author, Wadley HNG , Author, & Delale F , Reviewer. (2001). Metal Foams: A Design Guide. *Applied Mechanics Reviews*, *54*(6), B105–B106. https://doi.org/10.1115/1.1421119

45. Ashby, M. F. (2006). The properties of foams and lattices. *Philosophical Transactions of the Royal Society A: Mathematical, Physical and Engineering Sciences*, *364*(1838), 15–30. https://doi.org/10.1098/rsta.2005.1678

46. Bobbert, F. S. L., Lietaert, K., Eftekhari, A. A., Pouran, B., Ahmadi, S. M., Weinans, H., & Zadpoor, A. A. (2017). Additively manufactured metallic porous biomaterials based on minimal surfaces: A unique combination of topological, mechanical, and mass transport properties. *Acta Biomaterialia*, *53*, 572–584. https://doi.org/10.1016/J.ACTBIO.2017.02.024

47. Kadkhodapour, J., Montazerian, H., Darabi, A. Ch., Anaraki, A. P., Ahmadi, S. M., Zadpoor, A. A., & Schmauder, S. (2015). Failure mechanisms of additively manufactured porous biomaterials: Effects of porosity and type of unit cell. *Journal of the Mechanical Behavior of Biomedical Materials*, *50*, 180–191. https://doi.org/10.1016/j.jmbbm.2015.06.012

48. Ahmadi, S., Yavari, S., Wauthle, R., Pouran, B., Schrooten, J., Weinans, H., & Zadpoor, A. (2015). Additively Manufactured Open-Cell Porous Biomaterials Made from Six Different Space-Filling Unit Cells: The Mechanical and Morphological Properties. *Materials*, *8*(4), 1871–1896. https://doi.org/10.3390/ma8041871

49. Parthasarathy, J., Starly, B., Raman, S., & Christensen, A. (2010). Mechanical evaluation of porous titanium (Ti6Al4V) structures with electron beam melting (EBM). *Journal of the Mechanical Behavior of Biomedical Materials*, *3*(3), 249–259. https://doi.org/10.1016/j.jmbbm.2009.10.006

50. Kolken, H. M. A., Garcia, A. F., Du Plessis, A., Rans, C., Mirzaali, M. J., & Zadpoor, A. A. (2021). Fatigue performance of auxetic meta-biomaterials. *Acta Biomaterialia*, *126*, 511–523. https://doi.org/10.1016/j.actbio.2021.03.015

51. Amin Yavari, S., Wauthle, R., van der Stok, J., Riemslag, A. C., Janssen, M., Mulier, M., Kruth, J. P., Schrooten, J., Weinans, H., & Zadpoor, A. A. (2013). Fatigue behavior of porous biomaterials manufactured using selective laser melting. *Materials Science and Engineering: C*, *33*(8), 4849–4858. https://doi.org/10.1016/j.msec.2013.08.006

52. Li, S. J., Xu, Q. S., Wang, Z., Hou, W. T., Hao, Y. L., Yang, R., & Murr, L. E. (2014). Influence of cell shape on mechanical properties of Ti–6Al–4V meshes fabricated by electron beam melting method. *Acta Biomaterialia*, *10*(10), 4537–4547. https://doi.org/10.1016/j.actbio.2014.06.010

53. Sallica-Leva, E., Jardini, A. L., & Fogagnolo, J. B. (2013). Microstructure and mechanical behavior of porous Ti–6Al–4V parts obtained by selective laser melting. *Journal of the Mechanical Behavior of Biomedical Materials*, *26*, 98–108. https://doi.org/10.1016/j.jmbbm.2013.05.011

54. Maconachie, T., Leary, M., Lozanovski, B., Zhang, X., Qian, M., Faruque, O., & Brandt, M. (2019). SLM lattice structures: Properties, performance, applications and challenges. *Materials & Design*, *183*, 108137. https://doi.org/10.1016/j.matdes.2019.108137

55. Alomar, Z., & Concli, F. (2020). A Review of the Selective Laser Melting Lattice Structures and Their Numerical Models. *Advanced Engineering Materials*, *22*(12), 2000611. https://doi.org/https://doi.org/10.1002/adem.202000611

56. Sokollu, B., Gulcan, O., & Konukseven, E. I. (2022). Mechanical properties comparison of strut-based and triply periodic minimal surface lattice structures produced by electron beam melting. *Additive Manufacturing*, *60*, 103199. https://doi.org/10.1016/j.addma.2022.103199

57. Maconachie, T., Leary, M., Tran, P., Harris, J., Liu, Q., Lu, G., Ruan, D., Faruque, O., & Brandt, M. (2022). The effect of topology on the quasi-static and dynamic behaviour of SLM AlSi10Mg lattice structures. *International Journal of Advanced Manufacturing Technology*, *118*(11–12), 4085–4104. https://doi.org/10.1007/S00170-021-08203-Y/METRICS

58. Liang, Z., Chen, X., Sun, Z., Guo, Y., Li, Y., Chang, H., & Zhou, L. (2022). A study on the compressive mechanical properties of 316L diamond lattice structures manufactured by laser powder bed fusion based on actual relative density. *Journal of Manufacturing Processes*, *84*, 414–423. https://doi.org/10.1016/J.JMAPRO.2022.09.041

59. Zhao, S., Li, S. J., Hou, W. T., Hao, Y. L., Yang, R., & Misra, R. D. K. (2016). The influence of cell morphology on the compressive fatigue behavior of Ti-6Al-4V meshes fabricated by electron beam

melting. *Journal of the Mechanical Behavior of Biomedical Materials*, *59*, 251–264. https://doi.org/10.1016/j.jmbbm.2016.01.034

60. Sun, L., Chen, K., Geng, P., Zhou, Y., Wen, S., & Shi, Y. (2023). Mechanical and shape memory properties of NiTi triply periodic minimal surface structures fabricated by laser powder bed fusion. *Journal of Manufacturing Processes*, *101*, 1091–1100. https://doi.org/10.1016/j.jmapro.2023.06.034

61. Mulhi, A., Dehgahi, S., Waghmare, P., & Qureshi, A. (2023). Dimensional assessment of uniformly periodic porosity primitive TPMS lattices using additive manufacturing laser powder bed fusion technique. *The International Journal of Advanced Manufacturing Technology*, *124*(7–8), 2127–2148. https://doi.org/10.1007/s00170-022-10578-5

62. Qiu, N., Wan, Y., Shen, Y., & Fang, J. (2024). Experimental and numerical studies on mechanical properties of TPMS structures. *International Journal of Mechanical Sciences*, *261*. https://doi.org/10.1016/j.ijmecsci.2023.108657

63. Maxwell, J. C. (1864). L. On the calculation of the equilibrium and stiffness of frames. *The London, Edinburgh, and Dublin Philosophical Magazine and Journal of Science*, *27*(182). https://doi.org/10.1080/14786446408643668

64. Gibson, L. J., & Ashby, M. F. (1999). *Cellular_Solids*. Cambridge University Press.

65. Qiu, C., Yue, S., Adkins, N. J. E., Ward, M., Hassanin, H., Lee, P. D., Withers, P. J., & Attallah, M. M. (2015). Influence of processing conditions on strut structure and compressive properties of cellular lattice structures fabricated by selective laser melting. *Materials Science and Engineering: A*, *628*, 188–197. https://doi.org/10.1016/J.MSEA.2015.01.031

66. Mazur, M., Leary, M., McMillan, M., Sun, S., Shidid, D., & Brandt, M. (2017). Mechanical properties of Ti6Al4V and AlSi12Mg lattice structures manufactured by Selective Laser Melting (SLM). In *Laser Additive Manufacturing* (pp. 119–161). Elsevier. https://doi.org/10.1016/B978-0-08-100433-3.00005-1

67. Choy, S. Y., Sun, C.-N., Leong, K. F., & Wei, J. (2017). Compressive properties of Ti-6Al-4V lattice structures fabricated by selective laser melting: Design, orientation and density. *Additive Manufacturing*, *16*, 213–224. https://doi.org/10.1016/j.addma.2017.06.012

68. Cuadrado, A., Yánez, A., Martel, O., Deviaene, S., & Monopoli, D. (2017). Influence of load orientation and of types of loads on the mechanical properties of porous Ti6Al4V biomaterials. *Materials & Design*, *135*, 309–318. https://doi.org/10.1016/j.matdes.2017.09.045

69. Metzger, C. E., Burr, D. B., & Allen, M. R. (2020). Anatomy and Structural Considerations. In *Encyclopedia of Bone Biology* (pp. 218–232). Elsevier. https://doi.org/10.1016/B978-0-12-801238-3.62234-1

70. Kundu, J., Pati, F., Shim, J.-H., & Cho, D.-W. (2014). Rapid prototyping technology for bone regeneration. In R. Narayan (Ed.), *Rapid Prototyping of Biomaterials* (pp. 254–284). Elsevier. https://doi.org/10.1533/9780857097217.254

71. McGregor, M., Patel, S., McLachlin, S., & Mihaela Vlasea. (2021). Architectural bone parameters and the relationship to titanium lattice design for powder bed fusion additive manufacturing. *Additive Manufacturing*, *47*, 102273. https://doi.org/10.1016/j.addma.2021.102273

72. Morgan, E. F., Unnikrisnan, G. U., & Hussein, A. I. (2018). Bone Mechanical Properties in Healthy and Diseased States. *Annual Review of Biomedical Engineering*, *20*(1), 119–143. https://doi.org/10.1146/annurev-bioeng-062117-121139

73. Xue, W., Krishna, B. V., Bandyopadhyay, A., & Bose, S. (2007). Processing and biocompatibility evaluation of laser processed porous titanium. *Acta Biomaterialia*, *3*(6), 1007–1018. https://doi.org/10.1016/J.ACTBIO.2007.05.009

74. Zhao, D., Huang, Y., Ao, Y., Han, C., Wang, Q., Li, Y., Liu, J., Wei, Q., & Zhang, Z. (2018). Effect of pore geometry on the fatigue properties and cell affinity of porous titanium scaffolds fabricated by selective laser melting. *Journal of the Mechanical Behavior of Biomedical Materials*, *88*, 478–487. https://doi.org/10.1016/j.jmbbm.2018.08.048

75. Zhao, X., Li, S., Zhang, M., Liu, Y., Sercombe, T. B., Wang, S., Hao, Y., Yang, R., & Murr, L. E. (2016). Comparison of the microstructures and mechanical properties of Ti–6Al–4V fabricated by selective laser melting and electron beam melting. *Materials & Design*, *95*, 21–31. https://doi.org/10.1016/j.matdes.2015.12.135

76. Murr, L. E., Gaytan, S. M., Medina, F., Martinez, E., Martinez, J. L., Hernandez, D. H., Machado, B. I., Ramirez, D. A., & Wicker, R. B. (2010). Characterization of Ti–6Al–4V open cellular foams fabricated by additive manufacturing using electron beam melting. *Materials Science and Engineering: A*, *527*(7–8), 1861–1868. https://doi.org/10.1016/J.MSEA.2009.11.015

77. Cantaboni, F., Battini, D., Hauber, K. Z., Ginestra, P. S., Tocci, M., Avanzini, A., Ceretti, E., & Pola, A. (2024). Mechanical and microstructural characterization of Ti6Al4V lattice structures with and without solid shell manufactured via electron beam powder bed fusion. *The International Journal of Advanced Manufacturing Technology*, *131*(3–4), 1289–1301. https://doi.org/10.1007/s00170-024-13137-2

78. Hernández-Nava, E., Smith, C. J., Derguti, F., Tammas-Williams, S., Leonard, F., Withers, P. J., Todd, I., & Goodall, R. (2016). The effect of defects on the mechanical response of Ti-6Al-4V cubic lattice structures fabricated by electron beam melting. *Acta Materialia*, *108*, 279–292. https://doi.org/10.1016/j.actamat.2016.02.029

79. Zhang, B., Li, Y., & Bai, Q. (2017). Defect Formation Mechanisms in Selective Laser Melting: A Review. *Chinese Journal of Mechanical Engineering (English Edition)*, *30*(3). https://doi.org/10.1007/s10033-017-0121-5

80. Arabnejad, S., Burnett Johnston, R., Pura, J. A., Singh, B., Tanzer, M., & Pasini, D. (2016). High-strength porous biomaterials for bone replacement: A strategy to assess the interplay between cell morphology, mechanical properties, bone ingrowth and manufacturing constraints. *Acta Biomaterialia*, *30*, 345–356. https://doi.org/10.1016/j.actbio.2015.10.048

81. Lozanovski, B., Leary, M., Tran, P., Shidid, D., Qian, M., Choong, P., & Brandt, M. (2019). Computational modelling of strut defects in SLM manufactured lattice structures. *Materials and Design*, *171*. https://doi.org/10.1016/j.matdes.2019.107671

82. Zhang, L., Feih, S., Daynes, S., Chang, S., Wang, M. Y., Wei, J., & Lu, W. F. (2018). Energy absorption characteristics of metallic triply periodic minimal surface sheet structures under compressive loading. *Additive Manufacturing*, *23*, 505–515. https://doi.org/10.1016/J.ADDMA.2018.08.007

83. Melancon, D., Bagheri, Z. S., Johnston, R. B., Liu, L., Tanzer, M., & Pasini, D. (2017). Mechanical characterization of structurally porous biomaterials built via additive manufacturing: Experiments, predictive models, and design maps for load-bearing bone replacement implants. *Acta Biomaterialia*, *63*, 350–368. https://doi.org/10.1016/J.ACTBIO.2017.09.013

84. Leary, M., Mazur, M., Williams, H., Yang, E., Alghamdi, A., Lozanovski, B., Zhang, X., Shidid, D., Farahbod-Sternahl, L., Witt, G., Kelbassa, I., Choong, P., Qian, M., & Brandt, M. (2018). Inconel 625 lattice structures manufactured by selective laser melting (SLM): Mechanical properties, deformation and failure modes. *Materials & Design*, *157*, 179–199. https://doi.org/10.1016/j.matdes.2018.06.010

85. Suard, M., Martin, G., Lhuissier, P., Dendievel, R., Vignat, F., Blandin, J.-J., & Villeneuve, F. (2015). Mechanical equivalent diameter of single struts for the stiffness prediction of lattice structures produced by Electron Beam Melting. *Additive Manufacturing*, *8*, 124–131. https://doi.org/10.1016/j.addma.2015.10.002

86. Wang, G., Shen, L., Zhao, J., Liang, H., Xie, D., Tian, Z., & Wang, C. (2018). Design and Compressive Behavior of Controllable Irregular Porous Scaffolds: Based on Voronoi-Tessellation and for Additive Manufacturing. *ACS Biomaterials Science & Engineering*, *4*(2), 719–727. https://doi.org/10.1021/acsbiomaterials.7b00916

87. Abdeen, D. H., & Palmer, B. R. (2016). Effect of processing parameters of electron beam melting machine on properties of Ti-6Al-4V parts. *Rapid Prototyping Journal*, *22*(3), 609–620. https://doi.org/10.1108/RPJ-09-2014-0105

88. Hrabe, N., & Quinn, T. (2013). Effects of processing on microstructure and mechanical properties of a titanium alloy (Ti–6Al–4V) fabricated using electron beam melting (EBM), Part 2: Energy input, orientation, and location. *Materials Science and Engineering: A*, *573*, 271–277. https://doi.org/10.1016/J.MSEA.2013.02.065

89. Kessler, J., Balc, N., Gebhardt, A., & Abbas, K. (2017). Basic design rules of unit cells for additive manufactured lattice structures. *MATEC Web of Conferences*, *137*. https://doi.org/10.1051/matecconf/201713702005

90. Pyka, G., Kerckhofs, G., Papantoniou, I., Speirs, M., Schrooten, J., & Wevers, M. (2013). Surface roughness and morphology customization of additive manufactured open porous Ti6Al4V structures. *Materials*, *6*(10). https://doi.org/10.3390/ma6104737

91. Amani, Y., Dancette, S., Delroisse, P., Simar, A., & Maire, E. (2018). Compression behavior of lattice structures produced by selective laser melting: X-ray tomography based experimental and finite element approaches. *Acta Materialia*, *159*. https://doi.org/10.1016/j.actamat.2018.08.030

92. International Organization for Standardization. (2011). ISO 13314:2011 Mechanical testing of metals – Ductility testing – Compression test for porous and cellular metals (ISO Standard No. 13314:2011(E)). *International Organization for Standardization*, *2011*(1), 1–7.

93. Wu, M.-W., Chen, J.-K., Lin, B.-H., Chiang, P.-H., & Tsai, M.-K. (2020). Compressive fatigue properties of additive-manufactured Ti-6Al-4V cellular material with different porosities. *Materials Science and Engineering: A*, *790*, 139695. https://doi.org/10.1016/j.msea.2020.139695

94. Rodrigo, C., Xu, S., Durandet, Y., Fraser, D., & Ruan, D. (2023). Quasi-static and dynamic compression of additively manufactured functionally graded lattices: Experiments and simulations. *Engineering Structures*, *284*. https://doi.org/10.1016/j.engstruct.2023.115909

95. Alaña, M., Cutolo, A., Ruiz de Galarreta, S., & Van Hooreweder, B. (2021). Influence of relative density on quasi-static and fatigue failure of lattice structures in Ti6Al4V produced by laser powder bed fusion. *Scientific Reports*, *11*(1), 19314. https://doi.org/10.1038/s41598-021-98631-3

96. Zhang, X. Z., Leary, M., Tang, H. P., Song, T., & Qian, M. (2018). Selective electron beam manufactured Ti-6Al-4V lattice structures for orthopedic implant applications: Current status and outstanding challenges. *Current Opinion in Solid State and Materials Science*, *22*(3), 75–99. https://doi.org/10.1016/j.cossms.2018.05.002

97. Van Grunsven, W., Hernandez-Nava, E., Reilly, G. C., & Goodall, R. (2014). Fabrication and Mechanical Characterisation of Titanium Lattices with Graded Porosity. *Metals*, *4*(3), 401–409. https://doi.org/10.3390/met4030401

98. Xu, Y., Zhang, D., Zhou, Y., Wang, W., & Cao, X. (2017). Study on Topology Optimization Design, Manufacturability, and Performance Evaluation of Ti-6Al-4V Porous Structures Fabricated by Selective Laser Melting (SLM). *Materials*, *10*(9), 1048. https://doi.org/10.3390/ma10091048

99. Murr, L. E., Gaytan, S. M., Medina, F., Lopez, H., Martinez, E., Machado, B. I., Hernandez, D. H., Martinez, L., Lopez, M. I., Wicker, R. B., & Bracke, J. (2010). Next-generation biomedical implants using additive manufacturing of complex, cellular and functional mesh arrays. *Philosophical Transactions of the Royal Society A: Mathematical, Physical and Engineering Sciences*, *368*(1917), 1999–2032. https://doi.org/10.1098/rsta.2010.0010

100. Parthasarathy, J., Starly, B., & Raman, S. (2011). A design for the additive manufacture of functionally graded porous structures with tailored mechanical properties for biomedical applications. *Journal of Manufacturing Processes*, *13*(2), 160–170. https://doi.org/10.1016/j.jmapro.2011.01.004

101. Li, X., Luo, Y., & Wang, C. (2012). Preparation and characterization of porous Ti6Al4V/alginate hybrid implant by combination of electron beam melting and freeze-drying. *Materials Letters*, *81*, 23–26. https://doi.org/10.1016/j.matlet.2012.04.151

102. Harrysson, O. L. A., Cansizoglu, O., Marcellin-Little, D. J., Cormier, D. R., & West, H. A. (2008). Direct metal fabrication of titanium implants with tailored materials and mechanical properties using electron beam melting technology. *Materials Science and Engineering: C*, *28*(3), 366–373. https://doi.org/10.1016/j.msec.2007.04.022

103. Horn, T. J., Harrysson, O. L. A., Marcellin-Little, D. J., West, H. A., Lascelles, B. D. X., & Aman, R. (2014). Flexural properties of Ti6Al4V rhombic dodecahedron open cellular structures fabricated with electron beam melting. *Additive Manufacturing*, *1–4*, 2–11. https://doi.org/10.1016/J.ADDMA.2014.05.001

104. Heinl, P., Körner, C., & Singer, R. F. (2008). Selective Electron Beam Melting of Cellular Titanium: Mechanical Properties. *Advanced Engineering Materials*, *10*(9), 882–888. https://doi.org/10.1002/adem.200800137

105. Shi, W., Liu, B., Li, J., Zhang, Y., Cao, S., & Jiang, W. (2025). Numerical Simulation and Mechanical Property Evaluation of Novel Ti6Al4V BCCZ Lattice Structures Prepared by Laser Powder Bed Fusion with Various Bracing Positions. *Advanced Engineering Materials*, *27*(5), 2402108. https://doi.org/10.1002/adem.202402108

106. Arputharaj, J. D., Nafisi, S., & Ghomashchi, R. (2025). Compression Behaviour of L-PBF-Manufactured Ti6Al4V BCC Lattices. *Metals*, *15*(2), 220. https://doi.org/10.3390/met15020220

107. Timercan, A., Terriault, P., & Brailovski, V. (2023). Axial tension/compression and torsional loading of diamond and gyroid lattice structures for biomedical implants: Simulation and experiment. *Materials & Design*, *225*, 111585. https://doi.org/10.1016/J.MATDES.2022.111585

108. Li, P. Y., Ma, Y. E., Sun, W. B., Qian, X., Zhang, W., & Wang, Z. H. (2022). Mechanical behaviors and failure modes of additive manufactured Ti6Al4V lattice structures under compressive load. *Thin-Walled Structures*, *180*. https://doi.org/10.1016/j.tws.2022.109778

109. Wang, N., Meenashisundaram, G. K., Kandilya, D., Fuh, J. Y. H., Dheen, S. T., & Kumar, A. S. (2022). A biomechanical evaluation on Cubic, Octet, and TPMS gyroid Ti6Al4V lattice structures fabricated by selective laser melting and the effects of their debris on human osteoblast-like cells. *Biomaterials Advances*, *137*, 212829. https://doi.org/10.1016/j.bioadv.2022.212829

110. Karamooz Ravari, M. R., Kadkhodaei, M., Badrossamay, M., & Rezaei, R. (2014). Numerical investigation on mechanical properties of cellular lattice structures fabricated by fused deposition modeling. *International Journal of Mechanical Sciences*, *88*, 154–161. https://doi.org/10.1016/j.ijmecsci.2014.08.009

111. Meng, L., Qiu, X., Gao, T., Li, Z., & Zhang, W. (2020). An inverse approach to the accurate modelling of 3D-printed sandwich panels with lattice core using beams of variable cross-section. *Composite Structures*, *247*, 112363. https://doi.org/10.1016/J.COMPSTRUCT.2020.112363

112. Fallahi, H., Sadighi, M., & Samandari, S. S. (2023). Compressive mechanical properties of open-cell cubic and rhombic dodecahedron lattice structures of variable cross section fabricated by fused deposition modeling. *Mechanics of Materials*, *184*, 104712. https://doi.org/10.1016/j.mechmat.2023.104712

113. Zhao, M., Li, X., Zhang, D. Z., & Zhai, W. (2023). TPMS-based interpenetrating lattice structures: Design, mechanical properties and multiscale optimization. *International Journal of Mechanical Sciences*, *244*. https://doi.org/10.1016/j.ijmecsci.2022.108092

114. Dong, G., Ding, Y., Teawdeswan, L., Luo, C., & Yu, K. (2022). *Experimental and Numerical Analysis of Lattice Structures with Different Heterogeneities*. https://hdl.handle.net/2152/117527

115. Quevedo González, F. J., & Nuño, N. (2016). Finite element modelling approaches for well-ordered porous metallic materials for orthopaedic applications: Cost effectiveness and geometrical considerations. *Computer Methods in Biomechanics and Biomedical Engineering*, *19*(8). https://doi.org/10.1080/10255842.2015.1075009

116. Bai, L., Xu, Y., Chen, X., Xin, L., Zhang, J., Li, K., & Sun, Y. (2021). Improved mechanical properties and energy absorption of Ti6Al4V laser powder bed fusion lattice structures using curving lattice struts. *Materials and Design*, *211*, 110140. https://doi.org/10.1016/j.matdes.2021.110140

117. Radlof, W., Benz, C., & Sander, M. (2021). Numerical and experimental investigations of additively manufactured lattice structures under quasi-static compression loading. *Material Design & Processing Communications*, *3*(3), e164. https://doi.org/10.1002/mdp2.164

118. Crupi, V., Kara, E., Epasto, G., Guglielmino, E., & Aykul, H. (2017). Static behavior of lattice structures produced via direct metal laser sintering technology. *Materials & Design*, *135*, 246–256. https://doi.org/10.1016/J.MATDES.2017.09.003

119. Gümrük, R., & Mines, R. A. W. (2013). Compressive behaviour of stainless steel micro-lattice structures. *International Journal of Mechanical Sciences*, *68*, 125–139. https://doi.org/10.1016/J.IJMECSCI.2013.01.006

120. Gonzalez, F. J. Q., & Nuno, N. (2016). Finite element modeling of manufacturing irregularities of porous materials. *Biomaterials and Biomechanics in Bioengineering*, *3*(1). https://doi.org/10.12989/bme.2016.3.1.001

121. Mehboob, H., Tarlochan, F., Mehboob, A., & Chang, S.-H. (2018). Finite element modelling and characterization of 3D cellular microstructures for the design of a cementless biomimetic porous hip stem. *Materials & Design*, *149*, 101–112. https://doi.org/10.1016/j.matdes.2018.04.002

122. Guo, H., Takezawa, A., Honda, M., Kawamura, C., & Kitamura, M. (2020). Finite element simulation of the compressive response of additively manufactured lattice structures with large diameters. *Computational Materials Science*, *175*, 109610. https://doi.org/10.1016/j.commatsci.2020.109610

123. Wang, P., Yang, F., Lu, G., Bian, Y., Zhang, S., Zheng, B., & Fan, H. (2022). Anisotropic compression behaviors of bio-inspired modified body-centered cubic lattices validated by additive manufacturing. *Composites Part B: Engineering*, *234*, 109724. https://doi.org/10.1016/j.compositesb.2022.109724

124. Kappe, K., Hoschke, K., Riedel, W., & Hiermaier, S. (2024). Multi-objective optimization of additive manufactured functionally graded lattice structures under impact. *International Journal of Impact Engineering*, *183*. https://doi.org/10.1016/j.ijimpeng.2023.104789

125. Liu, Y. J., Li, S. J., Zhang, L. C., Hao, Y. L., & Sercombe, T. B. (2018). Early plastic deformation behaviour and energy absorption in porous β-type biomedical titanium produced by selective laser melting. *Scripta Materialia*, *153*, 99–103. https://doi.org/10.1016/j.scriptamat.2018.05.010

126. Vivien Challis, B. J., Roberts, A. P., Grotowski, J. F., Zhang, L.-C., Sercombe, T. B., Challis, V. J., Roberts, A. P., Grotowski, J. F., Zhang, L. C., & Sercombe, T. B. (2010). Prototypes for Bone Implant Scaffolds Designed via Topology Optimization and Manufactured by Solid Freeform Fabrication. *Advanced Engineering Materials*, *12*(11), 1106–1110. https://doi.org/10.1002/ADEM.201000154

127. Gong, H., Rafi, K., Gu, H., Starr, T., & Stucker, B. (2014). Analysis of defect generation in Ti–6Al–4V parts made using powder bed fusion additive manufacturing processes. *Additive Manufacturing*, *1–4*, 87–98. https://doi.org/10.1016/J.ADDMA.2014.08.002

128. Buhairi, M. A., Foudzi, F. M., Jamhari, F. I., Sulong, A. B., Radzuan, N. A. M., Muhamad, N., Mohamed, I. F., Azman, A. H., Harun, W. S. W., & Al-Furjan, M. S. H. (2022). Review on volumetric energy density: Influence on morphology and mechanical properties of Ti6Al4V manufactured via laser powder bed fusion. *Progress in Additive Manufacturing 2022 8:2*, *8*(2), 265–283. https://doi.org/10.1007/S40964-022-00328-0

129. Luo, Q., Yin, L., Simpson, T. W., & Beese, A. M. (2022). Effect of processing parameters on pore structures, grain features, and mechanical properties in Ti-6Al-4V by laser powder bed fusion. *Additive Manufacturing*, *56*, 102915. https://doi.org/10.1016/J.ADDMA.2022.102915

130. Dai, D., & Gu, D. (2014). Thermal behavior and densification mechanism during selective laser melting of copper matrix composites: Simulation and experiments. *Materials & Design*, *55*, 482–491. https://doi.org/10.1016/J.MATDES.2013.10.006

131. Salem, H., Carter, L. N., Attallah, M. M., & Salem, H. G. (2019). Influence of processing parameters on internal porosity and types of defects formed in Ti6Al4V lattice structure fabricated by selective laser melting. *Materials Science and Engineering: A*, *767*, 138387. https://doi.org/10.1016/j.msea.2019.138387

132. Karami, K., Blok, A., Weber, L., Ahmadi, S. M., Petrov, R., Nikolic, K., Borisov, E. V., Leeflang, S., Ayas, C., Zadpoor, A. A., Mehdipour, M., Reinton, E., & Popovich, V. A. (2020). Continuous and pulsed selective laser melting of Ti6Al4V lattice structures: Effect of post-processing on microstructural anisotropy and fatigue behaviour. *Additive Manufacturing*, *36*, 101433. https://doi.org/10.1016/j.addma.2020.101433

133. Galati, M., & Iuliano, L. (2018). A literature review of powder-based electron beam melting focusing on numerical simulations. *Additive Manufacturing*, *19*, 1–20. https://doi.org/10.1016/J.ADDMA.2017.11.001

134. De Pasquale, G., Luceri, F., & Riccio, M. (2019). Experimental Characterization of SLM and EBM Cubic Lattice Structures for Lightweight Applications. *Experimental Mechanics*, *59*(4), 469–482. https://doi.org/10.1007/S11340-019-00481-8/FIGURES/9

135. Mohammad, A., Alahmari, A. M., Mohammed, M. K., Renganayagalu, R. K., & Moiduddin, K. (2017). Effect of Energy Input on Microstructure and Mechanical Properties of Titanium Aluminide Alloy Fabricated by the Additive Manufacturing Process of Electron Beam Melting. *Materials 2017, Vol. 10, Page 211*, *10*(2), 211. https://doi.org/10.3390/MA10020211

136. Gong, H., Rafi, K., Starr, T., & Stucker, B. (2013). The Effects of Processing Parameters on Defect Regularity in Ti-6Al-4V Parts Fabricated By Selective Laser Melting and Electron Beam Melting. *International Solid Freeform Fabrication Symposium*. https://doi.org/http://dx.doi.org/10.26153/tsw/15565

137. Galati, M., Snis, A., & Iuliano, L. (2019). Experimental validation of a numerical thermal model of the EBM process for Ti6Al4V. *Computers & Mathematics with Applications*, *78*(7), 2417–2427. https://doi.org/10.1016/J.CAMWA.2018.07.020

138. Prisco, U., Astarita, A., El Hassanin, A., & Franchitti, S. (2019). Influence of processing parameters on microstructure and roughness of electron beam melted Ti-6Al-4V titanium alloy. *Materials and Manufacturing Processes*, *34*(15), 1753–1760. https://doi.org/10.1080/10426914.2019.1683576;REQUESTEDJOURNAL:JOURNAL:LMMP20;WGROUP:STRING:PUBLICATION

139. Scharowsky, T., Bauereiß, A., & Körner, C. (2017). Influence of the hatching strategy on consolidation during selective electron beam melting of Ti-6Al-4V. *International Journal of Advanced Manufacturing Technology*, *92*(5–8), 2809–2818. https://doi.org/10.1007/S00170-017-0375-1/METRICS

140. Wang, X., Gong, X., & Chou, K. (2015). Scanning Speed Effect on Mechanical Properties of Ti-6Al-4V Alloy Processed by Electron Beam Additive Manufacturing. *Procedia Manufacturing*, *1*, 287–295. https://doi.org/10.1016/J.PROMFG.2015.09.026

141. Galati, M., Giordano, M., & Iuliano, L. (2023). Process-aware optimisation of lattice structure by electron beam powder bed fusion. *Progress in Additive Manufacturing*, *8*(3). https://doi.org/10.1007/s40964-022-00339-x

142. Aiza, I., Baldi, C., de la Vega, F. M., Sebastiani, S., Veronese, N. E., Yousefi, M., Mosallanejad, M. H., Maleki, E., Guagliano, M., Iuliano, L., Saboori, A., & Bagherifard, S. (2025). Effects of build orientation and inclined features on physical, microstructural and mechanical properties of powder bed fusion additively manufactured metallic parts. *Progress in Materials Science*, *147*, 101357. https://doi.org/10.1016/J.PMATSCI.2024.101357

143. Hossain, U., Ghouse, S., Nai, K., & Jeffers, J. R. T. (2021). Mechanical and morphological properties of additively manufactured SS316L and Ti6Al4V micro-struts as a function of build angle. *Additive Manufacturing*, *46*, 102050. https://doi.org/10.1016/J.ADDMA.2021.102050

144. Dong, Z., Liu, Y., Li, W., & Liang, J. (2019). Orientation dependency for microstructure, geometric accuracy and mechanical properties of selective laser melting AlSi10Mg lattices. *Journal of Alloys and Compounds*, *791*. https://doi.org/10.1016/j.jallcom.2019.03.344

145. Pehlivan, E., Roudnicka, M., Dzugan, J., Koukolikova, M., Králík, V., Seifi, M., Lewandowski, J. J., Dalibor, D., & Daniel, M. (2020). Effects of build orientation and sample geometry on the mechanical response of miniature CP-Ti Grade 2 strut samples manufactured by laser powder bed fusion. *Additive Manufacturing*, *35*. https://doi.org/10.1016/j.addma.2020.101403

146. Barba, D., Alabort, C., Tang, Y. T., Viscasillas, M. J., Reed, R. C., & Alabort, E. (2020). On the size and orientation effect in additive manufactured Ti-6Al-4V. *Materials & Design*, *186*, 108235. https://doi.org/10.1016/J.MATDES.2019.108235

147. Murchio, S., Dallago, M., Zanini, F., Carmignato, S., Zappini, G., Berto, F., Maniglio, D., & Benedetti, M. (2021). Additively manufactured Ti–6Al–4V thin struts via laser powder bed fusion: Effect of building orientation on geometrical accuracy and mechanical properties. *Journal of the Mechanical Behavior of Biomedical Materials*, *119*, 104495. https://doi.org/10.1016/j.jmbbm.2021.104495

148. Sepe, R., De Luca, A., Giannella, V., Borrelli, R., Franchitti, S., Di Caprio, F., & Caputo, F. (2022). Influence of dimension, building position, and orientation on mechanical properties of EBM lattice Ti6Al4V trusses. *International Journal of Advanced Manufacturing Technology*, *122*(7–8), 3183–3198. https://doi.org/10.1007/S00170-022-10051-3/FIGURES/15

149. Wauthle, R., Vrancken, B., Beynaerts, B., Jorissen, K., Schrooten, J., Kruth, J.-P., & Van Humbeeck, J. (2015). Effects of build orientation and heat treatment on the microstructure and mechanical properties of selective laser melted Ti6Al4V lattice structures. *Additive Manufacturing*, *5*, 77–84. https://doi.org/10.1016/j.addma.2014.12.008

150. Dallago, M., Raghavendra, S., Luchin, V., Zappini, G., Pasini, D., & Benedetti, M. (2021). The role of node fillet, unit-cell size and strut orientation on the fatigue strength of Ti-6Al-4V lattice materials additively manufactured via laser powder bed fusion. *International Journal of Fatigue*, *142*, 105946. https://doi.org/10.1016/j.ijfatigue.2020.105946

151. Algardh, J. K., Horn, T., West, H., Aman, R., Snis, A., Engqvist, H., Lausmaa, J., & Harrysson, O. (2016). Thickness dependency of mechanical properties for thin-walled titanium parts manufactured by Electron Beam Melting (EBM)®. *Additive Manufacturing*, *12*, 45–50. https://doi.org/10.1016/j.addma.2016.06.009

152. Liu, L., Kamm, P., García-Moreno, F., Banhart, J., & Pasini, D. (2017). Elastic and failure response of imperfect three-dimensional metallic lattices: The role of geometric defects induced by Selective Laser Melting. *Journal of the Mechanics and Physics of Solids*, *107*, 160–184. https://doi.org/10.1016/j.jmps.2017.07.003

153. Li, D., Qin, R., Chen, B., & Zhou, J. (2021). Analysis of mechanical properties of lattice structures with stochastic geometric defects in additive manufacturing. *Materials Science and Engineering: A*, *822*, 141666. https://doi.org/10.1016/j.msea.2021.141666

154. Cao, X., Jiang, Y., Zhao, T., Wang, P., Wang, Y., Chen, Z., Li, Y., Xiao, D., & Fang, D. (2020). Compression experiment and numerical evaluation on mechanical responses of the lattice structures with stochastic geometric defects originated from additive-manufacturing. *Composites Part B: Engineering*, *194*, 108030. https://doi.org/10.1016/j.compositesb.2020.108030

155. Li, P., Sun, W., Zhang, W., & Ma, Y. E. (2024). Effect of geometric defects on the mechanical properties of additive manufactured Ti6Al4V lattice structures. *Thin-Walled Structures*, *205*, 112497. https://doi.org/10.1016/j.tws.2024.112497

156. Gong, H., Rafi, K., Gu, H., Janaki Ram, G. D., Starr, T., & Stucker, B. (2015). Influence of defects on mechanical properties of Ti–6Al–4 V components produced by selective laser melting and electron beam melting. *Materials & Design*, *86*, 545–554. https://doi.org/10.1016/j.matdes.2015.07.147

157. du Plessis, A., Yadroitsava, I., & Yadroitsev, I. (2020). Effects of defects on mechanical properties in metal additive manufacturing: A review focusing on X-ray tomography insights. *Materials & Design*, *187*, 108385. https://doi.org/10.1016/j.matdes.2019.108385

158. Yan, C., Hao, L., Hussein, A., & Raymont, D. (2012). Evaluations of cellular lattice structures manufactured using selective laser melting. *International Journal of Machine Tools and Manufacture*, *62*, 32–38. https://doi.org/10.1016/j.ijmachtools.2012.06.002

159. Wares, M. A., Kader, M. A., Islam, M. A., & Ahmed, S. (2025). Effects of artificial defects on the mechanical properties of additively manufactured gyroid unit cell. *Materials & Design*, *257*, 114477. https://doi.org/10.1016/j.matdes.2025.114477

160. Strauss, J., Salojee, M., Plessis, A. D., Zhirnov, I., Krakmale, P., & Khodja, M. (2022). An investigation into the properties of 3D printed Ti6Al4V FCC lattice structures with different strut thicknesses. *MATEC Web of Conferences*, *370*, 08002. https://doi.org/10.1051/matecconf/202237008002

161. du Plessis, A., Yadroitsava, I., Kouprianoff, D., & Yadroitsev, I. (2018). *Numerical and Experimental Study on the Effect of Artificial Porosity in a Lattice Structure Manufactured by Laser Based Powder Bed Fusion*. https://hdl.handle.net/2152/90158

162. Cutolo, A., Engelen, B., Desmet, W., & Van Hooreweder, B. (2020). Mechanical properties of diamond lattice Ti–6Al–4V structures produced by laser powder bed fusion: On the effect of the load direction. *Journal of the Mechanical Behavior of Biomedical Materials*, *104*, 103656. https://doi.org/10.1016/j.jmbbm.2020.103656

163. Soul, H., Terriault, P., & Brailovski, V. (2018). The Static and Fatigue Behavior of AlSiMg Alloy Plain, Notched, and Diamond Lattice Specimens Fabricated by Laser Powder Bed Fusion. *Journal of Manufacturing and Materials Processing*, *2*(2), 25. https://doi.org/10.3390/jmmp2020025

164. Butt, M. M., Laieghi, H., Kvvssn, V., Uddin, Z., Shah, M., Ansari, P., Salamci, M. U., Patterson, A. E., & Kizil, H. (2025). Fatigue performance in additively manufactured metal alloys. *Progress in Additive Manufacturing*, *10*(4), 1809–1841. https://doi.org/10.1007/s40964-024-00738-2

165. Yadollahi, A., Shamsaei, N., Thompson, S. M., Elwany, A., & Bian, L. (2017). Effects of building orientation and heat treatment on fatigue behavior of selective laser melted 17-4 PH stainless steel. *International Journal of Fatigue, Fatigue and Fracture Behavior of Additive Manufactured Parts*, *94*, 218–235. https://doi.org/10.1016/j.ijfatigue.2016.03.014

166. Özbilen, S., Liebert, D., Beck, T., & Bram, M. (2016). Fatigue behavior of highly porous titanium produced by powder metallurgy with temporary space holders. *Materials Science and Engineering: C*, *60*, 446–457. https://doi.org/10.1016/j.msec.2015.11.050

167. Boniotti, L., Beretta, S., Patriarca, L., Rigoni, L., & Foletti, S. (2019). Experimental and numerical investigation on compressive fatigue strength of lattice structures of AlSi7Mg manufactured by SLM. *International Journal of Fatigue*, *128*, 105181. https://doi.org/10.1016/j.ijfatigue.2019.06.041

168. Kwofie, S. (2001). An exponential stress function for predicting fatigue strength and life due to mean stresses. *International Journal of Fatigue*, *23*(9), 829–836. https://doi.org/10.1016/S0142-1123(01)00044-5

169. Prados-Privado, M., Prados-Frutos, J. C., Manchón, Á., Rojo, R., Felice, P., & Bea, J. A. (2015). Dental Implants Fatigue as a Possible Failure of Implantologic Treatment: The Importance of Randomness in Fatigue Behaviour. *BioMed Research International*, *2015*(1), 825402. https://doi.org/10.1155/2015/825402

170. Cutolo, A., & Van Hooreweder, B. (2022). Fatigue behaviour of diamond based Ti-6Al-4V lattice structures produced by laser powder bed fusion: On the effect of load direction. *Materials Today Communications*, *33*, 104661. https://doi.org/10.1016/j.mtcomm.2022.104661

171. Wu, Z. Y., Liu, Y. J., Wu, X., Liu, X. C., Wang, J. C., & Wang, Q. (2024). Fatigue performance of beta titanium alloy topological porous structures fabricated by laser powder bed fusion. *Journal of Materials Research and Technology*, *29*, 4772–4780. https://doi.org/10.1016/j.jmrt.2024.02.190

172. Ahmadi, S. M., Kumar, R., Borisov, E. V., Petrov, R., Leeflang, S., Li, Y., Tümer, N., Huizenga, R., Ayas, C., Zadpoor, A. A., & Popovich, V. A. (2019). From microstructural design to surface engineering: A tailored approach for improving fatigue life of additively manufactured meta-biomaterials. *Acta Biomaterialia*, *83*. https://doi.org/10.1016/j.actbio.2018.10.043

173. Van Hooreweder, B., Apers, Y., Lietaert, K., & Kruth, J.-P. (2017). Improving the fatigue performance of porous metallic biomaterials produced by Selective Laser Melting. *Acta Biomaterialia*, *47*, 193–202. https://doi.org/10.1016/j.actbio.2016.10.005

174. Amin Yavari, S., Ahmadi, S. M., Wauthle, R., Pouran, B., Schrooten, J., Weinans, H., & Zadpoor, A. A. (2015). Relationship between unit cell type and porosity and the fatigue behavior of selective laser melted meta-biomaterials. *Journal of the Mechanical Behavior of Biomedical Materials*, *43*, 91–100. https://doi.org/10.1016/j.jmbbm.2014.12.015

175. Li, S. J., Murr, L. E., Cheng, X. Y., Zhang, Z. B., Hao, Y. L., Yang, R., Medina, F., & Wicker, R. B. (2012). Compression fatigue behavior of Ti–6Al–4V mesh arrays fabricated by electron beam melting. *Acta Materialia*, *60*(3), 793–802. https://doi.org/10.1016/j.actamat.2011.10.051

176. Liu, Y. J., Wang, H. L., Li, S. J., Wang, S. G., Wang, W. J., Hou, W. T., Hao, Y. L., Yang, R., & Zhang, L. C. (2017). Compressive and fatigue behavior of beta-type titanium porous structures fabricated by electron beam melting. *Acta Materialia*, *126*, 58–66. https://doi.org/10.1016/j.actamat.2016.12.052

177. Liu, Y. J., Ren, D. C., Li, S. J., Wang, H., Zhang, L. C., & Sercombe, T. B. (2020). Enhanced fatigue characteristics of a topology-optimized porous titanium structure produced by selective laser melting. *Additive Manufacturing*, *32*, 101060. https://doi.org/10.1016/j.addma.2020.101060

178. Zhao, S., Li, S. J., Wang, S. G., Hou, W. T., Li, Y., Zhang, L. C., Hao, Y. L., Yang, R., Misra, R. D. K., & Murr, L. E. (2018). Compressive and fatigue behavior of functionally graded Ti-6Al-4V meshes fabricated by electron beam melting. *Acta Materialia*, *150*, 1–15. https://doi.org/10.1016/j.actamat.2018.02.060

179. Yuan, W., Hou, W., Li, S., Hao, Y., Yang, R., Zhang, L.-C., & Zhu, Y. (2018). Heat treatment enhancing the compressive fatigue properties of open-cellular Ti-6Al-4V alloy prototypes fabricated by electron beam melting. *Journal of Materials Science & Technology*, *34*(7), 1127–1131. https://doi.org/10.1016/j.jmst.2017.12.003

180. Radlof, W., Polley, C., Seitz, H., & Sander, M. (2021). Influence of structure-determining parameters on the mechanical properties and damage behavior of electron beam melted lattice structures under quasi-static and fatigue compression loading. *Materials Letters*, *289*, 129380. https://doi.org/10.1016/j.matlet.2021.129380

181. Peng, C., Tran, P., Nguyen-Xuan, H., & Ferreira, A. J. M. (2020). Mechanical performance and fatigue life prediction of lattice structures: Parametric computational approach. *Composite Structures*, *235*, 111821. https://doi.org/10.1016/j.compstruct.2019.111821

182. Hedayati, R., Hosseini-Toudeshky, H., Sadighi, M., Mohammadi-Aghdam, M., & Zadpoor, A. A. (2016). Computational prediction of the fatigue behavior of additively manufactured porous metallic biomaterials. *International Journal of Fatigue*, *84*, 67–79. https://doi.org/10.1016/J.IJFATIGUE.2015.11.017

183. Miner, M. A. (1945). Cumulative Damage in Fatigue. *Journal of Applied Mechanics*, *12*(3), A159–A164. https://doi.org/10.1115/1.4009458

184. Zargarian, A., Esfahanian, M., Kadkhodapour, J., & Ziaei-Rad, S. (2016). Numerical simulation of the fatigue behavior of additive manufactured titanium porous lattice structures. *Materials Science and Engineering: C*, *60*, 339–347. https://doi.org/10.1016/J.MSEC.2015.11.054

185. Murchio, S., Dallago, M., Rigatti, A., Luchin, V., Berto, F., Maniglio, D., & Benedetti, M. (2021). On the effect of the node and building orientation on the fatigue behavior of L-PBF Ti6Al4V lattice structure sub-unital elements. *Material Design and Processing Communications*, *3*(6). https://doi.org/10.1002/mdp2.258

186. De Biasi, R., Murchio, S., Sbettega, E., Carmignato, S., Luchin, V., & Benedetti, M. (2023). Efficient optimization framework for L-PBF fatigue enhanced Ti6Al4V lattice component. *Materials and Design*, *230*. https://doi.org/10.1016/j.matdes.2023.111975

187. Persenot, T., Burr, A., Martin, G., Buffiere, J. Y., Dendievel, R., & Maire, E. (2019). Effect of build orientation on the fatigue properties of as-built Electron Beam Melted Ti-6Al-4V alloy. *International Journal of Fatigue*, *118*, 65–76. https://doi.org/10.1016/j.ijfatigue.2018.08.006

188. Zhang, J. S., Deng, Y., Liu, H., Tang, Y. T., Lui, A., Grant, P. S., Alabort, E., Reed, R. C., & Cocks, A. C. F. (2024). Orientation matters: Assessing the cyclic deformation behaviour of laser powder bed fusion Ti-6Al-4V. *Materials & Design*, *248*, 113485. https://doi.org/10.1016/J.MATDES.2024.113485

189. Murakami, Y. (2019). *Metal Fatigue: Effects of Small Defects and Nonmetallic Inclusions* (2nd ed.). Academic Press. https://dx.doi.org/10.1016/C2016-0-05272-5

190. Qian, W., Wu, S., Wu, Z., Ahmed, S., Zhang, W., Qian, G., & Withers, P. J. (2022). *In situ* X-ray imaging of fatigue crack growth from multiple defects in additively manufactured AlSi10Mg alloy. *International Journal of Fatigue*, *155*, 106616. https://doi.org/10.1016/j.ijfatigue.2021.106616

191. Tammas-Williams, S., Withers, P. J., Todd, I., & Prangnell, P. B. (2017). The Influence of Porosity on Fatigue Crack Initiation in Additively Manufactured Titanium Components. *Scientific Reports*, *7*(1), 7308. https://doi.org/10.1038/s41598-017-06504-5

192. Kitagawa, H. (1976). Applicability of fracture mechanics to very small cracks or the cracks in the early stage. *Proc. 2nd Int. Conf. on Mechanical Behaviour of Materials*, 627–631.

193. El Haddad, M., Smith, K., & Topper, T. (1979). *Fatigue crack propagation of short cracks*.

194. Zerbst, U., Bruno, G., Buffière, J.-Y., Wegener, T., Niendorf, T., Wu, T., Zhang, X., Kashaev, N., Meneghetti, G., Hrabe, N., Madia, M., Werner, T., Hilgenberg, K., Koukolíková, M., Procházka, R., Džugan, J., Möller, B., Beretta, S., Evans, A., … Schnabel, K. (2021). Damage tolerant design of additively manufactured metallic components subjected to cyclic loading: State of the art and challenges. *Progress in Materials Science*, *121*, 100786. https://doi.org/10.1016/j.pmatsci.2021.100786

195. Pagliari, L., Gerosa, R., Panzeri, D., Fraccaroli, L., & Concli, F. (2025). High- and low-cycle fatigue behavior of additively manufactured Ti6Al4V and influence of surface finish. *Engineering Failure Analysis*, *180*, 109825. https://doi.org/10.1016/j.engfailanal.2025.109825

196. Liu, F., He, C., Chen, Y., Zhang, H., Wang, Q., & Liu, Y. (2020). Effects of defects on tensile and fatigue behaviors of selective laser melted titanium alloy in very high cycle regime. *International Journal of Fatigue*, *140*, 105795. https://doi.org/10.1016/j.ijfatigue.2020.105795

197. Heinz, S., & Eifler, D. (2016). Crack initiation mechanisms of Ti6Al4V in the very high cycle fatigue regime. *International Journal of Fatigue, Gigacycle Fatigue-Theory and Applications Dedicated to the Memory of Professor Claude Bathias*, *93*, 301–308. https://doi.org/10.1016/j.ijfatigue.2016.04.026

198. Javidrad, H., Koc, B., Bayraktar, H., Simsek, U., & Gunaydin, K. (2024). Fatigue performance of metal additive manufacturing: A comprehensive overview. *Virtual and Physical Prototyping*, *19*(1), e2302556. https://doi.org/10.1080/17452759.2024.2302556

199. Le, V.-D., Pessard, E., Morel, F., & Prigent, S. (2020). Fatigue behaviour of additively manufactured Ti-6Al-4V alloy: The role of defects on scatter and statistical size effect. *International Journal of Fatigue*, *140*, 105811. https://doi.org/10.1016/j.ijfatigue.2020.105811

200. Moore, M. C., Dubin, J. A., Monárrez, R., Bains, S. S., Hameed, D., Nace, J., Mont, M. A., & Delanois, R. E. (2024). Cemented Versus Cementless Femoral Fixation for Total Hip Arthroplasty Following Osteoarthritis. *Journal of Arthroplasty*, *39*(6), 1545–1549. https://doi.org/10.1016/j.arth.2023.12.024

201. Della Valle, A. G., Zoppi, A., Peterson, M. G. E., & Salvati, E. A. (2005). A Rough Surface Finish Adversely Affects the Survivorship of a Cemented Femoral Stem. *Clinical Orthopaedics and Related Research®*, *436*, 158.

202. Maggs, J., & Wilson, M. (2017). The Relative Merits of Cemented and Uncemented Prostheses in Total Hip Arthroplasty. *Indian Journal of Orthopaedics*, *51*(4), 377. https://doi.org/10.4103/ORTHO.IJORTHO_405_16

203. Holzwarth, U., & Cotogno, G. (2012). *Total hip arthroplasty: State of the art, challenges and prospects*. Publications Office of the European Union. https://doi.org/10.2788/31679

204. Feyen, H., & Shimmin, A. J. (2014). Is the length of the femoral component important in primary total hip replacement? *Bone and Joint Journal*, *96 B*(4), 442–448. https://doi.org/10.1302/0301-620X.96B4.33036/LETTERTOEDITOR

205. Khanuja, H. S., Vakil, J. J., Goddard, M. S., & Mont, M. A. (2011). Cementless femoral fixation in total hip arthroplasty. *Journal of Bone and Joint Surgery*, *93*(5), 500–509. https://doi.org/10.2106/JBJS.J.00774

206. Zimmer Biomet. (2024, September). *Total Hip Arthroplasty Z1 Triple Taper Hip Stem*.

207. Zimmer Biomet. (2021, February 19). *Avenir Complete ™ Hip System*.

208. Stryker. (2022). *Accolade ® II Femoral Hip System Surgical protocol Accolade II Femoral Hip System Surgical protocol*.

209. Stryker. (2022). *Insignia ® Hip Stem Design rationale*.

210. DePuy Synthes. (2022). *EMPHASYS™ Femoral Solutions*. https://www.jnjmedtech.com/en-US/product/emphasys-femoral-solutions

211. DePuy Synthes. (2022). *SUMMIT Tapered Hip System*. https://www.jnjmedtech.com/en-US/product/summit-tapered-hip-system

212. Pardo, F., Bordini, B., Castagnini, F., Giardina, F., Faldini, C., & Traina, F. (2021). Are powder-technology-built stems safe? A midterm follow-up registry study. *Journal of Materials Science: Materials in Medicine*, *32*(1), 1–6. https://doi.org/10.1007/S10856-020-06481-8/FIGURES/4

213. Gruen, T. A., McNeice, G. M., & Amstutz, H. C. (1979). "Modes of failure" of cemented stem-type femoral components. A radiographic analysis of loosening. *Clinical Orthopaedics and Related Research*, *NO 141*.

214. Limmahakhun, S., Oloyede, A., Chantarapanich, N., Jiamwatthanachai, P., Sitthiseripratip, K., Xiao, Y., & Yan, C. (2017). Alternative designs of load–sharing cobalt chromium graded femoral stems. *Materials Today Communications*, *12*, 1–10. https://doi.org/10.1016/j.mtcomm.2017.05.002

215. Rahmat, N., Kadkhodapour, J., & Arbabtafti, M. (2023). Study of cellular femoral stem for stress shielding and interface stability. *The International Journal of Artificial Organs*, *46*(6), 370–377. https://doi.org/10.1177/03913988231168158

216. Huiskes, R., Weinans, H., Grootenboer, H. J., Dalstra, M., Fudala, B., & Slooff, T. J. (1987). Adaptive bone-remodeling theory applied to prosthetic-design analysis. *Journal of Biomechanics*, *20*(11–12), 1135–1150. https://doi.org/10.1016/0021-9290(87)90030-3

217. Naghavi, S. A., Tamaddon, M., Garcia-Souto, P., Moazen, M., Taylor, S., Hua, J., & Liu, C. (2023). A novel hybrid design and modelling of a customised graded Ti-6Al-4V porous hip implant to reduce stress-shielding: An experimental and numerical analysis. *Frontiers in Bioengineering and Biotechnology*, *11*. https://doi.org/10.3389/fbioe.2023.1092361

218. Alkhatib, S. E., Tarlochan, F., Mehboob, H., Singh, R., Kadirgama, K., & Harun, W. S. B. W. (2019). Finite element study of functionally graded porous femoral stems incorporating body-centered cubic structure. *Artificial Organs*, *43*(7), E152–E164. https://doi.org/10.1111/aor.13444

219. Mehboob, H., Ahmad, F., Tarlochan, F., Mehboob, A., & Chang, S. H. (2020). A comprehensive analysis of bio-inspired design of femoral stem on primary and secondary stabilities using mechanoregulatory algorithm. *Biomechanics and Modeling in Mechanobiology*, *19*(6), 2213–2226. https://doi.org/10.1007/S10237-020-01334-3/FIGURES/8

220. Wang, S., Zhou, X., Liu, L., Shi, Z., & Hao, Y. (2020). On the design and properties of porous femoral stems with adjustable stiffness gradient. *Medical Engineering & Physics*, *81*, 30–38. https://doi.org/10.1016/j.medengphy.2020.05.003

221. Liu, B., Wang, H., Zhang, M., Li, J., Zhang, N., Luan, Y., Fang, C., & Cheng, C. K. (2023). Capability of auxetic femoral stems to reduce stress shielding after total hip arthroplasty. *Journal of Orthopaedic Translation*, *38*, 220–228. https://doi.org/10.1016/J.JOT.2022.11.001

222. Rana, M., Karmakar, S., Bandyopadhyay, A., & Roychowdhury, A. (2023). Design and manufacturing of patient-specific Ti6Al4V implants with inhomogeneous porosity. *Journal of the Mechanical Behavior of Biomedical Materials*, *143*, 105925. https://doi.org/10.1016/J.JMBBM.2023.105925

223. Hazlehurst, K. B., Wang, C. J., & Stanford, M. (2014). An investigation into the flexural characteristics of functionally graded cobalt chrome femoral stems manufactured using selective laser melting. *Materials & Design*, *60*, 177–183. https://doi.org/10.1016/j.matdes.2014.03.068

224. Simoneau, C., Terriault, P., Jetté, B., Dumas, M., & Brailovski, V. (2017). Development of a porous metallic femoral stem: Design, manufacturing, simulation and mechanical testing. *Materials & Design*, *114*, 546–556. https://doi.org/10.1016/j.matdes.2016.10.064

225. Jetté, B., Brailovski, V., Dumas, M., Simoneau, C., & Terriault, P. (2018). Femoral stem incorporating a diamond cubic lattice structure: Design, manufacture and testing. *Journal of the Mechanical Behavior of Biomedical Materials*, *77*, 58–72. https://doi.org/10.1016/j.jmbbm.2017.08.034

226. Marcellin-Little, D. J., Cansizoglu, O., Harrysson, O. L. A., & Roe, S. C. (2010). In vitro evaluation of a low-modulus mesh canine prosthetic hip stem. *American Journal of Veterinary Research*, *71*(9), 1089–1095. https://doi.org/10.2460/ajvr.71.9.1089

227. Abate, K. M., Nazir, A., & Jeng, J. Y. (2021). Design, optimization, and selective laser melting of vin tiles cellular structure-based hip implant. *International Journal of Advanced Manufacturing Technology*. https://doi.org/10.1007/s00170-020-06323-5

228. Cortis, G., Mileti, I., Nalli, F., Palermo, E., & Cortese, L. (2022). Additive manufacturing structural redesign of hip prostheses for stress-shielding reduction and improved functionality and safety. *Mechanics of Materials*, *165*, 104173. https://doi.org/10.1016/J.MECHMAT.2021.104173

229. Tan, N., & van Arkel, R. J. (2021). Topology Optimisation for Compliant Hip Implant Design and Reduced Strain Shielding. *Materials 2021, Vol. 14, Page 7184*, *14*(23), 7184. https://doi.org/10.3390/MA14237184

230. Cook, S. D., Patron, L. P., Lavernia, C. J., Gibian, J. T., Hong, T. S., & Bendich, I. (2023). Fracture of Contemporary Femoral Stems: Common Trends in This Rare Occurrence. *The Journal of Arthroplasty*, *38*(7), S285–S291. https://doi.org/10.1016/J.ARTH.2023.04.025

231. Nijenhuis, T. A., Bolink, S. A. A. N., & Brokelman, R. B. G. (2020). Fatigue fracture of an uncemented Zweymüller femoral stem at the neck–shoulder junction. *BMJ Case Reports CP*, *13*(11), e236328. https://doi.org/10.1136/BCR-2020-236328

232. Jang, B., Kanawati, A., Brazil, D., & Bruce, W. (2013). Laser etching causing fatigue fracture at the neck–shoulder junction of an uncemented femoral stem: A case report. *Journal of Orthopaedics*, *10*(2), 95–98. https://doi.org/10.1016/J.JOR.2013.04.007

233. Yang, C. T., Wei, H. W., Kao, H. C., & Cheng, C. K. (2009). Design and test of hip stem for medullary revascularization. *Medical Engineering & Physics*, *31*(8), 994–1001. https://doi.org/10.1016/J.MEDENGPHY.2009.06.001

234. Arabnejad Khanoki, S., & Pasini, D. (2013). Fatigue design of a mechanically biocompatible lattice for a proof-of-concept femoral stem. *Journal of the Mechanical Behavior of Biomedical Materials*, *22*, 65–83. https://doi.org/10.1016/j.jmbbm.2013.03.002

235. López, I., Echeverry-Mejía, J., Ortiz, J. G., & Juha, M. (2023). Selection methodology of femoral stems under fatigue loading conditions. *Computer Methods in Biomechanics and Biomedical Engineering*, *26*(10), 1198–1207. https://doi.org/10.1080/10255842.2022.2112186

236. Corda, J., Chethan, K. N., Shenoy, S., Shetty, S., Bhat, S., & Zuber, M. (2023). Fatigue life evaluation of different hip implant designs using finite element analysis. *Journal of Applied Engineering Science*, *21*(3), 896–907. https://doi.org/10.5937/jaes0-44094

237. Reginald, J., Kalayarasan, M., Chethan, K. N., & Dhanabal, P. (2023). Static, dynamic, and fatigue life investigation of a hip prosthesis for walking gait using finite element analysis. *International Journal of Modelling and Simulation*, *43*(5), 797–811. https://doi.org/10.1080/02286203.2023.2212346;CTYPE:STRING:JOURNAL

238. López Galiano, I. C., Echeverry-Mejía, J., Ortiz, J. G., Zambrano, H. R., & Juha, M. (2024). Design of titanium uncemented femoral stems for hip prosthesis suitable for the Colombian young adult population. *Computer Methods in Biomechanics and Biomedical Engineering*, *27*(7). https://doi.org/10.1080/10255842.2023.2205978

239. Galih, T., Aghni, U. S., Damisih, Nandang, S., Mirza, W., Giri, W. A., Nyoman, J. I., Winda, R., Siti, A. A., Muhammad, D. G., Dita, A. S., Saddam, H., & Riastuti, F. (2024). Fatigue Experimental of AS-CAST Ti-6Al-7Nb Implemented on Designed Femoral Stem for Indonesian People Through Finite Element Analysis. *Strojnícky Časopis - Journal of Mechanical Engineering*, *74*(3), 105–120. https://doi.org/10.2478/scjme-2024-0038

240. Wang, L., Li, S., Yan, M., Cheng, Y., Hou, W., Wang, Y., Ai, S., Yang, R., & Dai, K. (2020). Fatigue properties of titanium alloy custom short stems fabricated by electron beam melting. *Journal of Materials Science & Technology*, *52*, 180–188. https://doi.org/10.1016/j.jmst.2020.02.047

241. Delikanli, Y. E., & Kayacan, M. C. (2019). Design, manufacture, and fatigue analysis of lightweight hip implants. *Journal of Applied Biomaterials and Functional Materials*, *17*(2). https://doi.org/10.1177/2280800019836830

242. Croitoru, A. S. M., Pacioga, B. A., & Comsa, C. S. (2017). Personalized hip implants manufacturing and testing. *Applied Surface Science*, *417*, 256–261. https://doi.org/10.1016/j.apsusc.2017.02.185

243. Wu, M. W., Lin, Q. E., Ni, K., Wang, P., Ku, M. H., Chang, S. H., Chiu, J. L., Hsin, T. E., Li, C. L., & Wang, C. K. (2024). Novel functionally-graded material design of additive manufactured Corrax maraging stainless steel lattice. *Materials & Design*, *241*, 112940. https://doi.org/10.1016/J.MATDES.2024.112940

244. *Arcam EBM Q10plus*. (n.d.). Retrieved December 12, 2025, from https://www.landre.nl/wp-content/uploads/2024/04/Brochure-Arcam-EBM-Q10-Plus-Landre.pdf

245. Schijve, J. (2003). Fatigue of structures and materials in the 20th century and the state of the art. *International Journal of Fatigue*, *25*(8), 679–702. https://doi.org/10.1016/S0142-1123(03)00051-3

246. ASTM F 2996-13. (2013). F 2996-13 Standard Practice for Finite Element Analysis (FEA) of Non-Modular Metallic Orthopaedic Hip Femoral Stems. *ASTM International,West Conshohocken, PA, Www.Astm.Org*.

247. Eldesouky, I., Harrysson, O., Marcellin-Little, D. J., West, H., & El-Hofy, H. (2017). Pre-clinical evaluation of the mechanical properties of a low-stiffness cement-injectable hip stem. *Journal of Medical Engineering & Technology*, *41*(8), 681–691. https://doi.org/10.1080/03091902.2017.1394391

248. Foti, P., Astaraee, A. H., Bagherifard, S., du Plessis, A., Wan, D., Berto, F., & Razavi, N. (2026). Fatigue performance of Ti6Al4V lattices: Relative density as a partial quantitative predictor. *International Journal of Fatigue*, *206*, 109447. https://doi.org/10.1016/j.ijfatigue.2025.109447

249. *Topological Optimization of Ti-6Al-4V Knee Prostheses Through Lattice Structures for Enhanced Mechanical Performance | SpringerLink*. (n.d.). Retrieved September 7, 2025, from https://link.springer.com/chapter/10.1007/978-3-031-47784-3_9

250. Aziziderouei, M., Chen, Z., Pasang, T., Newby, M., & Tao, Y. (2020). Effect of Lack of Fusion Formed during Electron Beam Powder Bed Fusion of Ti-6Al-4V Alloy on Impact Toughness. *Journal of Materials Engineering and Performance*, *29*(8), 4978–4990. https://doi.org/10.1007/s11665-020-05004-4

251. Raghavendra, S., Molinari, A., Cao, A., Gao, C., Berto, F., Zappini, G., & Benedetti, M. (2021). Quasi-static compression and compression–compression fatigue behavior of regular and irregular cellular biomaterials. *Fatigue & Fracture of Engineering Materials & Structures*, *44*(5), 1178–1194. https://doi.org/10.1111/ffe.13422

252. Hao, Y. L., Yang, R., Niinomi, M., Kuroda, D., Zhou, Y. L., Fukunaga, K., & Suzuki, A. (2002). Young's modulus and mechanical properties of Ti-29Nb-13Ta-4.6Zr in relation to α″ martensite. *Metallurgical and Materials Transactions A*, *33*(10), 3137–3144. https://doi.org/10.1007/s11661-002-0299-7

253. Al Zoubi, N. F., Tarlochan, F., Mehboob, H., & Jarrar, F. (2022). Design of Titanium Alloy Femoral Stem Cellular Structure for Stress Shielding and Stem Stability: Computational Analysis. *Applied Sciences*, *12*(3), 1548. https://doi.org/10.3390/app12031548

254. Niu, J., Choo, H. L., Sun, W., & Mok, S. H. (2018). Numerical study on load-bearing capabilities of beam-like lattice structures with three different unit cells. *International Journal of Mechanics and Materials in Design*, *14*(3), 443–460. https://doi.org/10.1007/s10999-017-9384-3

255. Tsai, M.-H., Yang, C.-M., Hung, Y.-X., Jheng, C.-Y., Chen, Y.-J., Fu, H.-C., & Chen, I.-G. (2021). Finite Element Analysis on Initial Crack Site of Porous Structure Fabricated by Electron Beam Additive Manufacturing. *Materials*, *14*(23), 7467. https://doi.org/10.3390/ma14237467

256. *Compressive Mechanical Properties of Lattice Structures with Varied Structural Parameters Prepared by Stereolithography*. (n.d.). Retrieved November 19, 2025, from https://www.mdpi.com/1996-1944/18/16/3898

257. Güden, M., Alpkaya, A. T., Hamat, B. A., Hızlı, B., Taşdemirci, A., Tanrıkulu, A. A., & Yavaş, H. (2022). The quasi-static crush response of electron-beam-melt Ti6Al4V body-centred-cubic lattices: The effect of the number of cells, strut diameter and face sheet. *Strain*, *58*(3), e12411. https://doi.org/10.1111/str.12411

258. Schijve, J. (Ed.). (2009). *Fatigue of Structures and Materials*. Springer Netherlands. https://doi.org/10.1007/978-1-4020-6808-9

259. Critical assessment of the fatigue performance of additively manufactured Ti–6Al–4V and perspective for future research. (2016). *International Journal of Fatigue*, *85*, 130–143. https://doi.org/10.1016/j.ijfatigue.2015.12.003

260. Gao, X., Tao, C., & Wu, S. (2023). Anisotropic high cycle fatigue property estimation for laser additive manufactured Ti6Al4V alloy dependence on tomographic imaging of defect population. *Journal of Materials Research and Technology*, *22*, 1971–1982. https://doi.org/10.1016/j.jmrt.2022.12.069

261. Chen, B., Wu, Z., Yan, T., He, Z., Sun, B., Guo, G., & Wu, S. (2022). Experimental study on mechanical properties of laser powder bed fused Ti-6Al-4V alloy under post-heat treatment. *Engineering Fracture Mechanics*, *261*, 108264. https://doi.org/10.1016/j.engfracmech.2022.108264

262. Hu, Y., Wu, S., Xie, C., Wu, W., & Zhang, J. (2021). Fatigue life evaluation of Ti–6Al–4V welded joints manufactured by electron beam melting. *Fatigue & Fracture of Engineering Materials & Structures*, *44*(8), 2210–2221. https://doi.org/10.1111/ffe.13490

263. Zhai, Y., Galarraga, H., & Lados, D. A. (2016). Microstructure, static properties, and fatigue crack growth mechanisms in Ti-6Al-4V fabricated by additive manufacturing: LENS and EBM. *Engineering Failure Analysis, Special Issue on the International Conference on Structural Integrity*, *69*, 3–14. https://doi.org/10.1016/j.engfailanal.2016.05.036

264. Galarraga, H., Warren, R. J., Lados, D. A., Dehoff, R. R., & Kirka, M. M. (2017). Fatigue crack growth mechanisms at the microstructure scale in as-fabricated and heat treated Ti-6Al-4V ELI manufactured by electron beam melting (EBM). *Engineering Fracture Mechanics*, *176*, 263–280. https://doi.org/10.1016/j.engfracmech.2017.03.024

265. Bellini, C., Borrelli, R., Cocco, V. D., Franchitti, S., Iacoviello, F., Maletta, C., & Mocanu, L. P. (2024). Fatigue crack growth in Ti-6Al-4V EBMed samples: Impact of powder recycling. *Procedia*

Structural Integrity, Third European Conference on the Structural Integrity of Additively Manufactures Materials (ESIAM23), *53*, 129–135. https://doi.org/10.1016/j.prostr.2024.01.016